Reforming the Freedom of Information Act *p. 35*

Frigatebirds surf up-drafts to fly long and far *pp. 26 & 74*

Britain's EU exit: How big a blow to research? *p. 11*

Science

$15
1 JULY 2016
sciencemag.org

AAAS

REALITY CHECK

South Africa's challenging quest to end AIDS *p. 18*

CONTENTS

1 JULY 2016 • VOLUME 353 • ISSUE 6294

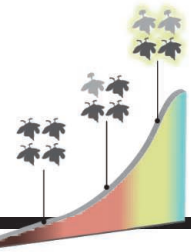

32 & 69
Plant reproduction in a changing climate

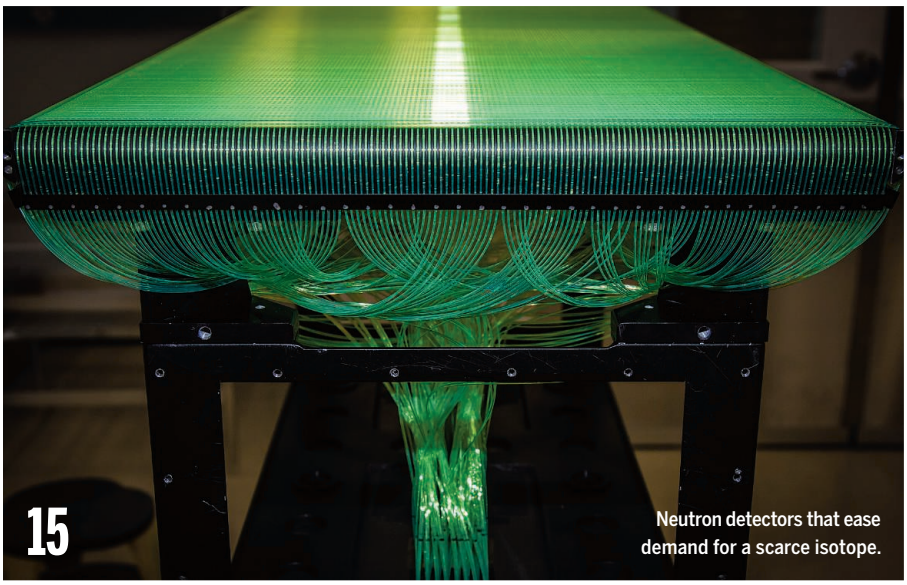

15 Neutron detectors that ease demand for a scarce isotope.

NEWS

IN BRIEF

IN DEPTH

FEATURE

INSIGHTS

LETTERS

PERSPECTIVES

POLICY FORUM

35

PHOTO (TOP): GENEVIEVE MARTIN/ORNL

Published by AAAS

CONTENTS

1 JULY 2016 • VOLUME 353 • ISSUE 6294

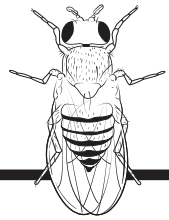

33 & 67
A genetic tool for malaria control?

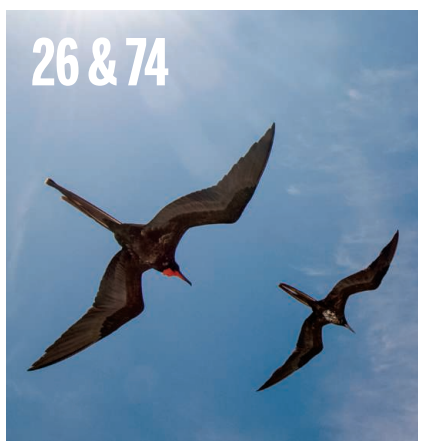

ON THE COVER

South Africa has pledged to end AIDS by 2030. Antiretroviral drugs like those on the cover are key to the effort because they make infected people less likely to transmit HIV. But with 18% of the world's HIV-infected people, the country faces the huge challenge of ramping up treatment to all in need. See page 18. *Photo: James Oatway*

SCIENCE (ISSN 0036-8075) is published weekly on Friday, except the last week in December, by the American Association for the Advancement of Science, 1200 New York Avenue, NW, Washington, DC 20005. Periodicals mail postage (publication No. 484460) paid at Washington, DC, and additional mailing offices. Domestic individual membership and subscription (51 issues): $165 ($74 allocated to subscription). Domestic institutional subscription (51 issues): $1522; Foreign postage extra: Mexico, Caribbean (surface mail) $55; other countries (air assist delivery) $89. First class, airmail, student, and emeritus rates on request. Canadian rates with GST available upon request, GST #1254 88122. Publications Mail Agreement Number 1069624. **Printed in the U.S.A.**
Change of address: Allow 4 weeks, giving old and new addresses and 8-digit account number. **Postmaster:** Send change of address to AAAS, P.O. Box 96178, Washington, DC 20090–6178. **Single-copy sales:** $15.00 current issue, $20.00 back issue prepaid includes surface postage; bulk rates on request. *Science* is indexed in the *Reader's Guide to Periodical Literature* and in several specialized indexes.

Published by AAAS

Science
AAAS
1200 New York Avenue, NW, Washington, DC 20005
Bateman House, 82-88 Hills Road, Cambridge, UK CB2 1LQ

SUBSCRIPTION SERVICES For change of address, missing issues, new orders and renewals, and payment questions: 866-434-AAAS (2227) or 202-326-6417, FAX 202-842-1065. Mailing addresses: AAAS, P.O. Box 96178, Washington, DC 20090-6178 or AAAS Member Services, 1200 New York Avenue, NW, Washington, DC 20005

INSTITUTIONAL SITE LICENSES 202-326-6730 **REPRINTS:** Author Inquiries 800-635-7181 **COMMERCIAL INQUIRIES** 803-359-4578 **PERMISSIONS** 202-326-6765, permissions@aaas.org **AAAS Member Services** 202-326-6417 or http://membercentral.aaas.org/discounts

Science serves as a forum for discussion of important issues related to the advancement of science by publishing material on which a consensus has been reached as well as including the presentation of minority of conflicting points of view. Accordingly, all articles published in *Science*—including editorials, news and comment, and book reviews—are signed and reflect the individual views of the authors and not official points of view adopted by AAAS or the institutions with which the authors are affiliated.

INFORMATION FOR AUTHORS See pages 624 and 625 of the 5 February 2016 issue or access www.sciencemag.org/authors/science-information-authors

EDITORIAL

Science and Brexit

Graeme Reid is Chair of Science and Research Policy at University College London, UK. Email: graeme.reid@ucl.ac.uk

Last week's dramatic vote by the United Kingdom (UK) to leave the European Union (EU) was the culmination of a heated referendum campaign that questioned the value of partnerships between the UK and the EU. Now, with many bridges burned—or at least charred—where do political leaders go next? Politicians in the UK and EU are going to need every available foundation on which to rebuild trust and mutual interests. They will need to discover once again how to work in partnership. It will be a long and difficult process; one in which science should play a crucial role.

The referendum provoked rousing exchanges, but there were also many calm analyses, notably from the House of Lords Science and Technology Committee and the Royal Society. The overwhelming majority of UK scientists supported membership in the EU at every stage of the debate, while opinion in the wider population was clearly divided. University leaders (who seldom reach consensus on anything) called with one voice for the UK to remain in the EU. A community of nations with a common framework for funding research, establishing priorities, sharing facilities, and moving people and ideas across borders brings advantages to its scientific community. Compromises, challenges, and regulatory burdens come as part of the package but, on balance, British scientists found the EU an enormously attractive feature of our continent. Those attractions remain.

Now, there is scope for science as one of the starting points for the critical process of building a new relationship between the EU and the UK. Existing commitments alone mean that UK science will have a major role in Europe for years to come. For example, the EU's Joint European Torus, located near Oxford, provides vital expertise to the much larger ITER nuclear fusion facility under construction in France. Also, EU-funded infrastructures for social science, biological data, and radio astronomy are based in the UK, and countless robust EU research programs depend on UK leadership and collaborations. Right now, over 18% of funding returned to the UK from EU resources is for R&D, making this one of the larger parts of the EU's relationship with the UK. Thus, many thousands of relationships between students, academics, and administrators bind together scientists in the UK and other European countries. All of this gives science enormous potential as a foundation for building a new relationship between the EU and the UK. But foundations are no use if they are undermined by political wrangling. There will need to be investment of time, political capital, and money to bolster the science UK-EU bridge.

"...science [has] enormous potential as a foundation for ...a new relationship between the EU and the UK."

British scientists must now work hard to urge policy-makers to promote continued scientific collaborations and advise on how to move ahead. Maybe the UK's next prime minister should offer to host new international research facilities along with the EU, or increase the support the UK gives to UK businesses and universities considering EU collaborations. Perhaps further research fellowships for talented scientists wishing to collaborate or move across the EU could be launched. These are not hollow gestures: They would bring benefits in their own right as well as rebuild trust. The scientific community could brainstorm such possibilities and work closely with the government on next steps. Indeed, wise policy-makers understand that R&D develops people for the wider labor market, creates new products and businesses, and makes huge contributions to health care, defense, the natural environment, and public services. These benefits are built on strong collaborative science.

One of the great strengths of UK science is its international culture and the recognition that the best minds, wherever they are from, can together tackle shared challenges. Leaving the EU does not mean an end of this quality, but it requires profound changes in the practicalities behind it.

– Graeme Reid

10.1126/science.aah4245

NEWS

> “There are several possible explanations, but they have not been investigated, which is really quite unfortunate.”
>
> **Pediatrician Carol J. Baker** at Baylor College of Medicine in Houston, Texas, on why the “nasal spray” flu vaccine apparently did not work last season. On 22 June, the Advisory Committee on Immunization Practices recommended that the vaccine not be used in the upcoming season.

IN BRIEF

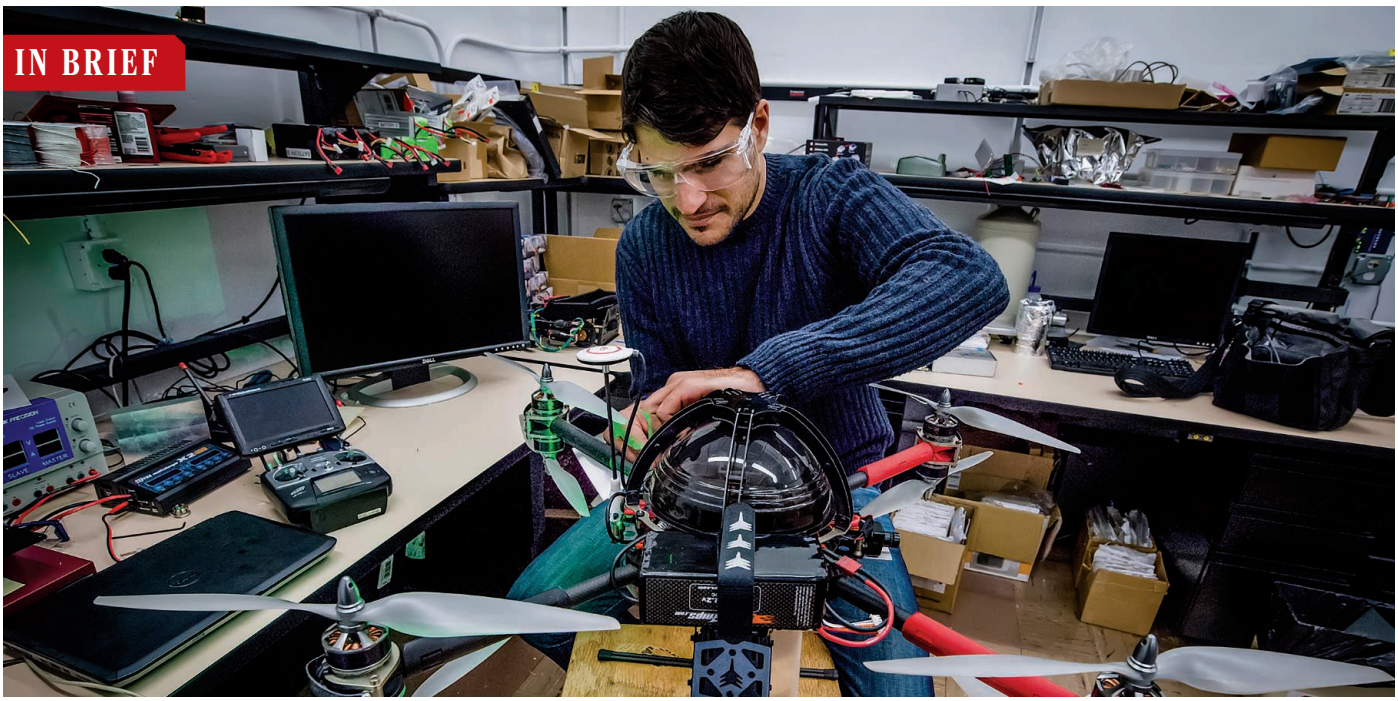

A researcher at the University of California, Berkeley, prepares a quadcopter drone for survey flight.

Scientists applaud new drone rules

New U.S. rules on drone operations are getting a general thumbs-up from researchers who rely on the unmanned aircraft to collect data and make observations. That marks a shift from a few years ago, when worried researchers went to court to block Federal Aviation Administration (FAA) drone regulations that they argued were overly restrictive and would harm academic science. The final FAA rules, released by the White House on 21 June and set to take effect in August, seem to have alleviated many concerns. The regulations apply to drones that are lighter than 25 kilograms and operate at 160 kilometers per hour or less. The rules forbid operators from flying the aircraft above 122 meters in altitude, or over people not participating in their operations. Flights must be during the daytime and the aircraft must remain in the pilot’s line of sight. And drone pilots must be at least 16 years old and take an online test to earn a government permit; unpermitted operators can fly a drone under the direct supervision of a pilot. The new regulations are “fantastic, just late,” says biogeographer Benjamin Heumann of Central Michigan University in Mount Pleasant, who uses drones to map biodiversity and invasive species and had been critical of early versions. “This is where we should have been 2 years ago.”

http://bit.ly/_dronerules

AROUND THE WORLD

A daring South Pole rescue

SOUTH POLE, ANTARCTICA | Two sick workers were evacuated from the National Science Foundation’s Amundsen-Scott South Pole research station last week in a rare and perilous rescue mission after doctors determined that the workers required treatment in a hospital for an unspecified medical emergency. Every February, after the scientists have left, a few dozen people hunker down to spend the long, dark austral winter at the station. Most medical problems are handled with medical personnel on site or in consultations with stateside doctors. The decision to evacuate someone is not made lightly, because such a rescue operation is both dangerous and elaborate: Medevacs require planes that can operate in the extreme cold and are equipped with skis, as the South Pole station has no tarmac. On 15 June, two propeller-driven Twin Otter planes departed from Calgary, Canada,

and traveled via South America to the British Antarctic Survey's Rothera Research Station on the Antarctic Peninsula. One remained there as a backup, while the other traveled another 2400 kilometers to the South Pole. On 22 June, the workers were transported from the South Pole station to Rothera and departed for South America the following day. Their specific medical conditions and destination hospital were not disclosed for medical privacy reasons.
http://bit.ly/southpolerescue

Antidoping lab suspended

RIO DE JANEIRO, BRAZIL | The World Anti-Doping Agency (WADA) has suspended the accreditation of the Brazilian Doping Control Laboratory, the lab tasked with drug testing for the Rio Olympics. In a statement issued 24 June, the agency cited an unspecified "non-conformity" with its international laboratory standards as the reason for the suspension. The same lab had previously lost its accreditation in 2013, after which Brazil invested $60 million to bring the lab's practices up to international standards in time for the Olympics. The lab has 21 days to appeal the decision, WADA says. Lab coordinator Francisco Radler did not comment on plans to appeal, but said he is "confident that after the visit of WADA auditors, which was already scheduled for early July, the situation will be cleared and settled."

Lionfish thrive in Mediterranean

LIMASSOL, CYPRUS | The venomous lionfish, native to tropical Indian and western Pacific waters, continues its march around the globe. In the last few decades, the invasive fish has spread rapidly, with sightings along the eastern U.S. coast, the Caribbean, and the southeastern coast of Brazil. Now, the lionfish (*Pterois miles*) is thriving in the Mediterranean Sea, scientists report this week in *Marine Biodiversity Records*. Reports by divers and fishermen reveal that *P. miles* has colonized the entire southeastern coast of Cyprus in just 1 year, the team found. Lionfish reproduce rapidly, spawning every 4 days; the voracious fish, which have venomous spines that deter predators, can also rapidly reduce biodiversity where they colonize. In the Mediterranean, the widening and deepening of the Suez Canal, combined with warming waters, may be helping the lionfish thrive.

A lionfish spotted in the Mediterranean Sea.

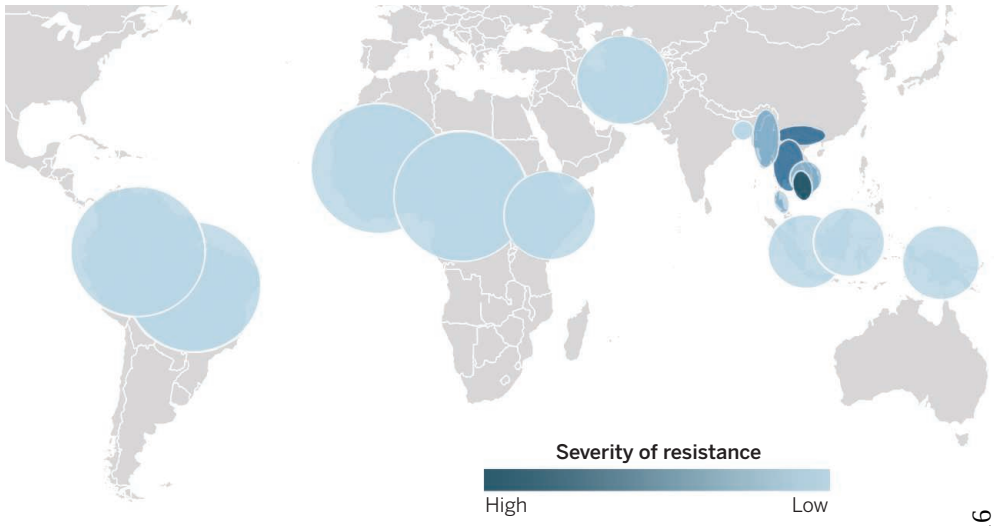

Mapping resistance to malaria drugs

Most modern malaria treatments are based on a derivative of artemisinin, a substance found in the leaves and flowers of the mugwort plant. But increasingly, malaria parasites are becoming resistant to artemisinin, particularly in Southeast Asia (*Science*, 22 April, p. 398). To map the spread of this resistance, an international group of scientists from more than 50 countries, led by the Pasteur Institute in Phnom Penh, examined some 14,000 samples of malaria parasites from around the world. Artemisinin resistance is centered in Southeast Asia at the moment, and hasn't affected African regions—yet, they reported last week in *The New England Journal of Medicine*. This map, the researchers say, should help identify and track new shifts in resistance more quickly.

Weed killer gets reprieve

BRUSSELS | The controversial herbicide glyphosate will remain on the market in Europe for another 18 months, after the European Commission this week extended a key deadline for its reapproval. The use of glyphosate has been hotly debated ever since the International Agency for Research on Cancer declared it a "probable human carcinogen" in March 2015. Regulatory agencies had previously declared glyphosate safe when properly used, and the European Food Safety Authority was on track to renew its approval (*Science*, 20 November, p. 892). But opponents of the herbicide campaigned for the commission not to renew the market license, which was to expire on 30 June. Glyphosate manufacturers and the farm lobby objected fiercely, and member states could not come to an agreement. This week, the commission granted the extension to give the European Chemicals Agency, which is responsible for classification and labeling of hazardous chemicals, time to complete a review of the carcinogenicity of glyphosate. Some member states had requested the review in May.

NEWSMAKERS

Three Qs

Conservationist **Mike Sutton** is one of two official proponents of a November ballot measure to legalize the cultivation and sale of marijuana in California. A similar 2010 ballot measure was defeated. Sutton was previously vice president of the Monterey Bay Aquarium and served for 8 years on the California Fish and Game Commission, including 2 years as its president. He is currently board chairman of the Capitola, California–based nonprofit Ocean Champions. *Science* talked with Sutton recently about the upcoming vote.

Q: Why is an environmentalist getting behind this effort?
A: I really got into this because of my service on the state Fish and Game Commission. I saw the consequences of the illegal [marijuana] industry in California. Believe it or not, it's California's biggest cash crop by value, and yet it's been subject to prohibition since the 1930s.

Q: What are the industry's ecological impacts?
A: These illegal grow operations are often on public land; they use fertilizers and pesticides [and] they steal water from nearby sources in the middle of the biggest drought in California history. And on top of that, [they] divert the attention of game wardens … who are supposed to be out there preventing poaching and protecting our wildlife.

Q: How would this ballot measure help?
A: Legalization will go a long way toward getting this industry out of the shadows and into the light. One of the biggest aspects of this ballot measure is that it would give rise to tax revenues in the tens of millions of dollars that are dedicated to environmental restoration and cleanup of these sites and public lands.

Architect of Tevatron dies

Helen Edwards, the physicist who led the design and construction of the United States's largest atom-smasher—the Tevatron collider at the Fermi National Accelerator Laboratory in Batavia, Illinois—died on 21 June at age 80. The first major accelerator to employ superconducting magnets, the Tevatron smashed protons into antiprotons from 1985 to 2011. Physicists there discovered the top quark in 1995. Edwards played a particularly prominent role in designing the accelerator, says Maury Tigner, a physicist emeritus at Cornell University. "She was determined, she was very skilled, and if she set out to do something she did it," Tigner says. "Everybody respected that." Born in Detroit, Michigan, Edwards earned her Ph.D. at Cornell in 1966. She was an "inspirational" leader, says Marion White, a physicist at Argonne National Laboratory in Lemont, Illinois, who worked with her in recent years. "She was very passionate about what she was doing," White says, "but it wasn't, 'I, Helen' … it was 'Go, team!'"

Smog obscures the morning sun over the Huangpu River in Shanghai, China. New data suggest that air pollution deaths will rise by 15% globally by 2040.

Helen Edwards in 1983 at the Tevatron's completion.

Surgeon faces new charges

Erstwhile star surgeon and stem cell pioneer **Paolo Macchiarini** faces preliminary charges of involuntary manslaughter and causing bodily injury, according to an Associated Press story. Macchiarini was already facing a slew of ethical accusations, including embellishing the success of his groundbreaking trachea transplants in published papers and lying on his CV. The most damning accusation, however, is that he used his risky technique on patients who weren't in a life-threatening condition and could have lived for many years. At

PHOTOS: (TOP TO BOTTOM) GEORGE CLERK/ISTOCK PHOTO; FERMI NATIONAL ACCELERATOR LABORATORY/U.S. DEPARTMENT OF ENERGY

A price tag on limiting air pollution deaths

A relatively modest investment in cleaner energy could prevent millions of deaths from air pollution in coming decades, concludes a 27 June analysis from the International Energy Agency (IEA) in Paris. Poor air quality is now the world's fourth leading cause of premature death, IEA reports in its *World Energy Outlook for 2016*, behind high blood pressure, poor diet, and smoking. And the agency predicts air pollution deaths will rise 15%, to 7.5 million annually, by 2040 unless nations act to reduce soot and fumes from vehicles, industry, and household stoves and heaters. Cities in Asia and Africa will be especially hard hit by pollution, even as urban air in Europe and North America gets cleaner. But "no country—rich or poor—can claim that the task of tackling air pollution is complete," said IEA Executive Director Fatih Birol in a statement. And nations could halve air pollution by spending $4.8 trillion by 2040 on emissions controls and clean energy sources, IEA concludes. The extra investment would amount to just 7% of expected global energy outlays.

least one of them, a Russian woman, has died. The scandal, rekindled by a three-part documentary on Swedish television in January, led the Karolinska Institute in Stockholm to fire Macchiarini in March (*Science*, 1 April, p. 14). Macchiarini has denied wrongdoing.

FINDINGS

Groundwater study sparks debate

California is in the fifth year of its worst drought in more than a millennium. In response, the state is pumping billions of gallons of water from the ground, depleting natural water reserves faster than they can be replenished. Now, a controversial new study suggests that the state may hold much more water than thought in very deep aquifers. The study, published online this week in the *Proceedings of the National Academy of Sciences*, is the first to measure California's groundwater below 300 meters. Satellite images can reveal changes in an aquifer's water storage, but not the total volume of water it contains; direct well samples, meanwhile, are costly and challenging to obtain. So the researchers turned to public records: They analyzed salinity data from 360 oil and gas fields in the state, as well as the geology of the region, to extrapolate the volume of water in aquifers beneath the state's Central Valley down to 5000 meters. The aquifers, they found, may hold three to four times more freshwater than thought. However, they note, up to 35% of it could be vulnerable to oil and gas development—and much of the water is so deep that it isn't practical to extract.
http://bit.ly/CalideepGW

BY THE NUMBERS

351

Number of U.S. businesses that advertise unapproved stem cell treatments online for health issues such as orthopedic injuries or neurological disorders. Beverly Hills, California, has the most individual clinics (18) offering such treatments; New York City follows with 14 (*Cell Stem Cell*).

€1.5 million

Amount bequeathed in an Italian accountant's will to University of Milan neuroscientist Elena Cattaneo "for her to use in scientific research as best she sees fit." Cattaneo says she plans to use it to create fellowships for young scientists.

€670 million

Amount of a new investment by France in genomics and personalized medicine, announced last week. The funds, of which about €230 million will come from industry, will go toward the establishment of a dozen genome sequencing centers in the country.

CORRECTION

In the 17 June issue of *Science*, a graphic on p. 1387 accompanying the Feature story "Ancient DNA divide" by Ann Gibbons omitted a credit for the data used. Citation numbers for papers in human ancient DNA in the past 5 years came from a search done for *Science* by Thomson Reuters's Web of Science. The search was designed to assess whether European labs had more citations than U.S. ones, rather than to rank labs with the most citations. In the same graphic, a grant to Eske Willerslev was reported at $7.6 million; this one-time grant was awarded to the University of Copenhagen's Centre for GeoGenetics as a whole and included funding for salaries, facilities, and three additional co–principal investigators.

EUROPE

'Brexit' casts pall on future of U.K. science

Funding, freedom of movement, and a voice in Europe's science policy are all in question

By **Daniel Clery**, *in London*

Days after the United Kingdom's momentous vote in favor of leaving the European Union, the U.K. science community is seething with anxiety. No one knows whether U.K. research will struggle or thrive when the divorce goes ahead. Neither the U.K. government nor the European Commission had thought through beforehand how U.K. research could untangle itself from the European enterprise—or whether it even needs to. "It was just unimaginable to us that they would actually leave," says Robert-Jan Smits, head of the European Union's Directorate-General for Research and Innovation in Brussels. "It's a big, big shock."

As *Science* went to press, it was not clear when, or whether, the United Kingdom would invoke Article 50 of the 2007 Lisbon Treaty, which would set in motion negotiations on how to leave the bloc. Some Brexit opponents still held out a faint hope that online petitions or economic crisis might force a rethink.

But scientists have pressing and practical questions: Can U.K. researchers continue to apply for E.U. grants? Will reviewers looking at a proposal involving U.K. scientists wonder about their commitment? Will U.K. postdocs have trouble taking up positions on the continent, and vice versa? What is the future for E.U. facilities on U.K. soil?

Some Brexit supporters—a minority among scientists—are sanguine. "What makes science brilliant is cooperation the world over, without having to be in a political union," says Jamie Martin, a science policy adviser to the pro-Leave group Scientists for Britain. Speaking at a gathering of scientists and politicians at the House of Commons on 28 June, U.K. science minister and Brexit opponent Jo Johnson stressed that "nothing changed overnight" and that for now, scientists can still apply for E.U. grants. "We need as a community to minimize the damage and maximize the opportunities ... I'm optimistic about the future," said Johnson, a brother of former London mayor and Leave campaign leader Boris Johnson.

But most scientists are dismayed by the looming rift. "This is a really serious worry for me ... I fear desperately for U.K. science," says Steve Cowley, director of the Culham Centre for Fusion Energy near Oxford, U.K. "There is no way I can pretend to be anything other than dispirited and disappointed," says Simon Wessely, president of the Royal College of Psychiatrists here. Former E.U. science adviser Anne Glover, now a vice-dean at the University of Aberdeen in the United Kingdom, says she's "a bit bewildered and ashamed by my own country."

E.U. money is one of the things that U.K. scientists will miss. They generally do well in the race for E.U. programs such as Horizon 2020, the 7-year, €80 billion scheme that ends in 2020; the United Kingdom has also managed to bag several billions for research from the so-called Structural Funds, a separate E.U. pot to help poorer regions in Europe develop. In the 7 years preceding 2014, the United Kingdom paid about €5.4 billion for both programs combined, according to a 2015 Royal Society report, and it got €8.8 billion in return.

That's a modest amount compared with the United Kingdom's own science spending; the Framework Programme 7, for instance, the predecessor to Horizon 2020, accounted for a mere 3% of the United

A modest contribution

Of the €226.3 billion the United Kingdom spent on R&D between 2007 and 2013, only 3% was funded by Framework Programme 7, Horizon 2020's predecessor.

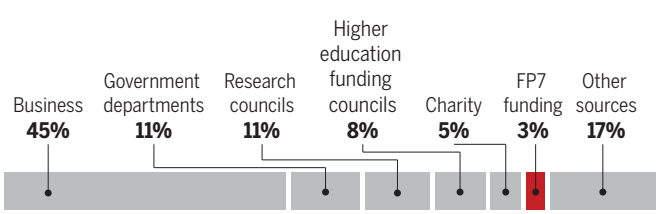

CREDITS: (PHOTO) REX FEATURES/AP IMAGES; (DATA) ROYAL SOCIETY; ADAPTED BY J. YOU/*SCIENCE*

Young pro–European Union campaigners protest outside the British Parliament in London.

Kingdom's investments in science and innovation between 2007 and 2013 (see graphic, p. 12). What's more, Brexit supporters have argued, the United Kingdom could easily make up for the shortfall using the money it saves on its total annual contribution to the European Union, currently some €17 billion.

The United Kingdom could also continue to participate in European funding schemes by becoming an "associate" member of Horizon 2020, in which case it would pay an annual contribution in line with gross domestic product. Fifteen non-E.U. countries already participate in this way, including Norway, Turkey, Israel, and Tunisia.

But those are all smaller countries; it's not clear whether the European Union is prepared to give a research powerhouse—and a deserting member state—a similar deal. "The U.K. will try to obtain an association agreement, but this will take time. And I don't know what the overall conditions will be to grant them the same status," says Helga Nowotny, a former president of the European Research Council (ERC) and a professor emerita at ETH Zurich in Switzerland.

The future of international collaborations and the freedom of students and researchers to move across the channel once the United Kingdom splits off are other key worries. Brexit "will disproportionately affect young European researchers, who are largely funded on soft money" and often move to follow grants, Nowotny says. "I find this extremely worrying." "Over the long term, it is hard to see how this doesn't lead to a reduction in the numbers of students and researchers choosing to come to the U.K.," adds James Wilsdon, a social scientist and expert on research policy at the University of Sheffield in the United Kingdom.

Even the current uncertainty may be enough to deter some scientists, Wilsdon says. "Let's imagine a talented postdoc in Italy or Germany who was thinking of taking her grant from the ERC if she got it to study at the London School of Economics or Cambridge. Will she really want to come now with this sort of uncertainty?"

The European Union may try to force the United Kingdom to retain an open immigration policy, however, as a condition for trade deals and access to E.U. programs. In 2014, when Switzerland sought to restrict immigration from new E.U. member states, the union suspended its associate status, which threatened to end Swiss participation in Horizon 2020; negotiations continue to resolve the issue. "The Swiss example is the most worrying thing," Brexit supporter Martin concedes. On the other hand, Europe benefits from keeping the United Kingdom in Horizon 2020, Martin says: "The opportunities British universities offer to European researchers and students are unparalleled."

Many other things are at stake. One is the United Kingdom's influence on international science policy. "We've taken away our policy voice," says science policy expert Mike Galsworthy of the London-based campaign group Scientists for EU. U.K. scientists were instrumental in shaping important agencies such as ERC and the European Strategy Forum on Research Infrastructures, Smits says. "They were so embedded in European science policy, so visible, so present," he says.

A withdrawal from the European Union almost certainly means that the United Kingdom can no longer host the European Medicines Agency, the bloc's medical watchdog, now headquartered in London. Another European facility sited in the United Kingdom is the Joint European Torus (JET), a fusion reactor operated by the United Kingdom on behalf of Euratom, the nuclear arm of the European Union. JET is a key testbed in preparations for the international ITER fusion project, currently under construction in France. "Even though it might not be easy, I am confident that we can find ways to continue the very successful collaboration with the U.K.," says Tony Donné, head of EUROfusion, a collaboration of European fusion labs that manages research on JET. Cowley agrees. "We've got to do it, having spent all this money" making JET as ITER-like as possible, he says. "To have a €2 billion piece of kit and throw it away because no agreement can be reached would be foolish in the extreme."

More problems are sure to emerge from the divorce, which Glover warns may be less than amicable. But in the end, the health of European science is "a pretty narrow slice of what most of us are feeling concerned about today, which is concern for our kids, for our community, for our country," Wilsdon says. One thing that has many scientists upset, he says, is the antielitist tone of the debate, particularly in the Leave campaign. The prominent Conservative politician and Brexiteer Michael Gove, for example, said that Brits "have had enough of experts."

"The contempt with which they have treated expertise and evidence in this process we cannot and we will not and we should not forget," Wilsdon says. "We can't go from this to a situation 12 months from now where Boris Johnson is prime minister and he is coming around and giving a speech at the Royal Society and we're all standing up and clapping like seals and saying thank you, prime minister, for grants."

Scientists and policymakers from around the continent will soon have a chance to commiserate on U.K. soil—and to discuss ways forward. The city of Manchester will host EuroScience Open Forum, a major biannual meeting sponsored by the European Commission, in July. "It's ironic that the meeting is in the U.K. this year," Smits says. "On the other hand, it will allow British scientists to send a strong signal that they see the value of the E.U. and of international collaboration—now more than ever." ■

With reporting by Kai Kupferschmidt, Gretchen Vogel, Erik Stokstad, Martin Enserink, and Tania Rabesandratana.

Benefits from Brussels

The United Kingdom was second only to Germany in funds received from Framework Programme 7 between 2007 and 2013, and it received additional support for science from the Structural Funds, for a total of €8.8 billion. It paid only €5.4 billion in return during that period.

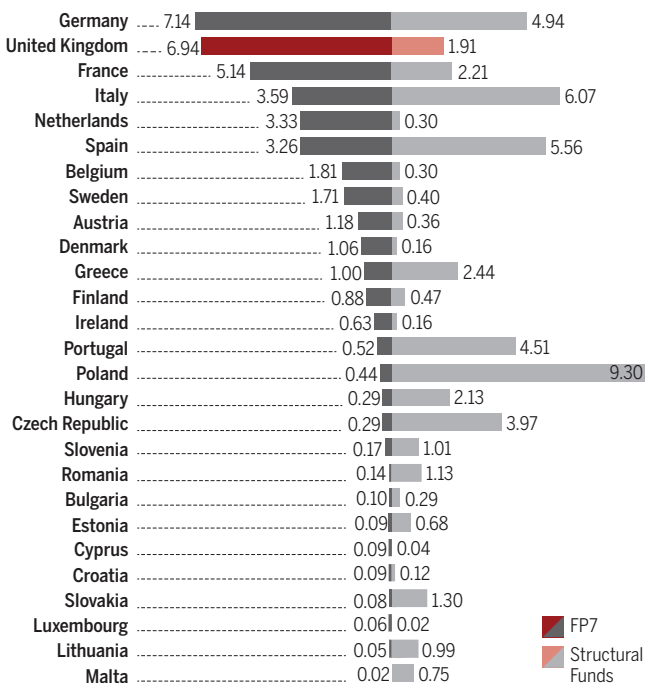

DATA: ROYAL SOCIETY. ADAPTED BY V. ALTOUNIAN/*SCIENCE*

IMMUNOLOGY

Fighting autoimmunity with immune cells

Engineered T cells can selectively destroy sources of enemy antibodies

By **Mitch Leslie**

Autoimmune diseases share a grim similarity with cancer: People's own cells become their enemies. But a new study published online in *Science* reveals a happier parallel, suggesting that a therapy designed to harness the immune system to attack cancer cells may also cull the turncoat immune cells behind certain autoimmune diseases.

The approach relies on chimeric antigen receptor T cells, or CAR T cells: immune cells genetically modified to home in on a desired target on cancer cells or—in this case—on rogue B cells, another immune cell type. The new study only gauged the CAR T cells' capabilities in the lab dish and in mice, but some scientists are already using the B word: breakthrough. Removing only the self-destructive cells has been the holy grail for treating autoimmune diseases, "but it hasn't been solved for any autoimmune disease up to now," says dermatologist Rüdiger Eming of the Philipp University of Marburg in Germany. "Using this approach you are able to specifically target the pathogenic immune cells without major side effects."

The basic recipe for producing CAR T cells dates to the late 1980s. Scientists remove some of a cancer patient's T cells and genetically tweak them so that receptors on their surface can detect a specific molecule, or antigen, on cancer cells. After the modified T cells are returned to the patient's bloodstream, they hunt down and destroy cancer cells carrying that antigen.

In some early clinical trials, CAR T cells showed dramatic results against blood cancers such as acute lymphoblastic leukemia, banishing all signs of disease from more than 90% of patients (*Science*, 20 December 2013, p. 1432). Now, researchers are starting to test them against solid tumors, with dozens of trials underway for cancers from glioblastoma to lymphoma.

A few scientists are also investigating whether CAR T cells could rein in our immune system. In some people with hemophilia, for example, the cells might be able to prevent the normal immune response from destroying recombinant factor VIII, a clot-promoting protein used to treat the condition. The new work goes further by suggesting that CAR T cells could be protective in an autoimmune disease.

For the study, dermatologist Aimee Payne and cancer immunotherapist Michael Milone of the University of Pennsylvania and their colleagues took aim at the autoimmune disease pemphigus vulgaris. In this illness, B cells pour out antibodies that attack desmoglein 3, a protein that helps lock together cells in the skin and mucous membranes. Sufferers develop painful blisters—on the skin; in the mouth or esophagus, where they can hinder eating and swallowing; and even in the eyes, nose, and genitals. Untreated, the disease can kill.

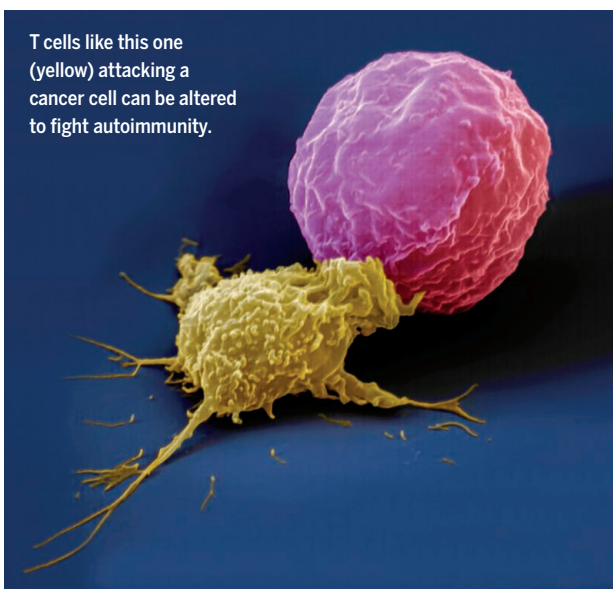

T cells like this one (yellow) attacking a cancer cell can be altered to fight autoimmunity.

The steroid prednisone and immune-suppressing drugs can improve quality of life, but they can cripple the immune system's ability to fight off pathogens, sometimes leading to fatal infections. A more specific drug, the monoclonal antibody rituximab, kills only B cells but can still dangerously undermine immune function.

To determine whether CAR T cells could do better, Payne, Milone, and colleagues engineered human T cells to recognize just those B cells that produce antibodies against desmoglein 3. They then showed that the engineered cells could kill cancerous B cells that pump out the same antibodies—first in a lab dish, then in mice injected with the B cells to mimic the human disease. The CAR T cells slashed the amount of anti–desmoglein 3 antibodies in the animals' blood and prevented them from developing mouth blisters.

One worry is that CAR T cells could go astray, for example by attacking incorrect targets in the skin. But the researchers saw no signs of such misdirected attacks in mice given human CAR T cells and human skin grafts. The scientists did see encouraging hints that some CAR T cells settled down in the mice and thus might keep symptoms from returning. "We show that these cells specifically kill the disease-specific B cells and have potential for long-term disease control," Payne says.

"This is a very unique, novel, and creative approach," says molecular immunologist A. Razzaque Ahmed of Tufts University School of Medicine in Boston. But hematologist Zachary Spigelman, also of Tufts, cautions that the mouse experiments didn't demonstrate that CAR T cells can reverse the disease, only that they can prevent symptoms from developing. "It's an excellent first step, but it's not a proof of concept."

Pemphigus vulgaris is rare, with fewer than 100,000 cases in the United States, but Payne and Milone think CAR T cells could be unleashed on other autoimmune diseases in which self-targeted antibodies attack a single main antigen. One is myasthenia gravis, which can cause severe weakness and even death as antibodies destroy the molecule that allows nerves to stimulate muscles.

CAR T cells may not work for more common and complex autoimmune diseases, such as multiple sclerosis or type 1 diabetes, and they have triggered serious side effects in some cancer patients. Because autoimmune diseases are not usually fatal immediately, "the bar [for safety] is higher than in the cancer setting," Milone says.

So he and his colleagues are moving cautiously. Next, "we want to cure dogs with pemphigus," Payne says. Dogs are one of the few species besides humans that naturally develop the disease. Besides benefitting the animals, she says, demonstrating that CAR T cells can alleviate pemphigus vulgaris in dogs "would break down barriers for potential future human trials." ■

IMAGE: EYE OF SCIENCE/SCIENCE SOURCE

A prototype lithium-based scintillator at Oak Ridge National Laboratory could save helium-3.

PHYSICAL SCIENCE

Researchers rise to challenge of replacing helium-3

New nuclear detector technologies forgo scarce isotope

By **Richard Stone**

U.S. researchers have finally overcome a little-known legacy of the 11 September 2001 terrorist attacks: a dire shortage of helium-3 (He-3). The rare isotope has unique properties that make it invaluable for applications from cryogenics to detecting hidden nuclear bomb material. But in 2008, experts feared that the U.S. stockpile, managed by the Department of Energy's (DOE's) Isotope Program, would run out as early as 2010, as terrorism fears drove up demand for detectors of nuclear material.

Faced with a crisis, DOE curtailed He-3 sales while it and other agencies raced to find He-3 alternatives. Observers hail the effort. "There's been a revolution over the past year and a half," says Jeffrey Lacy, president of Proportional Technologies Inc. (PTI), a Houston, Texas–based firm that has devised one alternative. A dozen others are in the pipeline or already on the market, and the He-3 stockpile is out of danger. DOE's reserves will top 160,000 liters by 2040, according to a new projection the department provided to *Science*. "The supply should last well over a century," says Isotope Program Director Jehanne Gillo in Germantown, Maryland.

He-3—ordinary helium minus one neutron—might have remained obscure if not for the Cold War. As the United States and other nuclear powers expanded their arsenals, they started accumulating He-3, which is produced by the decay of tritium, a radioactive isotope of hydrogen that vastly boosts the explosive power of hydrogen bombs. For years, weapons labs vented He-3, which is not radioactive, into the atmosphere as waste.

That changed after scientists learned how useful the exotic gas could be. In physics labs, refrigerators using a mix of He-3 and He-4 as a coolant attain temperatures of less than 0.01 K. The isotope is also adept at capturing neutrons. That has made it the material of choice for neutron detectors, which contain tubes filled with the gas. After capturing a neutron, He-3 splits into a tritium nucleus and a proton, which ionize other He-3 atoms and generate an electrical signal. "Helium-3 is the gold standard," says Richard Kouzes, a physicist at DOE's Pacific Northwest National Laboratory in Richland, Washington, who has led efforts there to deal with the He-3 crisis.

A major customer for He-3 is the Spallation Neutron Source (SNS), an accelerator at Oak Ridge National Laboratory in Tennessee that smashes neutrons into materials and molecules to reveal their structure. Some of SNS's detectors are tens of square meters in area. "We use a lot of helium-3, anywhere we can and where we can afford it," says Oak Ridge condensed matter physicist Ken Herwig, who oversees instrumentation at SNS.

But it wasn't until after the 9/11 attacks that the run on He-3 supplies began. To guard against nuclear terrorism, the U.S. Department of Homeland Security ordered hundreds of He-3 radiation portal monitors for screening people, vehicles, and cargo at border checkpoints and at embassies, military bases, and other facilities. The detectors look for neutrons streaming from so-called special nuclear materials: enriched uranium and weapons-grade plutonium.

"If you're detecting neutrons, you have a pretty good indication that there's special nuclear material around," says Jeffrey Musk, chief of nuclear technologies detection, research, and development at the U.S. Defense Threat Reduction Agency (DTRA) in Fort Belvoir, Virginia.

Skyrocketing demand for He-3 for portal monitors outstripped the 6000-odd liters of He-3 added to the U.S. reserve each year. As U.S. stocks were drawn down, the other major global supplier—Russia—sharply cut back on its sales. After DOE capped sales at 14,000 liters a year in 2009, federal programs rummaged for unused supplies, and the price of He-3 shot up from about $100 a liter to as much as $3000 a liter in 2011.

Unmasking hidden nuclear material

Fissile material emits fast neutrons. A moderator slows them, aiding capture by a detector containing helium-3 or another conversion material.

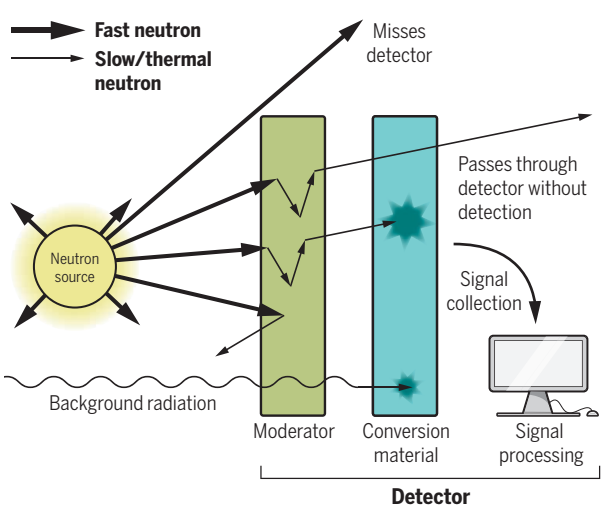

CREDITS: (PHOTO) GENEVIEVE MARTIN/ORNL; (GRAPHIC) C. BICKEL/*SCIENCE*; (DATA) GAO

He-3 alternatives were already in development. DTRA Program Manager Hongguo Zhu explains that agencies were aiming for detector materials "that can not only detect neutrons, but also measure the energy of neutrons" more precisely. The agencies also wanted better portable and hand-held devices. The supply crunch, however, put the research into overdrive.

One approach that has bolted ahead of the field is boron-coated straws. PTI, for example, coats the inside of copper straws with boron carbide enriched in boron-10, which, like He-3, is a fat target for neutrons. After capturing a neutron, the boron-10 atom transmutes into highly energetic lithium-7 and α particles, which ionize argon gas inside the tube. "It's the best helium-3 alternative technology for large area neutron detectors," Zhu says.

Two other firms—Radiation Monitoring Devices Inc. in Watertown, Massachusetts, and Kromek in Sedgefield, U.K.—have rolled out hand-held radioisotope detectors based on a different principle: scintillation, or light emitted by a substance when struck by an energetic particle. These scintillators rely on lithium-6, another isotope that's good at snaring neutrons. Combined with other materials, it yields a device that emits light when struck by a neutron or a gamma ray. The light pulses from neutrons have longer rise and decay times than those created by gamma rays, making it simple to tell the signals apart and giving scintillators a versatility that other neutron detectors lack.

The U.S. Defense Advanced Research Projects Agency (DARPA) in Arlington, Virginia, wants to do more than simply replace existing detectors. It's halfway into a 4-year program called SIGMA to develop detector networks that will continuously monitor radiation in U.S. cities. He-3 alternatives are key to making SIGMA viable, says DARPA Program Manager Vincent Tang, a plasma physicist. "DTRA and other agencies have been doing a great job of building up the base of technologies," he says.

Scientists, too, have big plans for neutron detectors. SNS, for example, intends to eventually add another 22 beam lines. "Where we can use helium-3, we will use it," Herwig says. But SNS already uses lithium-6 scintillators for some detectors, and it is exploring whether PTI's boron-coated straws are up to snuff for other detectors. Meanwhile, the SNOLAB near Sudbury, Canada, deep underground in a former mine, is considering boron-coated straws for a detector that would study neutrinos spawned in supernovae.

Because of the rapid rise of He-3 alternatives, "federal demand for He-3 has plummeted," Gillo says. Now, Tang says, "I don't worry about helium-3 anymore." ■

PHOTO: WORLD METEOROLOGICAL ORGANIZATION/FLICKR

ATMOSPHERIC SCIENCE

CFC bans pay off as Antarctic ozone layer starts to mend

Study shows hole has shrunk since 2000 thanks to restrictions on chlorine chemicals

By **Eric Hand**

Since it was discovered in 1985, the Antarctic ozone hole has been a potent symbol of humankind's ability to cause unintended environmental harm. But now comes a glimmer of good news: The void in the ozone layer is shrinking. "It's a big surprise," says Susan Solomon, an atmospheric chemist at the Massachusetts Institute of Technology in Cambridge. "I didn't think it would be this early."

Although the hole will not close completely until midcentury at the earliest, the healing is reassuring to scientists who pushed for the Montreal Protocol. The 1987 international agreement phased out the industrial production of chlorofluorocarbons (CFCs): chlorine-containing chemicals that help trigger the destruction of stratospheric ozone, which screens out cancer-causing ultraviolet light. "You want to be sure that the actions we've taken have had the intended effect," says Solomon, who led the study published online by *Science* this week.

Layers of depleted ozone open up over both poles just as winter gives way to spring. During the wintertime cold, nitric acid and water condense out of the atmosphere and form wispy clouds. The surfaces of the cloud particles host chemical reactions that release chlorine that came from CFCs. The chlorine, in turn, goes on to destroy ozone—but only in the presence of light. That is why, over Antarctica, ozone loss doesn't get going in earnest until September, the beginning of the southern spring, when light returns to the pole. Peak losses are usually in October, and that is when researchers have typically taken stock of year-to-year changes in the hole.

Solomon and her colleagues found that the healing trend was more apparent in the month of September. Using a combination of measurements from satellites, ground-based instruments, and weather balloons, her team found that, since 2000, the September hole has shrunk by 4 million square kilometers—an area bigger than India.

To determine whether declining pollutants deserve credit for the recovery, the researchers used a 3D atmospheric model to separate the effects of the chemicals from those of weather, which can affect ozone loss through winds and temperature, and volcanic eruptions, which deplete ozone by pumping sulfate particles into the upper

Weather balloon measurements and other data showed that last September, the ozone hole was 4 million square kilometers smaller than its peak size.

atmosphere. The sulfate can play the same role as cloud particles, activating chlorine.

The model helped explain why scientists saw a record ozone hole in October 2015, a glaring exception to the shrinking trend. Solomon and some other researchers at first wondered whether the recovery might be behind schedule. But the model showed that it was a fluke due to the eruption of the Calbuco volcano in southern Chile 6 months earlier, and it confirmed that declining levels of chlorine and its chemical cousin bromine were indeed responsible for the longer term healing trend. "To me, it's the first time that has been shown unequivocally," says Neil Harris, an atmospheric scientist at the University of Cambridge in the United Kingdom who was not involved in the work.

Solomon's study follows earlier claims of healing, including a 2011 study that got some attention (*Science*, 8 April 2011, p. 160). But those studies separated out the effects of natural variability using relatively simple statistical techniques, and many researchers questioned the assumptions that went into them. Using a 3D model to tease out the underlying trend is a "much more sophisticated way to do the attribution," says Ross Salawitch, an atmospheric scientist at the University of Maryland, College Park.

Still, Paul Newman, who runs NASA's Arctic Ozone Watch website at Goddard Space Flight Center in Greenbelt, Maryland, is puzzled by Solomon's finding that only half of the 4-million-square-kilometer shrinkage trend was due to a reduction in chlorine and bromine. The other half appeared to be due to weather. Weather effects ought to cancel out on average, resulting in no trend, he says. "If we can't explain half the signal, then can we really explain the 50% of the signal we think we know?" Newman says the finding could point to a problem with Solomon's model. Or, he says, it may reflect a real shift in polar weather, driven by climate change. "She's uncovered a real scientific puzzle here," he says.

Regardless, the result is a satisfying full-circuit ride for Solomon, who in 1986 led the study that first identified stratospheric clouds as the chlorine reaction sites, and who played important roles in the scientific assessments for the Montreal Protocol and subsequent status reports. "The fact that we've made a global choice to do something different and the planet has responded to our choice can't help but be uplifting," she says. ■

U.S. SCIENCE POLICY

Scientists cheer Senate bill

Long-awaited successor to COMPETES Act rejects controversial House approach to managing federal research

By **Jeffrey Mervis**

A bill working its way through the U.S. Senate may not show scientists the money, but it definitely shows them the love. The Senate commerce and science committee was expected this week to approve the authorization bill, which governs programs at the National Science Foundation (NSF) and the National Institute of Standards and Technology (NIST) and federal science education and innovation activities. It endorses NSF's current approach to choosing what research to fund, proposes ways for universities and scientists to save time and money complying with federal rules, and backs expansion of NSF's wildly popular Innovation Corps program to train budding academic entrepreneurs.

In sharp contrast to several related bills adopted by the Republican-controlled U.S. House of Representatives that have infuriated many researchers, the Senate bill enjoys support from both parties. That still may not be enough to win Senate passage, much less to prevail in any negotiations with the House. But research lobbyists say it demonstrates that the bill's chief sponsors, senators Cory Gardner (R–CO) and Gary Peters (D–MI), heard their pleas. "We very much appreciate the senators' consultation with the university and science community," says Peter McPherson, president of the Association of Public and Land-grant Universities in Washington, D.C.

> ***"[NSF's] peer review and merit review processes ... should be preserved."***
> Senate bill 3084

Two years in the making, the American Innovation and Competitiveness Act (S. 3084) would replace the 2010 America COMPETES Act, which expired in 2013. The bill backs the two criteria NSF has long used to select the best research—scientific quality and broader societal impacts—and the agency's overall approach to grantsmaking. "Its peer review and merit review processes have successfully identified and funded scientifically and societally relevant research and should be preserved," the bill declares.

Lobbyists hope the Senate's stance will help defuse a tense, 3-year battle between scientists and the House science committee. The committee's chairman, Representative Lamar Smith (R–TX), and other Republican legislators have ridiculed dozens of NSF grants as frivolous or a waste of money. The House bills would require that every NSF grant be "in the national interest," a provision NSF officials say is unnecessary and potentially restrictive. Smith and other lawmakers have also urged NSF to cut spending on the social sciences and geosciences.

University officials also welcome the Senate bill's approach to monitoring federal spending without strangling academic institutions in red tape. One change aims to avoid wasted effort by having funding agencies wait to collect some information from grant applicants until their proposals stand a good chance of being funded. Another would create a central database of investigator profiles that all agencies could tap during the grants-making process.

The 150-page bill would also create an outside advisory council to guide the government's $3 billion investment in training a tech-savvy workforce. It backs greater use of prizes, competitions, and crowdsourcing to foster innovation. It tells NSF to beef up efforts to broaden participation in science by women and underrepresented minorities. And by changing the first word in the title of the Experimental Program to Stimulate Competitive Research to "Established," the bill would make permanent a government-wide program launched 37 years ago at NSF that gives grants to states with relatively little federal research activity.

The bill urges NSF to create a program to fund "mid-sized projects," those costing tens of millions to a few hundred million dollars. The agency has previously balked at the idea, although officials agree that NSF currently has no mechanism to fund unsolicited proposals in that price range.

Authorization bills often set high spending targets for appropriators. But S. 3084 authorizes 2017 funding for NSF and NIST at levels already approved by a Senate spending panel, and proposes just a 4% increase in 2018. McPherson calls it "a positive step, but lagging when our global competitors are doubling down on their investment." ■

SOUTH AFRICA'S BID TO END AIDS

The tools exist, but the country's epidemic—the largest in the world—won't yield easily

By **Jon Cohen**, *in South Africa*; *Photography by* **James Oatway**

On a Wednesday morning in April, a line of 600 HIV-infected people snakes through the hallways to the first waiting room of the Themba Lethu Clinic, a wing of the Helen Joseph Hospital in Johannesburg, South Africa. In most places in the country, where clinics are overtaxed, this would presage a wait of up to 10 hours. But here something different is happening. Staffers at computer monitors swiftly log in people and dispatch them for triage or, if they have tuberculosis, a special area away from others. Those who only need their antiretroviral (ARV) drugs walk directly to the pharmacists, who retrieve each patient's electronic medical record and use a robotic system to pull drugs from shelves and fill orders. The average wait time is 30 minutes to 2 hours to complete a doctor or nurse visit and 15 minutes at the pharmacy. A prototype ATM promises to further speed visits by directly dispensing ARV pills; one day, it is hoped, similar pill machines in shopping malls could make some clinic visits unnecessary.

"This is an awesomely efficient place,"

Lesego Kgaladi, 20, who lives in Soweto, South Africa, was infected with HIV at birth. At school, she speaks out about stigma and misunderstandings about HIV.

says Ian Sanne, who heads Right to Care, a nongovernmental organization that runs this and several other clinics in collaboration with the health department. In developed countries, where patients complain about much shorter waits, this boast might seem absurd. But in South Africa, the Themba Lethu Clinic is celebrated as an example of what can be done to care for large numbers of HIV-infected people. This is at once a compliment to the clinic and a hint of the country's overwhelming HIV/AIDS challenge.

South Africa has pledged to ramp up efforts to end its massive HIV/AIDS epidemic, the world's largest. Come September, it will offer every infected person ARVs, which both stave off disease and make people less infectious. The immediate goal is to reach what is known as 90-90-90 by 2020: to have 90% of infected people aware of their status, 90% of known positives start ARVs, and 90% of that group drive the amount of virus in their bloodstream down to undetectable levels. The theory is that as viral levels drop, transmission will, too, leading the epidemic to spiral downward. This 90-90-90 target is the cornerstone of a grand campaign, articulated by the Joint United Nations Programme on HIV/AIDS (UNAIDS) and widely embraced by world leaders, to end the AIDS epidemic "as a global public health threat" by 2030.

In a nation estimated to have at least 6.6 million HIV-infected people—18% of the world's total—the drive to hit 90-90-90 by 2020 seems overly ambitious to many experts. And the obstacles faced by South Africa provide a sobering reality check to the lofty, laudable aspiration of ending AIDS, a topic that promises to occupy center stage later this month in Durban at the biannual International AIDS Conference.

SOUTH AFRICA has already made enormous gains against its HIV/AIDS epidemic. When it last hosted this international gathering in 2000, then-President Thabo Mbeki and his health minister questioned whether HIV even causes AIDS, triggering widespread outrage (*Science*, 28 April 2000, p. 590). At the time, only the wealthiest South Africans had access to ARVs, which cost about $5000 per person for an annual supply. But by the end of 2015, the price had dropped to $100, and 3.4 million HIV-infected South Africans were receiving ARVs—more than in any other country in the world. South Africa, in fact, consumes the same amount of the life-saving drugs as Asia and the Pacific, North America, and western and central Europe combined.

As a result, life expectancy jumped 9 years between 2005, when ARVs started to become widely available, and 2014. The country has pioneered innovative ways to deliver the drugs and help people stay on them. And South Africa's strong cadre of HIV/AIDS investigators has made the country a hub of cutting-edge basic research and clinical trials. "Given our resources, we've done amazing things," says Glenda Gray, an HIV/AIDS researcher who heads South Africa's Medical Research Council in Cape Town.

PODCAST

Hear a podcast with author Jon Cohen at http://bit.ly/pod_6294.

Yet almost half the infected population today is still untreated. Some have not suffered enough immune damage from the virus to merit ARVs under current government policy. Many other infected people don't know their status or never seek care, and still others who start treatment have difficulty taking their daily pills for years on end. Estimates suggest that because of failures in this "care continuum," only about one in four HIV-infected South Africans has fully suppressed the virus. "We have to ride two horses at the same time," says Fareed Abdullah, who heads the quasi-governmental South African National AIDS Council (SANAC) in Pretoria. "One is to improve our system so that the more than 3 million on treatment are retained in care and properly managed, and we also have to expand to a group that is largely asymptomatic and well."

Adding to those challenges is South Africa's alarming HIV incidence—the percentage of the population that becomes infected each year. The government reports that HIV incidence has dropped from a high of 1.67% in adults in 2005 to 1.22% last year, but that still translates into 330,000 new infections a year. The rate is shockingly high in women under 25, especially in the hardest hit province, KwaZulu-Natal, where incidence tops 6% in some communities.

Health Minister Aaron Motsoaledi, who acknowledges that the country's aggressive HIV/AIDS program got off to a late start because of Mbeki (*Science*, 22 February 2013, p. 898), is confident that South Africa has the willpower and the money to hit 90-90-90. "Can we afford not to treat people?" Motsoaledi asks. "Surely, we're going to pay much more dearly socially, politically, and economically if you can't." To that end, the government, which already spends $1.2 billion a year on HIV/AIDS and receives another $300 million in foreign aid, is adding $65 million annually through 2019.

But a new report concludes that meeting the UNAIDS target will require an additional $8 billion over the next 5 years. "UNAIDS is pushing very hard on our health ministry, which doesn't want to be caught short again and wants to make the case that we can reach 90-90-90," says Linda-Gail Bekker, who co-runs the Desmond Tutu HIV Foundation (DTHF) in Cape Town and is one of the co-authors of the report. The cost of drugs is just one part of the equation, she says. Reaching the target will also require massive HIV testing and the costly delivery of ARVs to patients who must be monitored and then helped if they're not suppressing the virus. "I'm really, really anxious about the resources it's going to take."

There are scientific questions, too. The assumption that reaching the 90-90-90 target will end AIDS is based on mathematical models that factor in ARV "coverage" in combination with other proven prevention strategies like male circumcision, condom promotion, and behavior change efforts. Researchers note that in large epidemics like the one in South Africa, which has spread far beyond "concentrated" populations such as men who have sex with men and sex workers, such strategies could prove less effective than expected, allowing HIV to continue spreading at high rates even after the country reaches 90-90-90.

Models and reality

A model predicts how different HIV/AIDS response scenarios would affect new infection rates, or incidence. As seen on the map, some areas of the country have far more HIV than others.

HIV incidence scenarios

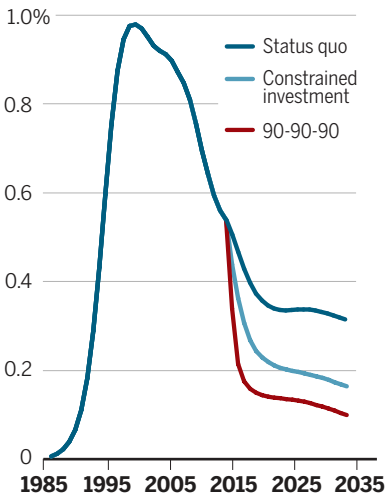

HIV antenatal clinic prevalence (2013)

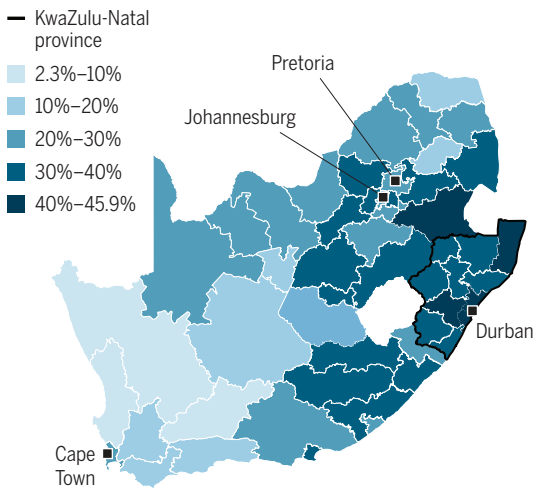

Sex and age

HIV infects far more girls and young women than boys and men of the same age in South Africa. The sex difference shrinks by age 35, then prevalence drops.

HIV prevalence by age groups (2012)

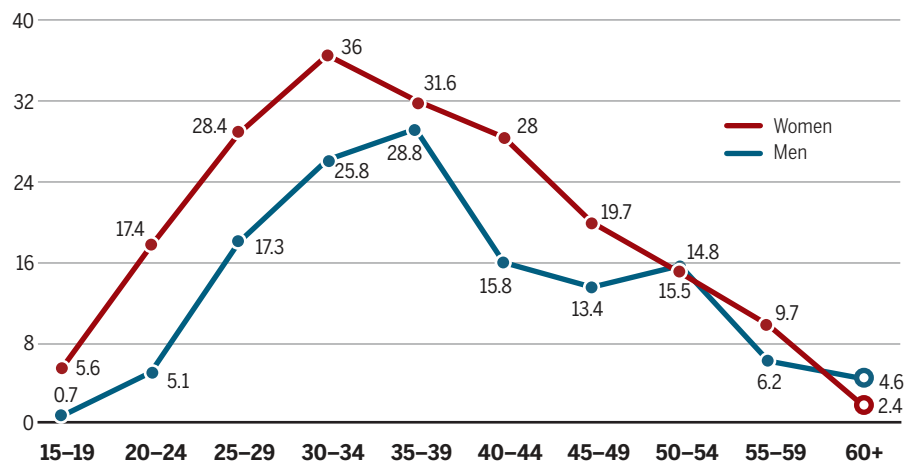

The cycle of infection in South Africa

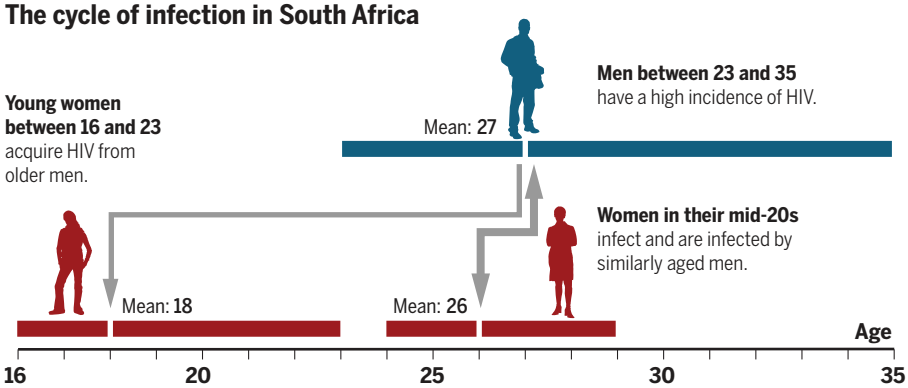

Epidemiologist Salim Abdool Karim, who runs the Centre for the AIDS Programme of Research in South Africa (CAPRISA) in Durban, points to recent data from Botswana that call into question the model's assumptions. Botswana, which is relatively wealthy and has a tiny population of 2 million, has nearly reached 90-90-90, as shown in a study published online on 23 March in *The Lancet*. But incidence has barely budged, in part because the missing 10-10-10 continue to spread the virus. "For a country that's close to 90-90-90, the incidence is ridiculously high," Karim says. "It's scandalous." A report published by SANAC and the health department further questions the 90-90-90 mathematical modeling. Even if 90-90-90 leads to big declines in new infections by 2030, that report suggests that incidence in South Africa's population of 53 million will not quite drop below 0.1%—the level that UNAIDS says it must reach for an epidemic to end.

The bottom line is that it remains an open question whether the 90-90-90 treatment goal really can stop the spread of HIV in South Africa. Some of the world's largest controlled trials of treatment as prevention (TasP) are underway in the country to try to answer it.

IN AN AREA known as Mfekayi in rural KwaZulu-Natal, two dozen people are sitting on the shaded porch of a plywood shack waiting their turn to see a counselor. The shack is the Egedeni Clinic, and the people are participants in a 28,000-person, multisite clinical trial that will assess the precise relationship between increased levels of HIV suppression in a community and drops in incidence. At Egedeni and 10 other clinics across the province, the TasP study offers ARVs to all infected participants. Another 11 TasP clinics instead offer treatment in keeping with current government recommendations, meaning that people start ARVs only after their immune systems show signs of damage.

One by one, the participants hand bottles of ARVs they received a month earlier to the counselors, who count the remaining pills. This ritual, which is a crude way to monitor adherence, underscores an obvious limitation of the underlying strategy: Even if ARVs make people less infectious, TasP relies on the fickle relationship humans have with taking daily medications.

Run by the Africa Centre for Population Health in nearby Mtubatuba, TasP is the furthest along of four similar large trials in sub-Saharan Africa that are examining the care continuum and the real-world outcome of "universal treatment." Early analysis of TasP results found that fewer than 40% of

CREDITS: (GRAPHIC) A. CUADRA/*SCIENCE*; (DATA SOURCES) PREVALENCE MAP: THE 2013 NATIONAL ANTENATAL SENTINEL HIV PREVALENCE SURVEY SOUTH AFRICA; INCIDENCE GRAPH: SOUTH AFRICAN HIV AND TB INVESTMENT CASE. SANAC AND NATIONAL DEPARTMENT OF HEALTH; PREVALENCE BY SEX: SOUTH AFRICAN NATIONAL HIV PREVALENCE, INCIDENCE AND BEHAVIOUR SURVEY, 2012. HUMAN SCIENCES RESEARCH COUNCIL; CYCLE: S. NEFTEL AND MICHAEL DELLAR *ET AL*., CAPRISA

the people who tested positive sought care within 3 months, as recommended. This first step still has remained a major stumbling block on the road to 90-90-90.

At the International AIDS Conference later this month, the researchers plan to reveal whether their intervention has reduced incidence. "This will be the first opportunity to assess whether, in fact, the biological rationale is actually true in practice," says Deenan Pillay, a clinical virologist who heads the Africa Centre. But Pillay says the study already has made clear that ending AIDS is not simply a matter of "let's just treat everyone and everything will be OK." In the final analysis, he says, the power of TasP depends as much on human behavior as it does on biology.

JACQUALINE NCUBE, a 19-year-old restaurant worker, first took an HIV test when she was in high school. At the time, Ncube spent many hours after school hanging out at DTHF's Youth Centre, which abuts the struggling township of Masiphumelele outside of Cape Town. The Youth Centre offers teens internet access, holds soccer matches, loans surfboards, and provides care at a health clinic. Kids also earn "Tutus," good for shopping vouchers or food, for everything from helping the community to taking an HIV test. When Ncube got her first results, she was overwhelmed. "I really screamed," she says. She was negative.

Ncube has repeatedly tested negative, and in April 2015 she joined the Youth Centre's Pillsplus, a study of what's known as pre-exposure prophylaxis, or PrEP, in 150 teens. With PrEP, uninfected people take daily ARV pills to prevent infection. Although PrEP is a proven strategy, South Africa recommends its use only in sex workers, and Ncube is one of the first heterosexual teens in the world to take ARVs for prevention. She still uses condoms with her boyfriend, but says she wanted to try PrEP because "no protection is 100%."

DTHF's Bekker, who is heading Pillsplus to assess PrEP's acceptability in teens, contends that PrEP should be provided to all people at high risk of infection. "When I sit opposite a 17-year-old young woman, I have nothing to offer her," Bekker says.

CAPRISA's Karim says using PrEP in young women could be key to breaking the epidemic's back. About 30% of new infections in South Africa occur in young women between 15 and 24 years of age. The new infection rate in men in the same age bracket is more than four times lower. In some districts of KwaZulu-Natal, a woman has a 60% chance of becoming infected by age 34.

To understand the pattern of viral spread, CAPRISA and the Africa Centre mapped out the infection cycle between men and women of different ages in KwaZulu-Natal. The study analyzed the genetic sequences of HIV isolated from 858 men and women, all between 16 and 35 years old, who belonged to the same sexual networks. The viral genetics linked different isolates and indicated which ones were older, allowing the researchers to infer who infected whom. Teenage girls were infected by men who were, on average, 8 years older. After the age of 24, people typically became infected by partners their own age, with transmission more frequently moving from woman to man. "They are trying to find lifetime partners at this age," Karim says. These older men are the same group having sex with the youngest women. "We have to break the chain between men in their late 20s and teen girls," he says.

PrEP can help address shortcomings of TasP, Karim says. In the infection-cycle study, men who infected younger women had extremely high HIV levels, indicating they recently acquired the virus and thus would not appear infected on standard antibody-based tests. "If your strategy is to test and treat these people, you're not going to catch them," Karim says. Men are also less connected to the health care system and often migrate for work, he adds, making it more difficult to help those who know they are infected fully suppress the virus. Giving PrEP to young women sidesteps the male dilemma. "We just have to protect girls for 5 years in that critical risk period until they find their partners," he says.

Karim says new biomedical interventions on the horizon may bolster prevention efforts. His group plans to report at the Durban meeting that it has identified an unusual microbe linked to vaginal inflammation in women in KwaZulu-Natal. Treating it could potentially lower their risk of HIV infection. Injectable ARVs that last for 2 months are also being tested in South Africa and elsewhere, and those could eliminate the challenge of taking daily pills—a key problem for both treatment and PrEP. Next fall, South Africa plans to launch the world's only efficacy trial of an AIDS vaccine—the strongest preventive medicine of all.

For now, 90-90-90 is the most powerful tool available to South Africa in its quest to end its epidemic, even if PrEP and other new strategies ultimately are needed. SANAC's Abdullah takes a pragmatic view of meeting the UNAIDS deadline. "I think we should plan for it, because if we don't hit it by 2020, we'll do it by 2022," he predicts. "What we're really after is bringing down new infections to low levels," along with getting as many HIV-infected people as possible on treatment and living longer lives. The virus itself, Abdullah says, "will be with us for the next 100 years." ■

The Pulitzer Center on Crisis Reporting provided support for the reporting in this story.

A robot pulls antiretroviral drugs off the shelf to help Rajan Gudala's pharmacy team at the Themba Lethu Clinic.

PHOTO: JAMES OATWAY

INSIGHTS

How frigate birds soar high and far p. 26 ▸

How electrons make their escape p. 28

LETTERS

Edited by **Jennifer Sills**

NEXTGEN VOICES

Science in brief

In April, we asked young scientists to **use exactly six words to create a story about the life of a scientist in your field.** We received almost 400 responses, some frustrated, some inspiring, some humorous, and all describing a life unique to a scientist. We have printed some of the most interesting responses here. Follow *Science*'s NextGen VOICES survey on Twitter with the hashtag #NextGenSci.

On careers

First job interview. Buy hair dye.
***Wen Jiang**, Oncology, USA*

Thank goodness: Yet another 6-month contract!
***Daniela Liebsch,** Plant Biology, Sweden*

Education: Multiple university degrees. Profession: n/a.
***Wioleta Kijewska**, Computational Neuroscience, Poland*

On data

Koch postulates: TB, or not TB?
***Digby F. Warner,** Mycobacteriology, South Africa*

Big data! Clean: No statistical power.
***Abhishek Niroula,** Bioinformatics, Sweden*

Data overload: Juggling balls, many fall.
***Noa Sher,** Cell Therapy, Israel*

Calculation first, interpretation later. Or, never.
***Bongjae Kim,** Computational Materials Science, South Korea*

P equals 0.051. Repeat? Abandon? Bayes?
***Rosa Li,** Psychology and Neuroscience, USA*

Science: seeking answers amidst whack-a-mole problems.
***David Jason Garfield,** Chemistry, USA*

On setbacks

Mice eaten by cats, graduation delayed.
***Chenggang Yan,** Intelligent Information Processing, China*

The experiment failed. Or did I?
***Irina Tiper,** Immunology, USA*

Exciting new result! No...coding mistake.
***Frank X. Vazquez,** Chemistry, USA*

Results were promising, until they weren't.
***David Edward Gilbert,** Energy and Environmental Genomics, USA*

ILLUSTRATION: YASMINE GATEAU

"My new discovery!" became old today.
Han Sang Kim, *Cancer Genomics, Medical Oncology, South Korea*

On funding

New outbreak. Funding reprioritized. New outbreak.
Jonathan J. Madara, *Virology, USA*

Scooped. No grant. Back to clinic.
Agnes Hou Ngee Tay, *Genetics, Singapore*

Grant seeker: Amazing skills, sadly unfunded.
Katie A. Clark, *Molecular Genetics, USA*

Asteroid-bound spacecraft, under proposal pressure.
Christine Hartzell, *Aerospace Engineering, USA*

Funding needed for error bar revisions.
Angela Claire Tomczik, *Neuroscience, USA*

On recognition

Epilogue: Changed the world, few knew.
Greg Maguire, *Physiology and Systems Biology, USA*

...but you're not a "doctor" Dr.
Kota Hatta, *Medical Sciences, Japan*

Frequently right. Never forgotten when wrong.
Marian Peleski, *Meteorolgy, USA*

"Unsung hero in sustainability," says tombstone.
Bing Xue, *Sustainability, China*

On diversity

You're brilliant, but you're not American.
Yuka Takemon, *Genomics, USA*

Female scientist, struggle for fairness persists.
Masha Georges Savelieff, *Chemistry and Biology, USA*

Developing countries: Brains of advanced countries.
Mahmoud Mohamed Shehata, *Molecular Virology and Infectious Diseases, Egypt*

On parenthood

Reproductive scientist. Freezing her own eggs.
Germaine Goh, *Cell Biology, Singapore*

Sorry son, I should be writing.
Timothy L. Easun, *Chemistry, UK*

"Planning on children?" No right answer.
Heather M. Lee, *Immunology, USA*

ILLUSTRATION: YASMINE GATEAU

Toward "reproducibility," not "reproducing ability," Mom.
Emily Kay Petruccelli, *Neurogenetics, USA*

"Postdoc. Father. Balanced today... but tomorrow?"
Matt Wiebe, *Virology, USA*

On discovery

There's something alive in the incubator.
N. H. Diane Kim, *Bioengineering, USA*

Modern ancient Palmyra. Civilization falls, again.
Daniel H. Sandweiss, *Archaeology, USA*

Scientist, looking closely, mistakenly finds truth.
Joshua Isaac James, *Digital Forensic Science, South Korea*

Controlled chaos revealing explosive stellar events.
Gregory R. Sivakoff, *Astronomy, Canada*

Planets found. Now searching for life.
David A. Weintraub, *Astronomy, USA*

Synthetic biologist: Engineering life over coffee!
Zarrin Basharat, *Bioinformatics, Microbiology, Environmental Sciences, Pakistan*

Deep sequencing can't replace deep thinking.
Dan Webster, *Cancer Genomics, USA*

Bridging scientists with software: Challenge accepted!
Michael A. Tarselli, *Chemistry Information Systems, USA*

Diving in sand, bridging adjacent ecosystems.
Kyle Aaron Emery, *Coastal Ecology, USA*

Animal, let me in your mind.
Mirjam Johanna Guesgen, *Ethology and Zoology, Canada*

Fire Science: Hot bodies, cool heads.
Norman Joseph Alvares, *Fire Science, USA*

Old rocks, new theory, old rocks.
David W. Szymanski, *Geology, USA*

Beware the restlessness of coastal sand.
Donald C. Barber, *Geology, USA*

Surgeons should wear masks! Possibly not?
Silvio Daniel Pitlik, *Infectious Diseases, Israel*

Look! He dreams about his mom!
Bohan Zhao, *Neuroscience, China*

Thinking over the nature of thought.
Rohan Sharma, *Neuroscience, India*

Everything in moderation, or maybe not?
Ryan Alexander Coots, *Nutritional Sciences, USA*

Drought approaches; previous symbionts become enemies.
Amelia Snyder, *Plant Ecology, USA*

Hybrid rice, whole life, unchanged farmer.
Rongjun Chen, *Rice Breeding, China*

Let's create a dancing colorful bacteria.
Anibal A. Arce, *Synthetic Biology–Plants, Chile*

β-cells: Hey! Come and kill me.
Ubaid Ullah, *Type-1 Diabetes, Finland*

Budding yeast research makes better beer.
V. Sriram, *Yeast Genetics, USA*

ADD YOUR STORY!
Do you have a six-word story to add? Post it on Twitter with the hashtag #NextGenSci and tag @sciencemagazine. We may print your story and your Twitter username in an upcoming issue!

Remote area, broken shoes, good papers.
Wenjin Xia, *Geography, China*

Cut jungle. Found temple. It rained.
Felicia Beardsley, *Archaeology in the Tropical Pacific, USA*

I bunsen burnt my 1118th worm.
Eugene L. Q. Lee, *Neuroscience, USA*

On schedules

Warning: No lunch at noon seminar.
Richard Kyle Lacher, *Immunology, USA*

Carpool partner available:
5am/11pm every day.
Hoang Lu, *Chemical and Biological Engineering, USA*

Science and life, compartmentalized, need integration.
King L. Chow, *Life Science, China*

Living my life under extreme pressure.
Alexandra Seclaman, *Mineral Physics, Germany*

Post Ph.D.: 30 is new 20.
Terry McCallum, *Organic Chemistry, Canada*

Scientists, no different from lab rats.
Kingston Mak, *Developmental Biology, Hong Kong*

On publishing

Dear incompetent reviewer,
we fully agree.
Mathias V. Schmidt, *Neuroscience, Germany*

Science journalist seeks acronym-free story.
Carol Lynn Alpert, *Science Communication, USA*

Now deleting: Negative results,
never published.
Yifan Li, *Chemistry, USA*

Reviewer wants "just one"
more experiment!
Luis Mendoza, *Computational Biology, Mexico*

No prestige given for null results.
John Protzko, *Psychology, USA*

Endlessly pipetting toward first
author dreams.
Heather M. Lee, *Immunology, USA*

On motivation

Living beings make me like fossils.
Shivangi Tiwari, *Geology, India*

Engineering life, to better everyone's lives.
Do Soon Kim, *Chemical Engineering and Synthetic Biology, USA*

Persist: You can make a difference.
Sean M. Hartzell, *Conservation Biology and Herpetology, USA*

A child, looking up, becomes explorer.
Paul Kevin Byrne, *Planetary Science, USA*

Continuous failure redeemed by
fleeting success.
Ken Halvorsen, *Biophysics, USA*

Completely frustrated; insight
precedes joy. Repeat.
Timothy Michael Kernan, *Microbiology and Bioengineering, Canada*

Try. Fail. Try harder. Fail again.
Robert Kumsta, *Psychology, Germany*

Scientists: Global citizens with local burdens.
Hari Krishna Bisoyi, *Synthesis and Study of Organic Liquid Crystalline Materials, USA*

Cradle to grave fight against waste.
Jingzheng Ren, *Environmental Engineering, Denmark*

ILLUSTRATION: YASMINE GATEAU

ECOLOGY

How frigate birds soar around the doldrums

Frigate birds forage over vast distances by getting boosts from thermals and trade winds

By **Raymond B. Huey**[1] *and* **Curtis Deutsch**[2]

In 1492, Columbus encountered frigate birds while en route to the New World and noted that the bird "does not alight on the sea nor depart from land 20 leagues" (*1*). Columbus observed correctly that frigate birds do not land on the sea, but he severely underestimated how far some frigate birds fly from land. On page 74 of this issue, Weimerskirch *et al*. (*2*) show that great frigate birds (*Fregata minor*) reduce transit costs by riding strong thermal updrafts beneath or inside cumulus clouds and then gliding long distances to another thermal, searching for food along the way. By exploiting cumulus clouds and trade winds in the Indian Ocean, the birds forage around the doldrums, a largely windless zone.

Satellite technology is revolutionizing migration studies on land and sea by tracking individuals in real time for long periods (*3*, *4*). To monitor the position and altitude of frigate birds, Weimerskirch *et al*. outfitted birds with solar-powered transmitters or data-loggers to measure heart rate, wing beat frequency, acceleration, altitude, and GPS coordinates. They used weather records to determine local wind speed and direction, and a bird's behavior and heart rate to infer whether the bird was actively flapping or soaring under or within cumulus updrafts.

[1]Department of Biology, University of Washington, Seattle, WA 98195, USA. [2]School of Oceanography, University of Washington, Seattle, WA 98195, USA. Email: hueyrb@uw.edu

After breeding on an islet in the Mozambique Channel, adult frigate birds fly north to the Seychelles and forage from there for months. Some adults tracked in the study launched multiday treks, circumnavigating the doldrums (see the figure). One flew continuously for 48 days, averaging 420 km per day. Recently fledged juveniles departed separately from the breeding site and flew even farther and longer than their parents. One juvenile stayed aloft for 2.1 months; others stopped briefly on small islands but still flew almost continuously. One juvenile covered more than 55,000 km (greater than Earth's circumference) in 185 days, resting on islands for less than 4 days during this time.

How can frigate birds manage these long-distance feats? Soaring and gliding are energetically efficient modes of transport, especially for frigate birds, which have very long wings and the lowest wing loading of any bird. But before they can glide, they need a lift from thermals of warm air rising under and within cumulus clouds. Thermals inside a cloud are especially powerful and lift a frigate bird at rates of 4 to 5 m/s. Once aloft, the birds can glide for up to 60 km, giving them time to spot another cumulus cloud. Weimerskirch *et al*. show that frigate birds do little work during lifts and glides, with heart rates and wing beat frequencies generally low during these times. The birds repeat these soar-glides multiple times per day, rising more than 15 km on average; they mainly use flapping flight when pursuing prey near the sea surface.

Only a few other bird species stay aloft for such extended periods; one alpine swift flew continuously for 200 days (*5*). Whether and how frigate birds, swifts, and other long-distance migrants sleep on the wing is still unresolved (*2*). Miniature loggers that monitor sleep-wave patterns (*6*) should answer whether birds sleep "with open eye," as Chaucer stated in *The Canterbury Tales*.

Frigate birds and human gliders have much in common. Both use cumulus clouds as conspicuous signals of thermals. Nonetheless, human gliders tend to avoid soaring in clouds (*7*), whereas frigate birds use these clouds to gain altitude and thus to glide extra distance (*2*).

Human gliders and frigate birds also share a risk of a premature "land-out." Forced landing on a field is usually just an inconvenience for humans. But an ocean landing would be catastrophic to frigate birds, because their feathers are not oiled and would wet quickly. Frigate birds do not take rest stops on the water, as Columbus noted (*1*), and they can switch to costly flapping flight when their glide paths run short of the next thermal (*8*). Even so, the local unpredictability of thermals places frigate birds at some risk on their transoceanic migrations.

The flight paths of frigate birds often skirt the nearly windless doldrums; ancient mariners famously avoided these zones unless forced (*9*). However, the trade winds and thermals that surround the doldrums are regionally reliable, providing frigate birds with crucial lifts and assists (*2*). Still, the

Frigate birds on the wing. Great frigate birds (*Fregata minor*) are gliders par excellence, staying aloft for months at a time. Weimerskirch *et al*. show that the birds travel economically by repeatedly hitching lifts on rising thermals and then gliding for tens of kilometers.

obvious question is why frigate birds even bother to circumnavigate this region.

Many other birds migrate seasonally as they shuttle between breeding and overwintering grounds. But for frigate birds, the migratory journey is a "movable feast" as they travel continuously in search of food (*10*). The Indian Ocean is productive, but unlike other equatorial oceans, its seasonally reversing wind patterns increase phytoplankton productivity toward the west and away from the equator. Fish and squid can be locally abundant (*10*), especially in the western regions (*11*). But if frigate birds cannot land on the ocean, how do they catch marine food? They sometimes steal food from other birds, but they catch most of their food by skimming fish and squid from the sea surface, or even snagging flying fish chased into the air by tuna or other predators (*10*).

Columbus reported seeing frigate birds, boobies, and tropic birds on days when the sea was "thick with tuna" (*1*). This spatial congruence of marine birds with tuna is likely not a coincidence. Tuna and dolphinfish can chase small fish to the surface, where frigate birds can catch them (*10*). Surface-foraging schools of tuna—or associated flocks of foraging seabirds—will be conspicuous to high-flying frigate birds, which can shift their flight directions accordingly. In fact, human fishermen use seabird flocks to locate tuna.

The doldrums, and the atmospheric and oceanic circulations that surround them, thus play multiple roles in the lives of frigate birds and other marine birds. As Weimerskirch *et al*. document, trade winds and their cumulus clouds allow frigate birds to soar and glide in search of food that is spatially and temporarily patchy (*10*). Moreover, these trade winds create seasonal patterns of upwelling and a large gyre of surface currents that sustain a rich marine ecosystem and coincide with transoceanic tuna migrations (*11*). Thus, atmospheric circulation provides both transportation and food for frigate birds. Curiously, frigate birds seem to avoid some productive areas near the doldrums (Arabian Sea, Bay of Bengal, southern Indian Ocean). Perhaps high storm frequencies or wind intensities in these areas (*12*) are too much of a good thing, or return winds are not available when needed.

Studies of bird migration over land are now elucidating how orographic and meteorological patterns influence bird flight trajectories (*13*). Similar studies of bird migration over oceans may require simultaneous information on spatial and temporal patterns of wind and clouds, currents and upwelling, primary productivity (*14*, *15*), forage fish accessibility, and even the abundance and depth of marine predators such as tuna (*11*) that can chase forage fish to the surface. Simultaneous studies both above and below the sea surface will be logistically challenging but should clarify why frigate birds and other marine birds go where they go, why they do not go elsewhere, and where they will be forced to go in the future.

It will also be interesting to compare detailed flight behavior of frigate birds and other marine birds (*8*) against an emerging stochastic theory of optimal glider flying (*7*). That theory will need expansion to account for small-scale ocean fronts and eddies that aggregate food resources but are spatially and temporally unpredictable on a local scale.

As Weimerskirch *et al*. caution, climate change may soon disrupt meteorological conditions that currently enable frigate birds to exploit these regions. Climate change is also rapidly warming surface temperatures in the Indian Ocean, phytoplankton populations are declining, and continued warming may convert this still-productive region into an "ecological desert" (*15*). For either or both reasons, great frigate birds and other marine birds may no longer soar and glide over these vast regions. ■

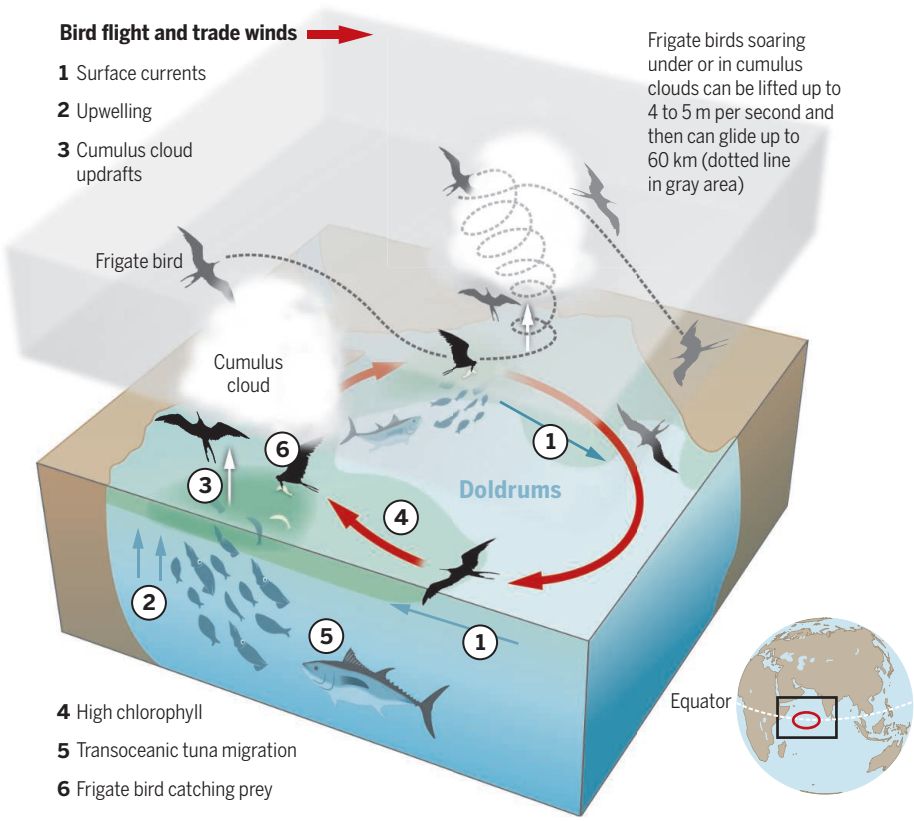

ILLUSTRATION: K. SUTLIFF/*SCIENCE*

Circumnavigating the doldrums. Weimerskirch *et al.* used satellite technology to track the flight paths of frigate birds around the Indian Ocean. Trade winds run clockwise around the doldrums, driving surface currents, upwelling, cumulus clouds, and high primary productivity (chlorophyll), especially in the west. Tuna chase fish and squid to the surface and make them accessible to frigate birds in these regions. Trade winds and their cumulus clouds thus give frigate birds low-cost access to rich foraging zones that can be distant from land.

REFERENCES AND NOTES

1. O. Dunn, J. E. Kelley Jr., Eds., *The Diario of Christopher Columbus's First Voyage to America , 1492–1493* (Univ. of Oklahoma Press, 1989).
2. H. Weimerskirch, C. Bishop, T. Jeanniard-du-Dot, A. Prudor, G. Sachs, *Science* **353**, 74 (2016).
3. R. Kays, M. C. Crofoot, W. Jetz, M. Wikelski, *Science* **348**, 1222 (2015).
4. N. E. Hussey *et al*., *Science* **348**, 1255642 (2015).
5. F. Liechti *et al*., *Nat. Commun.* **4**, 2554 (2013).
6. N. C. Rattenborg *et al*., *Biol. Lett.* **4**, 402 (2008).
7. R. Almgren, A. Tourin, *Optim. Control Appl. Meth.* **36**, 475 (2015).
8. N. Horvitz *et al*., *Ecol. Lett.* **17**, 670 (2014).
9. S. T. Coleridge, in *Lyrical Ballad, with a Few Other Poems*, W. Wordsworth, S. T. Coleridge, Eds. (Arch, London, 1798).
10. H. Weimerskirch, M. Le Corre, S. Jaquemet, M. Potier, F. Marsac, *Mar. Ecol. Prog. Ser.* **275**, 297 (2004).
11. D. M. Kaplan *et al*., *ICES J. Mar. Sci.* **71**, 1728 (2014).
12. M. A. C. Nicoll *et al*., *Global Change Biol.* 10.1111/gcb.13324 (2016).
13. N. Sapir, M. Wikelski, R. Avissar, R. Nathan, *Behav. Ecol. Sociobiol.* **65**, 1353 (2011).
14. S. Dodge *et al*., *Mov. Ecol.* **1**, 1 (2013).
15. M. K. Roxy *et al*., *Geophys. Res. Lett.* **43**, 826 (2016).

ACKNOWLEDGMENTS

Supported by NSF grant IOS 1038016 (R.B.H.), NSF grants OCE 1419323 and 1458967 (C.D.), and Gordon and Betty Moore Foundation grant GBMF 3775. We thank H. Weimerskirch for comments and W. Moody for the Chaucer quote.

10.1126/science.aag1865

PHYSICS

Timing photoemission—Final state matters

Ultrafast spectroscopy can track the electron dynamics of the photoemission process

By **Uwe Bovensiepen** *and* **Manuel Ligges**

The photoemission of electrons from atoms, molecules, and condensed matter provides the experimental basis of our understanding of electronic structure. During the process of photoemission, a sufficiently large quantum of electromagnetic radiation (a photon) is absorbed by matter and converted into an electronic excitation, promoting a bound electron into a final state above the vacuum energy E_{vac}. In photoemission spectroscopy, the kinetic energy and momentum of electrons in such final states are analyzed after their propagation to a distant detector. To determine the electronic structure of the sample, the "sudden approximation" has to be fulfilled, whereby the photoelectron leaves the sample fast enough, without further interaction with the remaining electronic structure. On page 62 of this issue, Tao *et al.* (*1*) provide unprecedented insight into final-state dynamics by measuring the time a photoelectron takes to leave a solid material for characteristically different final states. By comparing an electron excited to a final state of a nickel solid Ψ_f^{Ni} with one excited to a state of vacuum Ψ_f^{vac}, they establish that a photoelectron resides in the final state for 200 attoseconds (as) (2×10^{-16} s) before it leaves the nickel (see the figure). Such time scales would still allow for the electron to interact with its surroundings and, thus, are relevant for the validity of the sudden approximation.

Attosecond time-resolved spectroscopy uses the highly nonlinear interaction of intense femtosecond laser pulses with atoms to generate attosecond pulses in the vacuum (VUV) and extreme ultraviolet (XUV) spectral ranges synchronized with the driving laser field (*2*, *3*). The method was the key to observing atomic-scale electron dynamics in the time domain and was first applied to atoms and molecules in the gas phase (*4*). An investigation of attosecond electron dynamics in condensed matter was reported at the surface of a tungsten crystal, in which a 100-as delay was found between the photoemission from the conduction band and shallow core levels (*5*). To explain this effect, different propagation velocities and scattering in the respective final states, initial state and band structure characteristics, and dynamic screening are considered (*6*–*10*). Surprisingly, experiments on single-crystal magnesium surfaces did not provide evidence for such an attosecond delay (*11*), but it was seen in photoemission from magnesium monolayers grown on a tungsten surface (*12*). The photoelectrons emitted by single isolated attosecond pulses, which exhibit a spectral width of several electron volts, were analyzed in the presence of an intense infrared (IR) laser pulse; an approach that provides direct access to attosecond electron dynamics.

In a complementary scheme, also used by Tao *et al.*, attosecond pulse trains were used to analyze electron dynamics at solid surfaces (*13*) with the opportunity to operate at lower photon energy in the VUV spectral range and to spectrally resolve initial electronic states with a ~1-eV energy difference. The attosecond response is retrieved by analyzing the time evolution of photoemission sidebands in the presence of a streaking near-IR (NIR) laser field by using an interferometric technique (*14*). The observed attosecond delays in photoemission and corresponding experiments lead to the conclusion that bulk final-state effects must play an important role in photoemission from noble-metal surfaces (*15*).

Tao *et al.* measure the attosecond response as a function of photon energy. They identify the signature of resonant photoemission into a bulk final state Ψ_f^{Ni}, which represents a highly excited state of solid nickel, and distinguish it from that of a free-electron final state Ψ_f^{vac}, which resides outside the Ni in vacuum. The difference in photoemission from these final states corresponds to their damping inside the material (see the figure). Because Ψ_f^{vac} is off-resonance with bulk final states, it cannot propagate into the solid and is damped within one or two atomic layers. In contrast, Ψ_f^{Ni} resides in and outside the solid, although with a different frequency due to the different potential. The photoemission delay of 200 as at the energy of Ψ_f^{Ni} allows inferences regarding the depth inside the material at which photo-

Tracking electronic excitations

A schematic of the photoemission process and the experiment performed by Tao *et al.*, who observed a 200-as delay between photoemission from two characteristically different final states.

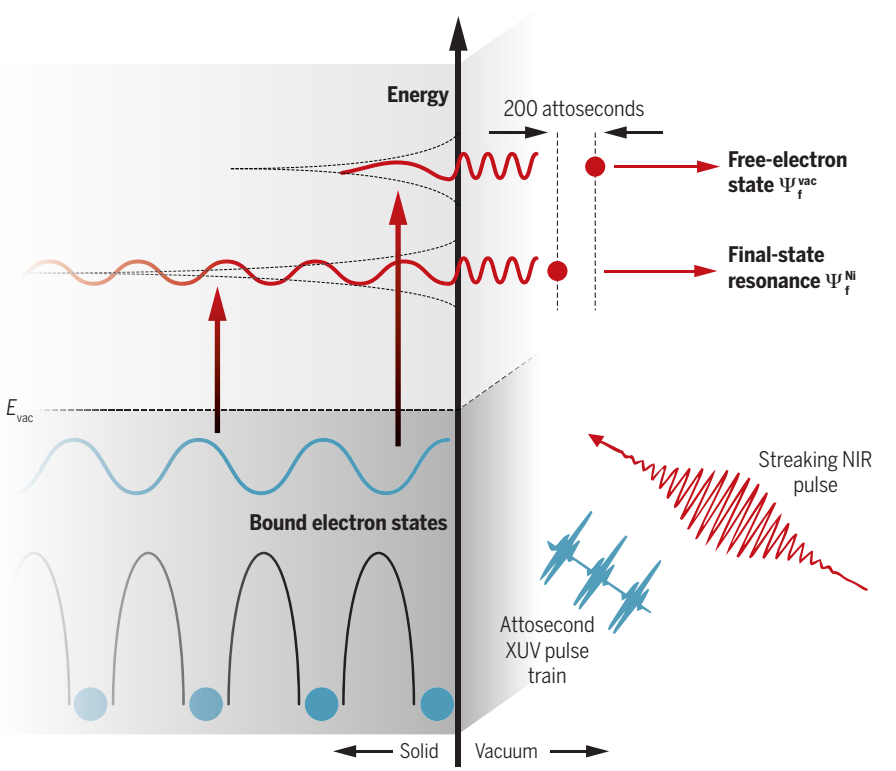

GRAPHIC: ADAPTED BY C. BICKEL/*SCIENCE*

University Duisburg-Essen, Faculty for Physics, 47048 Duisburg, Germany. Email: uwe.bovensiepen@uni-due.de

electrons are born, which may be viewed as an effective damping of Ψ_f^{Ni} in nickel. An essential question, though, is what distance an electron can propagate within the sample and still be detected as an electron populating Ψ_f^{Ni}. Finally, the high potential energy of the photoelectron, more than 20 eV above the Fermi level, makes it a highly excited state with an extremely short lifetime (t = 200 as). The distance d over which this electron can propagate with a velocity v without losing energy due to interaction with the solid is referred to as the inelastic mean free path. However, it is not obvious which v is the appropriate one. Tao *et al*. discuss that consideration of the group velocity of the electron inside Ni results in too-small values for d. To obtain this quantity in agreement with values from the literature, propagation of the electron inside nickel as a free electron has to be assumed, which is supported by earlier work on magnesium (*11*) and excited state theory. Essentially, the photoelectron leaves the crystal before it can experience the surrounding solid.

The experimental scheme and findings of Tao *et al*. might have widespread implications for future analysis of the electronic structure of solid materials. The extremely short inelastic mean free path of just a few angström makes photoemission a surface-sensitive method prone to complications if one aims at the electronic structure of three-dimensional bulk materials. Current efforts use x-ray photon energies in photoemission (*16*). However, the use of low photon energy in the UV spectral range promises bulk sensitivity in some limits as well, while providing ample opportunity for time-resolved experiments that address correlations in complex materials (*17*). Tao *et al*. have shown that attosecond spectroscopy of solids has the potential to analyze the fundamental processes limiting bulk sensitivity in photoemission and to develop this prominent spectroscopy further beyond current limitations. ■

REFERENCES

1. Z. Tao *et al.*, *Science* **353**, 62 (2016).
2. P. B. Corkum, *Phys. Rev. Lett.* **71**, 1994 (1993).
3. M. Hentschel *et al.*, *Nature* **414**, 509 (2001).
4. F. Krausz, M. Ivanov, *Rev. Mod. Phys.* **81**, 163 (2009).
5. A. L. Cavalieri *et al.*, *Nature* **449**, 1029 (2007).
6. C. Lemell *et al.*, *Phys. Rev. A* **79**, 062901 (2009).
7. A. K. Kazansky, P. M. Echenique, *Phys. Rev. Lett.* **102**, 177401 (2009).
8. E. E. Krasovskii, *Phys. Rev. B* **84**, 195106 (2011).
9. Q. Liao, U. Thumm, *Phys. Rev. Lett.* **112**, 023602 (2014).
10. S. R. Leone *et al.*, *Nat. Photon.* **8**, 162 (2014).
11. S. Neppl *et al.*, *Phys. Rev. Lett.* **109**, 087401 (2012).
12. S. Neppl *et al.*, *Nature* **517**, 342 (2015).
13. M. Lucchini *et al.*, *Phys. Rev. Lett.* **115**, 137401 (2015).
14. K. Klünder *et al.*, *Phys. Rev. Lett.* **106**, 143002 (2011).
15. R. Locher *et al.*, *Optica* **2**, 405 (2015).
16. C. S. Fadley, *J. Electron Spectrosc. Relat. Phenom.* **190**, 165 (2013).
17. L. Rettig *et al.*, *Nat. Commun.* **7**, 10459 (2016).

10.1126/science.aag1090

ANTHROPOLOGY

The evolutionary path of least resistance

Evolution favored teeth with thicker enamel over sharply crested teeth in hominins confronted with tough diets

By **P. S. Ungar**[1] *and* **L. J. Hlusko**[2]

Paleontologists typically reconstruct past behavior by assuming that function follows form. But there can be more than one function for a given form, and different forms can serve the same function. Deconstructing these relationships can be complicated. Here, we use an example from human evolution—markedly different tooth morphologies in early hominins—to show that insights about the underlying genetic architecture of form can help us to better infer function and deepen our understanding of evolution.

In the eastern and South African fossil record of human evolution during the Plio-Pleistocene (about 2.7 to 1.2 million years ago), there is a group of species with remarkably specialized craniodental anatomy. Exemplified by *Australopithecus/Paranthropus boisei* from eastern Africa and *A./P. robustus* from South Africa, these hominins evince large, flat, thickly enameled teeth (see the figure), heavily buttressed jaw and face, and attachment sites indicating massive chewing muscles (*1*). These characteristics are often interpreted as adaptive for crushing hard foods; the first fossil found was nicknamed the "nutcracker" man. But recent studies call into question a simple form-function relationship between masticatory morphology and diet (*2*), fueling a long-standing debate over their evolutionary relationships (*3*).

"Because the same anatomical solution may emerge from different adaptive challenges, genetic architecture provides a key piece of the puzzle when inferring function from form in the fossil record."

The carbon isotope values for *A./P. robustus* indicate that this species had a mixed diet of leaves, fruits, grasses, and sedges; a range of microscopic use-wear pitting on its teeth is consistent with only occasional consumption of hard objects. In contrast, *A./P. boisei* has carbon isotope values indicating a diet dominated by grasses or sedges. A pattern of dental microwear scratches on its teeth, along with an extreme gross tooth wear gradient, is consistent with grinding or milling softer, tougher, and perhaps more abrasive foods. So despite their similar masticatory morphology, chemical and wear traces of the foods eaten suggest that these two species differed markedly in their diets (*3*). Neither was a specialized "nutcracker," notwithstanding a craniodental toolkit that at first glance suggests otherwise.

One argument against the idea that *A./P. boisei* ate tough foods is the observation that no living leaf-eating primate has flat teeth. Gorillas, for example, have comparatively long shearing crests rather than blunt cusps, presumably because blades are more efficient for fracturing tough leaves (see the figure) (*4*).

We propose that although a flat-toothed grinding platform may be suboptimal for fracturing tough foods relative to a bladed (crested) morphology, it is a better solution than the smaller, less thickly enameled molars of *A./P. boisei*'s predecessor, *Australopithecus afarensis* (see the figure) (*5*). The latter lived between about 3.85 and 2.95 million years ago, whereas *A./P. boisei* lived between about 2.3 and 1.2 million years ago. The flat teeth of *A./P. boisei* would have been particularly advantageous when combined with masticatory structures capable of generating and transmitting repetitive loads associated with heavy grinding of tough vegetation. The key piece of evidence that unlocks this evolutionary puzzle lies in the genetic architecture of tooth shape.

Knowledge of genetic architecture of tooth shape comes mainly from developmental genetics research on mice, animals that last shared a common ancestor with humans about 70 million years ago. Despite

[1]*Department of Anthropology, University of Arkansas, Fayetteville, AR, USA.* [2]*Human Evolution Research Center, University of California, Berkeley, CA, USA. Email: pungar@uark.edu*

Morphology and development of hominin molars

Flat teeth with a thicker enamel cap can evolve more quickly than a crested morphology

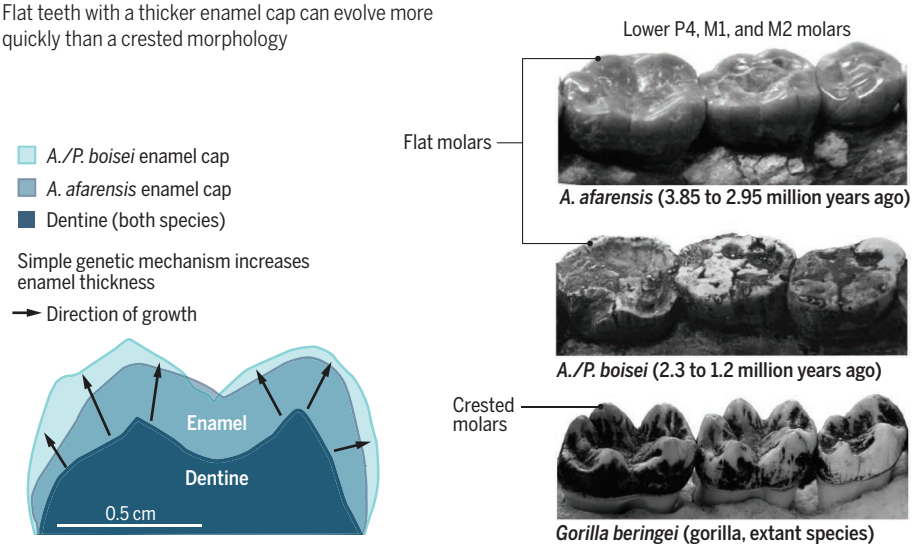

this evolutionary distance, there are numerous reasons to assume that the main mechanisms are similar (*6*). From a subset of the 300 genes involved in mouse molar development, Salazar-Ciudad and colleagues (*7*) have developed an in silico model of tooth development that shows how reaction-diffusion processes can modify cusp patterning. This model works well for the teeth of seals (which are essentially two-dimensional). However, it does not extend to more complex structures such as the rectangular teeth of most primates, nor does it explain why cusps with different heights form. Tooth cusp patterning is genetically complex. Consequently, the selection that leads to changes in cusp patterning has to persist over long periods of time. The paleontological record confirms this, showing that although shearing cusps have evolved repeatedly, they did so on time scales of many millions of years.

Had the *A./P. boisei* lineage persisted for longer than ~2 million years, perhaps their descendants might have eventually wound up with spiky, crested cusps more like those of gorillas. But the evolution of humans' closest relatives occurred over a much shorter interval, one in which selection would have acted first and foremost on phenotypes that were already variable within and between populations, and whose genetic architecture facilitated a rapid response.

At least four independent lines of evidence indicate that enamel thickness is such a phenotype in primates (see the figure). First, quantitative genetic analyses demonstrate that enamel is highly variable and heritable, without causing other phenotypic changes (*8*). Second, thicker enamel correlates with more abrasive diets across extant primates, which suggests that both fracture risk and abrasiveness can select for it (*9*). Third, enamel thickness is highly variable among closely related species (*10*). Fourth, there is evidence of selection in noncoding regions of two genes involved in enamel formation across the great apes (*11*).

Although sharp shearing crests may be better for fracturing tough plant parts, evolution tends to follow the path of least resistance. That path is defined by the structure of the underlying genetic covariance (*12*). Over the shorter time frames of hominin evolution, highly variable, highly heritable molar enamel thickness, with its simple genetic architecture, was probably the phenotypic response that came first when these creatures were confronted with a mechanically challenging diet. Because the same anatomical solution may emerge from different adaptive challenges, genetic architecture provides a key piece of the puzzle when inferring function from form in the fossil record. ■

REFERENCES AND NOTES

1. A. L. Smith *et al.*, *Anat. Rec.* **298**, 145 (2015).
2. For example, the present authors disagree about which genus these two species belong to; P.S.U. classifies them within the distinct genus *Paranthropus* and L.J.H. includes them in *Australopithecus*. Hence, here we use slashes to acknowledge both nomenclatures. L.J.H. also prefers Hominidae to Homininae, but for ease of discussion, we use hominin herein.
3. P. S. Ungar, M. Sponheimer, *Science* **334**, 190 (2011).
4. P. W. Lucas, *Dental Functional Morphology: How Teeth Work* (Cambridge Univ. Press, 2004).
5. A. Walker *et al.*, *Nature* **322**, 517 (1986).
6. L. J. Hlusko, R. D. Sage, M. C. Mahaney, *J. Exp. Zool.* **316B**, 21 (2011).
7. I. Salazar-Ciudad, *Curr. Opin. Genet. Dev.* **22**, 585 (2012).
8. L. J. Hlusko *et al.*, *Am. J. Phys. Anthropol.* **124**, 223 (2004).
9. J. D. Pampush *et al.*, *J. Hum. Evol.* **64**, 216 (2013).
10. A. Kato *et al.*, *Am. J. Phys. Anthropol.* **155**, 447 (2014).
11. J. E. Horvath *et al.*, *J. Hum. Evol.* **73**, 75 (2014).
12. D. Schluter, *Evolution* **50**, 1766 (1996).

10.1126/science.aaf8398

NEUROREGENERATION

Promoting CNS repair

What influences glial and neuronal response to neurodegeneration?

By **Evan G. Cameron** *and* **Jeffrey L. Goldberg**

A developmental loss of intrinsic reparative capacity and the inhibitory environment in injury and disease contribute to regenerative failure in the central nervous system (CNS). The same factors are thought to hinder endogenous and exogenous regenerative therapies, including cell-based replacement (*1*, *2*). In neurodegenerative disorders, the contributions of microglia, astrocytes, and peripheral immune cells may be both harmful and beneficial. For example, resident microglia and peripheral cells of the innate immune system promote inflammation and cell death (apoptosis) in response to CNS injury, but immune cell activation also has been associated with neuroprotection and repair (*3*). This duality suggests that stimulating protective functions while minimizing proapoptotic and inhibitory signals could prove critical in treating neurodegenerative disease. On page 43 of this issue, Neves *et al.* (*4*) show that a neurotrophic signaling pathway in microglia and innate immune cells that is activated in disease or injury can be leveraged to promote neuroprotection and tissue repair.

Neves *et al.* identify a conserved injury response pathway in innate immune cells that is mediated by mesencephalic astrocyte-derived neurotrophic factor (MANF), a macrophage-dependent, prosurvival signaling molecule. In a mouse model of progressive retinal degeneration, the authors found that macrophage-derived MANF exerts neuroprotective effects on damaged photoreceptors, and enhances transplanted photoreceptor integration that restored visual function.

Macrophages clear debris and produce pro- and anti-inflammatory cytokines in response to injury or in degenerative disease. The course of macrophage activation is influenced by the extrinsic environment, which drives their acquisition of either an M1 (inflammatory/proapoptotic) or M2 (anti-inflammatory/tissue-protective) phenotype, both of which

Department of Ophthalmology, Stanford University, Stanford, CA 94303, USA. Email: ecamer1@stanford.edu

are reported in neurodegeneration, as well as in neurogenesis, regeneration, and myelination (*3*, *5*, *6*). Using various genetic and cellular techniques in flies and mice, Neves *et al*. show that MANF expression is induced in macrophages by platelet-derived growth factor (PDGF)–like signaling originating from injured photoreceptor cells, and propose that this promotes M2-like phenotypes that are neuroprotective and support repair.

Injury responses in the CNS involve a complex interplay between multiple cell types, including glia, neurons, and immune cells, and the study of Neves *et al*. raises many questions about cell-cell and even subcellular signaling. Glia, including astrocytes, microglia, and retinal Müller glia, are nonneuronal cells that maintain CNS function by regulating homeostasis, survival, growth signaling, neurotransmission, and visual processing (*7*–*10*). As with macrophages, glial cells respond to injury by becoming activated or "reactive" in ways that can promote or inhibit neuronal survival and regeneration. Historically, reactive astrocytes have been thought to act primarily as barriers to axon growth through glial scar formation and associated inhibitory processes, including overproduction of reactive oxygen species and inflammatory, pro-death cytokines, as well as inhibitory factors that block retinal or other CNS repair. Correspondingly, associated signaling pathways, such as tumor necrosis factor–α (TNF-α), transforming growth factor–β1 (TGF-β1), and signal transducer and activator of transcription 3 (STAT3), among many others, are thought to be good targets for therapeutic intervention to promote neuroprotection, plasticity, and repair (*1*, *11*). By contrast, reactive astrocytes promote axon regeneration by reducing inflammation and sequestering damaged tissue (*12*). Such findings contradict the prevailing dogma that reactive astrocytes primarily act as inhibitors to axon growth, and support the hypothesis that CNS injury induces both "good" and "bad" glial phenotypes, depending on the context or injury. This hypothesis is supported by several studies, including that of Neves *et al*., that highlight the importance of neuroglial, neuroimmune, and glial-immune interactions (*4*, *13*, *14*). Interestingly, Neves *et al*. report that MANF is also expressed in Müller glia, but they do not expound on its contribution to innate immune cell activation or neuroprotection.

What, then, dictates whether cellular interactions and corresponding responses will be protective or harmful after injury? Multiple factors influence neuronal, glial, and immune cell communication in response to injury and disease, including location and distance from insult as well as temporal differences in acute versus chronic disease. Glial cells undergo a wide range of changes in gene expression, morphology, and function that vary with distance from and type of injury, and as the results of Neves *et al*. suggest, may lead to the formation of reparative and degenerative environments within injured tissue (*4*, *12*, *15*). Even more attractive is the hypothesis that single glial or immune cells may express phenotypes that both promote and prevent repair (see the figure). This is particularly compelling for microglial cells, astrocytes, and Müller glia, whose processes can ramify across neural tissues and interact simultaneously in degenerative and reparative zones (*15*). For instance, one process of an immune or glial cell may interact in a degenerative environment and secrete cytokines that contribute to axon injury or cell death, whereas another process of the same cell may signal through protective factors such as MANF to support the survival or regeneration of injured cells.

Thus, it is likely that modulation of multiple signaling pathways in different cell types, and even of compartmentalized signaling within single cell types, will have to be addressed to successfully achieve regeneration and functional recovery. Elucidating how MANF and other such factors exert protective effects both on a cellular and molecular level, as well as how different forms of immune recruitment influence glial and neuronal response to injury, will be paramount in understanding the basis of disease and in developing neuroregenerative therapies. ■

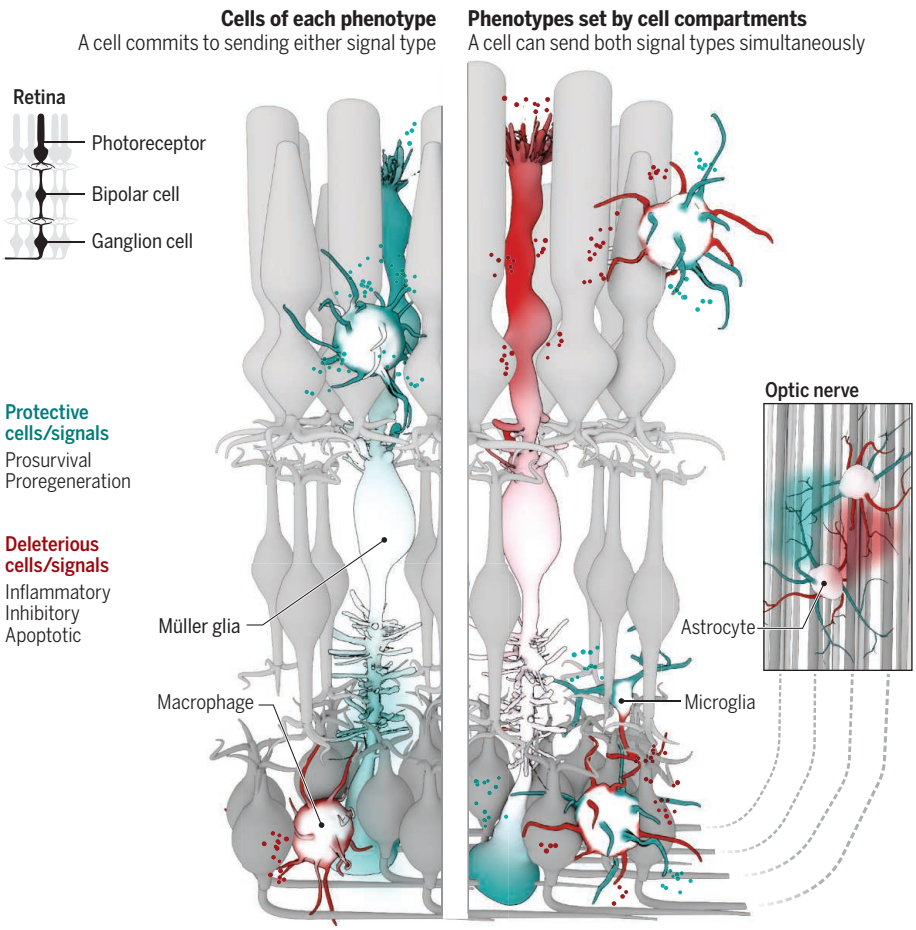

Protective or harmful? Activated glia and immune cells in the retina acquire protective and degenerative phenotypes in neuronal disease and injury. The extent to which cells polarize toward one phenotype could lead to zones of protective or deleterious signaling. Alternatively, reactive cells may express both signal types, compartmentalize such signaling across different processes extending into different tissue zones, and promote repair in one area and degeneration in another.

ILLUSTRATION: V. ALTOUNIAN/*SCIENCE*

REFERENCES AND NOTES

1. L. I. Benowitz, Z. He, J. L. Goldberg, *Exp. Neurol.* 10.1016/j.expneurol.2015.12.015 (2015).
2. Z. Kokaia *et al*., *Nat. Neurosci.* **15**, 1078 (2012).
3. S. David, A. Kroner, *Nat. Rev. Neurosci.* **12**, 388 (2011).
4. J. Neves *et al*., *Science* **353**, 43 (2016).
5. V. E. Miron *et al*., *Nat. Neurosci.* **16**, 1211 (2013).
6. Y. Yin *et al*., *Nat. Neurosci.* **9**, 843 (2006).
7. A. V. Gourine *et al*., *Science* **329**, 571 (2010).
8. L. E. Clarke, B. A. Barres, *Nat. Rev. Neurosci.* **14**, 311 (2013).
9. J. B. Zuchero, B. A. Barres, *Development* **142**, 3805 (2015).
10. A. Reichenbach, A. Bringmann, *Glia* **61**, 651 (2013).
11. A. Brosius Lutz, B. A. Barres, *Dev. Cell*. **28**, 7 (2014).
12. M. A. Anderson *et al*., *Nature* **352**, 195 (2016).
13. D. Sun *et al*., *J. Neurosci.* **30**, 14008 (2010).
14. A. Nimmerjahn *et al*., *Science* **308**, 1314 (2005).
15. M. A. Anderson *et al*., *Neurosci. Lett.* **565**, 23 (2014).

ACKNOWLEDGMENTS

Supported by NEI EY026766 (J.L.G.) and EY025915 (E.G.C.).

10.1126/science.aag3327

ECOLOGY

How climate change affects plants' sex lives

Shifts in plant sex ratios help plant species to expand upslope in a warmer climate

By **Julie R. Etterson**[1] *and* **Susan J. Mazer**[2]

Climate change affects wild plant species across their geographical ranges. Studies at the margins of species' ranges reveal upslope expansion, low-elevation range contraction, and, in some cases, a lack of geographic response to climate change (*1*). However, all populations, including those in the core of species' ranges, are subject to climate-driven natural selection that promotes adaptation to a warmer world (*2*). Theoretical models show that coupled spatial and temporal responses of populations can mediate the negative effects of climate change (*3*, *4*), but it remains unclear whether these processes can occur fast enough to rescue populations from extinction (*5*). On page 69 of this issue, Petry *et al*. (*6*) report rapid spatial and temporal change in plant sex ratios in response to changing climatic conditions. These changes could facilitate geographic range shifts in the montane perennial herb valerian (*Valeriana edulis*).

The authors examine change across an elevation gradient in a dioecious species, in which individuals are either male or female, over the course of 33 years (see the figure). In warmer and drier low-elevation sites, populations harbor more males than those in cooler and wetter high-elevation sites, apparently because of gender-specific differences in water-use efficiency and, ultimately, life expectancy. Because it has become warmer and drier in central Colorado over the past three decades, the proportions of males in high-elevation populations have increased (see the figure, top panel), resulting in greater pollination success and increased seed set for females—conditions that could facilitate upslope range expansion. This concordance between temporal and spatial change supports the assumption that space can substitute for time when forecasting responses to climate change.

Although a novel and compelling finding, this mechanism of change only applies to the ~6% of angiosperms composed of unisexual individuals. The vast majority of flowering plants are hermaphroditic—that is, they produce flowers that include both male and female reproductive parts (see the photo). Some hermaphrodites have sophisticated means of preventing self-fertilization (*7*), but ~42% have mixed mating systems where a single fruit can contain seeds from self-pollination and seeds pollinated by a different individual.

Mixed mating systems provide reproductive assurance, which is especially beneficial when mates or pollinators are scarce (*8*). However, this mating system also promotes self-fertilization, which is even more genetically risky than mating between close relatives. Any inbreeding increases the expression of deleterious mutations, thereby reducing reproductive fitness. Natural selection can gradually purge populations of harmful mutations, but mixed mating systems persist even in the presence of the negative effects of inbreeding; unfortunately, this also increases susceptibility to extinction (*9*).

How might climate change alter the sex lives of these hermaphroditic species? Clearly, warmer and drier conditions should favor attributes that directly benefit both male and female function, such as drought tolerance. But some climate responses could directly or indirectly lead to increased self-fertilization, along with its genetic risks.

First, in extreme environments, smaller flowers may be produced as a passive response to a stressful and deteriorating environment (*10*). This could also reduce the temporal and/or spatial separation between male and female organs (*11*), facilitating self-fertilization (see the figure, middle panel).

Second, smaller flowers may evolve indirectly through climate-driven selection that favors traits promoting rapid completion of the life cycle, including early flowering and rapid floral development. These two traits

Sex matters

Plant responses to climate change depend on their method of reproduction

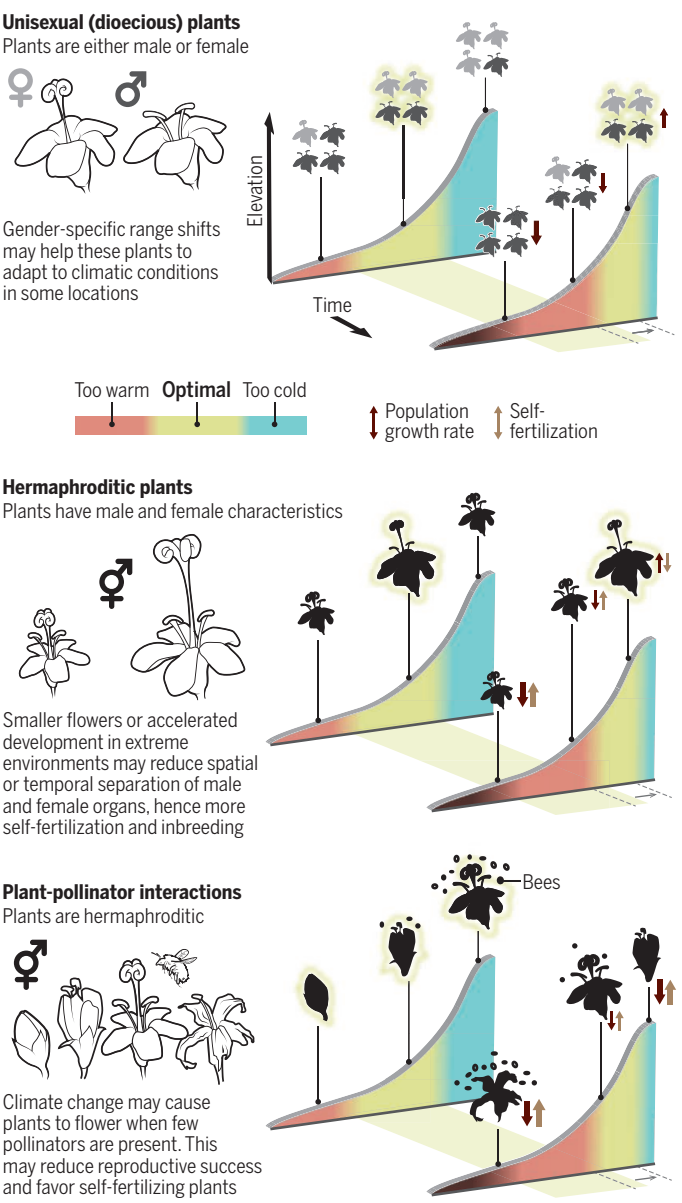

GRAPHIC: V. ALTOUNIAN/*SCIENCE*

Hermaphroditic flower of *Chamerion angustifolium*, a species that can self-fertilize.

PHOTO: J. R. ETTERSON

are associated with the production of small flowers with synchronously developing and proximate male and female organs (*11*), also facilitating self-fertilization.

Finally, coevolved biotic interactions between flowering plants and their pollinators can be disrupted if warmer temperatures cause a mismatch between the timing of flowering and pollinator abundance or presence (see the figure, bottom panel). In this case, natural selection could directly favor self-fertilization as a mechanism of reproductive assurance (*12*). If these processes occur very rapidly, the rate of self-fertilization could increase faster than the rate at which deleterious mutations are purged. This could ultimately cause population declines.

Petry *et al.*'s findings were possible because historical data was fortuitously available. In a few rare circumstances, it has been possible to observe evolutionary change between two time points by germinating ancestral seeds that were fortuitously available (e.g. preserved in tundra soils or seed vaults) simultaneously with contemporary seeds (*2*, *13*). Such direct comparison between ancestral and descendent populations show that climate change is already affecting traits associated with plant mating systems, such as the timing of flowering. Efforts are under way to vastly expand the availability of these rare and valuable historical seed resources (*14*, *15*). These collections should help to more definitively answer the knotty question of whether evolution can rescue populations of native species, including the wild relatives of crops, from climate change across their geographic ranges. ■

[1]*Department of Biology, University of Minnesota Duluth, 207A Swenson Science Building, Duluth, MN 55812, USA.*
[2]*Department of Ecology, Evolution, and Marine Biology, University of California, Santa Barbara, Santa Barbara, CA 93106, USA. Email: jetterso@d.umn.edu; mazer@lifesci.ucsb.edu*

REFERENCES

1. R. Bertrand *et al.*, *Nature* **479**, 517 (2011).
2. S. J. Franks, S. Sim, A. E. Weis, *Proc. Natl. Acad. Sci. U.S.A.* **104**, 1278 (2007).
3. C. M. Pease, R. Lande, J. Bull, *Ecology* **70**, 1657 (1989).
4. A. L. Hargreaves, C. G. Eckert, *Funct. Ecol.* **28**, 5 (2014).
5. R. G. Shaw, J. R. Etterson, *New Phytol.* **195**, 752 (2012).
6. W. K. Petry *et al.*, *Science* **353**, 69 (2016).
7. S. Takayama, A. Isogai, *Annu. Rev. Plant Biol.* **56**, 467 (2005).
8. D. G. Lloyd, *Am. Nat.* **113**, 67 (1979).
9. D. Newman, D. Pilson, *Evolution* **51**, 354 (1997).
10. C. Galen, *Am. Nat.* **156**, 72 (2000).
11. L. S. Dudley, S. J. Mazer, P. Galusky, *J. Evol. Biol.* **20**, 2200 (2007).
12. C. G. Eckert *et al.*, *Trends Ecol. Evol.* **25**, 35 (2010).
13. E. Nevo *et al.*, *Proc. Natl. Acad. Sci. U.S.A.* **109**, 3412 (2012).
14. H. Dempewof *et al.*, *Ag. Sust. Food Syst.* **38**, 369 (2014).
15. J. R. Etterson *et al.*, *Am. J. Bot.* **103**, 164 (2016).

10.1126/science.aag1624

SEX DETERMINATION

Yob *makes mosquitoes male*

A gender-switch gene opens avenues to malaria control

By **Steven P. Sinkins**

Most developmental processes show deep conservation across great phylogenetic distances. In contrast, the signal that triggers the primary genetic switch between the sexes has evolved with remarkable rapidity—entirely lacking the "respectable antiquity" (*1*) seen in other comparable systems. Coupled with the repeat-rich structure of Y chromosomes, this has made the identification of genetically dominant "M" male-determining factors especially challenging. On page 67 of this issue, Krzywinska *et al.* (*2*) compared gene transcript sequences from male and female embryos of the malaria mosquito *Anopheles gambiae* and identified an early-expressed gene on the Y chromosome, designated *Yob*. Crucially, they show that it controls sex-specific splicing of *dsx* (*doublesex*), the conserved binary switch between male and female development (*3*), fulfilling the criteria for M. *Yob* partly overlaps, and probably is a better-annotated version of, a previously identified gene called *YG2* (*4*), recently shown to be conserved across the *An. gambiae* species complex (*5*).

This landmark follows the identification of *Nix,* the male-determining M gene in *Aedes aegypti*—the primary mosquito vector of dengue and Zika viruses (*6*). *Yob* and *Nix* are certainly not homologous. *Aedes* and *Culex* mosquitoes, unlike *Anopheles*, do not posses Y chromosomes, and *Nix* is located in a nonrecombining region of chromosome 1. Dosage compensation, the equalization of gene expression between males and females, is thus not needed in *Aedes*, but in *Anopheles* operates by up-regulation of genes on the single male X (*7*). *Yob* seems to control both sex determination and dosage compensation, because embryos die when genetic females receive ectopically delivered *Yob* messenger RNA or when *Yob* is silenced in genetic males (*2*). In contrast, in *Aedes*,

Lancaster University, Lancaster LA1 4YQ, UK. Email: s.sinkins@lancaster.ac.uk

Meiotic death drive. The male-determining *Yob* gene provides a means to suppress mosquito populations (scanning electron micrograph of a male *An. gambiae* mosquito).

Nix converts genetic females to male development (*6*) (see the table).

The discovery of this primary male-specific switch gene should now greatly facilitate the process of filling in missing gaps lower down the sex determination cascade—such as whether any cofactors are needed, whether YOB acts directly or indirectly on *dsx* splicing, and to confirm the involvement of *Yob* in dosage compensation. Using *Nix* and *Yob* as the foundation for comparative studies in related species will hopefully provide a much better understanding of the evolution of sex determination pathways, and the selective forces that lead to such frequent shifts at the top of the sex determination cascade. Interestingly, in *An. stephensi*, there seems to be a functional analog (*Guy1*) of *Yob* of the same length and expressed very early in embryogenesis (*8*), but with no primary sequence homology.

Despite considerable recent progress using bednets and antimalarial drug combination therapies based on artemisinin, malaria still exacts a very high societal toll in Africa, and *An. gambiae* is its most deadly vector. Understanding mosquito sex determination could help future control efforts in the following ways. The use of *Yob* as a transgenic sexing mechanism—for example, by conditionally expressing it from the autosomes in order to kill female embryos—will allow male-only releases (male mosquitoes do not bite or spread disease). This will improve the efficiency of suppression strategies based on release of sterile males. However, these approaches are likely to be of only limited utility against *An. gambiae*—they would be prohibitively expensive to attempt over wide areas of rural Africa. More enticing are strategies that do not require continuous intervention, but are self-sustaining once implemented—such as mosquito population replacement to render them unable to transmit *Plasmodium* parasites—and here, again, an ability to release male-only cohorts could greatly assist implementation.

Perhaps the most exciting prospect in the context of malaria control is to resurrect an old idea for instigating a population crash through highly male-biased population sex ratios, using "driving Y" chromosomes (*9*). Meiotic drive, the mechanism underlying the driving Y chromosomes, is a process in which an allele and the chromosome bearing that allele are preferentially transmitted through meiotic cell division, at the expense of other alleles.

A natural meiotic drive system occurs in *Ae. aegypti* (*10*)—crucially, not by killing female embryos but by preferential recovery of the M-containing chromosome, through breakage of its M-containing chromosomal homolog during sperm formation. Naturally occurring suppressors of meiotic drive prevent this particular system being useful for disease control. However, in *An. gambiae*, a synthetic system has now been constructed by using a homing endonuclease gene that targets ribosomal repeats on the X chromosome. When expressed from the autosomes during spermatogenesis, it cleaved the paternal X and produced male-biased sex ratios (*11*).

To be really effective for population suppression—potentially only requiring small seeding releases into each population—such a construct would have to be inserted into the Y chromosome, in a region where genes can be actively expressed (most of the Y is transcriptionally inactive and effectively a "black hole" for transcribed genes); the *Yob/YG2* locus provides this. A close physical or regulatory association with the male-determining gene would also make it much more difficult for resistance modifiers to be selected that suppress the action of the X-cleaving construct. The much more readily manipulated clustered regularly interspaced short palindromic repeats (CRISPR)—Cas9 genome editing system, which works in *An. gambiae*, provides more flexibility in the design of mosquito synthetic drive systems (*12*). The prospect of being able to induce mosquito population crashes by manipulating sex ratios seems a step closer. ■

Making males and females

A summary of the main features of sex determination as currently understood in the dipteran flies *Drosophila melanogaster*, *Aedes aegypti*, and *Anopheles gambiae*.

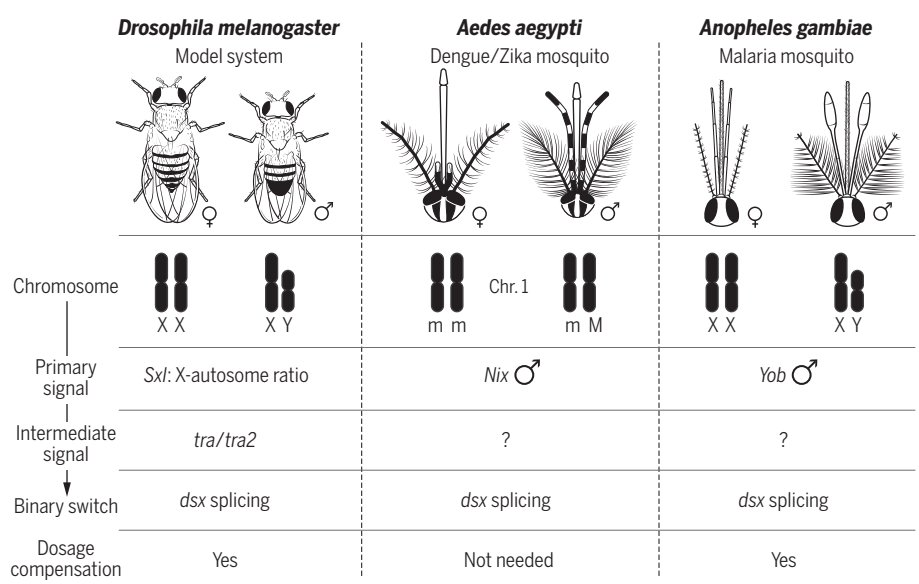

REFERENCES

1. I. Marin, B. S. Baker, *Science* **281**, 1990 (1998).
2. E. Krzywinska *et al.*, *Science* **353**, 67 (2016).
3. C. Scali, F. Catteruccia, Q. Li, A. Crisanti, *J. Exp. Biol.* **208**, 3701 (2005).
4. A. B. Hall *et al.*, *BMC Genomics* **14**, 273 (2013).
5. A. B. Hall *et al.*, *Proc. Natl. Acad. Sci. U.S.A.* **113**, E2114 (2016).
6. A. B. Hall *et al.*, *Science* **348**, 1268 (2015).
7. G. Rose *et al.*, *Genome Biol. Evol.* **8**, 243 (2016).
8. F. Criscione *et al.*, *Insect Mol. Biol.* **22**, 433 (2013).
9. W. D. Hamilton, *Science* **156**, 477 (1967).
10. W. A. Hickey, G. B. Craig Jr., *Genetics* **53**, 1177 (1966).
11. R. Galizi *et al.*, *Nat. Commun.* **5**, 3977 (2014).
12. A. Hammond *et al.*, *Nat. Biotechnol.* **34**, 78 (2016).

10.1126/science.aag1012

POLICY FORUM

GOVERNMENT TRANSPARENCY

Reforms to improve U.S. government accountability

Bill will encode a "presumption of openness" into law

By **Alexander B. Howard**[1] *and* **Patrice McDermott**[2]

Five decades after the United States first enacted the Freedom of Information Act (FOIA), Congress has voted to make the first major reforms to the statute since 2007. President Lyndon Johnson signed the first FOIA on 4 July 1966, enshrining in law the public's right to access to information from executive branch government agencies. Scientists and others around the world can use the FOIA to learn what the U.S. government has done in its policies and practices. Proposed reforms should be a net benefit to public understanding of the scientific process and knowledge, by increasing the access of scientists to archival materials and reducing the likelihood of science and scientists being suppressed by official secrecy or bureaucracy.

Although the FOIA has been important for accountability, reform is sorely needed. An analysis of the 15 federal government agencies that received the most FOIA requests found poor to abysmal compliance rates (*1*, *2*). In 2016, the Associated Press found that the Obama Administration had set a new record for unfulfilled FOIA requests (*3*). Although that has to be considered in the context of a rise in request volume without commensurate increases in resources to address them, researchers have found that most agencies simply ignore routine requests for travel schedules (*4*). An audit of 165 federal government agencies found that only 40% complied with the E-FOIA Act of 1996; just 67 of them had online libraries that were regularly updated with a substantial number of documents released under FOIA (*5*).

In the face of growing concerns about compliance, FOIA reform was one of the few recent instances of bicameral bipartisanship in Congress, with both the House and Senate each passing bills this spring with broad support. Now that Congress moved to send the Senate bill on to the president to sign into law, implementation of specific provisions will bear close scrutiny, including the potential impact of disclosure upon scientists who work in or with government agencies (*6*). Proposed revisions to the FOIA statute would improve how government discloses information to the public, while leaving intact exemptions for privacy, proprietary information, deliberative documents, and national security.

FEATURES OF REFORMS

One of the major reforms in the House and Senate bills was to codify the "presumption of openness" outlined by President Obama the day after he took office in January 2009 when he declared that FOIA should be administered with a clear presumption: In the face of doubt, "openness" would prevail. This presumption of openness was affirmed by U.S. Attorney General Holder in March 2009. Although these declarations have had limited effect in the agencies (as described above), codifying these reforms into law is crucial not only to ensure that this remains executive branch policy after this president leaves office but also to provide requesters with legal force beyond an executive order.

The Senate reform bill instructs all federal agencies to adopt a presumption in favor of disclosure, applied to all decisions involving FOIA. Senator Patrick Leahy (D-VT) has been trying to get such a provision passed for a decade, before President Obama entered office. The presumption of disclosure has two aspects. First, it means that agencies should not wait for specific requests from the public. Instead, agencies should create procedures for identifying records of general interest or use that are appropriate for public disclosure and should use modern technology to inform citizens about what is known and done by their government. This relates to a broader global trend around proactive disclosure of government data in open and accessible online formats.

Searches for documents and data are often cited by agencies as a rationale for high costs and slow release of FOIA requests. Proactively releasing open data that have been subject to frequent FOIA requests (and have been released)—for instance, those from commercial actors that are major users of the FOIA—is sorely needed.

The second aspect of proactive disclosure has to do with how agencies respond to FOIA requests for records where they invoke "discretionary" exemptions, i.e., those for which withholding the requested information is not mandatory. Exemption 5, for example, has been overused and abused by agencies to cover multiple privileges, including those that protect an attorney's work product and attorney-client communications. It also exempts "deliberative

[1]*Sunlight Foundation, Washington, DC 20036, USA.*
[2]*OpenTheGovernment.org, Washington, DC 20005, USA.*
Email: pmcdermott@openthegovernment.org

ILLUSTRATION: DAVIDE BONAZZI/@SALZMANART

processes," a privilege intended to protect documents reflecting opinions and recommendations that inform governmental decisions and policies, so as to preserve the quality of agency decisions by encouraging open discussions, to prevent "premature disclosure of proposed policies before they are finally adopted," and to preclude "public confusion that might result from disclosure of reasons and rationale that were not, in fact, ultimately the grounds for an agency's action" (*7*). The withholding of records as "deliberative process" has been of concern to both scientists working in the government and those seeking information from it. The bill establishes a limit on the ability of agencies to indefinitely claim that records are exempt from disclosure under the privilege afforded to deliberative processes (under exemption 5).

The Senate bill creates greater independence for an ombudsman's office for FOIA requesters, the Office of Government Information Services (OGIS). This office has struggled to maintain its independence since its creation in the OPEN Government Act of 2007. Now, OGIS will be authorized to make reports directly to Congress, without having to first get approval from the hierarchy at the National Archives (where the reports are housed) and the White House Office of Management and Budget (OMB). This independence is critical for OGIS to speak freely to Congress about problems with the implementation of FOIA in the executive branch.

The Senate bills would also mandate that the OMB create a consolidated online portal that would enable the public to make a request to any agency. Although the U.S. General Services Administration began working on a new FOIA hub (*8*) for the Department of Justice, to fulfill a commitment the United States made in 2013 to modernize the administration of FOIA (*9*), work on the new FOIA software stopped in July 2015 (*10*). Passing this requirement into law and putting responsibility for implementation in the hands of the OMB would create much-needed urgency for the federal government to create and adopt modern technology.

IMPACTS ON SCIENTISTS

Language on the presumption of openness in the Senate bill suggests that more of government scientists' actions, statements, work products, and correspondence might be presumed open and available through FOIA to any requester. Nongovernment scientists providing data, discussion, and input for consideration in agency processes might also be concerned that those materials would fall under a similar presumption, once submitted and incorporated into agency processes.

The reforms in the FOIA legislation will have limited effect on those sharing information meant to inform government policy decisions. The records relating to such information may still be withheld under the deliberative process privilege (exemption 5).

> ***"[I]ndependence is critical for OGIS to speak freely to Congress about… the implementation of FOIA…."***

For scientists seeking to obtain information about the policy process, some things will change, but others will not. Agencies seeking to withhold records under this privilege will still have the burden of proving that the materials are both "predecisional" and "deliberative" (*7*). A predecisional record is an antecedent to the adoption of an agency policy, even if no policy is adopted in the end. A deliberative record reflects the give and take of the consultative process, either by assessing the merits of a particular viewpoint or by articulating the process used by the agency to formulate a decision.

One notable change in the legislation is a mandate that the FOIA exemption cannot be applied to records that are 25 years old or older at the date of the request. This was a concession by the public interest community, although we continue to believe that 25 years is still much too long for records to be considered predecisional and deliberative. The concerns are not theoretical: The federal government has continued to prevent release of documents about the Bay of Pigs invasion (*11*), claiming that they are predecisional and deliberative, 53 years after the failed invasion of Cuba. Public interest advocates recommend that the exemption only apply for the same time period subsequent to a given decision as for presidential records: 12 years after the president leaves office.

The main effect of this particular FOIA reform will be to give requesters the right to challenge agencies' invocation of deliberative process for archival records. Moreover, as there is nothing in exemption 5 that mandates withholding of such records, they could also be released before the 25-year point—either in response to a request or proactively.

The "discretionary" exemption will, however, continue to give agencies power to decide to withhold up to the 25-year limit. Scientists seeking information on federal government activities who are trying to discern which materials would fall under the "deliberative process privilege" should not expect much to change. Given the demonstrated proclivities of agencies to overinvoke this exemption, it is unlikely that there will be a major shift in the release of more materials related to the development of agency policy.

The passage of FOIA reform is a welcome victory for bipartisanship in the service of good government. It was not at all certain. In 2014, both houses unanimously voted for historic FOIA reforms (*12*), only to see them die at the last minute (*13*) when the speaker of the House declined to bring up the bill for a final vote as the session closed. It is troubling that the Freedom of the Press Foundation found that the Obama Administration itself lobbied against FOIA reform (*14*), even though the legislative language mirrored the information disclosure policies the president and U.S. attorney general instructed the U.S. government to adopt.

Open-government advocates (including the authors) congratulate both chambers for passing S.337 and sending it to President Obama, who has confirmed that he will sign it into law. We anticipate that we will have a reformed and improved FOIA by the time we celebrate its 50th anniversary on 4 July. ■

REFERENCES

1. A. B. Howard, Federal government agencies receive .91 GPA in FOIA compliance from Center for Effective Government [blog] (E Pluribus Unum, 2014); http://bit.ly/Agenciesgrades.
2. G. Baker, S. Moulton, *Making the Grade: Access to Information Scorecard 2014 Shows Key Agencies Still Struggling to Effectively Implement the Freedom of Information Act* (Center for Effective Government, 2014); http://bit.ly/CEGScorecard.
3. B. Mullin, Obama administration sets record for unfulfilled FOIA requests (Poynter.org, 2015); http://bit.ly/ObamaAdminFOIA.
4. J. Snyder, D. Ivory, *Bloomberg News*, 28 September 2012; http://bit.ly/CabinetFlunksDisclosure.
5. N. Jones, L. Harper, J. Noguchi, Most agencies falling short on mandate for online records (The National Security Archive, Washington, DC, 2015); http://bit.ly/AgenciesFallShort.
6. D. Abel, *Boston Globe*, 19 March 2016; http://bit.ly/ShieldScientists.
7. M. R. Caramanica, Ed., *Federal FOIA Appeals Guide* (Reporters' Committee for Freedom of the Press, Arlington, VA, 2012); http://bit.ly/FOIA-Appeals.
8. 18F-FOIA Hub (GitHub, 2016); https://github.com/18F/foia-hub.
9. A. B. Howard, U.S. commits, yet again, to modernizing administration of Freedom of Information Act (TECHPRESIDENT.com, 31 October 2013); http://bit.ly/TechPres-news.
10. New federal website makes FOIA requests easier to understand, but still can't make them—yet, *Huffington Post*, 15 May 2015; http://huff.to/264hgZz.
11. J. Gerstein, CIA wins secrecy for Bay of Pigs history [blog] (Politico.com, 20 May 2014); http://bit.ly/CIA-BayofPigs.
12. A. B. Howard, "Do-nothing Congress" poised to enact historic FOIA reform (Mediashift, 2014); http://bit.ly/HistoricFOIAReform.
13. K. J. O'Brien, FOIA reform dies while the press looked the other way (Columbia Journalism Review, 12 December 2014); http://bit.ly/CJR-FOIAReformDies.
14. J. Leopold, It took a FOIA lawsuit to uncover how the Obama Administration killed the FOIA reform (VICENEWS, 9 March 2016); http://bit.ly/ObamaAdminKilledReform.

10.1126/science.aag2886

PHOTO: CDC

Having observed the devastating ecological effects of DDT firsthand, George Woodwell advocates closed-cycle control of industrial emissions.

ENVIRONMENT

Envisioning a different future

An ecologist asks how we can protect the global commons

By **Julia Fahrenkamp-Uppenbrink**

Almost 60 years ago, ecologist George Woodwell saw firsthand the effects of DDT on forest ecosystems. In 1968, the insecticide was sprayed from the air into the boreal forest of Maine to protect the trees from spruce budworm, a highly destructive indigenous pest. But other animal species also succumbed to the insecticide. Woodwell, on site to measure how much of the compound reached the ground and how long it remained on plants and in the soil, noted how quickly the forest became deadly still.

Nearly 40 years after Rachel Carson highlighted the dangers of DDT to wildlife (*1*), its use and that of a range of other organic pollutants became tightly restricted through the ratification of the Stockholm Convention. But as Woodwell argues in his latest book, *A World to Live In*, key lessons that might have been gleaned from the DDT story have not been learned, with devastating consequences for life on our planet.

A leading ecologist with decades of experience in the effects of disturbance on ecosystems, Woodwell shows that diverse industrial activities—from nuclear power production to fossil-fuel burning to contemporary agricultural practices—are affecting the chemical processes that underpin all life on Earth. Be it chemical pollution, radiation, or climate change, the result is the same: an impoverished biosphere that is less diverse and less resilient.

The reviewer is on staff at Science, *AAAS Science International, Cambridge CB2 1LQ, UK. Email: jfahrenkamp@science-int.co.uk*

A World to Live In
An Ecologist's Vision for a Plundered Planet
George M. Woodwell
MIT Press, 2016. 243 pp.

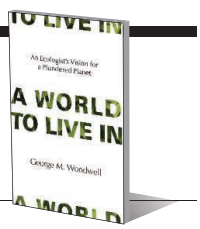

Woodwell puts the blame squarely on a dominant worldview that places the environment within the scope of economics and assumes there can be limitless growth. As the experience with DDT and other persistent organic pollutants has shown, nowhere on Earth, from the depths of the oceans to the poles, is so remote as to remain unaffected by our actions. Most recently, widespread use of neonicotinoid pesticides has been implicated in the declines of bees and other invertebrates. And with a growing human population, the biosphere's limits will be ever more tested.

The insights that Woodwell offers into the early days of environmental and climate politics are fascinating, showing how, but for political change, the world might have taken a different path in the 1980s. Public and political interest in environmental stewardship grew in the 1970s, particularly under President Jimmy Carter, but was sidelined under later leaders who viewed the role of government mostly as facilitating commerce. The failure of the U.S. Congress to ratify the Kyoto protocol in 1997 was a tragedy that has delayed progress globally.

Woodwell does not mention the discussions leading up to the United Nations' COP21 climate meeting in Paris in December 2015. The book went to press before the Paris Agreement—widely seen as a promising if still limited advance toward climate stabilization—was reached, but I wonder whether he considers the pledges approach to be promising. I would also have liked to know more about the author's views on the European Registration, Evaluation, Authorization and Restriction of Chemicals (REACH) legislation, which requires testing of most chemical substances manufactured in or imported into the European Union for their effect on human health and the environment.

But the author's main argument remains valid. As important as the Paris Agreement and legislation such as REACH are, they are but small steps toward addressing the fundamental problem: that many current industrial practices are inherently damaging to the environment and must change, and fast, to avoid catastrophic consequences.

Woodwell calls for a fundamental rethink to ensure the protection of the global commons. In contrast to most current climate policy efforts such as the Paris Agreement, which aim to stabilize carbon at levels that prevent dangerous climate change, he advocates a return to the much lower carbon levels of the late 19th century. In his solution, reduced fossil fuel use plays a role, of course, but he also advocates for vast reforestation and afforestation efforts to kick-start environmental and climatic recovery. More generally, he calls for closed-cycle industrial systems with no leakage of wastes, arguing that there are no safe thresholds for any toxins that can accumulate in the environment. It may seem unlikely that the world will follow this path, but Woodwell is to be commended for clearly outlining the threats and sketching out a bold solution.

As *A World to Live In* makes clear, climate change due to greenhouse gas emissions is a symptom of the same malaise that led to rampant pesticide use in industrial agriculture and a nuclear industry that is dependent on governments to limit its liability in case of accidents. A key concept that Woodwell returns to repeatedly is the legal principle of "Sic utere tuo ut alienum non laedas" ("So use your own as not to injure another's property"), which he interprets broadly to mean that we have a moral responsibility to protect the global commons. This seems a useful starting point for rethinking how humans should treat the planet and each other.

REFERENCES

1. R. Carson, *Silent Spring* (Houghton Mifflin, Boston, 1962).

10.1126/science.aag1405

SCIENCE POLICY

The battle lines are drawn

In a stirring call to action, an author probes the forces that undermine evidence-based science policy

The War on Science
Who's Waging It, Why It Matters, What We Can Do About It
Shawn Otto
Milkweed Editions, 2016. 530 pp.

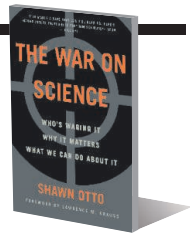

By **Peter R. Reczek**

After a close brush with the Catholic Church in 1624, the Italian scientist Galileo Galilei anonymously published a book advancing the heliocentric theory of Copernicus in 1632. Galileo called one of the book's fictitious characters Simplicio or simpleton—an unfortunate turn of phrase that Pope Urban VIII, a longtime friend and supporter, believed was a veiled reference to him. Outraged, he brought Galileo before a tribunal of the Roman Inquisition. The examiners coerced him into recanting his written statements, and he was placed under house arrest, where he died almost 10 years later.

In his new book, *The War on Science*, Shawn Otto documents the modern clash between what he calls the "authoritarians" (governments, large corporations, and religious groups) and the "antiauthoritarians" (scientists and other liberal thinkers). Drawing on recent examples ranging from the evolution debate to vaccine skepticism, Otto describes the emergence of an antiscience movement whose focus is to disrupt the creation of evidence-based policy for the sake of preserving profitable business models or entrenched religious dogma.

Otto is at his best when he describes the processes that culminated in the widespread denial of human-caused climate change. Exxon executives recognized climatic changes due to the burning of fossil fuels as long ago as 1977, he writes. At that time, Otto claims, a loose collaboration among several energy companies began a public relations campaign to discredit scientific reports of climate change. He meticulously references news reports, books, and email messages demonstrating techniques that parallel the steps taken by tobacco companies to deny a link between smoking and lung cancer. In doing so, Otto reminds us how advocates for both groups often cherry-picked data while focusing on anomalies in the results and played favorable games with statistics to minimize the dangers of smoking and climate change, respectively.

In a chapter entitled "The Industrial War on Science," Otto alleges that a carefully coordinated attack on scientists and the scientific process has undermined scientific credibility and has led to a position where "the climate debate" is all but unwinnable. Only unequivocal statements by highly regarded leaders will substantially reverse this trend, he argues. Pope Francis has taken such a step in his encyclical *Laudato Si'* (*1*).

Citing polls conducted at the beginning of the new millennium, Otto reveals that 52% of Americans believe that humans and dinosaurs once coexisted.

The problem, however, extends beyond climate change denial. The same tactics are being used to undermine other technocentric policies, including the push to "teach the [supposed] controversy" between evolution and intelligent design, as well as legislation governing stem cell research.

Evidence-based policy-making is a necessity if we are to continue to advance in a highly technologically dependent world. Otto outlines tactics that have been used successfully by such advocacy groups as the Union of Concerned Scientists and its Center for Science and Democracy, which broadened its focus to target issues such as climate change and scientific integrity, and Greenpeace, whose efforts to combine civil action with creative communication serve as an international model for other conservation-based organizations.

Using the language of warfare, Otto suggests that the first step is to know the enemy. Scientists must realize, for example, that antiscience groups often attempt to redefine scientific terms in such a way as to enable opponents to debate science as if it were an opinion. (Evolution is "just a theory," right?)

Otto also argues for direct engagement between scientists and the general public. To avoid the fate that befell Galileo, scientists must understand that 21st-century journalism has blurred the lines between objectivity and subjectivity, sometimes sacrificing deep investigation in the interests of expediency, he maintains. As more and more news outlets eliminate science sections, the journalistic inclination to give equal weight to "both sides" of topics for which there is widespread scientific consensus amplifies minority and extreme arguments.

Otto believes that unless we find ways to balance the rights of the individual with the interests of society, we are headed for what Garrett Hardin called "the tragedy of the commons" (*2*). To achieve this, he outlines 14 ambitious "battle plans" that include advice for everyone from educators ("Plan 6: Teachers Should Teach Science Civics") to funding agencies ("Plan 7: Granting Bodies Should Require and Fund More Outreach") to potential office holders ("Plan 11: Candidates Should Sign Science Pledges").

Scientists can no longer afford to remain sequestered in their laboratories. We need to fight back. "Call a spade a spade, and do it publicly," Otto urges. To regain the public's trust, we must demonstrate that science is an activity done by people for people.

The author is a freelance writer and former Science and Technology Policy Fellow of the American Association for the Advancement of Science. Email: peter.reczek@gmail.com

REFERENCES

1. Pope Francis, *Encyclical Letter "Laudato Si' of the Holy Father Francis, On the Care of Our Common Home"* (Holy See, Vatican City, 2015).
2. G. Hardin, *Science* **162**, 1243 (1968).

10.1126/science.aaf9243

PHOTO: IRFAN KHAN/CONTRIBUTOR

REVIEW SUMMARY

PROTEOSTASIS

In vivo aspects of protein folding and quality control

David Balchin, Manajit Hayer-Hartl, F. Ulrich Hartl*

BACKGROUND: Proteins are synthesized on ribosomes as linear chains of amino acids and must fold into unique three-dimensional structures to fulfill their biological functions. Protein folding is intrinsically error-prone, and how it is accomplished efficiently represents a problem of great biological and medical importance. During folding, the nascent polypeptide must navigate a complex energy landscape. As a result, misfolded molecules may accumulate that expose hydrophobic amino acid residues and thus are in danger of forming potentially toxic aggregates. To ensure efficient folding and prevent aggregation, cells in all domains of life express various classes of proteins called molecular chaperones. These proteins receive the nascent polypeptide chain emerging from the ribosome and guide it along a productive folding pathway. Because proteins are structurally dynamic, constant surveillance of the proteome by an integrated network of chaperones and protein degradation machineries, the proteostasis network (PN), is required to maintain protein homeostasis in a range of external and endogenous stress conditions.

ADVANCES: Over the past decade, we have gained substantial new insight into the overall behavior of the PN and the molecular mechanics of its components. Advances in structural biology and biophysical approaches have allowed chaperone mechanisms to be interrogated at an unprecedented level of detail. Recent work has provided fascinating insight into the process of protein folding on the ribosome and revealed how highly allosteric chaperones such as the heat shock protein 70 (Hsp70), Hsp90, and chaperonin systems modulate the folding energy landscapes of their protein clients. Studies of chaperone systems from bacteria and eukaryotes have revealed common principles underlying the organization of chaperone networks in different domains of life. Recently, we have begun to appreciate the relative complexity of eukaryotic chaperones and are starting to understand how eukaryotes deal with the challenge of folding a large proteome enriched in multidomain proteins. At the cellular level, the response of the PN to conformational stress, aging, and diseases of aberrant protein folding has been an area of intense investigation. Importantly, the capacity of the PN declines during aging and this leads to dysfunction of specific cell types and tissues, rendering the organism susceptible to chronic diseases. Among these, neurodegenerative syndromes associated with protein aggregation are increasingly prevalent in the aging human population. Notably, the accumulation of toxic protein aggregates is both a consequence and a cause of PN decline, driving a vicious cycle that ultimately leads to proteostasis collapse.

ON OUR WEBSITE

Read the full article at http://dx.doi.org/10.1126/science.aac4354

OUTLOOK: A new view of protein folding is emerging, whereby the energy landscapes that proteins navigate during folding in vivo may differ substantially from those observed during refolding in vitro. From the ribosome through to the major chaperone systems, the nascent protein interacts with factors that modulate its folding pathway. Future work should focus on obtaining the high-resolution structural and kinetic information necessary to define the pathways of protein folding during translation, and in association with molecular chaperones. Organisms have evolved various mechanisms to deal with misfolded and aggregated proteins to maintain proteostasis. It is becoming increasingly clear that besides removing these proteins by degradation, cells also strategically sequester them into transient or stable aggregates, often in defined cellular locations. Much remains to be understood about how this cellular decision-making occurs at a molecular level and how dysregulation of these mechanisms leads to proteotoxicity. From a medical perspective, the intimate relationship between proteostasis and disease, aging, and neurodegeneration makes components of the PN logical drug targets, with the goal of promoting healthy aging. Pharmacological manipulation of the PN will require a detailed understanding of how the network responds to perturbation and how its different components cooperate. ■

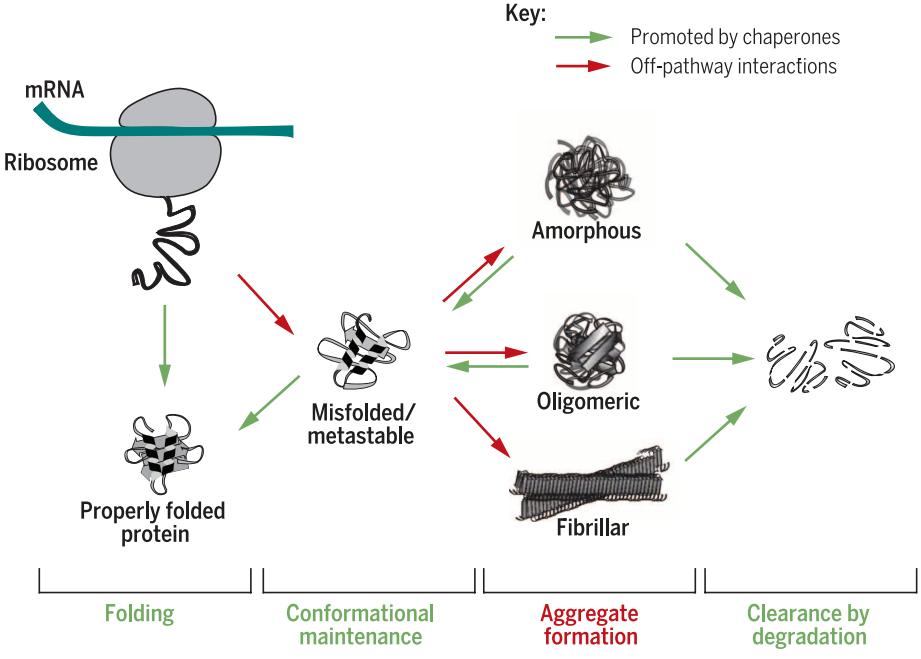

Molecular chaperones are key players in the cellular proteostasis network and serve to maintain a balanced proteome. They promote the folding of newly synthesized proteins, function in conformational maintenance, and prevent potentially toxic off-pathway aggregation. Chaperones also cooperate with other components of the proteostasis network, such as the proteasome system and autophagy, in the removal of terminally misfolded and aggregated proteins through proteolytic degradation.

The list of author affiliations is available in the full article online.
*Corresponding author. Email: uhartl@biochem.mpg.de
Cite this article as D. Balchin *et al.*, *Science* **353**, aac4354 (2016). DOI: 10.1126/science.aac4354

REVIEW

PROTEOSTASIS

In vivo aspects of protein folding and quality control

David Balchin, Manajit Hayer-Hartl, F. Ulrich Hartl*

Most proteins must fold into unique three-dimensional structures to perform their biological functions. In the crowded cellular environment, newly synthesized proteins are at risk of misfolding and forming toxic aggregate species. To ensure efficient folding, different classes of molecular chaperones receive the nascent protein chain emerging from the ribosome and guide it along a productive folding pathway. Because proteins are structurally dynamic, constant surveillance of the proteome by an integrated network of chaperones and protein degradation machineries is required to maintain protein homeostasis (proteostasis). The capacity of this proteostasis network declines during aging, facilitating neurodegeneration and other chronic diseases associated with protein aggregation. Understanding the proteostasis network holds the promise of identifying targets for pharmacological intervention in these pathologies.

Proteins are involved in almost every biological process. A typical mammalian cell expresses 10,000 to 20,000 different proteins, which are synthesized on ribosomes as linear chains up to several thousand amino acids (aa) in length. To function, most newly synthesized proteins must fold into a defined three-dimensional structure. How this is accomplished and how cells maintain the integrity of their proteome [proteostasis (*1*)] in a range of external and endogenous stress conditions are problems of paramount biological and medical relevance.

The folded structures of proteins are only marginally stable, and subtle changes due to mutation may tip the balance (*2*). Furthermore, a substantial fraction of proteins (15 to 30% of mammalian proteomes) lack ordered structure partially or entirely (*3*), and the formation of toxic aggregates by such metastable proteins is associated with Alzheimer's and Parkinson's disease. Thus, protein quality control and the maintenance of proteome balance are critical for cellular and organismal health. To ensure proteostasis, organisms from all domains of life invest in an extensive quality control network, integrating molecular chaperones, which mediate protein folding and conformational repair, with the ubiquitin-proteasome system (UPS) and autophagy, which remove terminally misfolded proteins and aggregates. Importantly, the capacity of the proteostasis network (PN) declines during aging (*4*), facilitating the emergence of chronic diseases caused by protein aggregation, including neurodegeneration, type II diabetes, heart disease, and certain forms of cancer.

Here we review advances made over the last 15 years in understanding how cells support protein folding and maintain proteostasis. We focus on the mechanisms of molecular chaperones in the cytosol and the ways that chaperone systems cooperate to form a functional PN. In particular, we highlight the differences in the pathways and energy landscapes of protein folding in vivo and in vitro. For a detailed discussion of the protein-folding machineries of the endoplasmic reticulum, see (*5*).

Department of Cellular Biochemistry, Max Planck Institute of Biochemistry, Am Klopferspitz 18, 82152 Martinsried, Germany.
*Corresponding author. Email: uhartl@biochem.mpg.de

Molecular chaperones—machineries of protein folding

Fundamental insight into protein folding was provided by Anfinsen's pioneering experiments in the 1950s, which showed that small proteins refold spontaneously in vitro on removal from denaturant (*6*). This finding demonstrated the primacy of the amino acid sequence in determining a protein's native conformation and also implied that folding occurs without the aid of additional factors. However, evidence began to emerge in the 1980s that certain proteins require assistance by molecular chaperones for folding in vivo (*7*). Research over the last two decades has firmly established the essential role of chaperone machineries in allowing newly synthesized proteins to fold efficiently and at a biologically relevant time scale.

Whereas small proteins up to ~100 aa may fold rapidly (within milliseconds) and with full yield in vitro (*8*), folding is often inefficient for larger proteins, owing to off-pathway aggregation. Proteins >100 aa constitute the major fraction of all proteomes, with large multidomain proteins strongly increasing in number from prokaryotes to eukaryotes (Fig. 1). The folding of such proteins in vivo is further compounded by macromolecular crowding (300 to 400 g of total protein per liter in the cytosol) (*9*), which enhances the tendency of folding intermediates and misfolded states to aggregate. A major function of the chaperone network is to prevent such aberrant interactions, which are often irreversible. We define a molecular chaperone as any protein that interacts with, stabilizes, or helps another protein to acquire its functionally active conformation, without being present in its final structure (*7*).

Folding and aggregation

The folding process is inherently error-prone, owing to the large number of possible conformations a protein chain can adopt (>10^{30} for a 100-aa protein). Moreover, folding relies on the cooperation of many weak, noncovalent interactions and involves amino acid contacts both close in sequence and far apart (*8*). Hydrophobic forces are particularly relevant in driving chain collapse and the burial of nonpolar amino acids within the core of the folding structure (in the case of soluble proteins), restricting the conformational space that must be searched during folding (*10*). However, the free-energy landscape toward the thermodynamically favorable native state is often rugged, which means the molecules need to cross substantial kinetic energy barriers and consequently populate folding intermediates (*8*) (Fig. 2A). Such kinetically trapped intermediates are the rule for larger proteins, entailing the danger of misfolding due to the formation of nonnative interactions (*10*). Slow steps in folding that lead to the accumulation of folding intermediates include prolyl isomerization and disulfide bond formation (in secretory proteins), which can be accelerated by prolyl isomerases and protein disulfide isomerases, respectively (*5*, *11*).

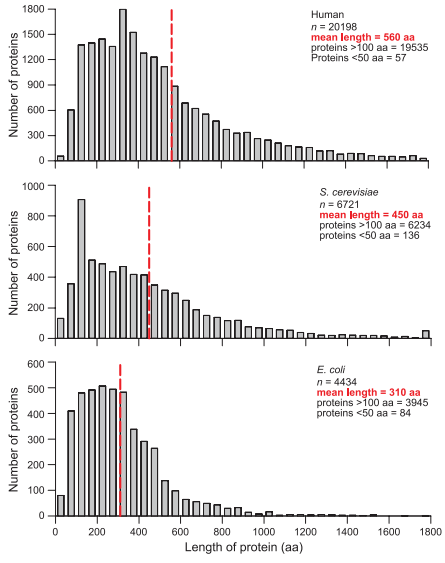

Fig. 1. Increasing complexity of proteomes from bacteria to humans. The total number of proteins and the numbers of proteins >100 aa and <50 aa in length are shown for the predicted proteomes of *E. coli*, *S. cerevisiae*, and humans. Note the increase in the number and fraction of proteins >100 aa and of large multidomain proteins from *E. coli* to *S. cerevisiae* to humans. Such proteins tend to populate intermediate states during folding, resulting in increased aggregation propensity and chaperone dependence.

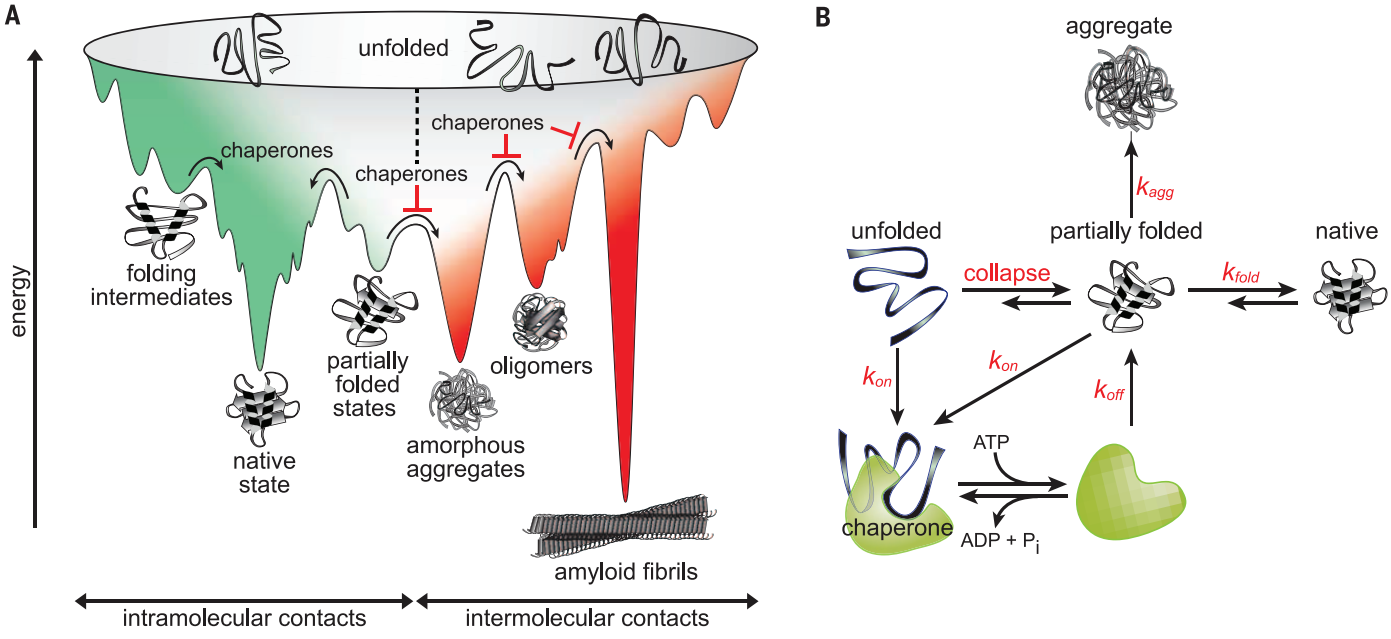

Fig. 2. Protein aggregation competes with folding. (**A**) During folding, protein molecules sample various conformations while traveling downhill on a potential free-energy surface (green) toward the thermodynamically favorable native state. Kinetically trapped on- or off-pathway intermediates occupy low-energy wells (folding intermediates and partially folded states). Molecular chaperones provide assistance to folding by lowering free-energy barriers and preventing aberrant intermolecular interactions (red), which can lead to various forms of aggregates (amorphous, oligomeric, fibrillar). Fibrillar (amyloid-like) aggregates may be thermodynamically the most stable. (**B**) Molecular chaperones promote protein folding by a generic mechanism of kinetic partitioning of nonnative states. Many chaperones use ATP binding and hydrolysis to switch between low- and high-affinity states for folding intermediates (unfolded, partially folded), exposing hydrophobic amino acid residues. Binding to chaperone blocks aggregation and reduces the concentration of aggregation-prone molecules. Release from chaperone allows folding (burial of hydrophobic residues). Efficient folding occurs when the rate constant of folding (k_{fold}) is faster than rebinding of folding intermediate to chaperone (k_{on}) and aggregation (k_{agg}) is slower than k_{on}. Figures modified from (*13*).

Partially folded or misfolded proteins typically expose hydrophobic amino acid residues and regions of unstructured polypeptide backbone to the solvent, features that can give rise to aggregation. Like folding, aggregation is largely driven by hydrophobic forces but is highly concentration dependent (*12*). Although most aggregates are amorphous, a subset of nonnative proteins aggregate to form so-called amyloid fibrils, which are structurally defined by β strands running perpendicular to the long fibril axis (cross-β-structure) (Fig. 2A). Fibril formation is often preceded by the accumulation of oligomeric aggregates, which are thought to play key roles in disease (Fig. 2A).

Molecular chaperones that function broadly in de novo folding include the chaperonins (Hsp60) and the Hsp70 and Hsp90 systems. They recognize hydrophobic amino acid residues exposed by nonnative proteins and promote folding through adenosine 5′-triphosphate (ATP)–regulated cycles of protein binding and release. In this mechanism of kinetic partitioning, release of hydrophobic elements allows folding to proceed, whereas (re)binding of nonnative protein blocks aggregation and may reverse misfolded states (Fig. 2B).

Protein folding in the context of translation

Protein folding in vivo occurs in the context of the vectorial translation of the polypeptide chain on the ribosome from N to C terminus, a fundamental difference from refolding of a chemically denatured protein in vitro, where all elements of the polypeptide chain are simultaneously available.

Translation is slow compared to folding. For example, it takes eukaryotic ribosomes ~25 s to synthesize a 100-aa protein (~5 s for bacterial ribosomes) (*13*), suggesting that folding can begin cotranslationally. The nascent chain exit channel of the large ribosome subunit is ~100 Å long and typically 10 to 20 Å wide, providing just enough space for α helices or small tertiary structure elements to form (*14*) (Fig. 3). As a consequence, the C-terminal 30 to 40 aa of the translating chain are topologically restricted and cannot participate in the long-range interactions necessary for the cooperative folding of larger domains. The exit channel expands toward its opening, however, forming an "exit port" that may allow the emerging chain to explore local peptide conformations (*15*, *16*). The channel of the bacterial ribosome was recently shown to provide sufficient space for the folding of a 29-aa zinc-binding protein (*17*). A limited number of small single-domain proteins (~80 proteins <50 aa in *E. coli*; see Fig. 1) may thus fold to completion before emerging from the ribosome. A five-helix domain of 70 aa was observed to form a compact nonnative intermediate in the exit port that rearranges into a native-like structure after the full domain sequence emerges from the ribosome (*18*). Moreover, the ribosome surface contributes to avoiding misfolding of incomplete chains that would aggregate in free solution (*19*, *20*). These studies provide fascinating evidence that the ribosome modulates the folding pathway: Because folding is rate-limited by translation, the nascent protein is allowed to sample available conformations in a quasi-equilibrium (*16*), with small modules beginning to form inside the channel and coalescing upon emergence from the ribosome, perhaps reducing kinetic traps along the folding pathway. Chaperone binding to the emerging chain may further avoid misfolding, as described in the following section.

Although most single-domain proteins reach their native state posttranslationally once all elements of the nascent chain are available outside the ribosome (*18*, *20*–*22*), cotranslational folding is critical for the biogenesis of many multidomain proteins. As noted previously (*23*), the sequential folding of domains emerging from the ribosome avoids the formation of misfolded states resulting from nonnative interdomain contacts (*24*, *25*) (Fig. 3). The cotranslational formation of folded domains also allows subunit assembly to initiate on ribosome-bound polypeptides, as shown for the LuxA and LuxB subunits of bacterial luciferase (*26*). Such a mechanism is facilitated by the operon structure of bacterial genes, where subunits of an oligomeric complex are often encoded by the same mRNA. Of note, adjacent ribosomes in polyribosome complexes have been observed to be closely associated in a manner that maximizes the distance between their polypeptide exit sites (*27*, *28*). This topology would disfavor aberrant

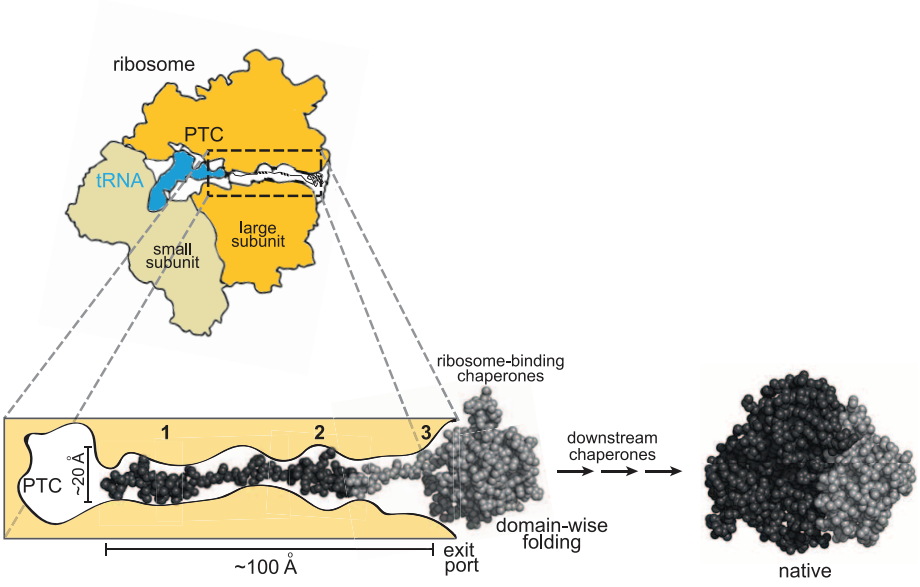

Fig. 3. Protein folding on the ribosome. The polypeptide exit tunnel of the large ribosomal subunit, as seen in a longitudinal cut through the bacterial ribosome, is magnified and shown schematically. The nascent polypeptide chain of a multidomain protein is modeled into the tunnel, forming a folded N-terminal domain of ~200 aa immediately outside the ribosomal exit port. This cotranslational folding process may be assisted by chaperones that dock onto the ribosome at the opening of the exit tunnel. Completion of folding is mediated by downstream chaperones that have no direct affinity for the ribosome. 1, 2, and 3 mark regions of the tunnel where structure formation of the nascent chain, including folding of domains <50 aa, has been observed. PTC, peptidyl transferase center.

interactions between nascent chains similar in length and folding status. Thus, a partially folded nascent chain may preferentially assemble with a completed subunit that has already left the ribosome.

The rate of translation can be manipulated by cells to optimize folding (*29*–*34*). Modifying translation speed by altering codon usage affects the conformation and function of the clock protein FREQUENCY (*35*) and the multidrug resistance efflux pump MDR1 (*36*). Thus, a nuanced picture of translation is emerging, in which the rate of protein synthesis has been tuned in evolution to optimize folding and prevent misfolding of the nascent polypeptide.

Chaperone networks in the cytosol

Several evolutionary conserved families of molecular chaperones guide proteins along productive folding pathways, avoiding and sometime reversing misfolding and aggregation. Their members are often referred to as stress proteins or heat shock proteins (Hsps) because they are upregulated in conditions of conformational stress. The major chaperone families are classified by molecular weight (Hsp40, Hsp60, Hsp70, Hsp90, Hsp100, and the small Hsp).

The organizational principles of cytosolic chaperone pathways are highly conserved. For most proteins too large to fold in association with the ribosome, chaperones delay chain compaction, preventing misfolding, until sufficient structural elements are available for folding to be productive. Ribosome-binding chaperones [Trigger factor (TF), in bacteria; ribosome-associated complex (RAC) and nascent-chain–associated complex (NAC) in eukarya] interact first with the nascent polypeptide, followed by chaperones that have no direct affinity for the ribosome, including the classical Hsp70 system (DnaK/DnaJ in bacteria; Hsp70/Hsp40 in eukarya) (Fig. 4). Completion of folding may either be accomplished by Hsp70 or require transfer to the chaperonin (GroEL/ES in bacteria; TRiC in eukarya) or the Hsp90 system (HtpG in bacteria) (Fig. 4). The different chaperone machineries interact directly, or use specific adapter proteins to facilitate client transfer. In this way, the folding protein is constantly protected from aberrant interactions and premature degradation in the cytosol (*37*, *38*). The ATP-independent small heat shock proteins (sHsps) function in buffering aggregation and cooperate with Hsp70 in folding reactions (*39*). In addition to these promiscuous chaperone systems, specific assembly chaperones may assist the formation of oligomeric protein complexes by interacting with their folded subunits (*40*, *41*).

Chaperone functions on the ribosome

In bacteria, the abundant TF binds to the large ribosome subunit at the opening of the polypeptide exit tunnel and interacts with the nascent chains of most proteins >100 aa in an ATP-independent manner (*42*, *43*). Although TF is not essential in *E. coli* under laboratory growth conditions, the combined deletion of TF and DnaK (the major bacterial Hsp70) is lethal above 30°C, resulting in bulk protein aggregation (*13*, *43*). TF (~50 kDa) has an elongated three-domain structure (*22*) and binds to hydrophobic stretches in nascent chains, thereby delaying chain collapse (*22*, *44*–*47*). As a result, TF slows the rate of cotranslational folding but increases the yield of the folding reaction (*48*). For longer nascent chains, TF cooperates with the ATP-regulated DnaK/DnaJ system (*13*) (Fig. 4A). Release from TF appears to be governed by the propensity of the bound peptide to bury hydrophobic segments as translation proceeds. A similar mechanism of folding is exemplified by the ATP-independent chaperone Spy in the bacterial periplasm, where client proteins remain associated with the chaperone until all hydrophobic elements are buried in the folded structure (*49*).

In eukaryotes, RAC and NAC may fulfill a role similar to that of TF in protein folding. RAC in *Saccharomyces cerevisiae* and other fungi is a complex of the Hsp70 chaperone Ssz1 and the ribosome-binding Hsp40 cochaperone zuotin (Hsp70L1 and Mpp11 in mammals) (*43*). RAC cooperates with the ribosome-binding isoforms of Hsp70, Ssb1, and Ssb2 (*50*) and has been suggested to couple cotranslational folding with the mechanics of peptide elongation by the ribosome (*51*, *52*). NAC, a dimeric complex of α (31 kDa) and β (22 kDa) subunits, associates with ribosomes via the β subunit and binds short nascent chains. Recent findings in *Caenorhabditis elegans* show that protein aggregates sequester NAC, thereby reducing translational capacity and implicating NAC as a sensor of protein quality control status (*53*). Moreover, NAC is required for correct intracellular protein sorting (*54*–*56*). Specifically, NAC modulates the fidelity of the signal recognition particle (SRP) in targeting proteins to the endoplasmic reticulum (ER) (*54*–*56*). Moreover, mistargeting of mitochondrial proteins to the ER occurs when NAC function is impaired (*56*).

Chaperone functions downstream of the ribosome

For proteins that are unable to fold with the ribosome-associated chaperones (≥30% of the proteome), the next layer of folding assistance is provided by the Hsp70 system, which is abundant in bacteria and eukarya (Fig. 4). Multiple Hsp70 molecules may interact with a nascent chain, preventing unproductive interdomain interactions and supporting cotranslational folding (*23*, *50*, *57*). In addition, Hsp70 functions as a hub, providing connections to the more specialized downstream chaperones, Hsp90 and chaperonins. Substrate-loaded Hsp70 is coupled to Hsp90 via the Hsp organizing protein (Hop), which physically connects Hsp70 to Hsp90 to facilitate client transfer (*58*, *59*) (Fig. 4B). Hsp70 also interacts directly with the eukaryotic chaperonin TRiC/CCT (*60*) (Fig. 4B), and in *E. coli* maintains certain proteins in a folding-competent state before transfer to the chaperonin GroEL (*23*) (Fig. 4A). In addition to Hsp70, in eukarya the jellyfish-like, hexameric prefoldin (Pfd) can bind to nascent chains and mediates transfer to the chaperonin (Fig. 4B). In archaea, many species of which lack Hsp70, Pfd may fulfill a more general role as a nascent chain–binding chaperone (*23*).

Chaperone paradigms

Several mechanistic paradigms of chaperone function in protein folding have been defined (*13*). In the following sections, we discuss major recent advances in understanding the mechanisms of the Hsp70, chaperonin, and Hsp90 machineries.

The Hsp70 system

Hsp70 (DnaK in bacteria) is a paradigm allosteric chaperone that binds to 5- to 7-aa sequence elements that are enriched in hydrophobic residues and are typically exposed by nonnative proteins (*61*, *62*). ATP-dependent binding and release of such segments allows Hsp70s to participate in a wide range of cellular processes, including protein folding, refolding, disaggregation, and protein transfer to cellular compartments or the proteolytic machinery (*61*, *62*).

Hsp70 has two domains: an N-terminal nucleotide-binding domain (NBD) of ~40 kDa and a C-terminal substrate-binding domain (SBD) of ~30 kDa, connected by a hydrophobic linker (*61*) (Fig. 5A). The SBD consists of a β-sandwich domain, harboring the peptide-binding site, and an α-helical lid segment. Peptide substrate binds in an extended conformation in a groove in the β-sandwich domain (Fig. 5A).

The Hsp70 reaction cycle is intimately regulated by Hsp40 proteins and nucleotide exchange factors (NEFs) (Fig. 5B). Hsp40 cochaperones (DnaJ in bacteria, jointly known as J-domain proteins) function in recognizing and transferring substrate proteins to Hsp70 in the ATP state, in which the hydrophobic interdomain linker and the α-helical lid of the SBD are associated with the NBD, and the SBD is in an open conformation (*63*–*65*). In this state, Hsp70 has high on and off rates for substrate. Interaction of Hsp40 with Hsp70 strongly accelerates (by >1000-fold) the hydrolysis of the bound ATP, generating the adenosine 5′-diphosphate (ADP) state, in which SBD and NBD are loosely associated (*61*, *66*) and the α-helical lid is in the closed conformation, trapping the bound substrate (low on and off rates) (*61*, *67*) (Fig. 5B). Subsequent NEF binding to the NBD facilitates ADP-ATP exchange, opening the SBD and allowing substrate release for folding or transfer to downstream chaperones or the degradation machinery. Rebinding prevents off-pathway aggregation and can reverse misfolding by removing long-range interactions present in unbound folding intermediate (kinetic partitioning mechanism) (*68*–*71*). It has also been suggested that DnaK binding can bias the folding pathway such that the bound substrate first forms secondary structure, followed by the development of longer-range contacts upon release (*71*, *72*). In metazoans the cycle is further regulated by the Hsp70 interacting protein Hip, which stabilizes Hsp70 in the ADP state, delaying client protein release (*73*) (Fig. 5B).

Compared to bacteria, the number of Hsp40 proteins is markedly expanded in eukarya. Human cells express ~50 different J-domain proteins (*74*), amplifying the ability of Hsp70 to recognize a diverse range of clients. For example, Hsp70 cooperates with the Hsp40 auxilin in disassembling clathrin cages of endocytic vesicles (*62*) and with other specific Hsp40s in supporting the life cycle of certain viruses (*75*). The NEFs of Hsp70 are less diverse (*76*). Bacteria contain only a single NEF, GrpE, whereas several structurally unrelated families of NEFs exist in eukarya, including the Bcl-2–associated anthanogene (BAG) domain proteins, as well as HspBP1 and Hsp110 (*76*). The Hsp110 proteins are Hsp70 homologs that function also as holding chaperones and cooperate with Hsp70 in protein disaggregation (*77*, *78*). In eukarya the C terminus of cytosolic Hsp70 is unstructured and mediates interactions between Hsp70 and Hsp90 (via Hop) or the ubiquitin-proteasome system (via CHIP) (*61*, *79*) (Fig. 5B). Both Hop and CHIP contain tetratricopeptide repeat (TPR) domains that bind the C terminus of Hsp70 and Hsp90 (*13*).

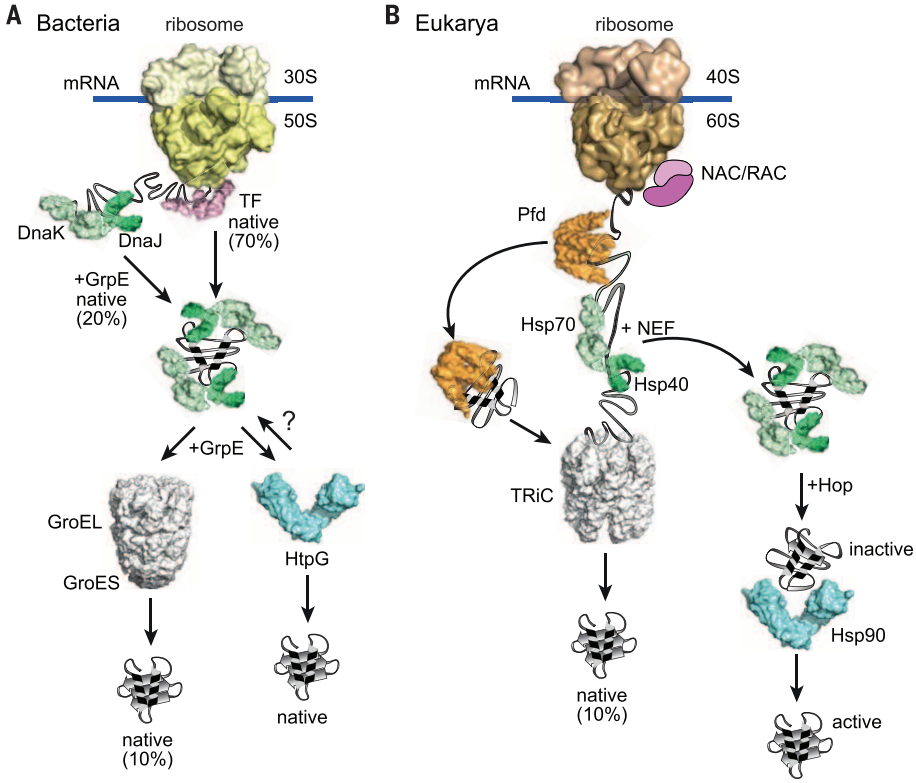

Fig. 4. Chaperone pathways of protein folding in the cytosol. For ~70% of bacterial (**A**) and eukaryotic (**B**) proteins, the ribosome and associated factors [trigger factor (TF) in bacteria; nascent chain–associated complex (NAC) and ribosome-associated complex (RAC) in eukaryotes] provide folding assistance. Downstream of the ribosome, Hsp70 (DnaK in bacteria) is the hub of the chaperone network. Hsp70 cooperates with Hsp40s (DnaJ in bacteria) and nucleotide exchange factors (NEFs; GrpE in bacteria) to fold ~20% of the proteome. The remaining ~10% of the proteome is passed on to the chaperonins for folding—GroEL/ES in bacteria and TRiC in eukaryotes. In eukaryotes, some nascent proteins are transferred directly to TRiC by prefoldin (Pfd). This alternative pathway dominates in archaea, which lack Hsp70 proteins. Eukaryotes also employ the Hsp90 chaperone system to catalyze the activation of metastable proteins such as kinases and transcription factors. Clients are transferred to Hsp90 via the Hsp70 system and the cochaperone Hop. The bacterial Hsp90, HtpG, is thought to act more generally in folding and functions without known cochaperones.

Chaperonins—nanocages for protein folding

The chaperonins (Hsp60s) are multisubunit cylindrical complexes that function by enclosing a single molecule of nonnative protein in their central cavity for folding to occur unimpaired by aggregation. They are essential in all three domains of life and are divided into two groups. Group I chaperonins occur in the bacterial cytosol (GroEL), mitochondria (Hsp60), and chloroplasts (Cpn60) (*80*); group II chaperonins, in archaea (thermosome) and the eukaryotic cytosol (TRiC, also known as CCT) (*81*). The two chaperonin classes share a common subunit organization and general architecture, both forming ~1-MDa complexes consisting of two rings of seven to nine subunits of ~60 kDa that are stacked back-to-back. Group I and II chaperonins are unable to fold client proteins interchangeably, implying important differences in substrate protein recognition or folding mechanism.

The group I chaperonin GroEL of the bacterial cytosol is involved in the folding of ~10% of the *E. coli* proteome, including proteins that cannot use the upstream chaperones for folding (*80*, *82*). GroEL cooperates with the lid-shaped GroES, a heptameric ring of ~10 kDa subunits that binds to the ends of the GroEL cylinder

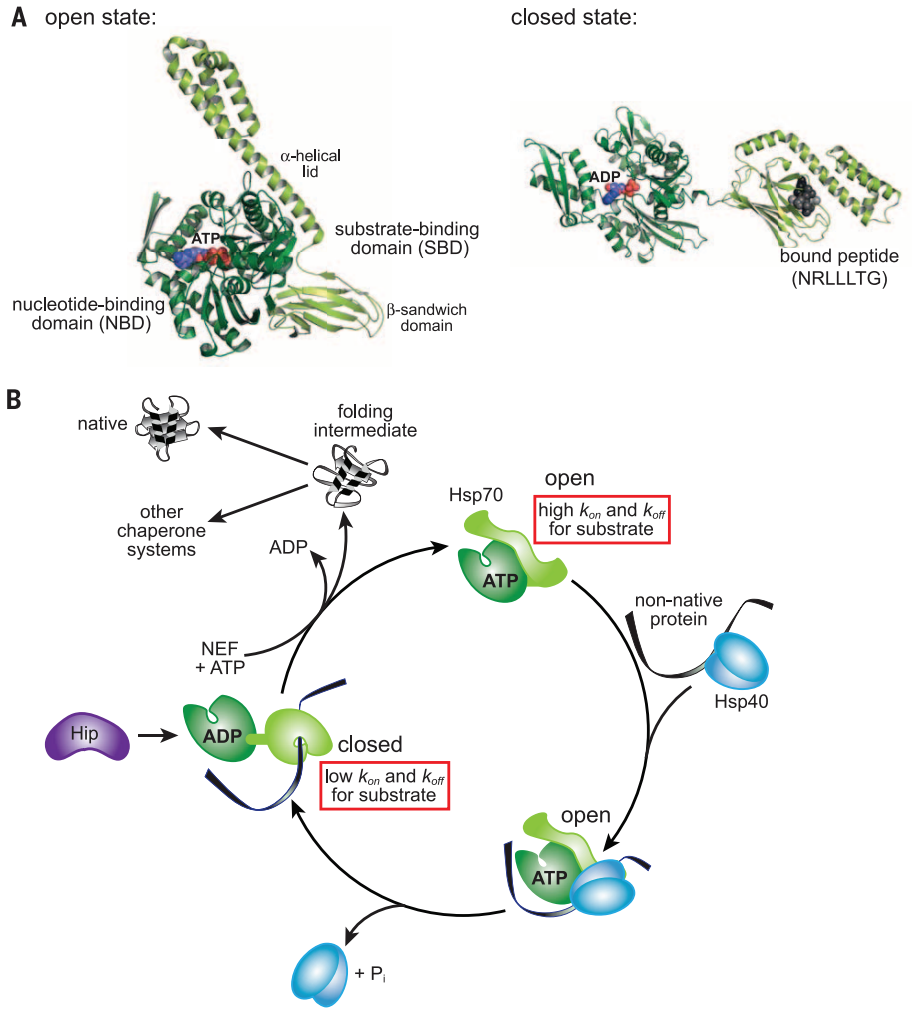

Fig. 5. Hsp70 conformational cycle. (**A**) Structure of the bacterial Hsp70, DnaK. ATP binding and hydrolysis at the nucleotide binding domain (NBD) drive large conformational changes in Hsp70. ATP binding induces the open state of Hsp70 (left; PDB 4B9Q), in which the α-helical lid of the substrate binding domain (SBD) is attached to the NBD. Upon hydrolysis of ATP to ADP, Hsp70 transitions from the open state with high on and off rates for peptide substrate to the closed state (right; PDB 2KHO), in which NBD and SBD are separated and the α-helical lid is closed over the peptide binding cleft (low on and off rates for peptide substrate). Bound nucleotide is shown with adenosine in blue and phosphate in red. Bound peptide with the sequence NRLLLTG (N, Asn; R, Arg; L, Leu; T, Thr; G, Gly) is shown in space-filling representation. (**B**) Cycle of substrate binding and release. Nonnative polypeptide substrate interacts first with Hsp40 and is delivered to ATP-bound Hsp70 (open state). Interaction with Hsp40 triggers ATP hydrolysis on Hsp70, generating the closed state. ADP release catalyzed by nucleotide exchange factor (NEF) and rebinding of ATP trigger substrate release for folding or possible transfer to downstream chaperones. Hip in metazoans stabilizes the ADP state, thereby delaying substrate release. Prolonged binding of nonnative protein to Hsp70 may favor degradation. Figure modified from (*13*).

(Fig. 6A). The GroEL subunits contain an equatorial adenosine triphosphatase (ATPase) domain, an intermediate hinge domain, and an apical domain (*82*) (Fig. 6A). The apical domains form the entrance to the cavity and expose hydrophobic residues for the binding of a nonnative substrate protein. The two rings of GroEL function sequentially as folding chambers, regulated allosterically by the GroEL ATPase (*83*, *84*). Binding of ATP and GroES to the substrate-bound ring causes the displacement of the nonnative substrate from its hydrophobic attachment sites into a cavity capped by GroES (Fig. 6B). This step is accompanied by extensive conformational changes of the GroEL subunits that enlarge the ring cavity and alter its physical properties from hydrophobic to hydrophilic (*80*, *82*). Proteins up to ~60 kDa in size are now free to fold in the chaperonin nanocage for the time it takes GroEL to hydrolyze its bound ATP to ADP (~2 s at 37°C) (*85*). Binding of ATP to the opposite GroEL ring then induces an allosteric signal that causes ADP to dissociate and GroES to unbind. Folded protein is released, while incompletely folded or misfolded molecules may rebind, resulting in possible unfolding in preparation for another folding cycle (*86*, *87*). Whether the GroEL rings function strictly sequentially in folding or sometimes in parallel, with both folding chambers being capped by GroES simultaneously, is a matter of ongoing research (*80*, *84*, *88*).

The GroEL-dependent proteins tend to populate aggregation-prone, kinetically trapped folding intermediates when folding in free solution (*89*, *90*). Although aggregation prevention is an important function of the chaperonin (*91*), recent studies show that GroEL/GroES can markedly accelerate the folding of some of these proteins by smoothing their folding energy landscape (*85*, *92*–*96*). The confining environment of the chaperonin cage allows complex topologies to form sequentially, thereby guiding the substrate along a folding pathway that avoids kinetic traps (*95*). Exactly how GroEL/GroES accelerates protein folding is not yet clear, but has been shown to depend on the volume of the cage, the negative charge of the cavity wall, and the flexible C termini of the GroEL subunits that protrude into the cavity (*80*).

The eukaryotic chaperonin TRiC also supports the folding of ~10% of the proteome, including the key cytoskeletal proteins actin and tubulin (*81*). Like GroEL, TRiC cycles between open and closed states, but substrate encapsulation is cofactor-independent and is mediated by helical protrusions from the tip of each subunit that function as a built-in lid (*97*) (Fig. 6C). The iris-like lid does not seal the cavity completely, but leaves a small pore that can accommodate extended polypeptide chains. This feature allows TRiC to encapsulate and fold large substrates in a domain-wise fashion and act cotranslationally (*98*) (Fig. 4B). Unlike the homo-oligomeric GroEL, each ring of TRiC consists of eight paralogous subunits, which differ in substrate recognition. Thus, TRiC may dictate the topology of the bound substrate (*99*) (Fig. 6D). The subunits also vary in their affinity for ATP, with low- and high-affinity subunits being spatially segregated within the ring (*100*). As a result, the ATP-driven conformational cycle may proceed sequentially (*101*). Moreover, the unique subunit arrangement creates a pronounced asymmetry in the distribution of charges in the folding chamber (*102*–*104*) (Fig. 6D), which may influence the folding trajectory of the encapsulated substrate. The TRiC-mediated folding of certain substrates, such as heterotrimeric GTP-binding protein (G protein) β subunits, is enhanced by cooperation with the cochaperone phosducin-like protein (*105*). Although the structure and conformational cycle of TRiC are now well understood, it remains unclear how exactly the special features of the eukaryotic chaperonin contribute to protein folding.

Hsp90—conformational surveillance of metastable clients

In eukaryotes, Hsp90 supports not only protein folding but also the conformational maturation and maintenance of a range of medically relevant signaling proteins, including proto-oncogenic kinases, steroid hormone receptors, and transcription factors (*106*–*110*). Owing to its involvement in multiple signaling pathways, Hsp90 also plays an

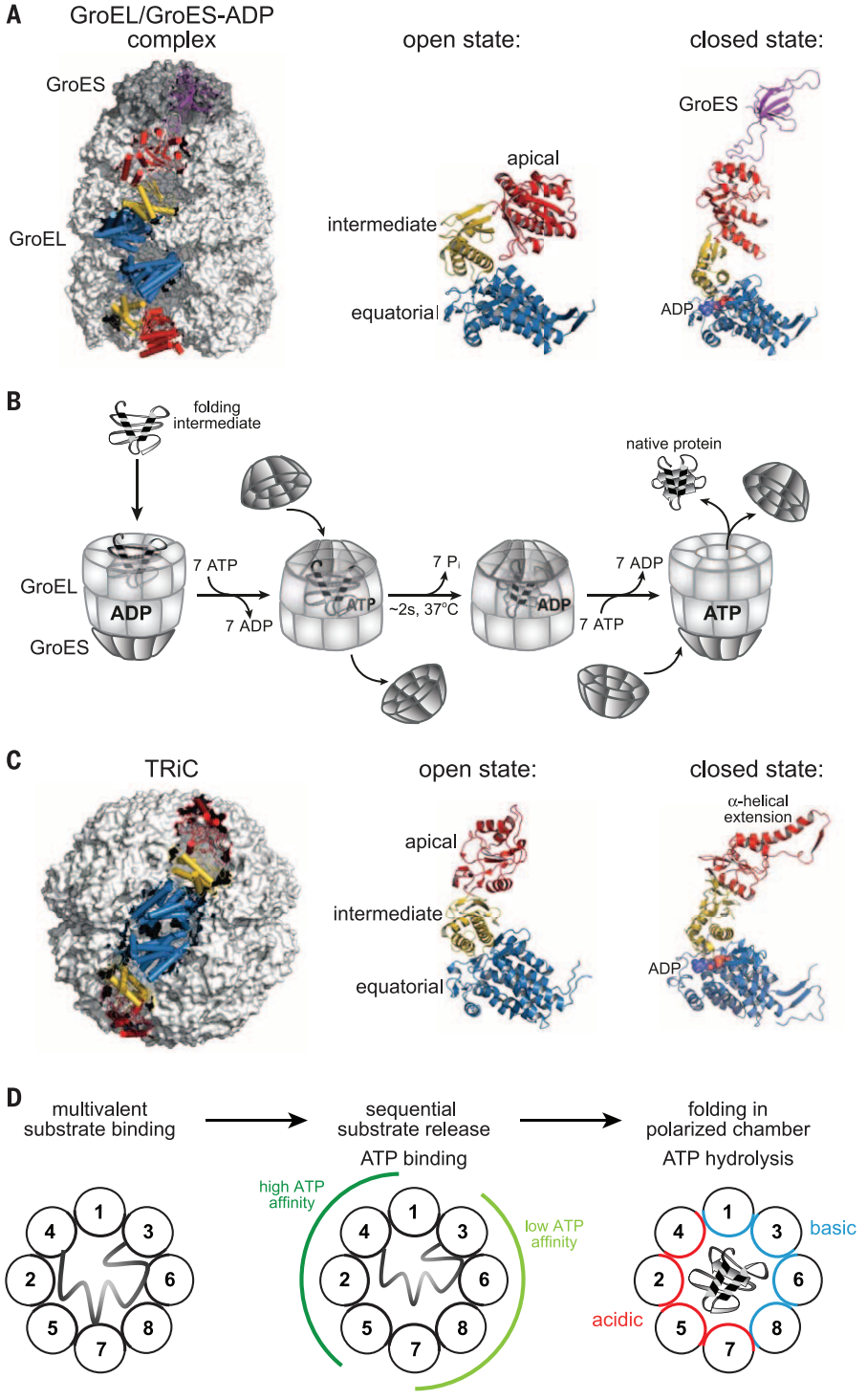

Fig. 6. The chaperonins. (**A**) Structure of the group I bacterial chaperonin system GroEL/GroES. The crystal structure of the asymmetrical GroEL:7ADP:GroES complex (PDB 1PFQ) is shown on the left in space-filling representation. One subunit in each ring is displayed in schematic representation with the equatorial domain in blue, the intermediate domain in yellow, and the apical domain in red. The conformations of the GroEL subunit in the open state and in the GroES-bound, closed state are shown in ribbon representation in the middle and on the right, respectively. (**B**) Reaction cycle of GroEL/GroES. Substrate protein binds as folding intermediate to the empty GroEL ring and is encapsulated by GroES in an ATP-dependent step. The protein is free to fold within the chaperonin nanocage for the time required to hydrolyze ATP on each subunit of the heptameric GroEL ring. ATP binding to the opposite ring then triggers the release of folded protein and GroES, completing the cycle. Incompletely folded protein will rebind after release. Figures modified from (*13*). (**C**) Structure of the eukaryotic chaperonin TRiC. The crystal structure of the hexadecameric TRiC complex with both rings in the closed conformation (PDB 4V94) is shown on the left in space-filling representation. One subunit in each ring is displayed in schematic representation with the domains color coded as above. The subunit conformation of the TRiC subunit in the open state (PDB 3KFK) and in the closed state (PDB 4V94) with the α-helical extensions covering the ring opening are shown in ribbon representation in the middle and on the right, respectively. ADP is bound in the equatorial domain in the closed state. (**D**) TRiC mechanism. The subunit orientation of the TRiC complex is shown schematically as a top view of the ring. Nonnative substrate protein binds in a distinct topology contacting the apical domains of specific subunits (left). Upon ATP binding, TRiC releases the protein in a sequential manner aided by asymmetry in ATP affinities of the TRiC subunits (middle). After release, the protein folds to completion inside the TRiC cage, the hemispheres of which are partitioned into acidic and basic character.

important evolutionary role by buffering destabilizing mutations in its client proteins (*111*).

Hsp90 is a homodimer, with each subunit consisting of an N-terminal nucleotide-binding domain (NTD) of ~25 kDa, a middle domain (MD) of ~40 kDa, and a C-terminal dimerization domain (CTD) of ~12 kDa (*107*, *112*, *113*) (Fig. 7A). A charged linker region connects the NTD with the MD. The Hsp90 dimer is dynamic and samples a range of conformations that are selectively stabilized by nucleotide, client protein, and various cofactors (*114*, *115*). In the absence of nucleotide, Hsp90 favors an open conformation (Fig. 7, A and B). Upon ATP binding, a lid segment of the NTD closes over the bound nucleotide, which leads to NTD dimerization via strand exchange. A flexible loop from the MD contacts the NTD, inducing a twisted closed conformation, with residues from the MD contributing to ATP hydrolysis (*112*) (Fig. 7, A and B). After ATP hydrolysis and nucleotide release, Hsp90 reverts to the open state (Fig. 7B). Although ATP contributes free energy and directionality to the Hsp90 conformational cycle, the rate-limiting step is not ATP hydrolysis, but the large conformational transition from the open to closed state (*116*).

How Hsp90 recognizes substrates and how its ATPase cycle is coupled to client maturation are not yet well understood. Recent evidence suggests that Hsp90 has an extended substrate-binding interface that crosses domain boundaries and exhibits specificity for proteins with exposed hydrophobic residues, independent of whether

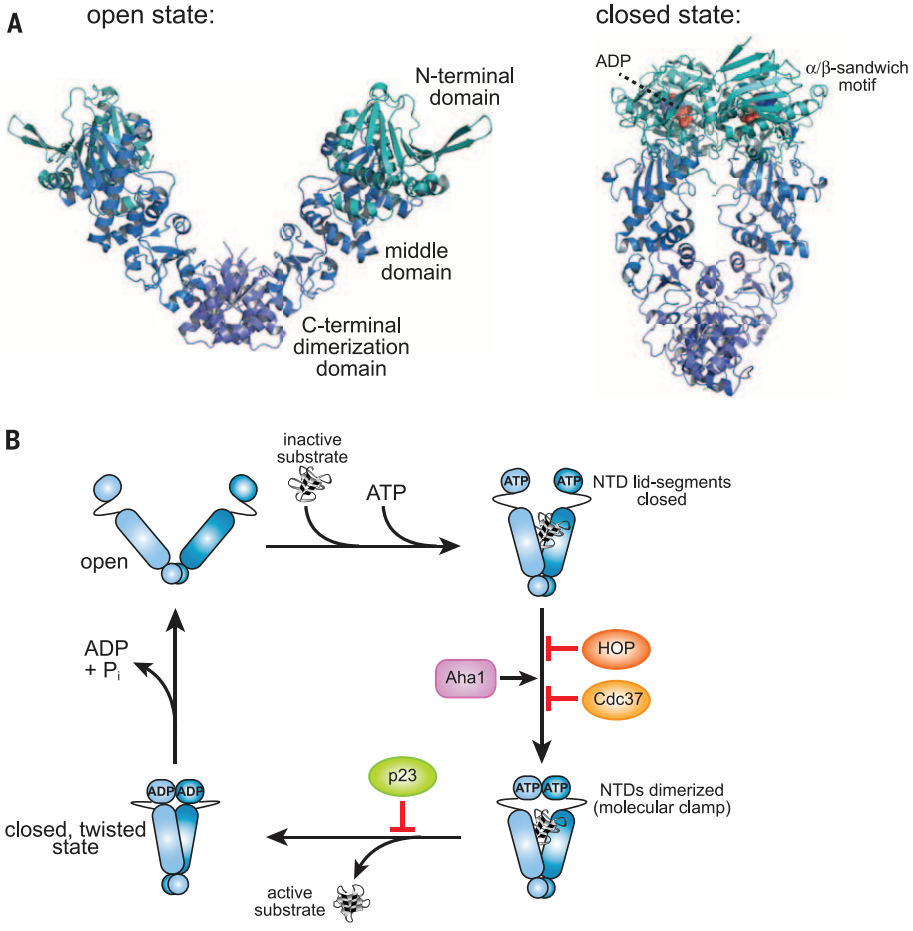

Fig. 7. Hsp90 conformational cycle. (**A**) Crystal structures of the open state of Hsp90 from bacteria (PDB 2IOQ) and the closed state from yeast (PDB 2CG9). Each subunit of the Hsp90 homodimer consists of an N-terminal nucleotide binding domain (NTD), a middle domain, and a C-terminal dimerization domain. (**B**) Hsp90 reaction cycle. Inactive substrate protein binds to the Hsp90 dimer. ATP binding shifts the Hsp90 conformational equilibrium to the closed state with the NTDs dimerized. This metastable state is committed to ATP hydrolysis, resulting in further conformational changes to the closed, twisted state. Release of ADP and P_i returns Hsp90 to the open state. The bound client protein is conformationally activated as Hsp90 proceeds through its cycle. Cofactors Hop and Cdc37 delay the ATP hydrolysis step of the cycle. Aha1 stabilizes NTD dimerization, thereby accelerating ATP hydrolysis. p23 stabilizes the closed dimer, slowing the release of substrate protein from Hsp90.

they are disordered, partly folded, or near native (*113*, *117*, *118*). Interaction with Hsp90 can selectively stabilize metastable client proteins in their active conformation, as shown for glucocorticoid receptor and v-Src kinase (*58*, *119*), explaining why Hsp90 is especially important in cancer cells where growth is driven by the constitutive activation of one or more oncoproteins.

Hsp90 cooperates with various cochaperones, which regulate its ATPase activity and recruit clients (*107*, *112*) (Fig. 7B). These factors act sequentially along the Hsp90 cycle, and in some cases form mixed complexes with the chaperone (*120*). Hop and Cdc37 stabilize the open conformation of the Hsp90 dimer, inhibit ATP hydrolysis, and facilitate client binding. Hop mediates client transfer from Hsp70 to Hsp90, whereas Cdc37 functions as an adapter for kinase clients. Aha1 binds asymmetrically to the MD and NTD of the Hsp90 dimer, facilitating transition to the closed conformation and thereby accelerating ATP hydrolysis (*121*, *122*). p23 acts toward the end of the cycle, and facilitates client maturation by stabilizing the closed state of the Hsp90 N domains and inhibiting ATP hydrolysis (*107*). In addition, Hsp90 cooperates with a range of other cofactors containing TPR domains. Some of these factors also contain peptidyl-prolyl-isomerase (PPIase) domains and participate in client folding on Hsp90 (*109*). In contrast to eukaryotic Hsp90, the bacterial Hsp90, HtpG, is independent of Hsp90 cochaperones.

The proteostasis network

Proteostasis, the state in which the proteome of an organism is in functional balance, must be tightly controlled within individual cells, tissues, and organs. To maintain proteome integrity, the different chaperone classes and their cofactors cooperate with the machineries of protein synthesis and protein degradation in a coordinated proteostasis network (PN), comprising ~1400 components in mammalian cells (*123*–*125*) (Fig. 8A). The PN must balance protein synthesis with turnover; clear surplus, misfolded, and aggregated proteins; and respond to stress. Importantly, decline or disruption of the PN is strongly associated with aging and diseases of aberrant protein folding and aggregation (*4*, *126*). The organization of the PN appears to be robust, displaying a high degree of redundancy. For example, only 55 of the 332 chaperones were found to be among the core fitness genes of human leukemia K562 cells (*123*, *127*) (Fig. 9). In *C. elegans*, knockdown of only ~20 of the 219 chaperones enhanced aggregation and toxicity of neurodegenerative disease proteins (*123*). The large size of the PN with built-in redundancy would facilitate adaptation to the needs of specific cell types and tissues, dependent on environmental and physical exposure, as well as requirements of the expressed proteome.

Stress conditions, including exposure to elevated temperature or oxidizing agents, upregulate multiple chaperones (stress proteins) by inducing transcriptional programs dedicated to specific cell compartments. These include the cytosolic stress response (*128*) and the unfolded protein response (UPR) pathways of the ER and mitochondria (*129*, *130*). The stress response of individual cell types and tissues is further coordinated at the organismal level by cell-nonautonomous signaling mechanisms (*4*, *131*).

Degradation of terminally misfolded proteins and control of protein stoichiometries is mainly performed by the UPS (*132*, *133*), which comprises several hundred components (*133*) and plays an important role in maintaining proteome balance (*134*) (Fig. 8A). Interestingly, certain misfolded proteins require chaperone-mediated transport from the cytosol into the nucleus for proteasomal degradation (*135*–*137*), defining the nucleus as a general protein quality control compartment. Clearance of aggregated proteins by the UPS requires disaggregation prior to degradation, which is performed by Hsp70 in cooperation with Hsp110 and a mixed-class Hsp40 complex (*77*, *78*) (Fig. 8A). In bacteria and fungi, AAA+ ATPase complexes of the Hsp100 family cooperate with the Hsp70 system in disaggregation (*138*). Protein aggregates resisting disassembly may be cleared by selective autophagy and lysosomal degradation (*133*) (Fig. 8A). Both proteasomal and lysosomal clearance pathways are tightly coupled to the Hsp70 and Hsp90 chaperone systems via BAG-domain proteins and specific ubiquitin ligases, such as the cochaperone CHIP (*139*, *140*).

Toxicity of protein misfolding and aggregation

Protein dysfunction resulting from misfolding due to mutation [single-nucleotide polymorphisms (SNPs)] renders proteins metastable and underlies many pathologies, including cystic fibrosis and a wide range of metabolic defects (*141*). Although

a fully functional PN may buffer the destabilizing effects of SNPs on protein conformation, metastable mutant proteins tend to aggregate when PN capacity is overwhelmed, as occurs progressively during aging (*142*, *143*). Age-dependent decline of the PN facilitates the toxic aggregation of neurodegenerative disease proteins (both wild-type and mutant forms), such as amyloid-beta peptide (Aβ) and Tau in Alzheimer's disease, α-synuclein in Parkinson's disease, and huntingtin in Huntington's disease. The hallmark of these pathologies is the intra- or extracellular deposition of aggregates containing amyloid-like β-sheet fibrils (Fig. 8A). Chaperones have been shown to interfere at various steps of the aggregation cascade (*144*), including primary nucleation, fibril elongation and fragmentation, and secondary nucleation by the fibril surface (*145*, *146*). Toxic aggregates are also produced when faulty translation products accumulate (*147*–*149*)—for example, when polypeptide chains that stall during translation on the ribosome are not efficiently cleared by ribosome quality control (RQC) machinery and the UPS (*149*–*151*).

The toxicity arising from aggregation underlies common structural properties of the aggregates (gain of toxic function) and may be entirely unrelated to the normal function of the affected protein. In parallel with assembling to insoluble end-stage fibrils, the disease proteins often accumulate toxic oligomers that expose "sticky" surfaces (hydrophobic amino acid residues and unpaired β-strands) (*152*). These features confer to the oligomers the ability to engage in aberrant interactions with multiple key cellular proteins (*153*, *154*). The proteins targeted by toxic aggregates are often themselves metastable (*155*, *156*); they are typically enriched in intrinsically unstructured regions and sequences of low amino acid complexity, characteristic features of many RNA-binding proteins (*154*–*157*). Toxic protein aggregation interferes with nucleocytoplasmic transport of RNA and protein and generally impairs RNA homeostasis (*156*, *158*). Moreover, the aggregates impair protein degradation by the proteasome and autophagy systems (*124*) and sequester critical components of the chaperone network, such as certain Hsp40 cochaperones (*137*, *149*, *151*). Protein aggregation therefore directly interferes with PN function and is both a symptom and cause of PN decline—setting in motion a vicious cycle that ultimately triggers proteostasis collapse (Fig. 8B).

Aggregate management is critical in determining cell viability and the life span of model organisms. Proteins have been optimized during evolution to maintain solubility at their physiological concentrations (*159*). Thus, even a modest increase in abundance, as might be caused by age-dependent proteome imbalance or due to aneuploidy (*160*, *161*), will result in loss of solubility. Interestingly, recent evidence indicates that cells contain machineries that actively sequester surplus and misfolded proteins into transient or stable deposits when their timely degradation fails (*161*–*168*), presumably an attempt to reduce toxic effects exerted by soluble oligomers (*169*).

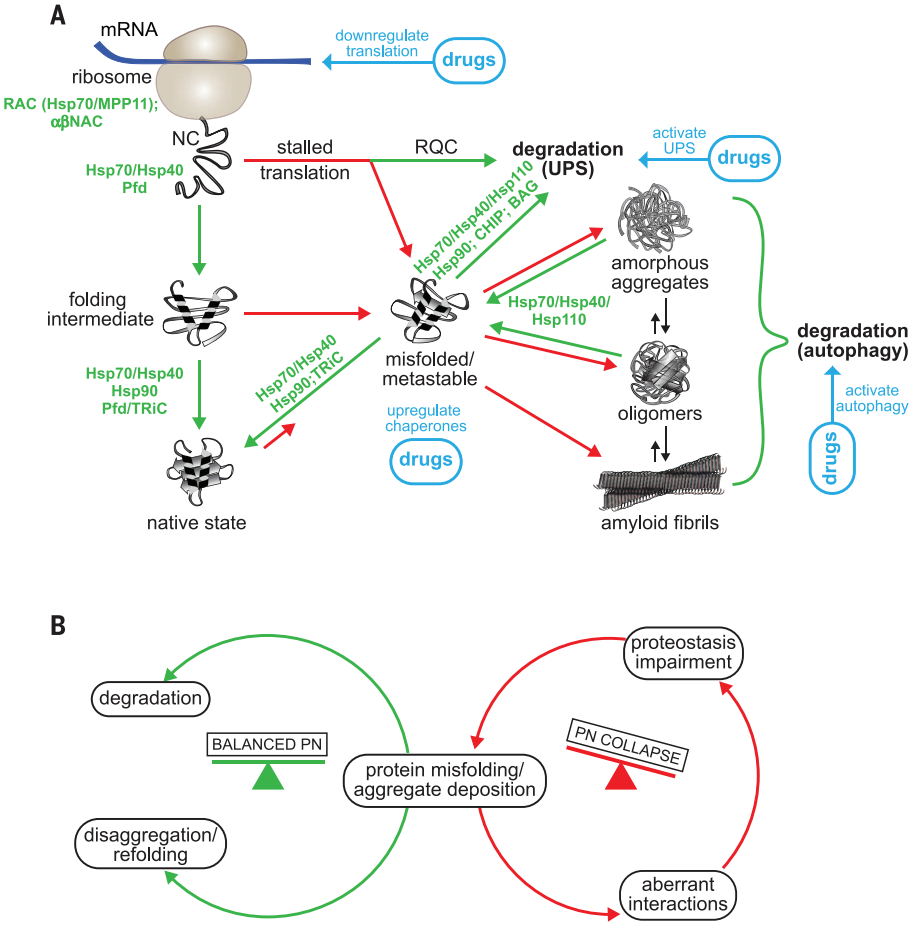

Fig. 8. The proteostasis network. (**A**) Cells employ an extensive network of molecular chaperones and other factors to maintain proteome integrity. Specific chaperone components are listed that participate in promoting the folding of newly synthesized proteins and destabilize nonnative protein conformations, as well as cooperate with the degradation machineries [the ubiquitin proteasome system (UPS) and autophagy and lysosomal degradation]. Pathways promoted by chaperones are shown with green arrows, off-pathway reactions with red arrows. Various options to modulate the PN pharmacologically are also indicated. RQC, ribosome quality control machinery. (**B**) Balanced versus imbalanced PN. Protein misfolding and aggregate formation is shown as the key process that puts pressure on the PN, resulting in possible destabilization. Green circle: The PN at full capacity copes with the load of misfolded proteins by either refolding/disaggregating or degrading aberrant proteins. Red circle: The PN is progressively overwhelmed through a positive feedback loop in which protein misfolding and aggregation leads to aberrant interactions with key proteins (including limiting PN components), resulting in proteostasis impairment and eventual collapse. This downhill spiral is accelerated by the age-dependent decline of proteostasis capacity and/or excessive production of aberrant proteins.

The PN as a drug target

Mechanisms that promote proteostasis have the potential to maintain mutant proteins in a functional, nonaggregated state; slow aging; and decrease the incidence of age-related diseases in model organisms. Thus, boosting PN capacity may be beneficial in both loss-of-function and gain-of-toxic-function diseases of protein misfolding (*170*). Conversely, attenuating the PN by inhibiting specific chaperone or degradation pathways is effective in cancer treatment, because oncogenic proteins are often metastable and thus highly chaperone dependent (*110*, *124*, *171*, *172*). For example, the inhibition of Hsp90 with molecules that block ATP binding prevents the activation of client proteins that promote tumor growth and directs them toward degradation (*110*, *171*). Similarly, pharmacologic inhibition of Hsp70 or its cofactor interactions may interfere with folding and promote protein degradation, defining a promising strategy in the treatment of cancer and certain neurodegenerative diseases (*172*).

In principle, PN capacity can be enhanced in several ways (Fig. 8A): (i) by down-regulating translation to reduce the load of misfolded proteins on the chaperone system; (ii) by up-regulating chaperone levels to improve folding and conformational repair; and (iii) by enhancing the clearance of misfolded proteins and aggregates or by promoting the formation of inclusions that are nontoxic. For example, the antihypertensive

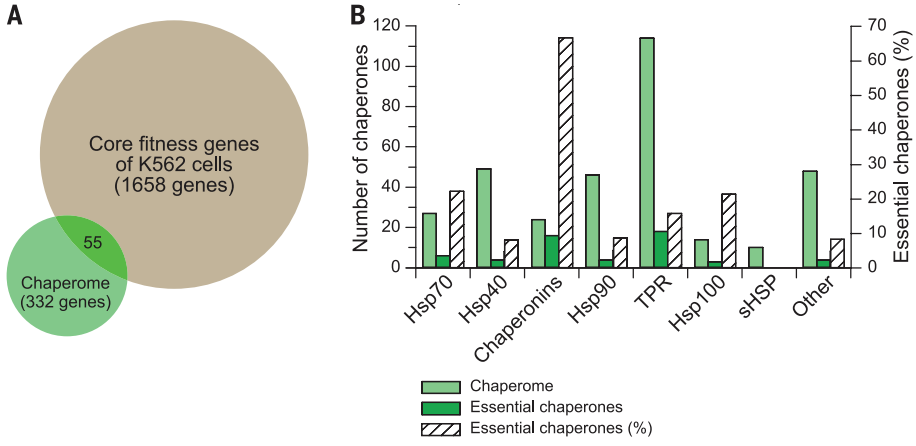

Fig. 9. The subset of chaperones that belong to the core fitness genes of transformed human cells. (**A**) Venn diagram showing the overlap between the human chaperome and the core fitness genes (the essentialome) of K562 leukemia cells. Data are from (*123*, *127*). (**B**) The chaperome (332) proteins divided into the major chaperone families. The number and fraction of essential chaperones (55 in total) are indicated for each family. TPR, tetratricopeptide repeat cochaperones. Note that the chaperonins contain the highest fraction of essential components, and the TPR proteins comprise the highest number of essential cochaperones. Data are from (*123*, *127*).

drug guanabenz has the additional effect of attenuating translation by maintaining eukaryotic translation initiation factor 2 alpha (eIF2α) in its inactive, phosphorylated state (*173*, *174*), which mimics the transient inhibition of translation upon unfolded protein stress. By contrast, certain neuronal cells are highly sensitive to translational attenuation (*175*), and the pharmacologic reversal of eIF2α phosphorylation has been shown to improve cognitive memory in mice (*176*–*178*). Numerous small-molecule compounds have been described that activate cellular stress response pathways and reduce the aggregation of disease proteins or enhance their clearance by increasing chaperone levels (*13*, *179*–*181*). A key role in aggregation prevention and aggregate dissociation is played by the Hsp70 machinery, as shown by overexpressing single or multiple components of the system in cellular and animal disease models (*124*, *154*, *182*, *183*). Finally, activating the UPS or inducing autophagy with small-molecule compounds can enhance degradation and reduce aggregate load (*184*, *185*). Much excitement has been caused by the recent development and approval of the first proteostasis modulator compounds for specific proteins. These include therapeutics for cystic fibrosis that specifically target the folding and trafficking defect of mutant CFTR (*186*) and drugs for the treatment of transthyretin amyloidoses, fatal aggregation diseases characterized by progressive neuropathy and cardiomyopathy (*187*).

Conclusions

Since the emergence of the molecular chaperone concept more than two decades ago, dramatic progress has been made toward understanding protein folding in vivo and how cells maintain proteome balance. The resulting field is exerting a major influence on several other areas, from basic biology to medicine. A number of intriguing questions remain, however, regarding both the mechanism of individual chaperone machines and how their functions are coordinated within the PN.

From a mechanistic perspective, it remains unclear how exactly the major ATP-dependent chaperone systems (Hsp70, Hsp90, chaperonins) support protein folding. Resolving this question will require detailed molecular descriptions of the folding pathways of respective client proteins. For example, it will be fascinating to discover why the eukaryotic chaperonin TRiC can fold proteins, like actin and tubulins, which the bacterial GroEL/GroES is unable to handle. The contribution of the ribosome to protein folding is another intriguing subject of current research. Going forward, it will be important to learn how the environment of the ribosome exit channel affects the energy landscape of cotranslational folding and whether this effect is a generic feature of folding in vivo. The confinement of small polypeptides within the negatively charged ribosome exit channel is reminiscent of the effect of the chaperonin folding cage, and the two systems may influence folding in similar ways, albeit for proteins of vastly different sizes.

The interactions among different chaperone systems and other components of the PN remain largely unexplored. In particular, little is known about how chaperone systems respond to increased load due to proteotoxic stress, and how cells achieve an optimum balance between different chaperone activities (e.g., folding versus holding and aggregation prevention, or transfer to the degradation machinery). The cross-talk between compartment-specific stress response pathways is another area of interest. A holistic understanding of the PN will be vital to future attempts to manipulate its activities pharmacologically and should offer new opportunities to treat the wide range of diseases associated with declining proteostasis.

REFERENCES AND NOTES

1. W. E. Balch, R. I. Morimoto, A. Dillin, J. W. Kelly, Adapting proteostasis for disease intervention. *Science* **319**, 916–919 (2008). doi: 10.1126/science.1141448; pmid: 18276881
2. A. Gershenson, L. M. Gierasch, A. Pastore, S. E. Radford, Energy landscapes of functional proteins are inherently risky. *Nat. Chem. Biol.* **10**, 884–891 (2014). doi: 10.1038/nchembio.1670; pmid: 25325699
3. A. K. Dunker, I. Silman, V. N. Uversky, J. L. Sussman, Function and structure of inherently disordered proteins. *Curr. Opin. Struct. Biol.* **18**, 756–764 (2008). doi: 10.1016/j.sbi.2008.10.002; pmid: 18952168
4. J. Labbadia, R. I. Morimoto, The biology of proteostasis in aging and disease. *Annu. Rev. Biochem.* **84**, 435–464 (2015). doi: 10.1146/annurev-biochem-060614-033955; pmid: 25784053
5. I. Braakman, D. N. Hebert, Protein folding in the endoplasmic reticulum. *Cold Spring Harb. Perspect. Biol.* **5**, a013201 (2013). doi: 10.1101/cshperspect.a013201; pmid: 23637286
6. C. B. Anfinsen, Principles that govern the folding of protein chains. *Science* **181**, 223–230 (1973). doi: 10.1126/science.181.4096.223; pmid: 4124164
7. F. U. Hartl, Molecular chaperones in cellular protein folding. *Nature* **381**, 571–580 (1996). doi: 10.1038/381571a0; pmid: 8637592
8. D. J. Brockwell, S. E. Radford, Intermediates: Ubiquitous species on folding energy landscapes? *Curr. Opin. Struct. Biol.* **17**, 30–37 (2007). doi: 10.1016/j.sbi.2007.01.003; pmid: 17239580
9. R. J. Ellis, A. P. Minton, Protein aggregation in crowded environments. *Biol. Chem.* **387**, 485–497 (2006). doi: 10.1515/BC.2006.064; pmid: 16740119
10. A. R. Dinner, A. Sali, L. J. Smith, C. M. Dobson, M. Karplus, Understanding protein folding via free-energy surfaces from theory and experiment. *Trends Biochem. Sci.* **25**, 331–339 (2000). doi: 10.1016/S0968-0004(00)01610-8; pmid: 10871884
11. P. A. Schmidpeter, F. X. Schmid, Prolyl isomerization and its catalysis in protein folding and protein function. *J. Mol. Biol.* **427**, 1609–1631 (2015). doi: 10.1016/j.jmb.2015.01.023; pmid: 25676311
12. F. Chiti, C. M. Dobson, Protein misfolding, functional amyloid, and human disease. *Annu. Rev. Biochem.* **75**, 333–366 (2006). doi: 10.1146/annurev.biochem.75.101304.123901; pmid: 16756495
13. Y. E. Kim, M. S. Hipp, A. Bracher, M. Hayer-Hartl, F. U. Hartl, Molecular chaperone functions in protein folding and proteostasis. *Annu. Rev. Biochem.* **82**, 323–355 (2013). doi: 10.1146/annurev-biochem-060208-092442; pmid: 23746257
14. D. N. Wilson, R. Beckmann, The ribosomal tunnel as a functional environment for nascent polypeptide folding and translational stalling. *Curr. Opin. Struct. Biol.* **21**, 274–282 (2011). doi: 10.1016/j.sbi.2011.01.007; pmid: 21316217
15. A. Kosolapov, C. Deutsch, Tertiary interactions within the ribosomal exit tunnel. *Nat. Struct. Mol. Biol.* **16**, 405–411 (2009). doi: 10.1038/nsmb.1571; pmid: 19270700
16. E. P. O'Brien, J. Christodoulou, M. Vendruscolo, C. M. Dobson, New scenarios of protein folding can occur on the ribosome. *J. Am. Chem. Soc.* **133**, 513–526 (2011). doi: 10.1021/ja107863z; pmid: 21204555
17. O. B. Nilsson *et al.*, Cotranslational protein folding inside the ribosome exit tunnel. *Cell Reports* **12**, 1533–1540 (2015). doi: 10.1016/j.celrep.2015.07.065; pmid: 26321634
18. W. Holtkamp *et al.*, Cotranslational protein folding on the ribosome monitored in real time. *Science* **350**, 1104–1107 (2015). doi: 10.1126/science.aad0344; pmid: 26612953
19. C. M. Kaiser, D. H. Goldman, J. D. Chodera, I. Tinoco Jr., C. Bustamante, The ribosome modulates nascent protein folding. *Science* **334**, 1723–1727 (2011). doi: 10.1126/science.1209740; pmid: 22194581
20. L. D. Cabrita *et al.*, A structural ensemble of a ribosome-nascent chain complex during cotranslational protein folding. *Nat. Struct. Mol. Biol.* **23**, 278–285 (2016). doi: 10.1038/nsmb.3182; pmid: 26926436
21. C. Eichmann, S. Preissler, R. Riek, E. Deuerling, Cotranslational structure acquisition of nascent polypeptides monitored by NMR spectroscopy. *Proc. Natl. Acad. Sci. U.S.A.*

107, 9111–9116 (2010). doi: 10.1073/pnas.0914300107; pmid: 20439768
22. O. B. Nilsson, A. Müller-Lucks, G. Kramer, B. Bukau, G. von Heijne, Trigger factor reduces the force exerted on the nascent chain by a cotranslationally folding protein. *J. Mol. Biol.* **428**, 1356–1364 (2016). doi: 10.1016/j.jmb.2016.02.014; pmid: 26906929
23. F. U. Hartl, M. Hayer-Hartl, Molecular chaperones in the cytosol: From nascent chain to folded protein. *Science* **295**, 1852–1858 (2002). doi: 10.1126/science.1068408; pmid: 11884745
24. Z. N. Scholl, W. Yang, P. E. Marszalek, Chaperones rescue luciferase folding by separating its domains. *J. Biol. Chem.* **289**, 28607–28618 (2014). doi: 10.1074/jbc.M114.582049; pmid: 25160632
25. A. Borgia *et al*., Transient misfolding dominates multidomain protein folding. *Nat. Commun.* **6**, 8861 (2015). doi: 10.1038/ncomms9861; pmid: 26572969
26. Y.-W. Shieh *et al*., Operon structure and cotranslational subunit association direct protein assembly in bacteria. *Science* **350**, 678–680 (2015). doi: 10.1126/science.aac8171; pmid: 26405228
27. F. Brandt *et al*., The native 3D organization of bacterial polysomes. *Cell* **136**, 261–271 (2009). doi: 10.1016/j.cell.2008.11.016; pmid: 19167328
28. F. Brandt, L.-A. Carlson, F. U. Hartl, W. Baumeister, K. Grünewald, The three-dimensional organization of polyribosomes in intact human cells. *Mol. Cell* **39**, 560–569 (2010). doi: 10.1016/j.molcel.2010.08.003; pmid: 20797628
29. G. W. Li, E. Oh, J. S. Weissman, The anti-Shine-Dalgarno sequence drives translational pausing and codon choice in bacteria. *Nature* **484**, 538–541 (2012). doi: 10.1038/nature10965; pmid: 22456704
30. S. Pechmann, J. Frydman, Evolutionary conservation of codon optimality reveals hidden signatures of cotranslational folding. *Nat. Struct. Mol. Biol.* **20**, 237–243 (2013). doi: 10.1038/nsmb.2466; pmid: 23262490
31. P. S. Spencer, E. Siller, J. F. Anderson, J. M. Barral, Silent substitutions predictably alter translation elongation rates and protein folding efficiencies. *J. Mol. Biol.* **422**, 328–335 (2012). doi: 10.1016/j.jmb.2012.06.010; pmid: 22705285
32. E. P. O'Brien, M. Vendruscolo, C. M. Dobson, Kinetic modelling indicates that fast-translating codons can coordinate cotranslational protein folding by avoiding misfolded intermediates. *Nat. Commun.* **5**, 2988 (2014). pmid: 24394622
33. S. J. Kim *et al*., Protein folding. Translational tuning optimizes nascent protein folding in cells. *Science* **348**, 444–448 (2015). doi: 10.1126/science.aaa3974; pmid: 25908822
34. F. Mohammad, C. J. Woolstenhulme, R. Green, A. R. Buskirk, Clarifying the translational pausing landscape in bacteria by ribosome profiling. *Cell Reports* **14**, 686–694 (2016). doi: 10.1016/j.celrep.2015.12.073; pmid: 26776510
35. M. Zhou *et al*., Non-optimal codon usage affects expression, structure and function of clock protein FRQ. *Nature* **495**, 111–115 (2013). doi: 10.1038/nature11833; pmid: 23417067
36. C. Kimchi-Sarfaty *et al*., A "silent" polymorphism in the MDR1 gene changes substrate specificity. *Science* **315**, 525–528 (2007). doi: 10.1126/science.1135308; pmid: 17185560
37. R. M. Vabulas, F. U. Hartl, Protein synthesis upon acute nutrient restriction relies on proteasome function. *Science* **310**, 1960–1963 (2005). doi: 10.1126/science.1121925; pmid: 16373576
38. S. Duttler, S. Pechmann, J. Frydman, Principles of cotranslational ubiquitination and quality control at the ribosome. *Mol. Cell* **50**, 379–393 (2013). doi: 10.1016/j.molcel.2013.03.010; pmid: 23583075
39. T. M. Treweek, S. Meehan, H. Ecroyd, J. A. Carver, Small heat-shock proteins: Important players in regulating cellular proteostasis. *Cell. Mol. Life Sci.* **72**, 429–451 (2015). doi: 10.1007/s00018-014-1754-5; pmid: 25352169
40. A. Chari, U. Fischer, Cellular strategies for the assembly of molecular machines. *Trends Biochem. Sci.* **35**, 676–683 (2010). doi: 10.1016/j.tibs.2010.07.006; pmid: 20727772
41. T. Hauser, L. Popilka, F. U. Hartl, M. Hayer-Hartl, Role of auxiliary proteins in Rubisco biogenesis and function. *Nature Plants* **1**, 15065 (2015). doi: 10.1038/nplants.2015.65; pmid: 27250005
42. E. Oh *et al*., Selective ribosome profiling reveals the cotranslational chaperone action of trigger factor in vivo. *Cell* **147**, 1295–1308 (2011). doi: 10.1016/j.cell.2011.10.044; pmid: 22153074
43. S. Preissler, E. Deuerling, Ribosome-associated chaperones as key players in proteostasis. *Trends Biochem. Sci.* **37**, 274–283 (2012). doi: 10.1016/j.tibs.2012.03.002; pmid: 22503700
44. C. M. Kaiser *et al*., Real-time observation of trigger factor function on translating ribosomes. *Nature* **444**, 455–460 (2006). doi: 10.1038/nature05225; pmid: 17051157
45. A. Hoffmann *et al*., Concerted action of the ribosome and the associated chaperone trigger factor confines nascent polypeptide folding. *Mol. Cell* **48**, 63–74 (2012). doi: 10.1016/j.molcel.2012.07.018; pmid: 22921937
46. A. Mashaghi *et al*., Reshaping of the conformational search of a protein by the chaperone trigger factor. *Nature* **500**, 98–101 (2013). doi: 10.1038/nature12293; pmid: 23831649
47. T. Saio, X. Guan, P. Rossi, A. Economou, C. G. Kalodimos, Structural basis for protein antiaggregation activity of the trigger factor chaperone. *Science* **344**, 1250494 (2014). doi: 10.1126/science.1250494; pmid: 24812405
48. V. R. Agashe *et al*., Function of trigger factor and DnaK in multidomain protein folding: Increase in yield at the expense of folding speed. *Cell* **117**, 199–209 (2004). doi: 10.1016/S0092-8674(04)00299-5; pmid: 15084258
49. F. Stull, P. Koldewey, J. R. Humes, S. E. Radford, J. C. Bardwell, Substrate protein folds while it is bound to the ATP-independent chaperone Spy. *Nat. Struct. Mol. Biol.* **23**, 53–58 (2016). doi: 10.1038/nsmb.3133; pmid: 26619265
50. F. Willmund *et al*., The cotranslational function of ribosome-associated Hsp70 in eukaryotic protein homeostasis. *Cell* **152**, 196–209 (2013). doi: 10.1016/j.cell.2012.12.001; pmid: 23332755
51. M. Chiabudini, C. Conz, F. Reckmann, S. Rospert, Ribosome-associated complex and Ssb are required for translational repression induced by polylysine segments within nascent chains. *Mol. Cell. Biol.* **32**, 4769–4779 (2012). doi: 10.1128/MCB.00809-12; pmid: 23007158
52. Y. Zhang *et al*., Structural basis for interaction of a cotranslational chaperone with the eukaryotic ribosome. *Nat. Struct. Mol. Biol.* **21**, 1042–1046 (2014). doi: 10.1038/nsmb.2908; pmid: 25362488
53. J. Kirstein-Miles, A. Scior, E. Deuerling, R. I. Morimoto, The nascent polypeptide-associated complex is a key regulator of proteostasis. *EMBO J.* **32**, 1451–1468 (2013). doi: 10.1038/emboj.2013.87; pmid: 23604074
54. M. del Alamo *et al*., Defining the specificity of cotranslationally acting chaperones by systematic analysis of mRNAs associated with ribosome-nascent chain complexes. *PLOS Biol.* **9**, e1001100 (2011). doi: 10.1371/journal.pbio.1001100; pmid: 21765803
55. Y. Zhang *et al*., NAC functions as a modulator of SRP during the early steps of protein targeting to the endoplasmic reticulum. *Mol. Biol. Cell* **23**, 3027–3040 (2012). doi: 10.1091/mbc.E12-02-0112; pmid: 22740632
56. M. Gamerdinger, M. A. Hanebuth, T. Frickey, E. Deuerling, The principle of antagonism ensures protein targeting specificity at the endoplasmic reticulum. *Science* **348**, 201–207 (2015). doi: 10.1126/science.aaa5335; pmid: 25859040
57. G. Calloni *et al*., DnaK functions as a central hub in the E. coli chaperone network. *Cell Reports* **1**, 251–264 (2012). doi: 10.1016/j.celrep.2011.12.007; pmid: 22832197
58. E. Kirschke, D. Goswami, D. Southworth, P. R. Griffin, D. A. Agard, Glucocorticoid receptor function regulated by coordinated action of the Hsp90 and Hsp70 chaperone cycles. *Cell* **157**, 1685–1697 (2014). doi: 10.1016/j.cell.2014.04.038; pmid: 24949977
59. N. Morgner *et al*., Hsp70 forms antiparallel dimers stabilized by post-translational modifications to position clients for transfer to Hsp90. *Cell Reports* **11**, 759–769 (2015). doi: 10.1016/j.celrep.2015.03.063; pmid: 25921532
60. J. Cuéllar *et al*., The structure of CCT-Hsc70 NBD suggests a mechanism for Hsp70 delivery of substrates to the chaperonin. *Nat. Struct. Mol. Biol.* **15**, 858–864 (2008). doi: 10.1038/nsmb.1464; pmid: 18660820
61. M. P. Mayer, Hsp70 chaperone dynamics and molecular mechanism. *Trends Biochem. Sci.* **38**, 507–514 (2013). doi: 10.1016/j.tibs.2013.08.001; pmid: 24012426
62. E. M. Clerico, J. M. Tilitsky, W. Meng, L. M. Gierasch, How hsp70 molecular machines interact with their substrates to mediate diverse physiological functions. *J. Mol. Biol.* **427**, 1575–1588 (2015). doi: 10.1016/j.jmb.2015.02.004; pmid: 25683596
63. R. Kityk, J. Kopp, I. Sinning, M. P. Mayer, Structure and dynamics of the ATP-bound open conformation of Hsp70 chaperones. *Mol. Cell* **48**, 863–874 (2012). doi: 10.1016/j.molcel.2012.09.023; pmid: 23123194
64. R. Qi *et al*., Allosteric opening of the polypeptide-binding site when an Hsp70 binds ATP. *Nat. Struct. Mol. Biol.* **20**, 900–907 (2013). doi: 10.1038/nsmb.2583; pmid: 23708608
65. A. Zhuravleva, L. M. Gierasch, Substrate-binding domain conformational dynamics mediate Hsp70 allostery. *Proc. Natl. Acad. Sci. U.S.A.* **112**, E2865–E2873 (2015). doi: 10.1073/pnas.1506692112; pmid: 26038563
66. M. Sikor, K. Mapa, L. V. von Voithenberg, D. Mokranjac, D. C. Lamb, Real-time observation of the conformational dynamics of mitochondrial Hsp70 by spFRET. *EMBO J.* **32**, 1639–1649 (2013). doi: 10.1038/emboj.2013.89; pmid: 23624933
67. P. De Los Rios, A. Barducci, Hsp70 chaperones are non-equilibrium machines that achieve ultra-affinity by energy consumption. *eLife* **3**, e02218 (2014). doi: 10.7554/eLife.02218; pmid: 24867638
68. S. K. Sharma, P. De los Rios, P. Christen, A. Lustig, P. Goloubinoff, The kinetic parameters and energy cost of the Hsp70 chaperone as a polypeptide unfoldase. *Nat. Chem. Biol.* **6**, 914–920 (2010). doi: 10.1038/nchembio.455; pmid: 20953191
69. J. M. Nunes, M. Mayer-Hartl, F. U. Hartl, D. J. Müller, Action of the Hsp70 chaperone system observed with single proteins. *Nat. Commun.* **6**, 6307 (2015). doi: 10.1038/ncomms7307; pmid: 25686738
70. A. Sekhar, R. Rosenzweig, G. Bouvignies, L. E. Kay, Mapping the conformation of a client protein through the Hsp70 functional cycle. *Proc. Natl. Acad. Sci. U.S.A.* **112**, 10395–10400 (2015). doi: 10.1073/pnas.1508504112; pmid: 26240333
71. A. Sekhar, R. Rosenzweig, G. Bouvignies, L. E. Kay, Hsp70 biases the folding pathways of client proteins. *Proc. Natl. Acad. Sci. U.S.A.* **113**, E2794–E2801 (2016). doi: 10.1073/pnas.1601846113; pmid: 27140645
72. J. H. Lee *et al*., Heterogeneous binding of the SH3 client protein to the DnaK molecular chaperone. *Proc. Natl. Acad. Sci. U.S.A.* **112**, E4206–E4215 (2015). doi: 10.1073/pnas.1505173112; pmid: 26195753
73. Z. Li, F. U. Hartl, A. Bracher, Structure and function of Hip, an attenuator of the Hsp70 chaperone cycle. *Nat. Struct. Mol. Biol.* **20**, 929–935 (2013). doi: 10.1038/nsmb.2608; pmid: 23812373
74. H. H. Kampinga, E. A. Craig, The HSP70 chaperone machinery: J proteins as drivers of functional specificity. *Nat. Rev. Mol. Cell Biol.* **11**, 579–592 (2010). doi: 10.1038/nrm2941; pmid: 20651708
75. S. Taguwa *et al*., Defining Hsp70 subnetworks in dengue virus replication reveals key vulnerability in flavivirus infection. *Cell* **163**, 1108–1123 (2015). doi: 10.1016/j.cell.2015.10.046; pmid: 26582131
76. A. Bracher, J. Verghese, The nucleotide exchange factors of Hsp70 molecular chaperones. *Front. Mol. Biosci.* **2**, 10 (2015). doi: 10.3389/fmolb.2015.00010; pmid: 26913285
77. H. Rampelt *et al*., Metazoan Hsp70 machines use Hsp110 to power protein disaggregation. *EMBO J.* **31**, 4221–4235 (2012). doi: 10.1038/emboj.2012.264; pmid: 22990239
78. N. B. Nillegoda *et al*., Crucial HSP70 co-chaperone complex unlocks metazoan protein disaggregation. *Nature* **524**, 247–251 (2015). doi: 10.1038/nature14884; pmid: 26245380
79. H. Zhang *et al*., A bipartite interaction between Hsp70 and CHIP regulates ubiquitination of chaperoned client proteins. *Structure* **23**, 472–482 (2015). doi: 10.1016/j.str.2015.01.003; pmid: 25684577
80. M. Hayer-Hartl, A. Bracher, F. U. Hartl, The GroEL-GroES chaperonin machine: A nano-cage for protein folding. *Trends Biochem. Sci.* **41**, 62–76 (2016). doi: 10.1016/j.tibs.2015.07.009; pmid: 26422689
81. T. Lopez, K. Dalton, J. Frydman, The mechanism and function of Group II chaperonins. *J. Mol. Biol.* **427**, 2919–2930 (2015). doi: 10.1016/j.jmb.2015.04.013; pmid: 25936650
82. H. R. Saibil, W. A. Fenton, D. K. Clare, A. L. Horwich, Structure and allostery of the chaperonin GroEL. *J. Mol. Biol.* **425**, 1476–1487 (2013). doi: 10.1016/j.jmb.2012.11.028; pmid: 23183375
83. D. K. Clare *et al*., ATP-triggered conformational changes delineate substrate-binding and -folding mechanics of the GroEL chaperonin. *Cell* **149**, 113–123 (2012). doi: 10.1016/j.cell.2012.02.047; pmid: 22445172
84. R. Gruber, A. Horovitz, Allosteric mechanisms in chaperonin machines. *Chem. Rev.* **116**, 6588–6606 (2016). doi: 10.1021/acs.chemrev.5b00556; pmid: 26726755

85. A. J. Gupta, S. Haldar, G. Miličić, F. U. Hartl, M. Hayer-Hartl, Active cage mechanism of chaperonin-assisted protein folding demonstrated at single-molecule level. *J. Mol. Biol.* **426**, 2739–2754 (2014). doi: 10.1016/j.jmb.2014.04.018; pmid: 24816391
86. Z. Lin, D. Madan, H. S. Rye, GroEL stimulates protein folding through forced unfolding. *Nat. Struct. Mol. Biol.* **15**, 303–311 (2008). doi: 10.1038/nsmb.1394; pmid: 18311152
87. S. Sharma *et al*., Monitoring protein conformation along the pathway of chaperonin-assisted folding. *Cell* **133**, 142–153 (2008). doi: 10.1016/j.cell.2008.01.048; pmid: 18394994
88. H. Taguchi, Reaction cycle of chaperonin GroEL via symmetric "football" intermediate. *J. Mol. Biol.* **427**, 2912–2918 (2015). doi: 10.1016/j.jmb.2015.04.007; pmid: 25900372
89. M. J. Kerner *et al*., Proteome-wide analysis of chaperonin-dependent protein folding in Escherichia coli. *Cell* **122**, 209–220 (2005). doi: 10.1016/j.cell.2005.05.028; pmid: 16051146
90. K. Fujiwara, Y. Ishihama, K. Nakahigashi, T. Soga, H. Taguchi, A systematic survey of in vivo obligate chaperonin-dependent substrates. *EMBO J.* **29**, 1552–1564 (2010). doi: 10.1038/emboj.2010.52; pmid: 20360681
91. A. L. Horwich, A. C. Apetri, W. A. Fenton, The GroEL/GroES cis cavity as a passive anti-aggregation device. *FEBS Lett.* **583**, 2654–2662 (2009). doi: 10.1016/j.febslet.2009.06.049; pmid: 19577567
92. Y.-C. Tang *et al*., Structural features of the GroEL-GroES nano-cage required for rapid folding of encapsulated protein. *Cell* **125**, 903–914 (2006). doi: 10.1016/j.cell.2006.04.027; pmid: 16751100
93. K. Chakraborty *et al*., Chaperonin-catalyzed rescue of kinetically trapped states in protein folding. *Cell* **142**, 112–122 (2010). doi: 10.1016/j.cell.2010.05.027; pmid: 20603018
94. A. L. Mallam, S. E. Jackson, Knot formation in newly translated proteins is spontaneous and accelerated by chaperonins. *Nat. Chem. Biol.* **8**, 147–153 (2011). doi: 10.1038/nchembio.742; pmid: 22179065
95. F. Georgescauld *et al*., GroEL/ES chaperonin modulates the mechanism and accelerates the rate of TIM-barrel domain folding. *Cell* **157**, 922–934 (2014). doi: 10.1016/j.cell.2014.03.038; pmid: 24813614
96. J. Weaver, H. S. Rye, The C-terminal tails of the bacterial chaperonin GroEL stimulate protein folding by directly altering the conformation of a substrate protein. *J. Biol. Chem.* **289**, 23219–23232 (2014). doi: 10.1074/jbc.M114.577205; pmid: 24970895
97. N. R. Douglas *et al*., Dual action of ATP hydrolysis couples lid closure to substrate release into the group II chaperonin chamber. *Cell* **144**, 240–252 (2011). doi: 10.1016/j.cell.2010.12.017; pmid: 21241893
98. F. Rüßmann *et al*., Folding of large multidomain proteins by partial encapsulation in the chaperonin TRiC/CCT. *Proc. Natl. Acad. Sci. U.S.A.* **109**, 21208–21215 (2012). doi: 10.1073/pnas.1218836109; pmid: 23197838
99. L. A. Joachimiak, T. Walzthoeni, C. W. Liu, R. Aebersold, J. Frydman, The structural basis of substrate recognition by the eukaryotic chaperonin TRiC/CCT. *Cell* **159**, 1042–1055 (2014). doi: 10.1016/j.cell.2014.10.042; pmid: 25416944
100. S. Reissmann *et al*., A gradient of ATP affinities generates an asymmetric power stroke driving the chaperonin TRIC/CCT folding cycle. *Cell Rep.* **2**, 866–877 (2012). pmid: 23041314
101. D. Rivenzon-Segal, S. G. Wolf, L. Shimon, K. R. Willison, A. Horovitz, Sequential ATP-induced allosteric transitions of the cytoplasmic chaperonin containing TCP-1 revealed by EM analysis. *Nat. Struct. Mol. Biol.* **12**, 233–237 (2005). doi: 10.1038/nsmb901; pmid: 15696173
102. N. Kalisman, C. M. Adams, M. Levitt, Subunit order of eukaryotic TRiC/CCT chaperonin by cross-linking, mass spectrometry, and combinatorial homology modeling. *Proc. Natl. Acad. Sci. U.S.A.* **109**, 2884–2889 (2012). doi: 10.1073/pnas.1119472109; pmid: 22308438
103. A. Leitner *et al*., The molecular architecture of the eukaryotic chaperonin TRiC/CCT. *Structure* **20**, 814–825 (2012). doi: 10.1016/j.str.2012.03.007; pmid: 22503819
104. N. Kalisman, G. F. Schröder, M. Levitt, The crystal structures of the eukaryotic chaperonin CCT reveal its functional partitioning. *Structure* **21**, 540–549 (2013). doi: 10.1016/j.str.2013.01.017; pmid: 23478063
105. R. L. Plimpton *et al*., Structures of the Gβ-CCT and PhLP1-Gβ-CCT complexes reveal a mechanism for G-protein β-subunit folding and Gβγ dimer assembly. *Proc. Natl. Acad. Sci. U.S.A.* **112**, 2413–2418 (2015). doi: 10.1073/pnas.1419595112; pmid: 25675501
106. M. Taipale, D. F. Jarosz, S. Lindquist, HSP90 at the hub of protein homeostasis: Emerging mechanistic insights. *Nat. Rev. Mol. Cell Biol.* **11**, 515–528 (2010). doi: 10.1038/nrm2918; pmid: 20531426
107. J. Li, J. Soroka, J. Buchner, The Hsp90 chaperone machinery: Conformational dynamics and regulation by co-chaperones. *Biochim. Biophys. Acta* **1823**, 624–635 (2012). doi: 10.1016/j.bbamcr.2011.09.003; pmid: 21951723
108. K. Sharma *et al*., Quantitative proteomics reveals that Hsp90 inhibition preferentially targets kinases and the DNA damage response. *Mol. Cell. Proteomics* **11**, 014654 (2012). doi: 10.1074/mcp.M111.014654; pmid: 22167270
109. M. Taipale *et al*., Quantitative analysis of HSP90-client interactions reveals principles of substrate recognition. *Cell* **150**, 987–1001 (2012). doi: 10.1016/j.cell.2012.06.047; pmid: 22939624
110. W. B. Pratt, J. E. Gestwicki, Y. Osawa, A. P. Lieberman, Targeting Hsp90/Hsp70-based protein quality control for treatment of adult onset neurodegenerative diseases. *Annu. Rev. Pharmacol. Toxicol.* **55**, 353–371 (2015). doi: 10.1146/annurev-pharmtox-010814-124332; pmid: 25292434
111. S. Lindquist, Protein folding sculpting evolutionary change. *Cold Spring Harb. Symp. Quant. Biol.* **74**, 103–108 (2009). doi: 10.1101/sqb.2009.74.043; pmid: 20375316
112. A. Röhl, J. Rohrberg, J. Buchner, The chaperone Hsp90: Changing partners for demanding clients. *Trends Biochem. Sci.* **38**, 253–262 (2013). doi: 10.1016/j.tibs.2013.02.003; pmid: 23507089
113. G. E. Karagöz, S. G. D. Rüdiger, Hsp90 interaction with clients. *Trends Biochem. Sci.* **40**, 117–125 (2015). doi: 10.1016/j.tibs.2014.12.002; pmid: 25579468
114. M. Mickler, M. Hessling, C. Ratzke, J. Buchner, T. Hugel, The large conformational changes of Hsp90 are only weakly coupled to ATP hydrolysis. *Nat. Struct. Mol. Biol.* **16**, 281–286 (2009). doi: 10.1038/nsmb.1557; pmid: 19234469
115. T. O. Street, L. A. Lavery, D. A. Agard, Substrate binding drives large-scale conformational changes in the Hsp90 molecular chaperone. *Mol. Cell* **42**, 96–105 (2011). doi: 10.1016/j.molcel.2011.01.029; pmid: 21474071
116. M. Hessling, K. Richter, J. Buchner, Dissection of the ATP-induced conformational cycle of the molecular chaperone Hsp90. *Nat. Struct. Mol. Biol.* **16**, 287–293 (2009). doi: 10.1038/nsmb.1565; pmid: 19234467
117. G. E. Karagöz *et al*., Hsp90-Tau complex reveals molecular basis for specificity in chaperone action. *Cell* **156**, 963–974 (2014). doi: 10.1016/j.cell.2014.01.037; pmid: 24581495
118. T. O. Street *et al*., Elucidating the mechanism of substrate recognition by the bacterial Hsp90 molecular chaperone. *J. Mol. Biol.* **426**, 2393–2404 (2014). doi: 10.1016/j.jmb.2014.04.001; pmid: 24726919
119. E. E. Boczek *et al*., Conformational processing of oncogenic v-Src kinase by the molecular chaperone Hsp90. *Proc. Natl. Acad. Sci. U.S.A.* **112**, E3189–E3198 (2015). doi: 10.1073/pnas.1424342112; pmid: 26056257
120. J. Li, K. Richter, J. Buchner, Mixed Hsp90-cochaperone complexes are important for the progression of the reaction cycle. *Nat. Struct. Mol. Biol.* **18**, 61–66 (2011). doi: 10.1038/nsmb.1965; pmid: 21170051
121. A. V. Koulov *et al*., Biological and structural basis for Aha1 regulation of Hsp90 ATPase activity in maintaining proteostasis in the human disease cystic fibrosis. *Mol. Biol. Cell* **21**, 871–884 (2010). doi: 10.1091/mbc.E09-12-1017; pmid: 20089831
122. M. Retzlaff *et al*., Asymmetric activation of the hsp90 dimer by its cochaperone aha1. *Mol. Cell* **37**, 344–354 (2010). doi: 10.1016/j.molcel.2010.01.006; pmid: 20159554
123. M. Brehme *et al*., A chaperome subnetwork safeguards proteostasis in aging and neurodegenerative disease. *Cell Reports* **9**, 1135–1150 (2014). doi: 10.1016/j.celrep.2014.09.042; pmid: 25437566
124. M. S. Hipp, S.-H. Park, F. U. Hartl, Proteostasis impairment in protein-misfolding and -aggregation diseases. *Trends Cell Biol.* **24**, 506–514 (2014). doi: 10.1016/j.tcb.2014.05.003; pmid: 24946960
125. M. Taipale *et al*., A quantitative chaperone interaction network reveals the architecture of cellular protein homeostasis pathways. *Cell* **158**, 434–448 (2014). doi: 10.1016/j.cell.2014.05.039; pmid: 25036637
126. R. C. Taylor, A. Dillin, Aging as an event of proteostasis collapse. *Cold Spring Harb. Perspect. Biol.* **3**, a004440 (2011). doi: 10.1101/cshperspect.a004440; pmid: 21441594
127. T. Wang *et al*., Identification and characterization of essential genes in the human genome. *Science* **350**, 1096–1101 (2015). doi: 10.1126/science.aac7041; pmid: 26472758
128. J. Anckar, L. Sistonen, Regulation of HSF1 function in the heat stress response: Implications in aging and disease. *Annu. Rev. Biochem.* **80**, 1089–1115 (2011). doi: 10.1146/annurev-biochem-060809-095203; pmid: 21417720
129. P. Walter, D. Ron, The unfolded protein response: From stress pathway to homeostatic regulation. *Science* **334**, 1081–1086 (2011). doi: 10.1126/science.1209038; pmid: 22116877
130. A. M. Schulz, C. M. Haynes, UPR(mt)-mediated cytoprotection and organismal aging. *Biochim. Biophys. Acta* **1847**, 1448–1456 (2015). doi: 10.1016/j.bbabio.2015.03.008; pmid: 25857997
131. R. Schinzel, A. Dillin, Endocrine aspects of organelle stress—cell non-autonomous signaling of mitochondria and the ER. *Curr. Opin. Cell Biol.* **33**, 102–110 (2015). doi: 10.1016/j.ceb.2015.01.006; pmid: 25677685
132. A. Shemorry, C. S. Hwang, A. Varshavsky, Control of protein quality and stoichiometries by N-terminal acetylation and the N-end rule pathway. *Mol. Cell* **50**, 540–551 (2013). doi: 10.1016/j.molcel.2013.03.018; pmid: 23603116
133. A. Ciechanover, Y. T. Kwon, Degradation of misfolded proteins in neurodegenerative diseases: Therapeutic targets and strategies. *Exp. Mol. Med.* **47**, e147 (2015). doi: 10.1038/emm.2014.117; pmid: 25766616
134. D. Vilchez *et al*., Increased proteasome activity in human embryonic stem cells is regulated by PSMD11. *Nature* **489**, 304–308 (2012). doi: 10.1038/nature11468; pmid: 22972301
135. J. W. Heck, S. K. Cheung, R. Y. Hampton, Cytoplasmic protein quality control degradation mediated by parallel actions of the E3 ubiquitin ligases Ubr1 and San1. *Proc. Natl. Acad. Sci. U.S.A.* **107**, 1106–1111 (2010). doi: 10.1073/pnas.0910591107; pmid: 20080635
136. R. Prasad, S. Kawaguchi, D. T. Ng, A nucleus-based quality control mechanism for cytosolic proteins. *Mol. Biol. Cell* **21**, 2117–2127 (2010). doi: 10.1091/mbc.E10-02-0111; pmid: 20462951
137. S.-H. Park *et al*., PolyQ proteins interfere with nuclear degradation of cytosolic proteins by sequestering the Sis1p chaperone. *Cell* **154**, 134–145 (2013). doi: 10.1016/j.cell.2013.06.003; pmid: 23791384
138. A. Mogk, E. Kummer, B. Bukau, Cooperation of Hsp70 and Hsp100 chaperone machines in protein disaggregation. *Front. Mol. Biosci.* **2**, 22 (2015). doi: 10.3389/fmolb.2015.00022; pmid: 26042222
139. M. Gamerdinger *et al*., Protein quality control during aging involves recruitment of the macroautophagy pathway by BAG3. *EMBO J.* **28**, 889–901 (2009). doi: 10.1038/emboj.2009.29; pmid: 19229298
140. N. Kettern, M. Dreiseidler, R. Tawo, J. Höhfeld, Chaperone-assisted degradation: Multiple paths to destruction. *Biol. Chem.* **391**, 481–489 (2010). doi: 10.1515/bc.2010.058; pmid: 20302520
141. N. Sahni *et al*., Widespread macromolecular interaction perturbations in human genetic disorders. *Cell* **161**, 647–660 (2015). doi: 10.1016/j.cell.2015.04.013; pmid: 25910212
142. A. Ben-Zvi, E. A. Miller, R. I. Morimoto, Collapse of proteostasis represents an early molecular event in *Caenorhabditis elegans* aging. *Proc. Natl. Acad. Sci. U.S.A.* **106**, 14914–14919 (2009). doi: 10.1073/pnas.0902882106; pmid: 19706382
143. R. Gupta *et al*., Firefly luciferase mutants as sensors of proteome stress. *Nat. Methods* **8**, 879–884 (2011). doi: 10.1038/nmeth.1697; pmid: 21892152
144. T. P. Knowles *et al*., An analytical solution to the kinetics of breakable filament assembly. *Science* **326**, 1533–1537 (2009). doi: 10.1126/science.1178250; pmid: 20007899
145. G. Schaffar *et al*., Cellular toxicity of polyglutamine expansion proteins: Mechanism of transcription factor deactivation. *Mol. Cell* **15**, 95–105 (2004). doi: 10.1016/j.molcel.2004.06.029; pmid: 15225551
146. S. I. Cohen *et al*., A molecular chaperone breaks the catalytic cycle that generates toxic Aβ oligomers. *Nat. Struct. Mol. Biol.* **22**, 207–213 (2015). doi: 10.1038/nsmb.2971; pmid: 25686087
147. D. D. Nedialkova, S. A. Leidel, Optimization of codon translation rates via tRNA modifications maintains proteome integrity. *Cell* **161**, 1606–1618 (2015). doi: 10.1016/j.cell.2015.05.022; pmid: 26052047
148. S. Preissler *et al*., Not4-dependent translational repression is important for cellular protein homeostasis in yeast. *EMBO J.*

34, 1905–1924 (2015). doi: 10.15252/embj.201490194; pmid: 25971775
149. Y.-J. Choe *et al*., Failure of RQC machinery causes protein aggregation and proteotoxic stress. *Nature* **531**, 191–195 (2016). doi: 10.1038/nature16973; pmid: 26934223
150. O. Brandman, R. S. Hegde, Ribosome-associated protein quality control. *Nat. Struct. Mol. Biol.* **23**, 7–15 (2016). doi: 10.1038/nsmb.3147; pmid: 26733220
151. R. Yonashiro *et al*., The Rqc2/Tae2 subunit of the ribosome-associated quality control (RQC) complex marks ribosome-stalled nascent polypeptide chains for aggregation. *eLife* **5**, e11794 (2016). doi: 10.7554/eLife.11794; pmid: 26943317
152. L. Breydo, V. N. Uversky, Structural, morphological, and functional diversity of amyloid oligomers. *FEBS Lett.* **589** (19PartA), 2640–2648 (2015). doi: 10.1016/j.febslet.2015.07.013; pmid: 26188543
153. K. L. Sugars, D. C. Rubinsztein, Transcriptional abnormalities in Huntington disease. *Trends Genet.* **19**, 233–238 (2003). doi: 10.1016/S0168-9525(03)00074-X; pmid: 12711212
154. H. Olzscha *et al*., Amyloid-like aggregates sequester numerous metastable proteins with essential cellular functions. *Cell* **144**, 67–78 (2011). doi: 10.1016/j.cell.2010.11.050; pmid: 21215370
155. A. Patel *et al*., A liquid-to-solid phase transition of the ALS protein FUS accelerated by disease mutation. *Cell* **162**, 1066–1077 (2015). doi: 10.1016/j.cell.2015.07.047; pmid: 26317470
156. A. C. Woerner *et al*., Cytoplasmic protein aggregates interfere with nucleocytoplasmic transport of protein and RNA. *Science* **351**, 173–176 (2016). doi: 10.1126/science.aad2033; pmid: 26634439
157. S. Calabretta, S. Richard, Emerging roles of disordered sequences in RNA-binding proteins. *Trends Biochem. Sci.* **40**, 662–672 (2015). doi: 10.1016/j.tibs.2015.08.012; pmid: 26481498
158. B. D. Freibaum *et al*., GGGGCC repeat expansion in C9orf72 compromises nucleocytoplasmic transport. *Nature* **525**, 129–133 (2015). doi: 10.1038/nature14974; pmid: 26308899
159. P. Ciryam, G. G. Tartaglia, R. I. Morimoto, C. M. Dobson, M. Vendruscolo, Widespread aggregation and neurodegenerative diseases are associated with supersaturated proteins. *Cell Reports* **5**, 781–790 (2013). doi: 10.1016/j.celrep.2013.09.043; pmid: 24183671
160. A. B. Oromendia, A. Amon, Aneuploidy: Implications for protein homeostasis and disease. *Dis. Model. Mech.* **7**, 15–20 (2014). doi: 10.1242/dmm.013391; pmid: 24396150
161. D. M. Walther *et al*., Widespread Proteome Remodeling and Aggregation in Aging C. elegans. *Cell* **161**, 919–932 (2015). doi: 10.1016/j.cell.2015.03.032; pmid: 25957690
162. E. Cohen, J. Bieschke, R. M. Perciavalle, J. W. Kelly, A. Dillin, Opposing activities protect against age-onset proteotoxicity. *Science* **313**, 1604–1610 (2006). doi: 10.1126/science.1124646; pmid: 16902091
163. D. Kaganovich, R. Kopito, J. Frydman, Misfolded proteins partition between two distinct quality control compartments. *Nature* **454**, 1088–1095 (2008). doi: 10.1038/nature07195; pmid: 18756251
164. S. F. Falsone *et al*., SERF protein is a direct modifier of amyloid fiber assembly. *Cell Reports* **2**, 358–371 (2012). doi: 10.1016/j.celrep.2012.06.012; pmid: 22854022
165. S. Escusa-Toret, W. I. Vonk, J. Frydman, Spatial sequestration of misfolded proteins by a dynamic chaperone pathway enhances cellular fitness during stress. *Nat. Cell Biol.* **15**, 1231–1243 (2013). doi: 10.1038/ncb2838; pmid: 24036477
166. S. M. Hill, X. Hao, B. Liu, T. Nyström, Life-span extension by a metacaspase in the yeast Saccharomyces cerevisiae. *Science* **344**, 1389–1392 (2014). doi: 10.1126/science.1252634; pmid: 24855027
167. E. M. Sontag, W. I. M. Vonk, J. Frydman, Sorting out the trash: The spatial nature of eukaryotic protein quality control. *Curr. Opin. Cell Biol.* **26**, 139–146 (2014). doi: 10.1016/j.ceb.2013.12.006; pmid: 24463332
168. E. W. J. Wallace *et al*., Reversible, specific, active aggregates of endogenous proteins assemble upon heat stress. *Cell* **162**, 1286–1298 (2015). doi: 10.1016/j.cell.2015.08.041; pmid: 26359986
169. M. Arrasate, S. Mitra, E. S. Schweitzer, M. R. Segal, S. Finkbeiner, Inclusion body formation reduces levels of mutant huntingtin and the risk of neuronal death. *Nature* **431**, 805–810 (2004). doi: 10.1038/nature02998; pmid: 15483602
170. E. T. Powers, R. I. Morimoto, A. Dillin, J. W. Kelly, W. E. Balch, Biological and chemical approaches to diseases of proteostasis deficiency. *Annu. Rev. Biochem.* **78**, 959–991 (2009). doi: 10.1146/annurev.biochem.052308.114844; pmid: 19298183
171. Y. Miyata, H. Nakamoto, L. Neckers, The therapeutic target Hsp90 and cancer hallmarks. *Curr. Pharm. Des.* **19**, 347–365 (2013). doi: 10.2174/138161213804143725; pmid: 22920906
172. X. Li, H. Shao, I. R. Taylor, J. E. Gestwicki, Targeting allosteric control mechanisms in heat shock protein 70 (Hsp70). *Curr. Top. Med. Chem.* (2016). pmid: 27072701
173. P. Tsaytler, H. P. Harding, D. Ron, A. Bertolotti, Selective inhibition of a regulatory subunit of protein phosphatase 1 restores proteostasis. *Science* **332**, 91–94 (2011). doi: 10.1126/science.1201396; pmid: 21385720
174. I. Das *et al*., Preventing proteostasis diseases by selective inhibition of a phosphatase regulatory subunit. *Science* **348**, 239–242 (2015). doi: 10.1126/science.aaa4484 pmid: 25859045
175. J. Leitman *et al*., ER stress-induced eIF2-α phosphorylation underlies sensitivity of striatal neurons to pathogenic huntingtin. *PLOS ONE* **9**, e90803 (2014). doi: 10.1371/journal.pone.0090803; pmid: 24594939
176. C. Sidrauski *et al*., Pharmacological brake-release of mRNA translation enhances cognitive memory. *eLife* **2**, e00498 (2013). doi: 10.7554/eLife.00498; pmid: 23741617
177. Y. Sekine *et al*., Stress responses. Mutations in a translation initiation factor identify the target of a memory-enhancing compound. *Science* **348**, 1027–1030 (2015). doi: 10.1126/science.aaa6986; pmid: 25858979
178. C. Sidrauski *et al*., Pharmacological dimerization and activation of the exchange factor eIF2B antagonizes the integrated stress response. *eLife* **4**, e07314 (2015). doi: 10.7554/eLife.07314; pmid: 25875391
179. B. Calamini *et al*., Small-molecule proteostasis regulators for protein conformational diseases. *Nat. Chem. Biol.* **8**, 185–196 (2011). doi: 10.1038/nchembio.763; pmid: 22198733
180. C. B. Cooley *et al*., Unfolded protein response activation reduces secretion and extracellular aggregation of amyloidogenic immunoglobulin light chain. *Proc. Natl. Acad. Sci. U.S.A.* **111**, 13046–13051 (2014). doi: 10.1073/pnas.1406050111; pmid: 25157167
181. A. S. Mendez *et al*., Endoplasmic reticulum stress-independent activation of unfolded protein response kinases by a small molecule ATP-mimic. *eLife* **4**, e05434 (2015). doi: 10.7554/eLife.05434; pmid: 25986605
182. V. Kakkar *et al*., The S/T-rich motif in the DNAJB6 chaperone delays polyglutamine aggregation and the onset of disease in a mouse model. *Mol. Cell* **62**, 272–283 (2016). doi: 10.1016/j.molcel.2016.03.017; pmid: 27151442
183. M. Nagy, W. A. Fenton, D. Li, K. Furtak, A. L. Horwich, Extended survival of misfolded G85R SOD1-linked ALS mice by transgenic expression of chaperone Hsp110. *Proc. Natl. Acad. Sci. U.S.A.* **113**, 5424–5428 (2016). doi: 10.1073/pnas.1604885113; pmid: 27114530
184. B. H. Lee *et al*., Enhancement of proteasome activity by a small-molecule inhibitor of USP14. *Nature* **467**, 179–184 (2010). doi: 10.1038/nature09299; pmid: 20829789
185. D. C. Rubinsztein, C. F. Bento, V. Deretic, Therapeutic targeting of autophagy in neurodegenerative and infectious diseases. *J. Exp. Med.* **212**, 979–990 (2015). doi: 10.1084/jem.20150956; pmid: 26101267
186. G. Veit *et al*., From CFTR biology toward combinatorial pharmacotherapy: Expanded classification of cystic fibrosis mutations. *Mol. Biol. Cell* **27**, 424–433 (2016). doi: 10.1091/mbc.E14-04-0935; pmid: 26823392
187. A. Baranczak, J. W. Kelly, A current pharmacologic agent versus the promise of next generation therapeutics to ameliorate protein misfolding and/or aggregation diseases. *Curr. Opin. Chem. Biol.* **32**, 10–21 (2016). doi: 10.1016/j.cbpa.2016.01.009; pmid: 26859714

ACKNOWLEDGMENTS

This Review focuses mainly on original publications of the last 15 years. We apologize to all colleagues whose work could not be cited owing to space limitations. We thank G. Jayaraj for bioinformatics analyses and members of the group for critically reading the manuscript. Work in the authors' laboratory was supported by a European Molecular Biology Organization long-term fellowship to D.B. (ALTF 1116-2014), a European Research Council Advanced Grant (to F.U.H.), the Center for Integrated Protein Science Munich (CiPSM), and the Munich Cluster for Systems Neurology (SyNergy). M.H.-H. acknowledges funding by the Minerva Foundation. F.U.H. holds stock options in, receives consulting fees from, and is the chair of the scientific advisory board of Proteostasis Therapeutics, Inc.

10.1126/science.aac4354

RESEARCH ARTICLE SUMMARY

RETINAL REPAIR

Immune modulation by MANF promotes tissue repair and regenerative success in the retina

Joana Neves, Jie Zhu, Pedro Sousa-Victor, Mia Konjikusic, Rebeccah Riley, Shereen Chew, Yanyan Qi, Heinrich Jasper,* Deepak A. Lamba*

INTRODUCTION: Regenerative therapies based on cell replacement hold promise for the treatment of a range of age-related degenerative diseases but are limited by unfavorable microenvironments in degenerating tissues. A promising strategy to improve success is to harness endogenous repair mechanisms that promote tissue integrity and function. Innate immune cells are central to such repair mechanisms because they coordinate local and systemic responses to tissue injury by secreting inflammatory and anti-inflammatory signals in a context-dependent manner. A proper balance between these opposing phenotypes of innate immune cells is essential for efficient tissue repair, and immune modulation may be an effective way to promote repair and enhance regenerative therapies. Here, we identified a new evolutionarily conserved immune modulatory function for mesencephalic astrocyte-derived neurotrophic factor (MANF) that biases immune cells toward an anti-inflammatory phenotype, thereby promoting tissue repair in both vertebrates and invertebrates and enhancing retinal regenerative therapy.

RATIONALE: In *Drosophila*, interactions between damaged tissues and hemocytes are essential for tissue repair. We used this model to identify immune cell–derived factors with immune modulatory activity that promote tissue repair after retinal injury. The identification of MANF as such a factor prompted us to test its role in mammalian retinal repair and ask whether its immune modulatory activity helped cell replacement therapies in degenerating retinas.

RESULTS: Using a combination of transcriptome analysis and genetic studies, we identified MANF as a hemocyte-derived factor that is induced by platelet-derived growth factor (PDGF)– and vascular endothelial growth factor (VEGF)–related factor 1 (Pvf-1)/PDGF- and VEGF-receptor related (PvR) signaling. MANF was necessary and sufficient to promote retinal repair after ultraviolet-light–induced retinal injury in *Drosophila*. MANF also had an autocrine immune-modulatory function in fly hemocytes, which was necessary for its tissue repair–promoting activity. This regulation and function of MANF was evolutionarily conserved: Mouse photoreceptors expressed PDGF-A (a Pvf-1 homolog) in response to damage signals, which promoted MANF expression in innate immune cells. This PDGF-A/MANF signaling cascade was required to limit photoreceptor apoptosis in the retina. Exogenously supplied recombinant MANF protected photoreceptors in several paradigms of retinal injury and degeneration. As in flies, this prorepair function was associated with alternative activation of macrophages and microglia in the retina. Ablation of CD11b$^+$ immune cells and deletion of Cx3Cr1, a chemokine receptor required for MANF-induced alternative activation, prevented MANF-induced repair. Thus, the protective effects of MANF in retinal injury rely on its immune modulatory activity. Finally, MANF supplementation to photoreceptors transplanted into congenitally blind mice increased integration efficiency and accelerated and improved visual function recovery.

ON OUR WEBSITE

Read the full article at http://dx.doi.org/10.1126/science.aaf3646

CONCLUSION: Combining genetic studies in invertebrates and vertebrates has rapidly identified factors with promising therapeutic potential. Immune modulation is a promising strategy to optimize regenerative therapies. With its conserved immune modulatory function, MANF is a particularly promising molecule that is likely to be useful for the treatment of inflammatory conditions in many different disease contexts. ■

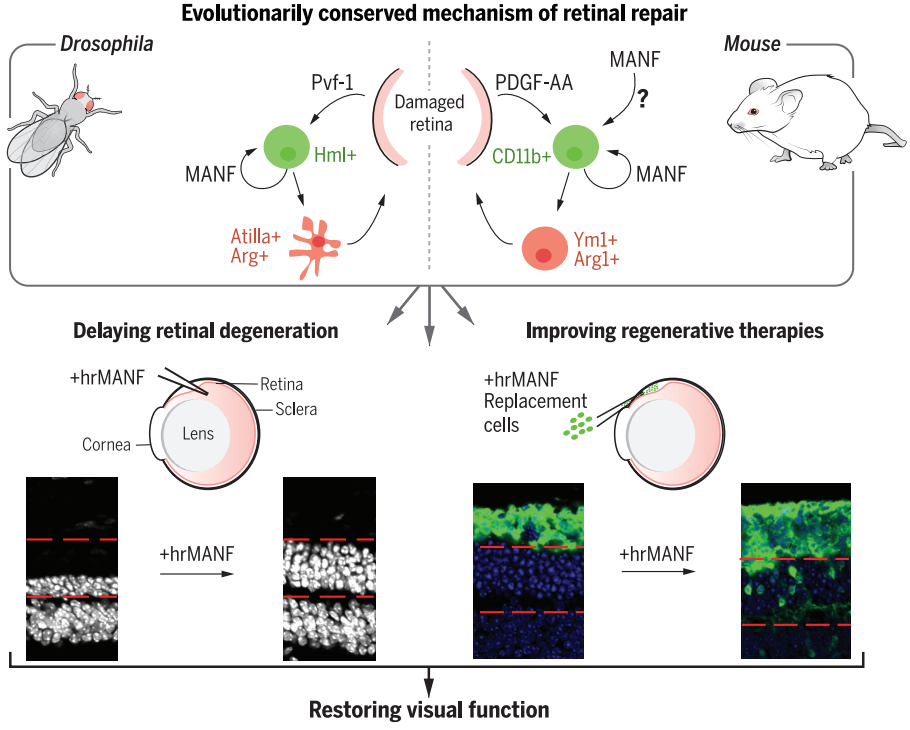

MANF in retinal repair. In *Drosophila* (left) or mouse (right), the damaged retina secretes Pvf-1/PDGF-A, which acts on innate immune cells. MANF derived from innate immune cells (and other sources) promotes phenotypic changes in immune cells as part of a mechanism required for tissue repair. Therapeutically, MANF supplementation can delay retinal degeneration and improve the success of cell-replacement regenerative therapies in the retina.

Author affiliations are available in the full article online.
*Corresponding author. Email: hjasper@buckinstitute.org (H.J.); dlamba@buckinstitute.org (D.A.L.)
Cite this article as J. Neves *et al.*, *Science* 353, aaf3646 (2016). DOI: 10.1126/science.aaf3646

RESEARCH ARTICLE

RETINAL REPAIR

Immune modulation by MANF promotes tissue repair and regenerative success in the retina

Joana Neves, Jie Zhu, Pedro Sousa-Victor, Mia Konjikusic, Rebeccah Riley, Shereen Chew, Yanyan Qi, Heinrich Jasper,* Deepak A. Lamba*

Regenerative therapies are limited by unfavorable environments in aging and diseased tissues. A promising strategy to improve success is to balance inflammatory and anti-inflammatory signals and enhance endogenous tissue repair mechanisms. Here, we identified a conserved immune modulatory mechanism that governs the interaction between damaged retinal cells and immune cells to promote tissue repair. In damaged retina of flies and mice, platelet-derived growth factor (PDGF)–like signaling induced mesencephalic astrocyte-derived neurotrophic factor (MANF) in innate immune cells. MANF promoted alternative activation of innate immune cells, enhanced neuroprotection and tissue repair, and improved the success of photoreceptor replacement therapies. Thus, immune modulation is required during tissue repair and regeneration. This approach may improve the efficacy of stem-cell–based regenerative therapies.

Regenerative therapies based on cell replacement hold promise for the treatment of a range of age-related degenerative diseases (*1*, *2*). Moreover, aged and diseased tissues provide a poor microenvironment for integration (*3*). A case in point is attempting to regenerate the vertebrate retina, a tissue where endogenous repair mechanisms are inefficient and that is subject to a variety of irreversible age-related degenerative pathologies. Human pluripotent stem cells can provide a virtually unlimited source of photoreceptors and retinal pigment epithelial (RPE) cells for replacement and restoration of vision (*4*), yet the poor integration efficiency of transplanted cells into the host retina has limited clinical applications. Retinal diseases targeted by this therapeutic approach, such as age-related macular degeneration or retinitis pigmentosa, are characterized by microglial activation and proinflammatory microenvironments (*5*–*9*) that will negatively affect integration and repair (*3*, *10*).

Microglia, monocyte-derived macrophages, and other innate immune cell types can both promote and resolve inflammation. Managing these inflammatory responses is essential for tissue repair and regeneration (*11*). In the central nervous system, resident (microglia) and invading innate immune cells orchestrate a complex response to damage aimed at restoring tissue integrity but can also promote damaging neuroinflammation (*12*–*15*). This antagonism is at least in part a consequence of different states of immune cell activation. Classical or M1 activation is associated with proinflammatory conditions that can cause tissue damage, whereas alternative or M2 activation is associated with resolution of inflammation and tissue repair (*16*, *17*). This M1/M2 paradigm has been used to describe outcomes of in vitro perturbation of macrophages, yet there is evidence that macrophages in vivo can adopt similar phenotypes and functions (*18*, *19*). Because of these opposing effects of different immune cell phenotypes, immune modulation rather than immune suppression may be an effective way to promote tissue repair and improve regenerative therapies.

Studies in *Drosophila* have substantially advanced our understanding of tissue repair and regeneration in metazoans (*20*–*22*). This work has highlighted the critical role of the interaction between hemocytes (*Drosophila* blood cells with macrophage-like activities) and damaged epithelia in the repair process. Hemocytes are activated in response to tissue damage and coordinate localized and systemic repair responses (*23*–*26*) but have also been implicated in inflammatory processes in flies (*27*). A productive model for the genetic dissection of tissue and hemocyte interactions in repair processes is the pupal retina, which responds to ultraviolet (UV) damage by inducing photoreceptor apoptosis in a dose-dependent manner (*28*, *29*). A paracrine interaction between UV-damaged photoreceptors and hemocytes through the platelet-derived growth factor (PDGF)– and vascular endothelial growth factor (VEGF)–related factor 1 (Pvf-1) and PDGF- and VEGF-receptor related (PvR) pathway governs repair of the damaged retina: Damaged photoreceptors secrete Pvf-1 and activate PvR in hemocytes, promoting repair of UV-induced tissue damage (Fig. 1A) (*26*).

Buck Institute for Research on Aging, 8001 Redwood Boulevard, Novato, CA 94945-1400, USA.
*Corresponding author. Email: hjasper@buckinstitute.org (H.J.); dlamba@buckinstitute.org (D.A.L.)

We performed RNA sequencing (RNA-seq) on isolated hemocytes to identify PvR-dependent genes encoding secreted proteins that were induced after epithelial damage (fig. S1 and table S1). Mesencephalic astrocyte-derived neurotrophic factor (MANF) was found in this screen and, based on its evolutionarily conserved neurotrophic activity (*30*–*32*), we decided to explore its potential as a retinal repair factor.

Hemocyte-derived MANF is activated downstream of Pvf-1/PvR paracrine signaling to promote retinal repair in *Drosophila*

We confirmed that MANF is expressed in fly innate immune cells (hemocytes) using immunohistochemistry of hemolymph smears from late second-instar larvae (Fig. 1B, left). In these smears, hemocytes were identified by green fluorescent protein (GFP) expression driven by the hemocyte-specific driver hemolectin:Gal4 (HmlΔ:Gal4) (*33*). MANF was also detected by immunoblot in the plasma fraction of the hemolymph, confirming its secretion (Fig. 1B, right). Consistent with the RNA-seq data, reverse transcription and real-time quantitative polymerase chain reaction (RT-qPCR) analysis revealed that MANF mRNA levels were significantly higher in hemocytes from UV-treated larvae compared with untreated controls (Fig. 1C, left) and that this induction was PvR dependent (Fig. 1C, right, and figs. S1C and S2A). Overexpression of Pvf-1 in the retina [using GMR:Gal4 (glass multimer reporter) (*34*) as a driver] was sufficient to induce MANF mRNA specifically in hemocytes, in the absence of damage (Fig. 1D, left), and was accompanied by a significant increase in MANF protein in the hemolymph (Fig. 1D, right, and fig. S2B).

Flies overexpressing MANF in hemocytes (fig. S2C, left) showed significant tissue preservation after UV exposure, even after PvR knockdown in hemocytes (*26*) (Fig. 1E, left and middle), without affecting PvR^{RNAi} knockdown efficiency (fig. S2A). This protective activity of hemocyte-derived MANF was further confirmed in two genetic models of retinal damage, in which degeneration is induced by retinal (GMR driven) overexpression of the pro-apoptotic gene *grim* or of mutant Rhodopsin ($Rh1^{G69D}$) (*35*, *36*) (fig. S2, D and E).

Null mutations in the *manf* gene ($manf^{mut96}$ and $manf^{mut112}$) (*31*) are homozygous lethal at early first-instar larval stages, yet MANF heterozygotes [which express significantly lower levels of MANF in hemocytes compared with wild type (fig. S2F)] had a significantly increased tissue degeneration response to UV (Fig. 1F, gray dots, and fig. S2G). This increase in tissue loss could be rescued by MANF overexpression in hemocytes (Fig. 1F, black dots) and was recapitulated by hemocyte-specific knockdown of MANF (Fig. 1E, right, and fig. S2C, right).

MANF has immune modulatory properties that are required for retinal repair in *Drosophila*

The protective effect of hemocyte-derived MANF could be caused by direct neuroprotective activity

of MANF on retinal cells or could reflect an indirect effect of MANF on the microenvironment of the damaged retina. To distinguish between these possibilities, we investigated whether MANF could influence hemocyte phenotypes. Hemocytes can acquire lamellocyte phenotypes, characterized by down-regulation of plasmatocyte markers (*hemolectin* and *hemese*) and expression of Atilla protein (*37*), during sterile wound healing (*38*). These phenotypes correlate with hemocyte activation and may influence tissue repair capabilities, and we recapitulated them in our UV damage paradigm (Fig. 2A). Overexpression of MANF in hemocytes in vivo or treatment of hemocytes in culture with human recombinant MANF (hrMANF) significantly increased the proportion of lamellocytes in hemocyte smears, as detected by Atilla expression (Fig. 2A). This correlated

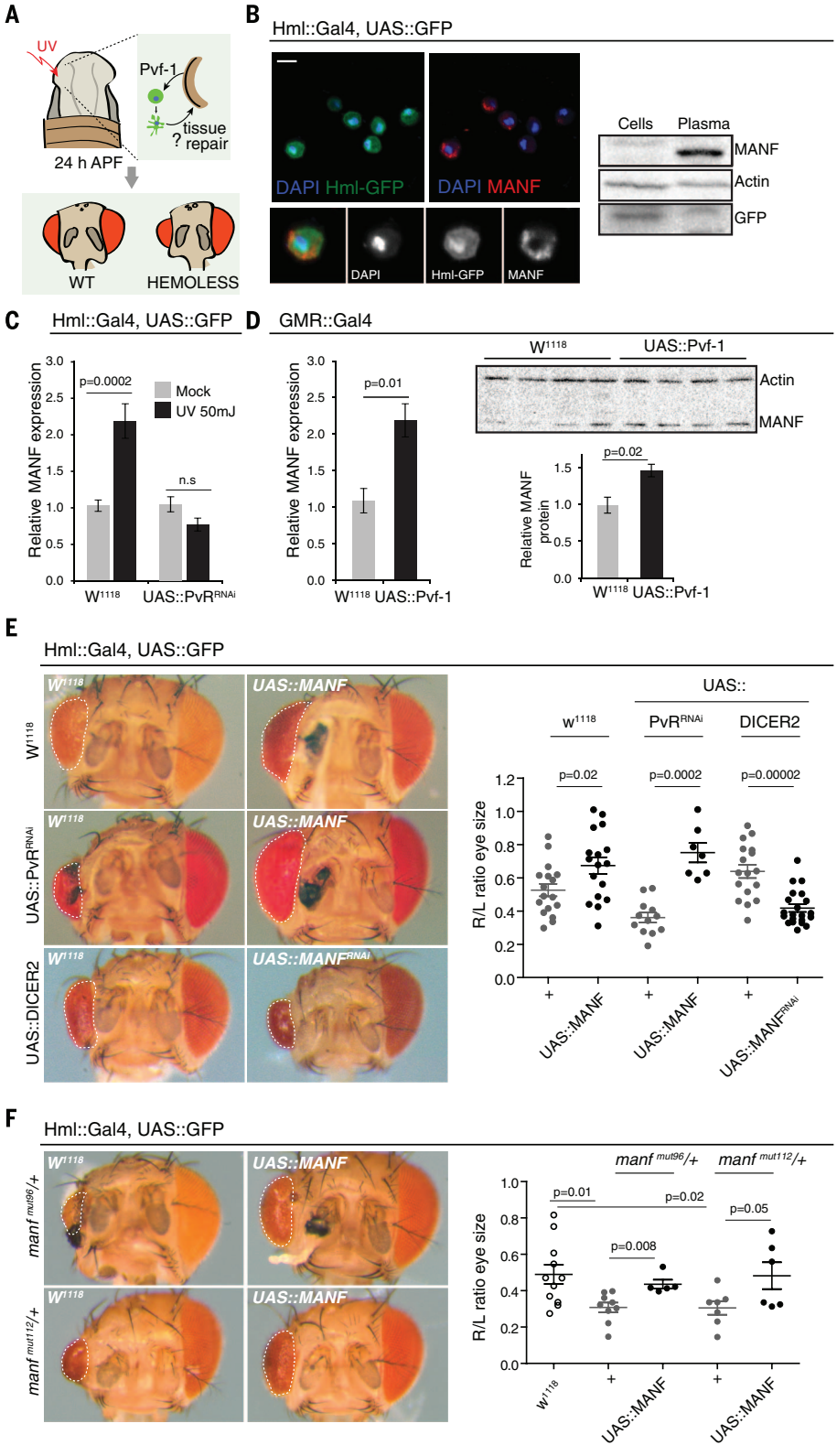

Fig. 1. MANF is a hemocyte-derived damage response factor and promotes retinal repair in *Drosophila*. (**A**) Experimental design and current model for hemocyte-mediated retinal repair in *Drosophila*. (**B**) (Left) Representative image of hemocyte smears from third-instar larvae (HmlΔ::Gal4; UAS::GFP) detecting MANF (red) in Hml>GFP^{+} cells. GFP, green; 4′,6-diamidino-2-phenylindole (DAPI), blue. Scale bar, 5 μm. (Right) Western blot analysis of MANF and GFP proteins in cellular and plasma fractions from hemolymph of third-instar larvae (HmlΔ::Gal4; UAS::GFP). (**C**) Relative mRNA levels of MANF detected by RT-qPCR in hemocyte samples collected from third-instar larvae of the designated genotypes and treatments ($n \geq 5$ for all conditions). For UV treatments, larvae were exposed to 50 mJ of UV at second-instar stage and hemocytes collected 24 hours after. (**D**) (Left) Relative mRNA levels of MANF detected by RT-qPCR in hemocyte samples collected from third-instar larvae overexpressing Pvf-1 in the retina ($n \geq 5$ for all conditions). (Right) Western blot analysis of MANF (intracellular in hemocytes and secreted into the hemolymph) and actin (intracellular in hemocytes) proteins in whole hemolymph collected from third-instar larvae overexpressing Pvf-1 in the retina. (Bottom) Average relative levels of MANF in whole-hemolymph samples normalized to actin. (**E** and **F**) (Left) Representative images of adult eye phenotypes from flies with the designated genotypes, after exposure of the right eye of P24 pupae to 17.5 mJ of UV light. Right, average relative size of the UV-treated eye when compared to the untreated eye of the same fly ($6 < n < 17$ for each genotype; each dot represents one fly). For all quantifications, error bars represent SEM and *P* values are from Student's *t* test.

with a decrease in the proportion of cells expressing GFP driven by HmlΔ:Gal4 and a decrease in *hml* transcripts (fig. S3A). Furthermore, MANF was necessary and sufficient to induce the *Drosophila* homolog of the mammalian M2 marker *arginase1* (*arg*) (*39*) in hemocytes (Fig. 2B and fig. S3B), suggesting that these cells may be able to acquire phenotypes similar to alternative activation (*16*, *17*). Most MANF-expressing hemocytes also expressed Arg, suggesting that there is an association between MANF expression and M2-like activation of hemocytes.

To determine whether MANF's immune modulatory function is required for retinal repair, we assessed retinal tissue preservation in conditions in which hemocytes express and secrete high levels of MANF but are unable to be activated in response to this signal. We generated such a condition by overexpressing MANF in the absence of Kdel receptors (KdelRs). In human cells, KdelRs modulate MANF secretion and cell surface binding. Intracellular KdelR prevents MANF secretion, whereas cell-surface-bound KdelR promotes binding of extracellular MANF (*40*). Knockdown of the one *Drosophila* KdelR homolog (*41*) in hemocytes resulted in a significant induction of MANF transcripts and the detection of MANF protein in the hemolymph (fig. S3, C and D), suggesting that KdelR-depleted hemocytes secrete high levels of MANF. In these hemocytes, MANF-induced lamellocyte formation and Arg expression were significantly decreased (Fig. 2, C and D). Hemocyte activation by extracellular MANF is thus impaired after KdelR knockdown. This genetic perturbation also resulted in a significant enhancement of UV-induced tissue loss, which could not be rescued by MANF overexpression (Fig. 2E). Thus, immune modulation by MANF is critical for tissue repair.

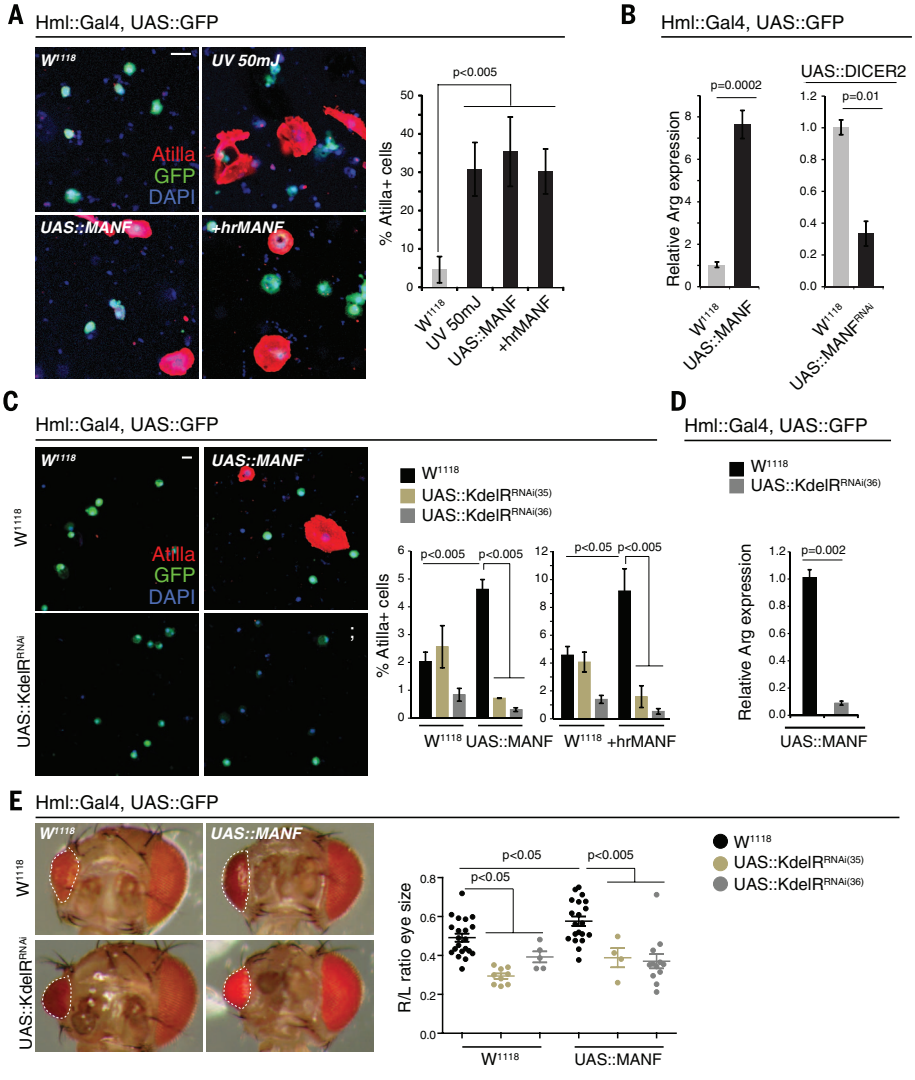

Fig. 2. MANF-dependent hemocyte activation is required for neuroprotection in *Drosophila*. (**A** and **C**) Representative IHC images of hemocyte smears from third-instar larvae of the designated genotypes and treatments, detecting Atilla protein in red. Hml^{+} cells are identified by GFP expression, green; DAPI, blue. Scale bar, 5 μm. For UV treatments, larvae were exposed to 50 mJ of UV at the second-instar stage, and hemocytes were collected 24 hours later. In (A), all analyses were performed after 24-hour culture in control media [wild-type (WT), UV 50 mJ, and UAS:MANF] or media supplemented with hrMANF protein. In (C), hemocytes were assayed directly after collection and were not cultured (images and left graph) or assayed, as in (A) (right graphs). Percentage of Atilla^{+} cells in the hemocyte population collected from third-instar larvae of the designated genotypes and treatments is shown ($n \geq 3$ for each genotype/treatment). (**B** and **D**) Relative mRNA levels of Arg detected by RT-qPCR in hemocyte samples collected from third-instar larvae of the designated genotypes ($n \geq 3$ for all conditions). (**E**) Representative images of adult eyes from flies with the designated genotypes, after exposure of the right eye of P24 pupae to 17.5 mJ of UV light. Right, average relative size of the UV-treated eye when compared to the untreated eye of the same fly ($5 < n < 20$ for each genotype; each dot represents one fly). For all quantifications, error bars represent SEM and *P* values are from Student's *t* test. RNAi(35) and RNAi(36) correspond to two independent double-stranded RNA interference–expressing lines targeting KdelR transcripts.

Damage response–associated PDGF-A/MANF paracrine signaling is conserved in mammals

MANF is an evolutionarily conserved protein (*31*), and we sought to explore its regulation and its potential to allay retinal degeneration and improve retinal repair in vertebrates. We used focal exposure of the central retina of C57BL/6 mice to 8000 lux of bright light for 1.5 hours to induce a retinal innate immune response without generalized photoreceptor apoptosis [C57BL/6 mice carry a protective variant of the *Rpe65* gene, preventing excessive retinal damage in response to light (*42*)]. This protocol resulted in a moderate and transient increase in the presence of innate immune cells in the retina (Fig. 3 and fig. S4, A and B).

PDGF-family and VEGF-family proteins are the mammalian homologs of *Drosophila* Pvf-type ligands (*43*, *44*), and we detected PDGF-A–expressing cells in the neural retina 6 hours after light exposure (Fig. 3B). The induction of PDGF-A was followed by a significant increase in MANF transcripts (Fig. 3C) and the detection of MANF^{+} innate immune cells, identified by CD11b expression (*45*, *46*), in the vitreous (Fig. 3D and fig. S4A, 12 hours). Resting microglia, localized to the plexiform layers [inner plexiform layer (IPL) and outer plexiform layer (OPL)] in control retinas, did not express MANF (Fig. 3D, no light exposure). Thirty-six hours later, MANF^{+} innate immune cells were found within the outer nuclear layer (ONL) (Fig. 3D and fig. S4A, 36 hours). This innate immune cell activation and/or recruitment was also accompanied by a redistribution of MANF protein from the cell bodies of Müller glia [where it is detected in control conditions in the inner nuclear layer (INL)] to glial processes (identified by staining against glial fibrillary acidic protein) (fig. S4C). Microglia and/or macrophages recruited and/or activated after light exposure expressed reduced levels of MANF when PDGF signaling was inhibited using neutralizing antibodies against PDGFRα (*47*) (fig. S4, D and E).

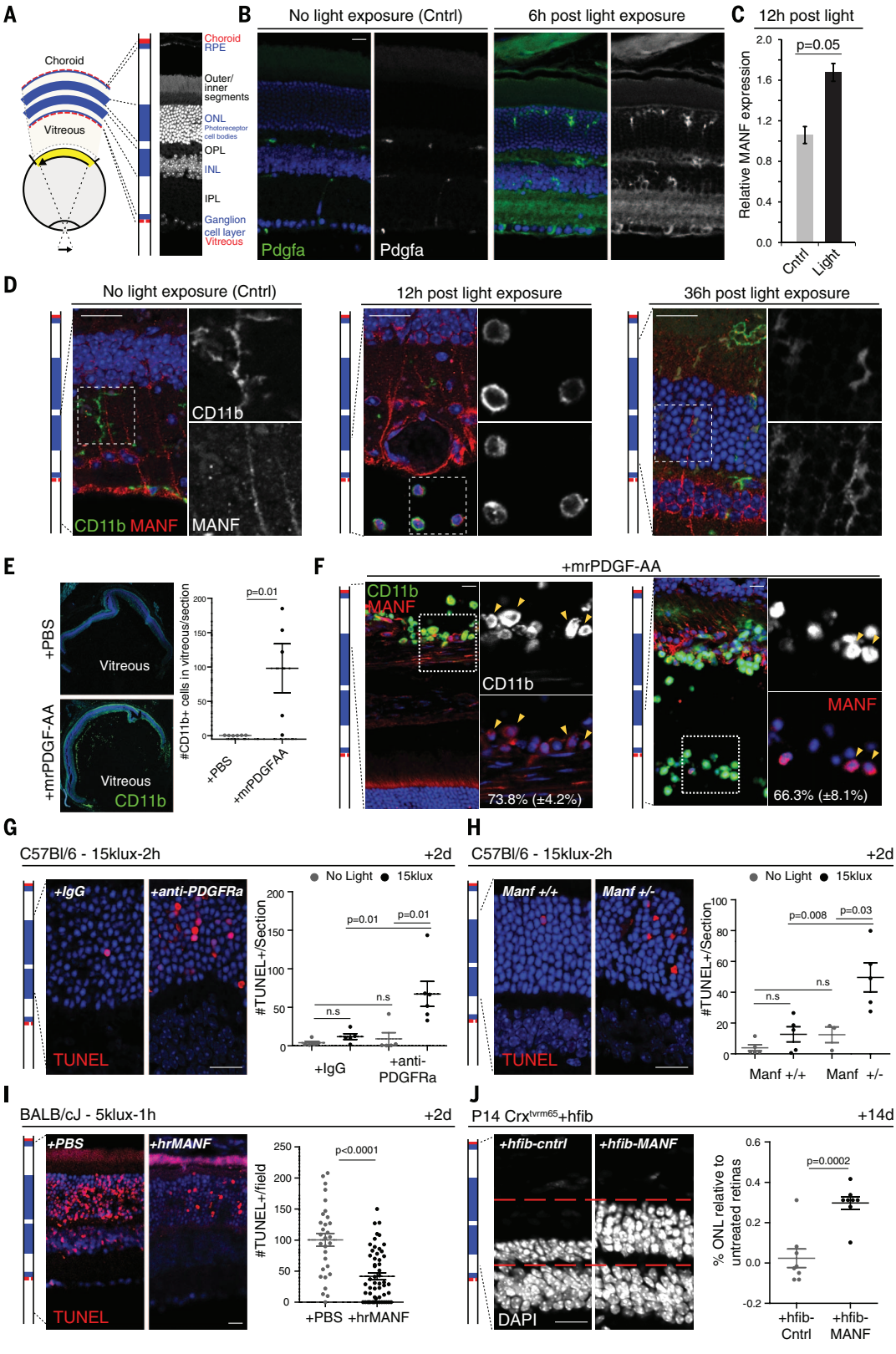

Fig. 3. PDGF-A/MANF damage–associated paracrine signaling is conserved in mammals. (**A**) Cellular layers in the mouse eye. (B) to (H) are from C57BL/6 mice. (**B** and **D**) IHC showing expression of PDGF-A, CD11b, and MANF after light exposure or in controls. See also fig. S4, A and B. (**C**) Retinal mRNA levels of MANF (RT-qPCR) relative to controls (n = 3). (**E** and **F**) IHC showing expression of CD11b [(E) and (F)] and MANF (F), 1 day after intravitreal injection of mrPDGF-AA or vehicle (PBS). Details in (F) highlight CD11b$^+$ cells detected in the vitreous (right) and choroid (left) blood vessels and MANF coexpression. (E) Average number of CD11b$^+$ cells in the vitreous (mrPDGF-AA, n = 5; PBS, n = 6; three sections per eye for each animal; each dot represents one animal). (**G** and **H**) TUNEL staining, 2 days after light exposure. (G) After intravitreal injection of antibody to PDGFRα or vehicle [goat immunoglobulin G (IgG)]. (H) In Manf$^{+/-}$ and Manf$^{+/+}$ littermates. Average number of TUNEL$^+$ nuclei is quantified [(G) No light: antibody to PDGFRα, n = 5; IgG, n = 5; light exposure: antibody to PDGFRα, n = 6; IgG, n = 5. (H) No light: Manf$^{+/+}$, n = 5; Manf$^{+/-}$, n = 3; light exposure: Manf$^{+/+}$, n = 5; Manf$^{+/-}$, n = 5. Twelve sections per eye for each animal; each dot represents one animal). (**I**) Retina of BALB/cJ mice, stained with TUNEL, 2 days after intravitreal injection of hrMANF or vehicle (PBS) and exposure to 5000 lux of bright light for 1 hour. Average number of TUNEL$^+$ nuclei per retinal field is shown (hrMANF, n = 8; PBS, n = 8; each dot represents one retinal field). (**J**) Retina of P28 Crx^{tvrm65} mice, stained with DAPI, 14 days after intravitreal injection of hfib-MANF or hfib-Cntrl. Red dashed lines indicate the thickness of the ONL after hfib-MANF delivery for comparison. Quantification of photoreceptor preservation as a percentage of nuclei rows in ONL relative to untreated controls (hfib-MANF, n = 8; hfib-Cntrl, n = 8, five sections per eye, untreated controls for relative quantifications; n = 4, five sections per eye; each dot represents one animal). For all quantifications, error bars represent SEM and P values are from Student's t test. Scale bars, 20 μm.

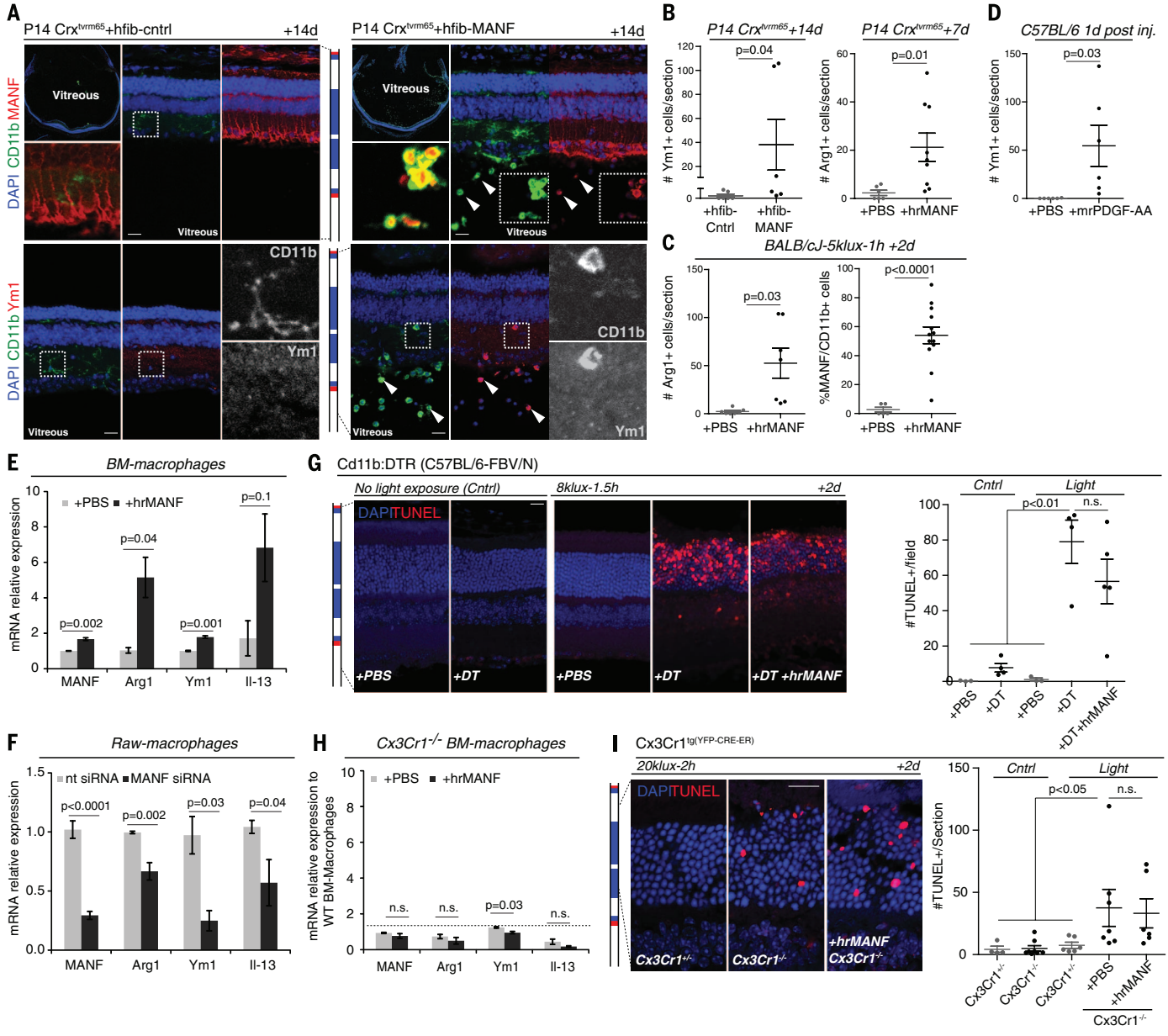

Fig. 4. MANF-dependent immune modulation mediates retinal neuroprotection. (**A**) IHC showing expression of CD11b, MANF, and Ym1 in P28 Crx^{tvrm65} mice 14 days after intravitreal injection of hfib-MANF or hfib-Cntrl. Arrowheads indicate coexpression. (**B**) Average number of Ym1$^+$ or Arg1$^+$ cells, per eye cryosection, in P28 or P21 Crx^{tvrm65} mice, 14 or 7 days after intravitreal injection of hfib (hfib-MANF, $n = 6$; hfib-Cntrl, $n = 6$; five sections per eye; each dot represents one animal) or recombinant protein (hrMANF, $n = 6$; PBS, $n = 6$; each dot represents one section). (**C**) (Left) Average number of Arg1$^+$ cells per eye cryosection, in BALB/cJ mice, 2 days after intravitreal injection of hrMANF or vehicle (PBS) and light exposure (hrMANF, $n = 7$; PBS, $n = 7$; three sections per eye; each dot represents one animal). (Right) Percentage of CD11b$^+$/MANF$^+$ cells in the retina of BALB/cJ mice after the same treatment (hrMANF, $n = 13$ sections; PBS, $n = 5$ sections; each dot represents one section). See also fig. S6A. (**D**) Average number of Ym1$^+$ cells, per eye cryosection, in C57BL/6 mice, 1 day after intravitreal injection of mrPDGF-AA or vehicle (mrPDGF-AA, $n = 5$; PBS, $n = 6$; three sections per eye; each dot represents one animal). See also fig. S6B. (**E**, **F**, and **H**) Relative mRNA levels (RT-qPCR) in BMDMs from WT [(E), $n = 3$] or Cx3Cr1-deficient [(H), $n = 3$] mice, stimulated with hrMANF or vehicle (PBS) or raw macrophages transfected with MANF targeting siRNA pool or a nontargeting siRNA pool [(F), $n = 5$]. See also fig. S9. (**G** and **I**) TUNEL staining, 2 days after intravitreal injection of hrMANF or vehicle (PBS) and light exposure of CD11b:DTR (G) or Cx3Cr1$^{tg(YFP\text{-}CRE\text{-}ER)}$ (Cx3Cr1$^{-/-}$) mice (I). Average number of TUNEL$^+$ nuclei is shown [(G) No light: PBS, $n = 3$; DT, $n = 4$. Light: PBS, $n = 3$; DT, $n = 4$; DT+hrMANF, $n = 5$; four sections per eye. (I) No light: Cx3Cr1$^{+/-}$, $n = 4$; Cx3Cr1$^{-/-}$, $n = 8$. Light: Cx3Cr1$^{+/-}$, $n = 6$; Cx3Cr1$^{-/-}$: PBS, $n = 7$; hrMANF, $n = 6$; 12 sections per eye; each dot represents one animal). For all quantifications, error bars represent SEM and P values are from Student's t test. Scale bars, 20 μm.

Conversely, intravitreal injection of mouse recombinant PDGF-AA (mrPDGF-AA) significantly increased CD11b$^+$ innate immune cells in eyes in the absence of light exposure (Fig. 3E). These CD11b$^+$ cells also expressed MANF and were found in the vitreous (Fig. 3F, right, arrowheads) and the choroidal blood vessels (Fig. 3F, left, arrowheads).

Reduction of PDGFRα signaling or MANF levels [in heterozygotes for a null allele (*48*)] significantly enhanced photoreceptor apoptosis [detected by terminal deoxynucleotidyl transferase–mediated deoxyuridine triphosphate nick end labeling (TUNEL)] in response to light exposure (Fig. 3, G and H). Homozygotes for this MANF allele are embryonic or perinatal lethal (*48*). Reduction of

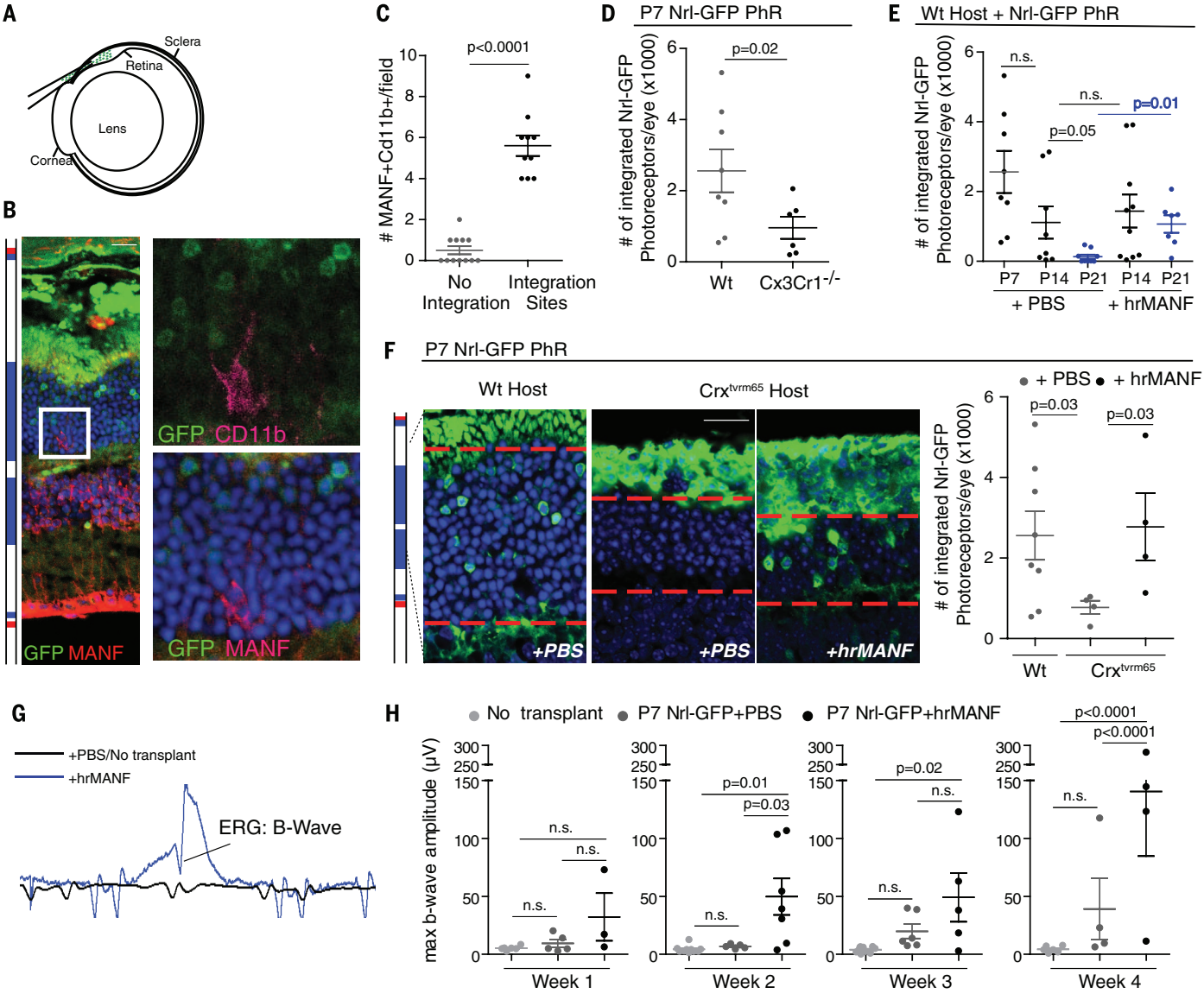

Fig. 5. MANF enhances the efficiency of retinal regenerative therapies. (**A**) Cartoon representing the transcorneal subretinal injection method. (**B**) IHC showing expression of CD11b, MANF, and GFP at an integration site of Nrl-GFP donor photoreceptors 1 week after transplantation. (**C**) Average number of $MANF^{+}CD11b^{+}$ cells/field in integration sites versus sites of no integration (10 fields per condition; all fields contained cells in the subretinal space; each dot represents one field). (**D**) Quantification of integration into WT (n = 8) or $Cx3Cr1^{-/-}$ (n = 6) mice, analyzed by IHC for GFP expression, 7 days after subretinal injection of P7 Nrl-GFP donor photoreceptors (PhR). Each dot represents one animal. (**E**) Quantification of integration in C57BL/6 mice, analyzed by IHC for GFP expression, 7 days after subretinal injection of Nrl-GFP donor photoreceptors (PhR) supplemented with hrMANF protein (n = 10, P14; n = 7, P21) or vehicle (PBS) (n = 8, P7 and P14; n = 9, P21). Each dot represents one animal. See also fig. S8A for representative images of P21 transplants. (**F**) Representative images and quantification of integration in WT (n = 8, same as in Fig. 5D) or Crx^{tvrm65} mice, analyzed by IHC for GFP expression, 7 days after subretinal injection of P7 Nrl-GFP donor photoreceptors (PhR) supplemented with hrMANF protein (hrMANF, n = 4) or vehicle (PBS, n = 4). Each dot represents one animal. (**G**) Examples of ERG waves obtained in MANF-supplemented (blue) and PBS-supplemented (black) transplants of P7 Nrl-GFP PhRs in Crx^{tvrm65} mice. (**H**) Maximal b-wave amplitudes measured 1 to 4 weeks after subretinal injections of P7 Nrl-GFP PhRs supplemented with MANF (n = 3 to 7 at each time point), PBS (n = 4 to 6 at each time point) and of eyes that did not receive a transplant (n = 6 to 10), all in Crx^{tvrm65} host. Each dot represents one animal. See also fig. S8B for b waves after hrMANF or PBS injection without cells and fig. S8C for b waves of WT eyes. P values are from a two-way ANOVA analysis. For all quantifications, error bars represent SEM. P values in (C) to (F) are from Student's t test. Scale bars, 20 μm.

MANF expression in bone marrow–derived macrophages (BMDMs) of these mice was confirmed by RT-qPCR (fig. S4F).

Damage signals from retinal cells thus engage a conserved retinal repair response in both flies and mice that involves the Pvf/PDGF-mediated recruitment/activation of MANF-expressing innate immune cells and that is essential to prevent excessive apoptosis in response to light.

MANF has a conserved neuroprotective function in the mammalian retina

To determine whether MANF protein supplementation would be sufficient to ameliorate retinal degeneration, we used the light-sensitive BALB/cJ strain, which lacks the protective variant of the *Rpe65* allele, rendering them susceptible to light-induced retinal damage (*42*). This phenotype is accompanied by activation of proinflammatory microglia and by chemokine production that modulates photoreceptor degeneration (*49*). Exposure

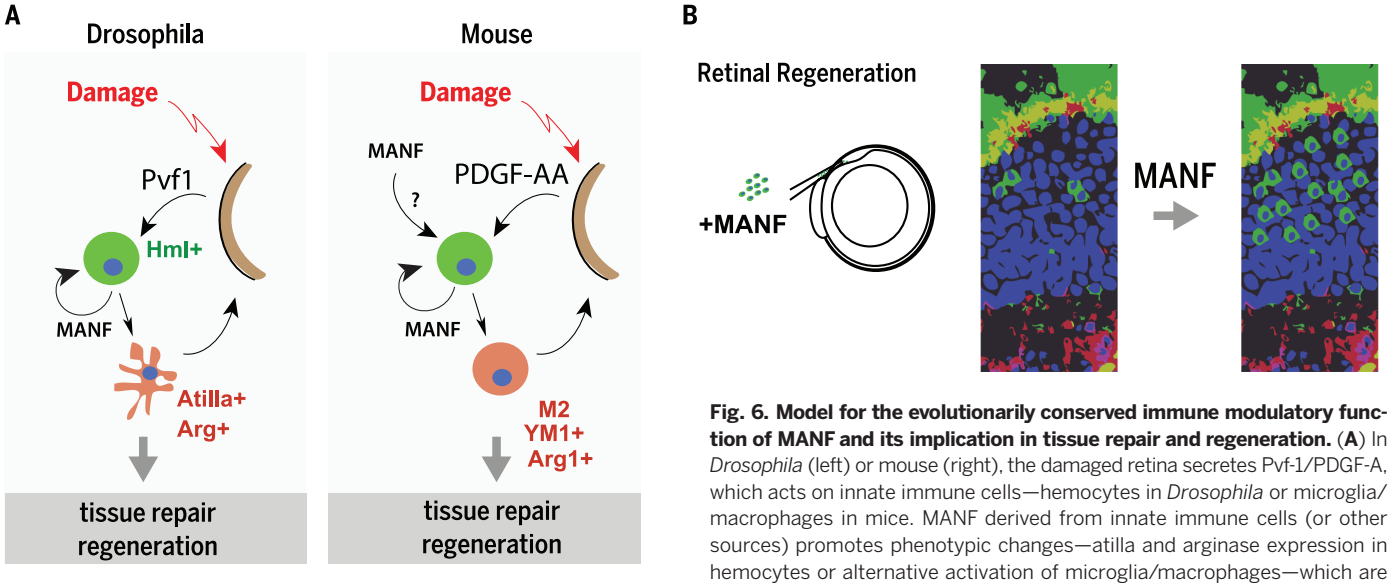

Fig. 6. Model for the evolutionarily conserved immune modulatory function of MANF and its implication in tissue repair and regeneration. (**A**) In *Drosophila* (left) or mouse (right), the damaged retina secretes Pvf-1/PDGF-A, which acts on innate immune cells—hemocytes in *Drosophila* or microglia/macrophages in mice. MANF derived from innate immune cells (or other sources) promotes phenotypic changes—atilla and arginase expression in hemocytes or alternative activation of microglia/macrophages—which are part of the mechanism involved in tissue protection. (**B**) MANF supplementation is an enhancer of retinal regenerative therapies by increasing the integration efficiency of exogenously supplied photoreceptors for retinal repair.

of these mice to 5000 lux of bright light for 1 hour resulted in photoreceptor apoptosis (fig. S4G). In addition, we used two genetic models of retinal degeneration (Crx^{tvrm65}, a slow model of genetically induced retinal degeneration, and $Pde6b^{Rd1}$, a fast model of genetically induced retinal degeneration), whose dynamics of photoreceptor loss have been previously described (*50*–*52*).

We injected hrMANF protein or vehicle [phosphate-buffered saline (PBS)] into the vitreous immediately before light exposure or at the onset of retinal degeneration [postnatal day 14 (P14) for Crx^{tvrm65} mice and P7 for $Pde6b^{Rd1}$ mice] and evaluated photoreceptor apoptosis by TUNEL. MANF injection significantly reduced apoptosis in all three models of retinal degeneration (Fig. 3I and fig. S5, A and B). As photoreceptors degenerate, the number of nuclei in the ONL is reduced, and in Crx^{tvrm65} mice there are on average five to six rows left at P21. In hrMANF-treated eyes, there was a significant preservation of photoreceptors in the ONL (fig. S5C), suggesting that inhibition of apoptosis effectively slows retinal degeneration in this model. Similar results were observed in the $Pde6b^{Rd1}$ mouse model analyzed 5 days after intravitreal delivery of hrMANF (fig. S5, D and E).

Finally, we asked whether a persistent source of MANF could further delay retinal degeneration in Crx^{tvrm65} mice. We infected human fibroblasts (hfib) with a lentivirus driving the expression of a functional MANF-GFP fusion protein (*40*). MANF-GFP expression could readily be detected in these fibroblasts and in the media supernatant, confirming that the fusion protein was efficiently secreted (fig. S5, F and G). When MANF-secreting fibroblasts were injected into the vitreous of P14 Crx^{tvrm65} mice, their retinas degenerated more slowly than control fibroblast-injected retinas, and a significant amount of photoreceptors were preserved in the ONL (Fig. 3J). Survival of injected fibroblasts was confirmed at the time of analysis (2 weeks after injection) by detecting the presence of GFP-expressing cellular aggregates within the vitreous.

MANF can thus prevent photoreceptor apoptosis broadly and delay retinal degeneration, independently of the damaging stimulus.

MANF-dependent modulation of immune cell phenotypes mediates retinal protection

After intravitreal injection of MANF-secreting fibroblasts, $MANF^+$ innate immune cells ($CD11b^+$) could be detected in the vitreous of Crx^{tvrm65} mice (Fig. 4A, top panel). These $CD11b^+$ cells with round morphology also expressed markers of alternative activation (*16*, *17*) (Fig. 4A, bottom panel, and Fig. 4B, left; fibroblasts injected into the vitreous were detected by GFP expression at the time of dissection and were completely removed along with the lens). Intravitreal delivery of hrMANF had similar effects on innate immune cell phenotypes in Crx^{tvrm65} (Fig. 4B, right) and light-damaged retinas (Fig. 4C and fig. S6A), supporting an immune modulatory function for MANF. Accordingly, the recruitment of $MANF^+$ innate immune cells in response to PDGF-AA treatment (Fig. 3, E and F) was accompanied by a significant increase in the number of $CD11b^+$ cells colabeled with $Ym1^+$ (Fig. 4D and fig. S6B).

The innate immune cell population recruited after MANF delivery was mostly composed of monocytes and monocyte-derived macrophages (60 to 80%, identified by F4/80 or CD68 expression). $Ly6\text{-}G^+$ ($Gr\text{-}1^{high}$) neutrophils represented about 15% of the population. The majority of both macrophages and neutrophils (80%) expressed MANF and Arg1, suggesting that MANF expression is associated with markers of alternative activation (fig. S6C), similar to what we observed in fly hemocytes (fig. S3B).

In vitro stimulation with hrMANF for 3 hours was also sufficient to induce markers of alternative activation (Arg1 and Ym1) (*16*, *17*) and Il-13, an anti-inflammatory cytokine (*53*), in BMDMs (Fig. 4E) and in a macrophage cell line [RAW264.7 (*54*)] (fig. S7, A and B). Silencing of MANF with a targeting small interfering RNA (siRNA) pool in this cell line resulted in the repression of the same set of genes (Fig. 4F). This suggests that MANF has a direct immune modulatory function in macrophages and that at least part of the mechanism is autocrine.

To determine whether immune modulation by MANF is required for its neuroprotective activity, we assessed retinal damage after light exposure and after MANF supplementation in mice with impaired immune cell function. We depleted macrophages and microglia using diphtheria toxin (DT) administration in CD11b:DTR mice (*55*, *56*). DT, but not sham (PBS), injection resulted in a significant reduction in the number of innate immune cells in the retina (fig. S7C) and induction of photoreceptor apoptosis in response to light exposure (Fig. 4G). Intravitreal supplementation of hrMANF protein did not significantly reduce photoreceptor apoptosis in these mice (Fig. 4G), supporting an essential role for immune cells in mediating the protective effects of MANF.

We further used mice deficient in Cx3Cr1 (*57*, *58*) to test the requirement of immune modulation for the protective effects of MANF. Here, we aimed at generating a condition in which immune cells were present but failed to induce alternative activation in response to MANF signaling, similar to KdelR deficiency in flies. Cx3Cr1 is a chemokine receptor expressed in different immune cell populations, including retinal microglia and peripheral monocytes (*58*). High Cx3Cr1 expression has been associated with a functionally distinct class of monocytes with immune patrolling activity and with a molecular profile of macrophage differentiation resembling alternative activation (*18*, *19*). Loss of

Cx3Cr1 results in retinal degeneration in response to several stimuli and is associated with proinflammatory activation of immune cells (*9*, *14*, *59*). Thus, we hypothesized that loss of Cx3Cr1 could be an effective way to impair MANF-induced alternative activation. Indeed, BMDMs derived from Cx3Cr1-deficient mice failed to induce genes associated with alternative activation upon MANF stimulation (Fig. 4H), despite expressing normal levels of MANF (fig. S7, D and E). Light-induced photoreceptor apoptosis in Cx3Cr1-deficient mice could not be rescued by intravitreal delivery of hrMANF (Fig. 4I), suggesting that it is not only MANF derived from macrophages that mediates the protective effects but rather a more complex mechanism that depends on MANF immune modulatory activity. We cannot exclude, however, that Cx3Cr1 deficiency may also result in other alterations that contribute to the loss of protective effects of MANF observed in these conditions, which may be independent of macrophage functions.

MANF promotes cell integration and restoration of visual function in the mammalian retina

Retinal repair by transplantation of mouse and human photoreceptor precursors can restore vision in mouse models of retinal degeneration (*60*, *61*). Integration efficiency depends on the ontogenetic stage of donor cells (*60*) and on the status of the degenerative microenvironment (*62*) and negatively correlates with the presence of classically activated macrophages within the retinal tissue (*63*). We injected photoreceptors derived from Nrl-GFP mice subretinally into wild-type retinas and found that microglia and/or macrophages located at sites of integration expressed MANF, suggesting a possible role for MANF-mediated immune modulation in promoting integration (Fig. 5, A to C). Supporting this hypothesis, integration efficiency was significantly reduced in Cx3Cr1 mice (Fig. 5D).

To further test this hypothesis, we asked whether MANF supplementation would increase integration of subretinal-delivered photoreceptors derived from Nrl-GFP mice into a wild-type host. Integration efficiency declines with increased maturity of injected photoreceptors (*60*, *64*). Accordingly, we observed a strong decline in integration efficiency (assessed 1 week after injection) when using P21 rather than P7 or P14 photoreceptors in a wild-type host (Fig. 5E). hrMANF supplementation rescues this decline while having no effect on P14 cells (Fig. 5E and fig. S8A), suggesting that MANF may act either directly on refractory photoreceptors to improve their integration capabilities or indirectly by inducing a more supportive environment for such cells.

To distinguish between these possibilities, we tested the effects of MANF on integration efficiency in degenerating retinas. The inflammatory microenvironment in degenerating retinas is a likely cause for poor integration efficiency (*62*) and thus a critical limitation in clinical settings. We used Crx^{tvrm65} retinas to model a degenerating environment and found that integration of even young (P7) Nrl-GFP photoreceptors, which efficiently integrated into wild-type retinas (Fig. 5E), was significantly reduced in Crx^{tvrm65} retinas (Fig. 5F). MANF supplementation significantly improved integration in this context (Fig. 5F), supporting the notion that MANF improves the environment for integration even in a disease context.

Importantly, MANF accelerated and improved restoration of visual function, as evaluated by maximal b-wave amplitudes measured in sequential electroretinogram (ERG) testing over the course of 4 weeks (Fig. 5, G and H). Eyes that received MANF-supplemented transplants showed signs of light responsiveness based on a detectable b-wave as early as 1 week after transplantation, whereas eyes that received control transplants had the earliest detectable b-wave only at 3 weeks. Comparing ERG b-wave amplitudes of untreated Crx^{tvrm65} mice (no transplant) to treated mice at 1 to 4 weeks confirmed a functional improvement in vision in the MANF-supplemented cohort only, whereas the PBS-supplemented group did not significantly differ from untreated controls. The ERG changes reflected cell integration and not an effect of MANF supplementation alone (fig. S8B) and represented a recovery of about 60% of visual function when compared with normal ERG b-wave amplitudes of wild-type mice (Fig. 5H and fig. S8C). This is a significant improvement over nonsupplemented transplants, which yield about 20% of visual function recovery (Fig. 5H and fig. S8C) [see also (*61*)].

Discussion

Our results identify MANF as an evolutionarily conserved immune modulator that plays a critical role in the regulatory network mediating tissue repair in the retina (Fig. 6A). The ability of MANF to increase regenerative success in the mouse retina highlights the promise of modulating the immune environment as a strategy to improve regenerative therapies (Fig. 6B).

The usefulness of immune modulation for regenerative medicine has been anticipated based on studies of tissues where regeneration is sustained endogenously by resident stem cells (*3*, *11*, *65*–*69*). Our study provides strong support for this hypothesis.

MANF has previously been described as a neurotrophic factor (*30*, *70*, *71*), and it may also exert a direct neuroprotective effect in the retina, yet our data suggest a more expansive role: Because MANF cannot promote tissue repair in flies in which the hemocyte response to MANF is selectively ablated, or in mammalian retinas depleted of innate immune cells or containing macrophages that are unresponsive to MANF, we propose that MANF's role in promoting alternative activation of innate immune cells is central to its function in tissue repair. Further studies will be required to determine the specific contribution of alternative-activated macrophages in mediating these effects. Although our data point to an important role of macrophages in mediating the effects, it does not exclude the possibility that other cell types are involved in the process or that macrophages' functions other than polarization may influence the outcome of MANF's protective effects.

Clinically, MANF may thus have a distinct advantage over previously described neurotrophic factors both in improving survival of transplanted cells directly and in promoting a microenvironment supportive of local repair and integration. Because integration efficiency correlates with the extent of vision restoration (*61*), it can be anticipated that MANF supplementation will have an important effect in clinical settings.

Further studies involving tissue-specific knockdown of MANF in mammals will be required to evaluate the relative contribution of different cellular and tissue sources for MANF in homeostatic and damage conditions. Although we found that MANF is strongly expressed in immune cells, we also observed MANF expression in other cell types, in agreement with previous reports (*72*).

Similarly, the molecular mechanism involved in MANF signaling remains elusive. To date, a signal-transducing receptor for MANF has not been identified, although protein kinase C signaling has been described to be activated downstream of MANF (*73*). MANF can further negatively regulate nuclear factor κB (NF-κB) signaling in mammalian cells (*74*), and loss of MANF in *Drosophila* results in the infiltration of pupal brains with cells resembling hemocytes with high Rel/NF-κB activity, potentially representing proinflammatory, M1-like phenotypes (*75*). The identification of immune cells as a target for MANF in our study may accelerate the discovery of putative MANF receptors and downstream signaling pathways.

Because neurotoxic inflammation has been implicated in Parkinson's disease (*76*), it is possible that the protective effects of MANF in this context (*71*) are also mediated by immune modulation, as we show here for retinal disease. Indeed, recent reports suggest that the MANF paralog, cerebral dopamine neurotrophic factor, has an anti-inflammatory function in murine models of Parkinson's disease (*77*) and in nerve regeneration after spinal cord injury (*78*). A recent study has further shown that loss of MANF leads to beta cell loss in the pancreas (*48*). Beta cell loss is commonly associated with chronic inflammation, and it is thus tempting to speculate that MANF is broadly required in various contexts to aid conversion of proinflammatory macrophages into prorepair anti-inflammatory macrophages. Future studies will clarify the role of MANF in resolving inflammation and promoting tissue repair not only in the retina and brain but also in other tissues. A deeper understanding of MANF-mediated immune modulation and its effect on stem cell function, wound repair, and tissue maintenance is thus expected to help in the development of effective regenerative therapies.

Materials and methods

Mice

All mice used in the described studies were housed and bred at the Association for Assessment and

Accreditation of Laboratory Animal Care International accredited vivarium of the Buck Institute for Research on Aging, in a specific-pathogen-free facility, in individually ventilated cages on a standard 12:12 light cycle. All procedures were approved by the Buck Institute Institutional Animal Care and Use Committee. For details on the mouse strains and lines used, see the supplementary materials (SM).

Drosophila stocks and culture

Fly stocks were raised on standard cornmeal- and molasses-based food. All experiments were performed at 25°C. Both sexes gave the same results in all experiments, unless otherwise described. For details on the fly lines used, see SM.

Intraocular injections in mice

For intravitreal injection, recombinant proteins or cells in 1-μl volume were injected into the right eye using a graduated pulled glass pipet and a wire plunger (Wiretrol II, 5-0000-2005, Drummond Scientific Company). For details on the test articles injected and the procedure for intravitreal injections, see SM.

For subretinal injection, dissociated GFP-expressing mouse retinal cells from the Nrl-GFP mice were transplanted into the subretinal space of recipient mice using the transcorneal subretinal injection method. For details on the preparation of Nrl-GFP cells and the procedure for transplantation, see SM.

Light damage in mice

Mice were dark-adapted for 18 hours before the procedure. Test eyes were exposed to 5000 to 20,000 lux of bright light using a 144 light-emitting diode microscope ring light (AmScope) for 1 to 2 hours. After light damage, mice were allowed to recover from anesthesia, returned to their cages, and housed in darkness until analysis. Undamaged control mice were housed in regular conditions throughout the experiment. For details, see SM.

UV damage in *Drosophila* pupae retina and larvae

Pupae retinas were exposed to 17.5 mJ of UV light as previously described (*26*, *28*). Second-instar larvae were exposed to 50 mJ of UV light as previously described (*25*). For details on the procedures and quantification methods, see SM.

Histological analysis, imaging, and quantification methods

Retinal sections, macrophages, and hemocyte smears were analyzed by immunohistochemistry (IHC) and other histological methods (see SM for details) and imaged using a LSM 700 confocal laser-scanning microscope; images were used for quantification purposes. For details on staining methods and quantification methods, see SM.

Electroretinogram

All ERGs were carried out under scotopic conditions using a handheld multispecies electroretinograph (HMsERG, OcuScience) and analyzed using ERGVIEW Version 4.3 (OcuScience). For details on the procedures, see SM.

Cell culture

Raw 264.7 macrophages (ATCC, TIB-71, lot 61524889) and BMDMs were used in hrMANF stimulation experiments and MANF knockdown experiments. BMDMs were differentiated in culture from bone marrow using 20 ng/ml of macrophage colony-stimulating factor (M-CSF, Sigma, M9170) for 7 days. Raw 264.7 and BMDMs were stimulated for 3 hours with 10 μg/ml of hrMANF before analysis. For details on the procedures and on the knockdown experiments, see SM.

Expression analyses

RNA sequencing and RT-qPCR were used to quantify mRNA levels, and Western blot analysis was used to quantify protein levels. For details on the methods employed in each technique, see SM.

Statistical analysis

All counts are presented as average and standard error of mean (SEM). Statistical analysis was carried out using Microsoft Excel or GraphPad Prism, and Student's *t* test or two-way analysis of variance (ANOVA) was used to determine statistical significance, assuming normal distribution and equal variance.

REFERENCES AND NOTES

1. I. J. Fox *et al*., Use of differentiated pluripotent stem cells as replacement therapy for treating disease. *Science* **345**, 1247391 (2014). doi: 10.1126/science.1247391; pmid: 25146295
2. A. Trounson, C. McDonald, Stem cell therapies in clinical trials: Progress and challenges. *Cell Stem Cell* **17**, 11–22 (2015). doi: 10.1016/j.stem.2015.06.007; pmid: 26140604
3. S. J. Forbes, N. Rosenthal, Preparing the ground for tissue regeneration: From mechanism to therapy. *Nat. Med.* **20**, 857–869 (2014). doi: 10.1038/nm.3653; pmid: 25100531
4. J. Reynolds, D. A. Lamba, Human embryonic stem cell applications for retinal degenerations. *Exp. Eye Res.* **123**, 151–160 (2014). doi: 10.1016/j.exer.2013.07.010; pmid: 23880530
5. N. Gupta, K. E. Brown, A. H. Milam, Activated microglia in human retinitis pigmentosa, late-onset retinal degeneration, and age-related macular degeneration. *Exp. Eye Res.* **76**, 463–471 (2003). doi: 10.1016/S0014-4835(02)00332-9; pmid: 12634111
6. H. Y. Zeng *et al*., Identification of sequential events and factors associated with microglial activation, migration, and cytotoxicity in retinal degeneration in *rd* mice. *Invest. Ophthalmol. Vis. Sci.* **46**, 2992–2999 (2005). doi: 10.1167/iovs.05-0118; pmid: 16043876
7. X. Cao *et al*., Macrophage polarization in the maculae of age-related macular degeneration: A pilot study. *Pathol. Int.* **61**, 528–535 (2011). doi: 10.1111/j.1440-1827.2011.02695.x; pmid: 21884302
8. N. Yoshida *et al*., Laboratory evidence of sustained chronic inflammatory reaction in retinitis pigmentosa. *Ophthalmology* **120**, e5–e12 (2013). doi: 10.1016/j.ophtha.2012.07.008; pmid: 22986110
9. C. Combadière *et al*., CX3CR1-dependent subretinal microglia cell accumulation is associated with cardinal features of age-related macular degeneration. *J. Clin. Invest.* **117**, 2920–2928 (2007). doi: 10.1172/JCI31692; pmid: 17909628
10. R. A. Pearson, C. Hippert, A. B. Graca, A. C. Barber, Photoreceptor replacement therapy: Challenges presented by the diseased recipient retinal environment. *Vis. Neurosci.* **31**, 333–344 (2014). doi: 10.1017/S0952523814000200; pmid: 24945529
11. A. B. Aurora, E. N. Olson, Immune modulation of stem cells and regeneration. *Cell Stem Cell* **15**, 14–25 (2014). doi: 10.1016/j.stem.2014.06.009; pmid: 24996166
12. A. London, M. Cohen, M. Schwartz, Microglia and monocyte-derived macrophages: Functionally distinct populations that act in concert in CNS plasticity and repair. *Front. Cell. Neurosci.* **7**, 34 (2013). doi: 10.3389/fncel.2013.00034; pmid: 23596391
13. K. A. Kigerl *et al*., Identification of two distinct macrophage subsets with divergent effects causing either neurotoxicity or regeneration in the injured mouse spinal cord. *J. Neurosci.* **29**, 13435–13444 (2009). doi: 10.1523/JNEUROSCI.3257-09.2009; pmid: 19864556
14. B. Peng *et al*., Suppression of microglial activation is neuroprotective in a mouse model of human retinitis pigmentosa. *J. Neurosci.* **34**, 8139–8150 (2014). doi: 10.1523/JNEUROSCI.5200-13.2014; pmid: 24920619
15. M. Karlstetter, S. Ebert, T. Langmann, Microglia in the healthy and degenerating retina: Insights from novel mouse models. *Immunobiology* **215**, 685–691 (2010). doi: 10.1016/j.imbio.2010.05.010; pmid: 20573418
16. S. Gordon, Alternative activation of macrophages. *Nat. Rev. Immunol.* **3**, 23–35 (2003). doi: 10.1038/nri978; pmid: 12511873
17. C. D. Mills, M1 and M2 Macrophages: Oracles of health and disease. *Crit. Rev. Immunol.* **32**, 463–488 (2012). doi: 10.1615/CritRevImmunol.v32.i6.10; pmid: 23428224
18. C. Auffray *et al*., Monitoring of blood vessels and tissues by a population of monocytes with patrolling behavior. *Science* **317**, 666–670 (2007). doi: 10.1126/science.1142883; pmid: 17673663
19. F. Geissmann *et al*., Development of monocytes, macrophages, and dendritic cells. *Science* **327**, 656–661 (2010). doi: 10.1126/science.1178331; pmid: 20133564
20. J. Neves, M. Demaria, J. Campisi, H. Jasper, Of flies, mice, and men: Evolutionarily conserved tissue damage responses and aging. *Dev. Cell* **32**, 9–18 (2015). doi: 10.1016/j.devcel.2014.11.028; pmid: 25584795
21. Y. Belacortu, N. Paricio, *Drosophila* as a model of wound healing and tissue regeneration in vertebrates. *Dev. Dyn.* **240**, 2379–2404 (2011). doi: 10.1002/dvdy.22753; pmid: 21953647
22. W. Razzell, W. Wood, P. Martin, Swatting flies: Modelling wound healing and inflammation in *Drosophila*. *Dis. Model. Mech.* **4**, 569–574 (2011). doi: 10.1242/dmm.006825; pmid: 21810906
23. D. T. Babcock *et al*., Circulating blood cells function as a surveillance system for damaged tissue in *Drosophila* larvae. *Proc. Natl. Acad. Sci. U.S.A.* **105**, 10017–10022 (2008). doi: 10.1073/pnas.0709951105; pmid: 18632567
24. J. C. Pastor-Pareja, M. Wu, T. Xu, An innate immune response of blood cells to tumors and tissue damage in *Drosophila*. *Dis. Model. Mech.* **1**, 144–154 (2008). doi: 10.1242/dmm.000950; pmid: 19048077
25. J. Karpac, A. Younger, H. Jasper, Dynamic coordination of innate immune signaling and insulin signaling regulates systemic responses to localized DNA damage. *Dev. Cell* **20**, 841–854 (2011). doi: 10.1016/j.devcel.2011.05.011; pmid: 21664581
26. E. M. Kelsey, X. Luo, K. Brückner, H. Jasper, Schnurri regulates hemocyte function to promote tissue recovery after DNA damage. *J. Cell Sci.* **125**, 1393–1400 (2012). doi: 10.1242/jcs.095323; pmid: 22275438
27. L. Wang, I. Kounatidis, P. Ligoxygakis, *Drosophila* as a model to study the role of blood cells in inflammation, innate immunity and cancer. *Front. Cell. Infect. Microbiol.* **3**, 113 (2013). pmid: 24409421
28. O. W. Jassim, J. L. Fink, R. L. Cagan, Dmp53 protects the *Drosophila* retina during a developmentally regulated DNA damage response. *EMBO J.* **22**, 5622–5632 (2003). doi: 10.1093/emboj/cdg543; pmid: 14532134
29. X. Luo, O. Puig, J. Hyun, D. Bohmann, H. Jasper, Foxo and Fos regulate the decision between cell death and survival in response to UV irradiation. *EMBO J.* **26**, 380–390 (2007). doi: 10.1038/sj.emboj.7601484; pmid: 17183370
30. P. Petrova *et al*., MANF: A new mesencephalic, astrocyte-derived neurotrophic factor with selectivity for dopaminergic neurons. *J. Mol. Neurosci.* **20**, 173–188 (2003). doi: 10.1385/JMN:20:2:173; pmid: 12794311
31. M. Palgi *et al*., Evidence that DmMANF is an invertebrate neurotrophic factor supporting dopaminergic neurons. *Proc. Natl. Acad. Sci. U.S.A.* **106**, 2429–2434 (2009). doi: 10.1073/pnas.0810996106; pmid: 19164766
32. P. Lindholm, M. Saarma, Novel CDNF/MANF family of neurotrophic factors. *Dev. Neurobiol.* **70**, 360–371 (2010). pmid: 20186704
33. S. A. Sinenko, B. Mathey-Prevot, Increased expression of *Drosophila* tetraspanin, Tsp68C, suppresses the abnormal proliferation of ytr-deficient and Ras/Raf-activated hemocytes.

Oncogene **23**, 9120–9128 (2004). doi: 10.1038/sj.onc.1208156; pmid: 15480416
34. M. Freeman, Reiterative use of the EGF receptor triggers differentiation of all cell types in the *Drosophila* eye. *Cell* **87**, 651–660 (1996). doi: 10.1016/S0092-8674(00)81385-9; pmid: 8929534
35. Z. Song *et al*., Biochemical and genetic interactions between *Drosophila* caspases and the proapoptotic genes *rpr*, *hid*, and *grim*. *Mol. Cell. Biol.* **20**, 2907–2914 (2000). doi: 10.1128/MCB.20.8.2907-2914.2000; pmid: 10733594
36. M. J. Kang, H. D. Ryoo, Suppression of retinal degeneration in *Drosophila* by stimulation of ER-associated degradation. *Proc. Natl. Acad. Sci. U.S.A.* **106**, 17043–17048 (2009). doi: 10.1073/pnas.0905566106; pmid: 19805114
37. C. J. Zettervall *et al*., A directed screen for genes involved in *Drosophila* blood cell activation. *Proc. Natl. Acad. Sci. U.S.A.* **101**, 14192–14197 (2004). doi: 10.1073/pnas.0403789101; pmid: 15381778
38. R. Márkus, E. Kurucz, F. Rus, I. Andó, Sterile wounding is a minimal and sufficient trigger for a cellular immune response in *Drosophila melanogaster*. *Immunol. Lett.* **101**, 108–111 (2005). doi: 10.1016/j.imlet.2005.03.021; pmid: 15964636
39. M. L. Samson, *Drosophila* arginase is produced from a nonvital gene that contains the *elav* locus within its third intron. *J. Biol. Chem.* **275**, 31107–31114 (2000). doi: 10.1074/jbc.M001346200; pmid: 10878001
40. M. J. Henderson, C. T. Richie, M. Airavaara, Y. Wang, B. K. Harvey, Mesencephalic astrocyte-derived neurotrophic factor (MANF) secretion and cell surface binding are modulated by KDEL receptors. *J. Biol. Chem.* **288**, 4209–4225 (2013). doi: 10.1074/jbc.M112.400648; pmid: 23255601
41. E. W. Abrams, Y. L. Cheng, D. J. Andrew, *Drosophila* KDEL receptor function in the embryonic salivary gland and epidermis. *PLOS ONE* **8**, e77618 (2013). doi: 10.1371/journal.pone.0077618; pmid: 24204897
42. A. Wenzel, C. E. Reme, T. P. Williams, F. Hafezi, C. Grimm, The Rpe65 Leu450Met variation increases retinal resistance against light-induced degeneration by slowing rhodopsin regeneration. *J. Neurosci.* **21**, 53–58 (2001). pmid: 11150319
43. T. I. Heino *et al*., The *Drosophila* VEGF receptor homolog is expressed in hemocytes. *Mech. Dev.* **109**, 69–77 (2001). doi: 10.1016/S0925-4773(01)00510-X; pmid: 11677054
44. P. Duchek, K. Somogyi, G. Jékely, S. Beccari, P. Rørth, Guidance of cell migration by the *Drosophila* PDGF/VEGF receptor. *Cell* **107**, 17–26 (2001). doi: 10.1016/S0092-8674(01)00502-5; pmid: 11595182
45. S. Dziennis *et al*., The CD11b promoter directs high-level expression of reporter genes in macrophages in transgenic mice. *Blood* **85**, 319–329 (1995). pmid: 7811988
46. T. Springer, G. Galfré, D. S. Secher, C. Milstein, Mac-1: A macrophage differentiation antigen identified by monoclonal antibody. *Eur. J. Immunol.* **9**, 301–306 (1979). doi: 10.1002/eji.1830090410; pmid: 89034
47. Z. Tang *et al*., Survival effect of PDGF-CC rescues neurons from apoptosis in both brain and retina by regulating GSK3β phosphorylation. *J. Exp. Med.* **207**, 867–880 (2010). doi: 10.1084/jem.20091704; pmid: 20231377
48. M. Lindahl *et al*., MANF is indispensable for the proliferation and survival of pancreatic β cells. *Cell Reports* **7**, 366–375 (2014). doi: 10.1016/j.celrep.2014.03.023; pmid: 24726366
49. C. Zhang *et al*., Activation of microglia and chemokines in light-induced retinal degeneration. *Mol. Vis.* **11**, 887–895 (2005). pmid: 16270028
50. J. Won *et al*., Mouse model resources for vision research. *J. Ophthalmol.* **2011**, 391384 (2011). doi: 10.1155/2011/391384; pmid: 21052544
51. C. Keeler, Retinal degeneration in the mouse is rodless retina. *J. Hered.* **57**, 47–50 (1966). pmid: 5916892
52. S. J. Pittler, C. E. Keeler, R. L. Sidman, W. Baehr, PCR analysis of DNA from 70-year-old sections of rodless retina demonstrates identity with the mouse rd defect. *Proc. Natl. Acad. Sci. U.S.A.* **90**, 9616–9619 (1993). doi: 10.1073/pnas.90.20.9616; pmid: 8415750
53. T. M. Doherty, R. Kastelein, S. Menon, S. Andrade, R. L. Coffman, Modulation of murine macrophage function by IL-13. *J. Immunol.* **151**, 7151–7160 (1993). pmid: 7903102
54. W. C. Raschke, S. Baird, P. Ralph, I. Nakoinz, Functional macrophage cell lines transformed by Abelson leukemia virus. *Cell* **15**, 261–267 (1978). doi: 10.1016/0092-8674(78)90101-0; pmid: 212198
55. J. F. Cailhier *et al*., Conditional macrophage ablation demonstrates that resident macrophages initiate acute peritoneal inflammation. *J. Immunol.* **174**, 2336–2342 (2005). doi: 10.4049/jimmunol.174.4.2336; pmid: 15699170
56. M. Ueno *et al*., Layer V cortical neurons require microglial support for survival during postnatal development. *Nat. Neurosci.* **16**, 543–551 (2013). doi: 10.1038/nn.3358; pmid: 23525041
57. C. N. Parkhurst *et al*., Microglia promote learning-dependent synapse formation through brain-derived neurotrophic factor. *Cell* **155**, 1596–1609 (2013). doi: 10.1016/j.cell.2013.11.030; pmid: 24360280
58. S. Jung *et al*., Analysis of fractalkine receptor CX_3CR1 function by targeted deletion and green fluorescent protein reporter gene insertion. *Mol. Cell. Biol.* **20**, 4106–4114 (2000). doi: 10.1128/MCB.20.11.4106-4114.2000; pmid: 10805752
59. M. Chen, C. Luo, R. Penalva, H. Xu, Paraquat-induced retinal degeneration is exaggerated in CX3CR1-deficient mice and is associated with increased retinal inflammation. *Invest. Ophthalmol. Vis. Sci.* **54**, 682–690 (2013). doi: 10.1167/iovs.12-10888; pmid: 23299473
60. R. E. MacLaren *et al*., Retinal repair by transplantation of photoreceptor precursors. *Nature* **444**, 203–207 (2006). doi: 10.1038/nature05161; pmid: 17093405
61. D. A. Lamba, J. Gust, T. A. Reh, Transplantation of human embryonic stem cell-derived photoreceptors restores some visual function in Crx-deficient mice. *Cell Stem Cell* **4**, 73–79 (2009). doi: 10.1016/j.stem.2008.10.015; pmid: 19128794
62. A. C. Barber *et al*., Repair of the degenerate retina by photoreceptor transplantation. *Proc. Natl. Acad. Sci. U.S.A.* **110**, 354–359 (2013). doi: 10.1073/pnas.1212677110; pmid: 23248312
63. E. L. West *et al*., Long-term survival of photoreceptors transplanted into the adult murine neural retina requires immune modulation. *Stem Cells* **28**, 1997–2007 (2010). doi: 10.1002/stem.520; pmid: 20857496
64. J. Gust, T. A. Reh, Adult donor rod photoreceptors integrate into the mature mouse retina. *Invest. Ophthalmol. Vis. Sci.* **52**, 5266–5272 (2011). doi: 10.1167/iovs.10-6329; pmid: 21436277
65. Z. Kokaia, G. Martino, M. Schwartz, O. Lindvall, Cross-talk between neural stem cells and immune cells: The key to better brain repair? *Nat. Neurosci.* **15**, 1078–1087 (2012). doi: 10.1038/nn.3163; pmid: 22837038
66. T. Kurimoto *et al*., Neutrophils express oncomodulin and promote optic nerve regeneration. *J. Neurosci.* **33**, 14816–14824 (2013). doi: 10.1523/JNEUROSCI.5511-12.2013; pmid: 24027282
67. V. E. Miron *et al*., M2 microglia and macrophages drive oligodendrocyte differentiation during CNS remyelination. *Nat. Neurosci.* **16**, 1211–1218 (2013). doi: 10.1038/nn.3469; pmid: 23872599
68. R. Shechter *et al*., Infiltrating blood-derived macrophages are vital cells playing an anti-inflammatory role in recovery from spinal cord injury in mice. *PLOS Med.* **6**, e1000113 (2009). pmid: 19636355
69. A. London *et al*., Neuroprotection and progenitor cell renewal in the injured adult murine retina requires healing monocyte-derived macrophages. *J. Exp. Med.* **208**, 23–39 (2011). pmid: 21220455
70. P. Lindholm *et al*., Novel neurotrophic factor CDNF protects and rescues midbrain dopamine neurons in vivo. *Nature* **448**, 73–77 (2007). pmid: 17611540
71. M. H. Voutilainen *et al*., Mesencephalic astrocyte-derived neurotrophic factor is neurorestorative in rat model of Parkinson's disease. *J. Neurosci.* **29**, 9651–9659 (2009). doi: 10.1523/JNEUROSCI.0833-09.2009; pmid: 19641128
72. P. Lindholm *et al*., MANF is widely expressed in mammalian tissues and differently regulated after ischemic and epileptic insults in rodent brain. *Mol. Cell. Neurosci.* **39**, 356–371 (2008). doi: 10.1016/j.mcn.2008.07.016; pmid: 18718866
73. S. Yang, S. Huang, M. A. Gaertig, X. J. Li, S. Li, Age-dependent decrease in chaperone activity impairs MANF expression, leading to Purkinje cell degeneration in inducible SCA17 mice. *Neuron* **81**, 349–365 (2014). doi: 10.1016/j.neuron.2013.12.002; pmid: 24462098
74. L. Chen *et al*., Mesencephalic astrocyte-derived neurotrophic factor is involved in inflammation by negatively regulating the NF-κB pathway. *Sci. Rep.* **5**, 8133 (2015). doi: 10.1038/srep08133; pmid: 25640174
75. V. Stratoulias, T. I. Heino, MANF silencing, immunity induction or autophagy trigger an unusual cell type in metamorphosing *Drosophila* brain. *Cell. Mol. Life Sci.* **72**, 1989–2004 (2015). doi: 10.1007/s00018-014-1789-7; pmid: 25511196
76. E. C. Hirsch, S. Hunot, Neuroinflammation in Parkinson's disease: A target for neuroprotection? *Lancet Neurol.* **8**, 382–397 (2009). doi: 10.1016/S1474-4422(09)70062-6; pmid: 19296921
77. R. Nadella *et al*., Transient transfection of human CDNF gene reduces the 6-hydroxydopamine-induced neuroinflammation in the rat substantia nigra. *J. Neuroinflammation* **11**, 209 (2014). doi: 10.1186/s12974-014-0209-0; pmid: 25511018
78. H. Zhao *et al*., Transplantation of cerebral dopamine neurotrophic factor transducted BMSCs in contusion spinal cord injury of rats: Promotion of nerve regeneration by alleviating neuroinflammation. *Mol. Neurobiol.* **53**, 187–199 (2016). pmid: 25421210

ACKNOWLEDGMENTS

We acknowledge Amarantus Biosciences Inc. for kindly supplying the hrMANF protein used in these studies. Work in H.J.'s laboratory is supported by NIH grant EY018177, and some of the fly work was supported by Amarantus Biosciences Inc. Work in D.A.L.'s laboratory is supported by NIH grant EY025779 and the Foundation for Retinal Research. J.N. is supported by the Glenn Foundation for Medical Research. The full RNA-seq data set is provided as supplementary materials. J.N., H.J., and D.A.L. are the inventors and the Buck Institute for Research on Aging is the applicant for an international patent application for the use of MANF as an enhancer of cell replacement therapies.

SUPPLEMENTARY MATERIALS

www.sciencemag.org/content/353/6294/aaf3646/suppl/DC1
Materials and Methods
Figs. S1 to S9
Tables S1 to S5
References (*79*–*82*)

29 January 2016; resubmitted 1 April 2016
Accepted 18 May 2016
10.1126/science.aaf3646

RESEARCH ARTICLE SUMMARY

CENTROSOMES

A mechanism for the elimination of the female gamete centrosome in *Drosophila melanogaster*

A. Pimenta-Marques,*† I. Bento,*† C. A. M. Lopes, P. Duarte, S. C. Jana, M. Bettencourt-Dias†

INTRODUCTION: Centrioles are small microtubule-based cellular structures that are critical for cilia and centrosome assembly. During successful fertilization in animals, centrioles are asymmetrically inherited. Centrioles are eliminated from the egg and contributed by the sperm. Paternal centrioles organize the first zygote centrosome, the major microtubule-organizing center that ensures proper mitotic progression and successful embryo development. Centriole elimination from the oocyte during development is thought to ensure correct centriole number and proper mitosis upon fertilization, and to prevent parthenogenesis (i.e., embryonic development without fertilization).

RATIONALE: Centrioles are thought to be exceptionally stable structures, so their disappearance in oogenesis is paradoxical and the elimination mechanism remains elusive. In addition, the consequences of retaining maternal centrioles for oogenesis progression, meiosis, and reproduction are unclear. Here, we used *Drosophila melanogaster* oogenesis to identify the molecular mechanisms underlying centriole elimination and the consequences of preventing it.

RESULTS: To investigate the mechanism of centriole elimination, we first looked into the timing and order of disappearance of multiple centrosome components. Each centrosome is composed of two centrioles and a surrounding pericentriolar matrix (PCM) that is important for microtubule nucleation. *Drosophila* oocytes inherit all centrosomes from their neighboring nurse cells, which form a large microtubule-organizing center. We analyzed multiple markers along oogenesis process and found that centrosome elimination occurs in a stepwise manner: First, centrosomes lost PCM components, whereas centriole components only disappeared in the last stages of oogenesis before meiotic division. Because Polo kinase is the major PCM recruitment factor, we then investigated the regulation of this protein in the oocyte microtubule-organizing center. Polo was down-regulated in similar stages, as were the PCM components. We thus hypothesized that Polo is important for PCM maintenance and that the PCM protects centrioles from elimination. To confirm this prediction, we depleted either Polo or the PCM, or both together, in *Drosophila* cultured cells arrested in S phase (where centriole content is maintained constant). In all cases, we observed centriole loss. Moreover, depletion of Polo in oogenesis induced premature centriole elimination.

ON OUR WEBSITE

Read the full article at http://dx.doi.org/10.1126/science.aaf4866

To test the hypothesis that Polo and the PCM are critical for centriole maintenance, we ectopically expressed a Polo kinase that localizes to the oocyte's centrioles. Expression of this protein prevented PCM loss and maintained functional centrioles even during meiotic division, when normally they would all have been eliminated, supporting our hypothesis. Finally, we investigated the consequences of maintaining centrioles in the female germ line. Retained centrioles nucleated microtubules that interfered with meiotic divisions. Despite this, centriole-containing oocytes were fertilized but could only undergo very few divisions, arresting very early in development.

CONCLUSIONS: Our study revealed that centriole stability is not an intrinsic property of those structures, as previously thought, but requires a Polo kinase– and PCM-dependent maintenance program. By artificially maintaining this program, we retained maternal centrosomes through oogenesis, which led to defective meiosis and aborted early embryonic development. We propose that regulation of this centriole maintenance program is essential for successful sexual reproduction and is likely to define centriole life span in different tissues, thereby shaping the cytoskeleton. ■

Drosophila oogenesis

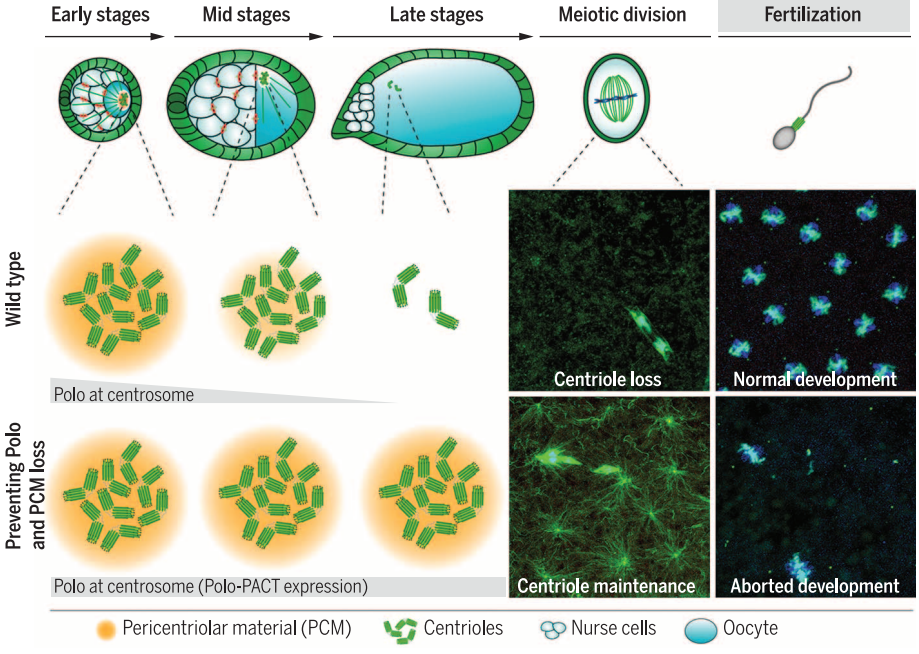

Down-regulation of a Polo- and PCM-dependent centriole maintenance program leads to centriole elimination in oogenesis and successful embryonic development. In early oogenesis stages, centrioles from nurse cells migrate to the oocyte, forming a large microtubule organizing center. Polo and the pericentriolar matrix (PCM) that surrounds centrioles are lost from the centrioles in middle and late stages, leading to centriole elimination before meiotic division. By anchoring Polo (and consequently PCM) to the oocyte centrioles, centrioles are maintained throughout oogenesis, leading to abnormal meiotic and mitotic divisions and consequently failed zygotic development.

The list of author affiliations is available in the full article online.
*These authors contributed equally to this work.
†Corresponding author. Email: mdias@igc.gulbenkian.pt (M.B.-D.); armarques@igc.gulbenkian.pt (A.P.-M.); inesbento@hotmail.com (I.B.)
Cite this article as A. Pimenta-Marques *et al.*, *Science* 353, aaf4866 (2016). DOI: 10.1126/science.aaf4866

RESEARCH ARTICLE

CENTROSOMES

A mechanism for the elimination of the female gamete centrosome in *Drosophila melanogaster*

A. Pimenta-Marques,*† I. Bento,*†‡ C. A. M. Lopes, P. Duarte, S. C. Jana, M. Bettencourt-Dias†

An important feature of fertilization is the asymmetric inheritance of centrioles. In most species it is the sperm that contributes the initial centriole, which builds the first centrosome that is essential for early development. However, given that centrioles are thought to be exceptionally stable structures, the mechanism behind centriole disappearance in the female germ line remains elusive and paradoxical. We elucidated a program for centriole maintenance in fruit flies, led by Polo kinase and the pericentriolar matrix (PCM): The PCM is down-regulated in the female germ line during oogenesis, which results in centriole loss. Perturbing this program prevents centriole loss, leading to abnormal meiotic and mitotic divisions, and thus to female sterility. This mechanism challenges the view that centrioles are intrinsically stable structures and reveals general functions for Polo kinase and the PCM in centriole maintenance. We propose that regulation of this maintenance program is essential for successful sexual reproduction and defines centriole life span in different tissues in homeostasis and disease, thereby shaping the cytoskeleton.

Some organelles are asymmetrically inherited upon fertilization. For example, mitochondria are provided maternally, whereas the paternal sperm mitochondrion is actively degraded (*1*). Centrosomes, the major microtubule-organizing centers (MTOCs) in animal cells, are composed of two very stable microtubule (MT) cylinders, the centrioles, and a pericentriolar matrix (PCM). The PCM is indispensable for centriole biogenesis and the centrosome function of nucleating and anchoring MTs (*2*). The number of centrioles, and consequently the number of centrosomes, is tightly controlled in actively dividing cells: Centriole duplication is coupled to DNA replication, so that in mitosis there is one centrosome with two centrioles at each pole of the mitotic spindle, ensuring faithful chromosome segregation. Surprisingly, centrioles are eliminated in the oocytes of most metazoan species, and the embryo relies on the centriole provided by the sperm, which subsequently duplicates and forms two centrosomes supporting successful mitotic divisions (*3*–*6*). Centriole elimination in the egg is commonly regarded as a strategy to ensure correct centriole number upon fertilization, preventing abnormal first embryonic mitosis. Moreover, it is also thought to prevent parthenogenesis, because the microinjection of centrioles in frog eggs induces successful embryonic development without fertilization (*7*).

Two different timings and strategies for centriole elimination occur in the female germ line of different animals. In mollusks and echinoderms, centrosomes with centrioles are present in meiosis; in starfish, most centrioles are eliminated by extrusion in the polar bodies (*4*, *8*). By contrast, in fruit flies, worms, and humans, centrioles are eliminated before meiotic division, representing one of the few acentriolar divisions in those species (*3*, *4*, *6*, *9*). Even though centriole elimination before meiotic division is such a widespread event, little is known concerning the molecular mechanism governing this process. Additionally, the real consequences of retaining centrioles with respect to oogenesis progression, meiosis, and reproduction are still unclear. Here, we used *Drosophila melanogaster* oogenesis to identify the molecular mechanisms of centriole elimination and the consequences of preventing it.

Centrioles are eliminated in late oogenesis

Huettner first pointed out in 1933 (*10*) the acentriolar nature of *Drosophila* female meiotic division, intensifying the discussion among cell biology pioneers on centriole inheritance—a problem he considered "very intricate and perplexing." Almost half a century later, Mahowald (*11*) beautifully showed by electron microscopy (EM) the complex behavior of centrioles during *Drosophila* oogenesis. Oogenesis begins with the asymmetric division of a stem cell to give rise to a new stem cell and a cystoblast, which undergoes four successive mitotic cycles with incomplete cytokinesis, forming a large cyst composed of 16 interconnected cells (Fig. 1A). Mahowald (*11*) detected up to 25 identifiable mature centrioles and additional procentrioles in the entire cyst. Those results suggest that centriole duplication occurs in the 16-cell cyst, predicting a total count of 64 centrioles and procentrioles in one cyst. One of the 16 cells becomes the oocyte, while the others are called nurse cells (Fig. 1A). Early in oogenesis, most centrioles from each of the 15 nurse cells migrate to the oocyte and cluster, forming a very large MTOC that organizes the microtubule cytoskeleton from stages 2 to 6 (*11*) (Fig. 1A), and can be detected up until stage 9 by EM (*12*).

To investigate when centrioles are eliminated, we initially divided oogenesis into three easily recognizable stages: early [germarium (G) to stage 6], mid (stages 7 and 8, when the oocyte is repolarized), and late (stages 9 to 12) (Fig. 1A). We first examined the oocyte for the presence of a conserved centriole-specific protein, ANA1, expressed under the control of its endogenous promoter and fused to tdTomato (*13*) (Fig. 1, B and C). We observed centrioles at the beginning of late stages (stage 9), confirming previous studies (*12*, *14*). However, we were surprised to detect centrioles later than that, in all oocytes from stage 9 to 12 (Fig. 1, C and E). In accordance with published EM studies, in early stages, we observed centrioles clustered at the posterior end of the oocyte between the nucleus and the follicular cell border, mostly as a single, uniform, very large structure (*11*). In late stages, ANA1 was present in either one or very few discrete large dots in the nucleus vicinity (Fig. 1C), suggesting that centrioles were also clustered.

We next investigated the presence of centrioles upon nuclear envelope breakdown at the spindle of meiosis I (stage 14). Confirming Huettner's light microscopy pioneering studies (*10*), we were unable to detect centrioles at the poles of the spindle (Fig. 1F). Thus, centrioles are present until later stages than previously described (*12*), but they disappear just before meiotic spindle assembly.

Centrosome disassembly is a stepwise process: PCM first, centrioles last

We reasoned that centrosome elimination could occur in different ways: (i) abruptly, with all the structure being lost simultaneously, or (ii) with different components of the centrosome disappearing at different time points throughout oogenesis. To answer this question, we investigated the presence of several centrosome components—the centriole and PCM constituents (Fig. 1B)—during passage through oogenesis. We first tested the centriolar components SAS6 and BLD10/CEP135 (Fig. 1B), which are part of the cartwheel, a hallmark structure of the centriole that helps to define its nine-fold symmetry (*2*). Although the presence of SAS6 until late stages corroborated the ANA1 observations, we found a decrease in the number of oocytes containing BLD10, which suggests that centrioles start to lose components at those stages (Fig. 1, D and E, and fig. S1A). We then checked the presence of different PCM constituents (Fig. 1B):

Instituto Gulbenkian de Ciência, Rua da Quinta Grande, 2780-156 Oeiras, Portugal.
*These authors contributed equally to this work. **†Corresponding author. Email: mdias@igc.gulbenkian.pt (M.B.-D.); armarques@igc.gulbenkian.pt (A.P.-M.); inesbento@hotmail.com (I.B.)**
‡Present address: Instituto de Medicina Molecular, Avenida Professor Egas Moniz, 1649-028 Lisboa, Portugal.

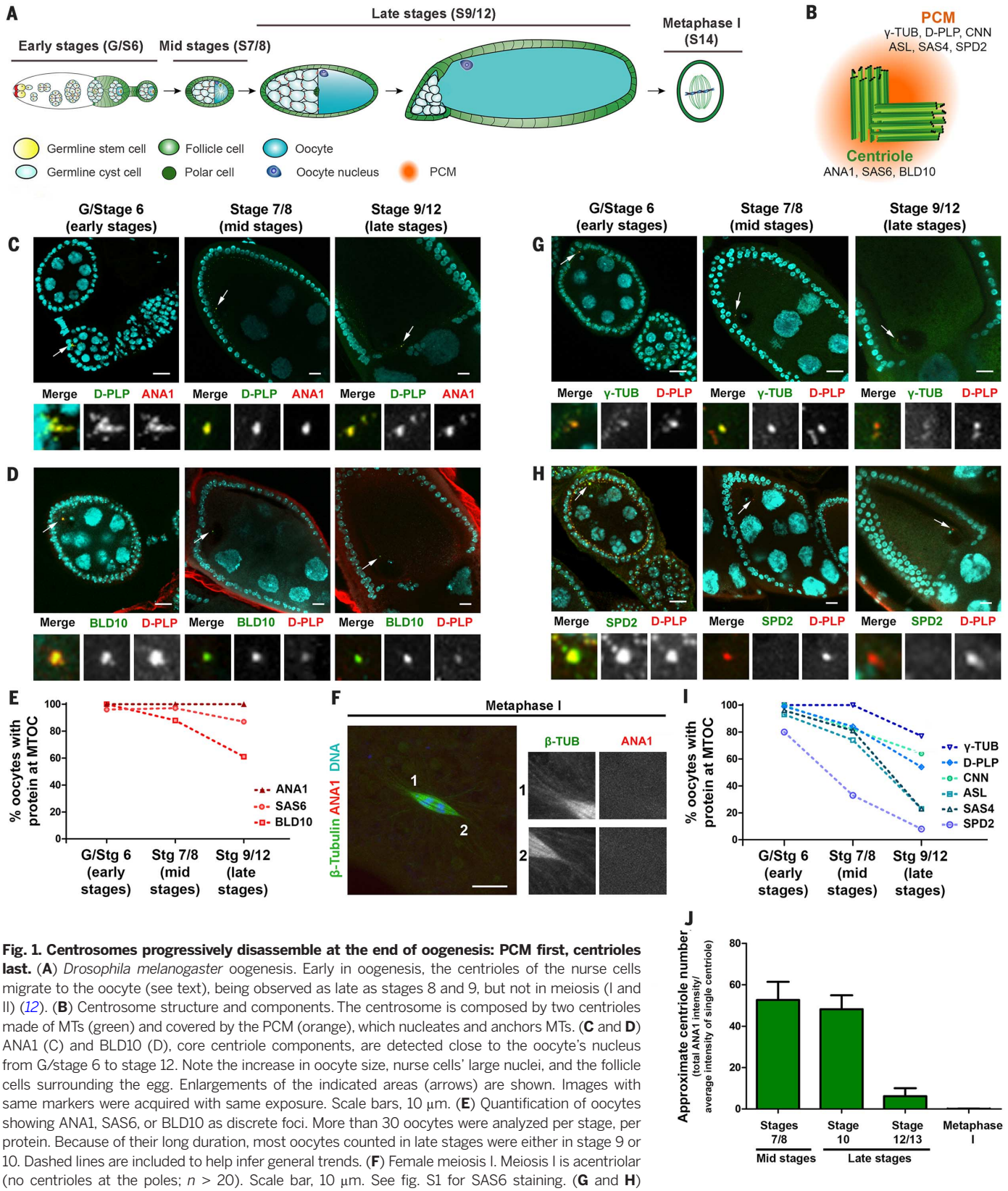

Fig. 1. Centrosomes progressively disassemble at the end of oogenesis: PCM first, centrioles last. (**A**) *Drosophila melanogaster* oogenesis. Early in oogenesis, the centrioles of the nurse cells migrate to the oocyte (see text), being observed as late as stages 8 and 9, but not in meiosis (I and II) (*12*). (**B**) Centrosome structure and components. The centrosome is composed by two centrioles made of MTs (green) and covered by the PCM (orange), which nucleates and anchors MTs. (**C** and **D**) ANA1 (C) and BLD10 (D), core centriole components, are detected close to the oocyte's nucleus from G/stage 6 to stage 12. Note the increase in oocyte size, nurse cells' large nuclei, and the follicle cells surrounding the egg. Enlargements of the indicated areas (arrows) are shown. Images with same markers were acquired with same exposure. Scale bars, 10 μm. (**E**) Quantification of oocytes showing ANA1, SAS6, or BLD10 as discrete foci. More than 30 oocytes were analyzed per stage, per protein. Because of their long duration, most oocytes counted in late stages were either in stage 9 or 10. Dashed lines are included to help infer general trends. (**F**) Female meiosis I. Meiosis I is acentriolar (no centrioles at the poles; $n > 20$). Scale bar, 10 μm. See fig. S1 for SAS6 staining. (**G** and **H**) Localization of γ-tubulin (γ-TUB) (G) and SPD2 (H), PCM markers, in the oocyte. Note decrease of PCM intensity and size. Scale bars, 10 μm. (**I**) Quantification of the oocytes positive for PCM components: γ-TUB, D-PLP, CNN, ASL, SAS4, and SPD2. Note that the presence of PCM proteins decreases in mid-stage oocytes. More than 30 oocytes were analyzed per stage, per protein. See fig. S1 for SAS4, ASL, and CNN staining. (**J**) Estimate of total centriole number in the oocyte. Until stage 10, centrioles are found in very tight clusters. To estimate centriole numbers, we divided total intensity of ANA1 at each stage by the average intensity of single centrioles encountered in early stages in nurse cells. GFP-PACT was used as a centriole marker, ensuring colocalization. Total $n \geq 20$, mean ± SEM (*16*).

(i) γ-tubulin, which is very important for microtubule nucleation; (ii) PCM components that recruit γ-tubulin (D-PLP/pericentrin, CNN/CDK5RAP2, SPD2/CEP192) (*14*–*18*), and (iii) peripheral centriole components that recruit the PCM (SAS4/CPAP and ASL/CEP152) (*19*, *20*). In early stages, all PCM components were present at the centrosomes (Fig. 1, G to I, and fig. S1, B to D). However, unlike centriolar components, in mid stages some PCM components started to disappear and their loss was aggravated in later stages, with SPD2 loss being particularly evident (only 33% of the oocytes had SPD2 in mid stages and 8% in late stages; Fig. 1, H and I). γ-Tubulin, which can be recruited by several PCM components (*21*), was the most stable PCM constituent (77% of late-stage oocytes were positive; Fig. 1, G and I). Thus, in this system the PCM disappears before centrioles.

We then characterized in more detail the mid and late stages of this process, when the centrosome starts losing some of its components. Because centrioles are very small structures and are densely packed at the late stages of oogenesis, we quantified the total signal for what we observed to be the most stable centriole marker, ANA1 (Fig. 1E), as a proxy for total centriole mass (Fig. 1J). We observed similar total intensities of ANA1-tdTomato per oocyte in mid stages and at the beginning of late stages (stage 10); these intensities were greater than those of single centrioles encountered in very early stages by a factor of about 50 (Fig. 1J). Our experimental approximations to centriole number support the initial calculations and assumptions, based on Mahowald's studies, that most centrioles from the 16 cells duplicate in the germarium and migrate to the oocyte [64 expected centrioles (*11*)]. The similarity in intensity found in mid stages and stage 10 suggests that little centriole breakdown occurs at that time in oogenesis. In contrast, in stages 12 and 13, the intensity of ANA1 was much lower, similar to the intensity of six "early" centrioles (Fig. 1J). Finally, when we investigated stage 14 (meiotic division; Fig. 1, F and J), we observed only 2 of 20 eggs showing one or two cortex-localized, non–MT-nucleating centrioles (fig. S1E), supporting nearly complete centriole elimination at that stage. Thus, the centrosome does not disassemble abruptly; it starts losing several PCM components in mid stages, followed by the loss of centriolar components in late stages (steeper between stages 10 and 12) and leading to complete centriole loss at meiotic division (stage 14).

Loss of PCM leads to centriole elimination in *Drosophila* somatic cells

Our data suggest that centriole elimination could be a consequence of PCM loss. Although little is known about the regulation of the PCM in stable interphasic centrosomes, most interphase centrioles are coated by at least one PCM component in all organisms (*22*), which might contribute to their stability. *Tetrahymena* centrioles (called basal bodies) are unstable upon depletion of γ-tubulin (*23*), further suggesting a role for the PCM in centriole stability. Although a role for the PCM in centriole biogenesis has been acknowledged (*2*), we hypothesized that the PCM also has an important function in centriole maintenance. To test this hypothesis, we developed a "centriole stability assay" in *Drosophila* cultured cells. This assay allowed us to simultaneously (i) deplete several PCM components, circumventing the absence of phenotypes resulting from their known redundant roles, and (ii) uncouple centrosome maintenance from centrosome biogenesis. We thus arrested *Drosophila* tissue culture cells (DMEL) in S phase (fig. S2A) to halt the centriole biogenesis cycle after centriole duplication (*20*). In interphase, *Drosophila* centrioles are coated by a thin PCM layer composed of components such as ASL, D-PLP, and SPD2, and additionally by CNN in G_2 phase (*24*). We asked whether centrioles were destabilized upon depletion of *ASL*, *D-PLP*, *SPD2*, and *CNN* individually or together ("*All PCM*") for 4 days (fig. S2, A to E). We observed a significant decrease in centriole number (i.e., a higher percentage of cells with 0 or 1 centrioles) when *All PCM* was depleted, rather than individual depletion of different PCM components (fig. S2C). Thus, the PCM is required for centriole stability in somatic cells, and PCM components are redundant in that role.

Loss of Polo from the oocyte centrosome co-occurs with PCM loss

Our results strongly suggest that centriole elimination results from PCM loss. Upon mitotic entry, Polo-like kinase 1 (called PLK1 in most species, Polo in *Drosophila*) is a major regulator of PCM recruitment to the centriole (*25*, *26*). Polo and its orthologs directly phosphorylate several core scaffold PCM proteins in different organisms, including pericentrin (PLP), SPD2, and CNN, contributing toward γ-tubulin accumulation on centrosomes as well as PCM assembly and expansion (*16*, *21*, *27*–*31*). PLK1 also plays a role in PCM maintenance (*31*, *32*).

In *Drosophila* oogenesis, Polo is required at early stages to restrict meiosis to the oocyte (*33*), and later (in stage 14) to trigger nuclear envelope breakdown (*34*). Polo was shown recently to be transcriptionally down-regulated in the oocyte in between those stages (*35*), and so it is possible that lack of Polo on centrosomes leads to PCM disappearance and centriole loss. We thus examined Polo's subcellular localization in those stages. Although 89% of early-stage oocytes (stages 2 to 6) showed the presence of Polo at the centrioles (Fig. 2, A and B), its centriolar localization decreased markedly during mid and late stages of oogenesis (Fig. 2, A and B), which coincides with our observations on PCM loss (Fig. 1I). Indeed, most centrioles disappeared from the oocyte between stage 10 and stage 12/13 (see Fig. 1J), when Polo is absent from the MTOC. Thus, Polo loss from the oocyte's centrosome could be a critical event in triggering loss of the PCM, followed by centriole elimination.

Down-regulating Polo accelerates centriole loss

We next tested whether Polo could have a role in centriole maintenance. Polo mutants have a strong loss-of-function phenotype early in oogenesis (*33*), precluding an analysis of the effect of its loss of function in centriole maintenance. We thus used RNA interference (RNAi) to down-regulate Polo only after oocyte determination, when Polo is naturally still present. RNAi depletion led to loss of Polo protein (fig. S3A) and to female sterility, as reported previously for mutants of *Polo* (*36*). We analyzed centriole maintenance by investigating the levels of two centriole markers, ANA1-tdtomato and PACT-GFP [the centriole-targeting domain of pericentrin (*14*, *30*, *37*, *38*) fused to green fluorescent protein]. We focused on stage 10, when normally centrioles are still present (Fig. 1J). Levels of both markers were significantly reduced upon *Polo* down-regulation, in contrast to a *mCherry* control, strongly suggesting the presence of fewer centrioles and thus the acceleration of centriole loss (Fig. 2, C and D). We observed very similar results in tissue culture cells upon down-regulation of *Polo* in the centriole stability assay (Fig. 3, A to C, and fig. S3, B and C). As readouts, we used a centriole marker, BLD10; a centriole and PCM marker, SAS4; and a PCM marker, D-PLP (Fig. 3, B and C). *Polo* depletion alone had an effect on PCM depletion, similar to its effect on centriole loss (Fig. 3, B and C). Furthermore, co-depletion of *Polo* and *All PCM* led to a similar phenotype to that obtained with depletion of *All PCM* alone, which suggests that Polo and the PCM work on the same pathway to maintain centrioles (Fig. 3, B and C).

Ectopic tethering of Polo to centrioles prevents PCM loss

To further test the role of Polo at the centrosome for PCM and centriole maintenance, we asked whether overexpression of this kinase (Polo-Myc) throughout oogenesis (starting at stage 3/4), could overcome centriole loss. However, despite an increase in total Polo levels (fig. S4A), Polo did not localize to most oocyte centrioles in late stages (fig. S4C) and induced only a modest increase in the percentage of late oocytes showing γ-tubulin on centrioles (fig. S4B). Because Polo is a very dynamic protein, localizing to different subcellular structures at different cell cycle stages (*26*), we reasoned that overexpression of Polo might not be sufficient to force its concentration to the centrioles and thus to retain the PCM there.

We took advantage of an approach to force Polo to the oocyte's centrioles. Several molecules, including the ortholog of Polo, PLK1, have been artificially tethered to the centriole by fusion to pericentrin or its centriole-targeting domain, PACT (*14*, *30*, *37*, *38*). We thus targeted Polo to the centriole in *Drosophila* by fusing GFP-Polo to PACT. This strategy previously led to higher accumulation of PCM in interphase centrioles in human cultured cells (*30*), and we observed the same phenotype (fig. S4D). We thus induced GFP-Polo-PACT expression in oogenesis. GFP-Polo-PACT and GFP-PACT (control) always localized to the oocyte's centrioles from stages 2 to 12 (GFP signal always colocalized with ANA1-tdTomato; Fig. 4A). We then asked whether the constant presence of Polo at the centrioles could prevent PCM loss. We

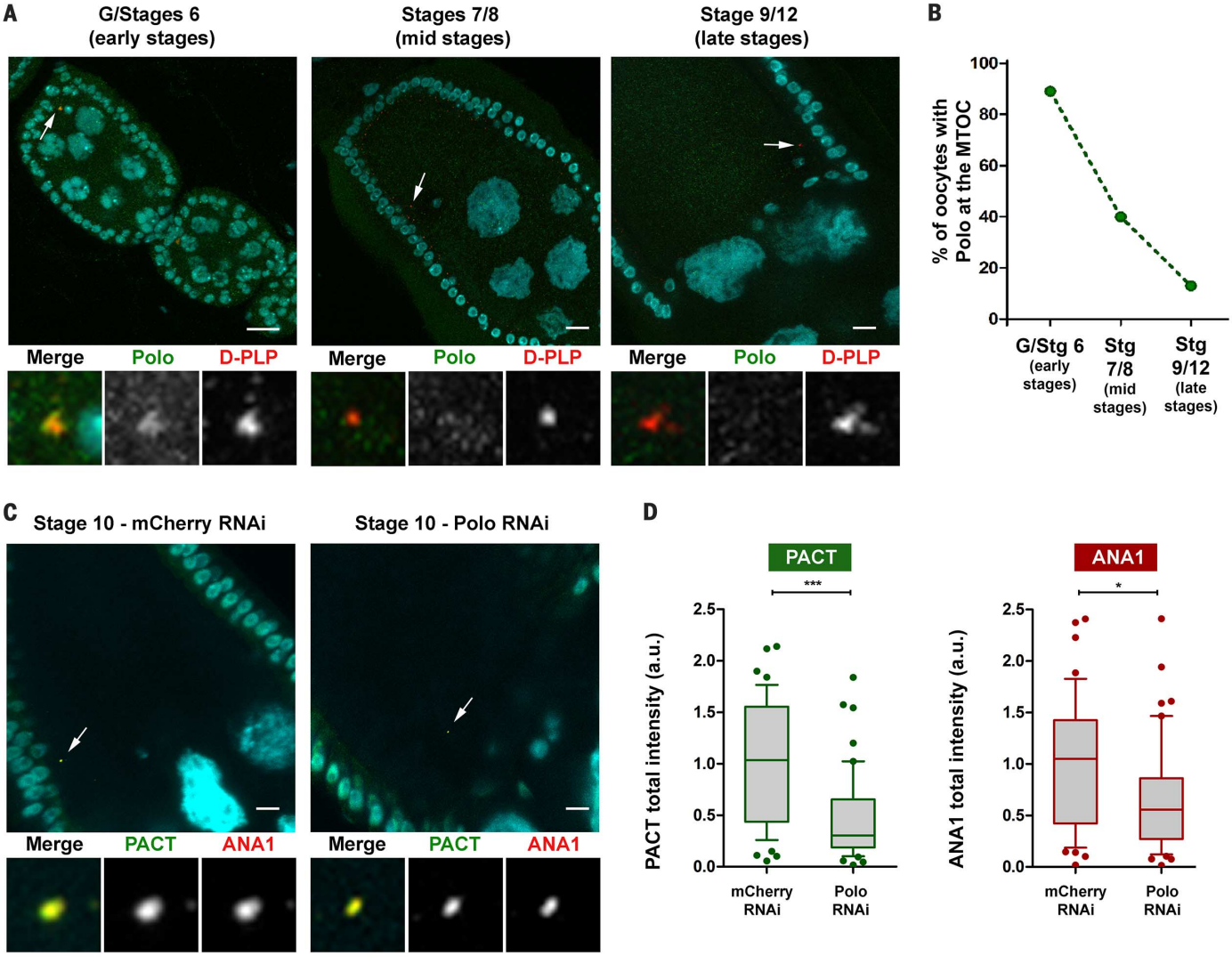

Fig. 2. Centrosomal Polo is naturally down-regulated in mid and late stages of oogenesis; down-regulation of Polo accelerates centriole loss. (**A**) Localization of endogenous Polo. Oocytes were immunostained for Polo and D-PLP (clustered centrosomes, i.e., oocyte MTOC). More than 30 oocytes were analyzed per stage. Enlargements of the indicated areas (arrows) are shown. All images were acquired with same exposure. Scale bars, 10 μm. (**B**) Quantification of oocytes positive for Polo at the oocyte MTOC. Note that the majority of late-stage oocytes do not have Polo at the MTOC. Dashed lines are included to help infer general trends. (**C**) Depletion of *Polo* by RNAi. *mCherry*-RNAi (control) and *Polo*-RNAi were expressed in the germ line using a driver that only expresses after stage 3/4 (i.e., after oocyte specification). Expression of both GFP-PACT [under polyubiquitin promoter; PACT is the centriolar targeting domain of PLP (*37*)] and ANA1-tdTomato (under endogenous promoter) were used as robust centriolar markers. Enlargements of the indicated areas (arrows) are shown. All images were acquired with same exposure. We investigated the presence of centrioles at stage 10, before they normally disappear (see Fig. 1J). Note the smaller size of MTOCs after *Polo* RNAi relative to the control (*mCherry* RNAi), seen both with the PACT and Ana1 centriole markers. Scale bars, 10 μm. Western blot showing Polo depletion is shown in fig. S3A. (**D**) Quantification of total colocalized GFP-PACT and ANA1-tdTomato levels as proxy for centriole numbers in stages 10. Box-and-whisker plot (10th and 90th percentiles) of the total integrated intensity of either GFP-PACT or Ana1-tdTomato from $n = 47$ oocytes for *mCherry*-RNAi (control) and $n = 49$ for *Polo*-RNAi. $^{*}P < 0.05$, $^{***}P < 0.001$ (unpaired Mann-Whitney test).

used γ-tubulin as a readout, because this component is downstream of the other PCM constituents (Fig. 1, G and I). In addition, we detailed the characterization of mid and very late (less abundant) stages of oogenesis, when centrosome components started to disappear. In very late and less abundant stages (12 to 13), where we rarely observed GFP-PACT oocytes (control) containing centrioles with γ-tubulin, 90% of the GFP-Polo-PACT oocytes showed centrioles with γ-tubulin (Fig. 4, A and B). Moreover, centriolar γ-tubulin levels were increased in oocytes expressing GFP-Polo-PACT (Fig. 4, A and C). Thus, tethering Polo to the oocytes centrioles prevents PCM loss in mid and late oogenesis.

Polo-dependent PCM maintenance prevents centriole elimination

Next, we asked whether maintaining centrioles coated by PCM would prevent their normal elimination. We quantified the levels and presence of the core centriolar protein ANA1 in mid and late oogenesis (Fig. 5, A and B). Upon expression of GFP-Polo-PACT, ANA1 levels in mid stages (7 to 8) were very similar to the control (GFP-PACT, Fig. 5A; roughly equivalent to 50 early-stage centrioles, Fig. 1J). However, in late stages (12 to 13), 68% of control oocytes (Fig. 5B) had few remaining centrioles (considering ANA1 levels) (Fig. 5A), whereas all GFP-Polo-PACT–expressing oocytes retained centrioles (Fig. 5B) and had similar levels of ANA1 signal distributed in different clusters (Fig. 5A). Because ANA1 total signal in the oocyte did not change throughout oogenesis when GFP-Polo-PACT was expressed (Fig. 5A), this finding strongly suggests that there is neither centriole

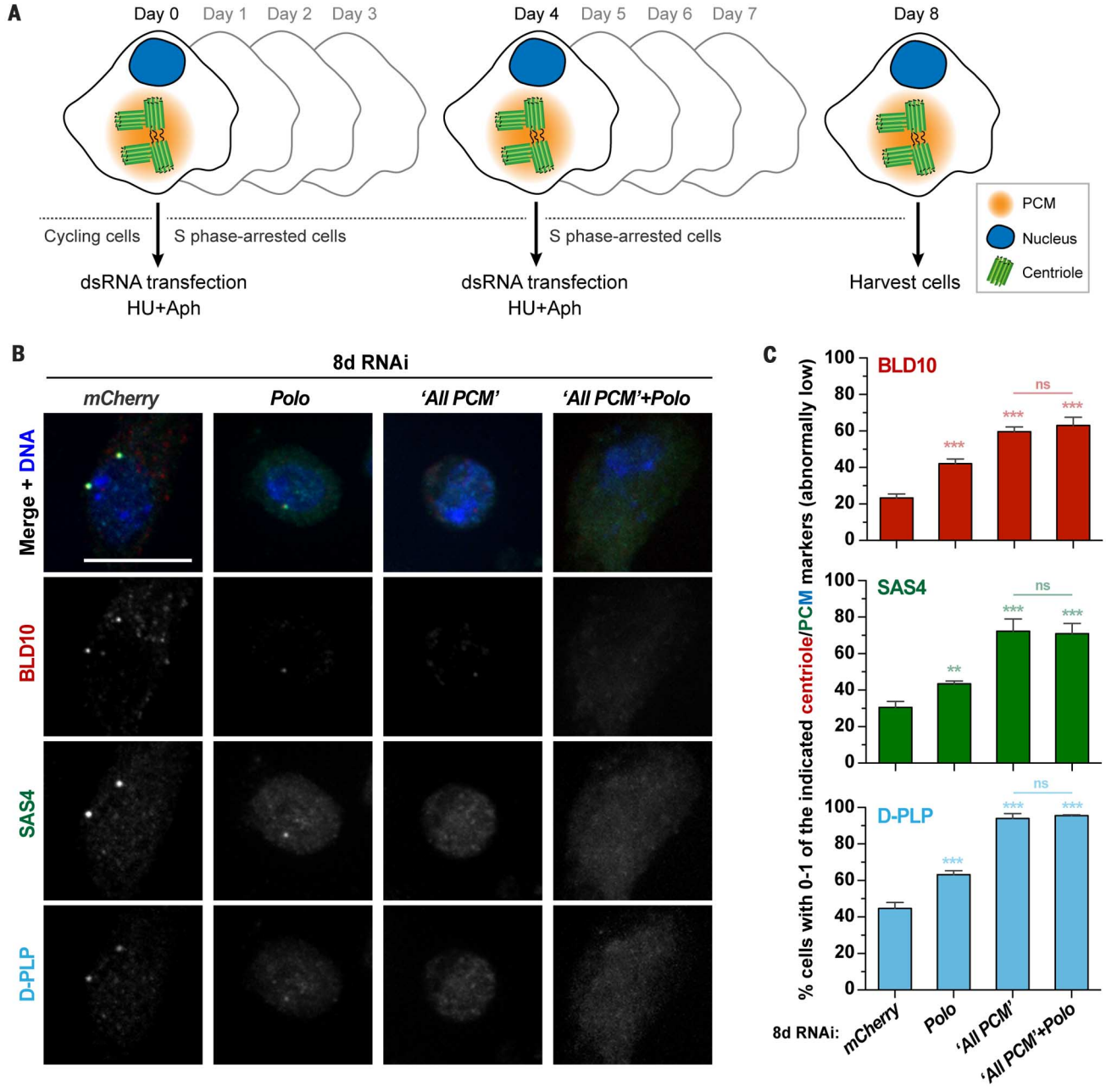

Fig. 3. Depletion of *Polo* and the PCM induces centriole loss in *Drosophila* culture cells. (**A**) Schematic representation of the centriole stability assay. This assay is an optimization of the assay shown in fig. S2, as it runs for longer (8 versus 4 days), resulting in the elimination of more centrioles. After the initial 4-day assay, cells were subject to a second round of double-stranded RNA transfection and treatment with HU (hydroxyurea) and APH (aphidicolin) for 4 more days. After 8 days of RNAi and HU+APH, cells were harvested and assayed for centriole numbers by immunofluorescence. (**B** and **C**) Centriole stability assay in DMEL cells depleted of *Polo*, *All PCM* (*CNN* + *ASL* + *PLP* + *SPD2*), or *All PCM* + *Polo*. *mCherry* RNAi was used as a negative control. (B) Cells were stained for BLD10 (red), SAS4 (green), D-PLP (cyan), and DNA (blue). Representative images are shown. Scale bar, 10 μm. (C) Histograms show the percentage of cells with abnormally low numbers (i.e., 0 to 1) of the indicated centriole (BLD10) and PCM (SAS4 and D-PLP) markers. Data are means ± SEM of three independent experiments ($n \geq 100$ cells per condition in each experiment). $^{**}P < 0.01$, $^{***}P < 0.001$; ns, not significant (analysis of variance). Note that depletion of *Polo* alone has an effect on PCM loss, similar to its effect on centriole loss; moreover, Polo and the PCM are likely to be acting on the same "centriole maintenance pathway," as the effect of co-depletion is similar to depletion of *All PCM*. Note that the effect of the loss of the PCM on centriole loss was increased as compared to fig. S2, where a 4-day assay was used. See also fig. S3 for the corresponding reverse transcription polymerase chain reactions to confirm RNAi efficiency and cell cycle profile by flow cytometry.

loss (in contrast to what is observed in the control) nor extra centriole biogenesis (either canonical or de novo) at any time point along oogenesis.

Centrioles have an unequivocal cylindrical structure, but because they are very small (diameter 250 nm, approximate length 400 nm), their walls cannot be resolved by conventional light microscopy. They have been traditionally resolved by EM, or more recently by super-resolution microscopy. We developed a protocol, structured illumination microscopy, in which super-resolution microscopy

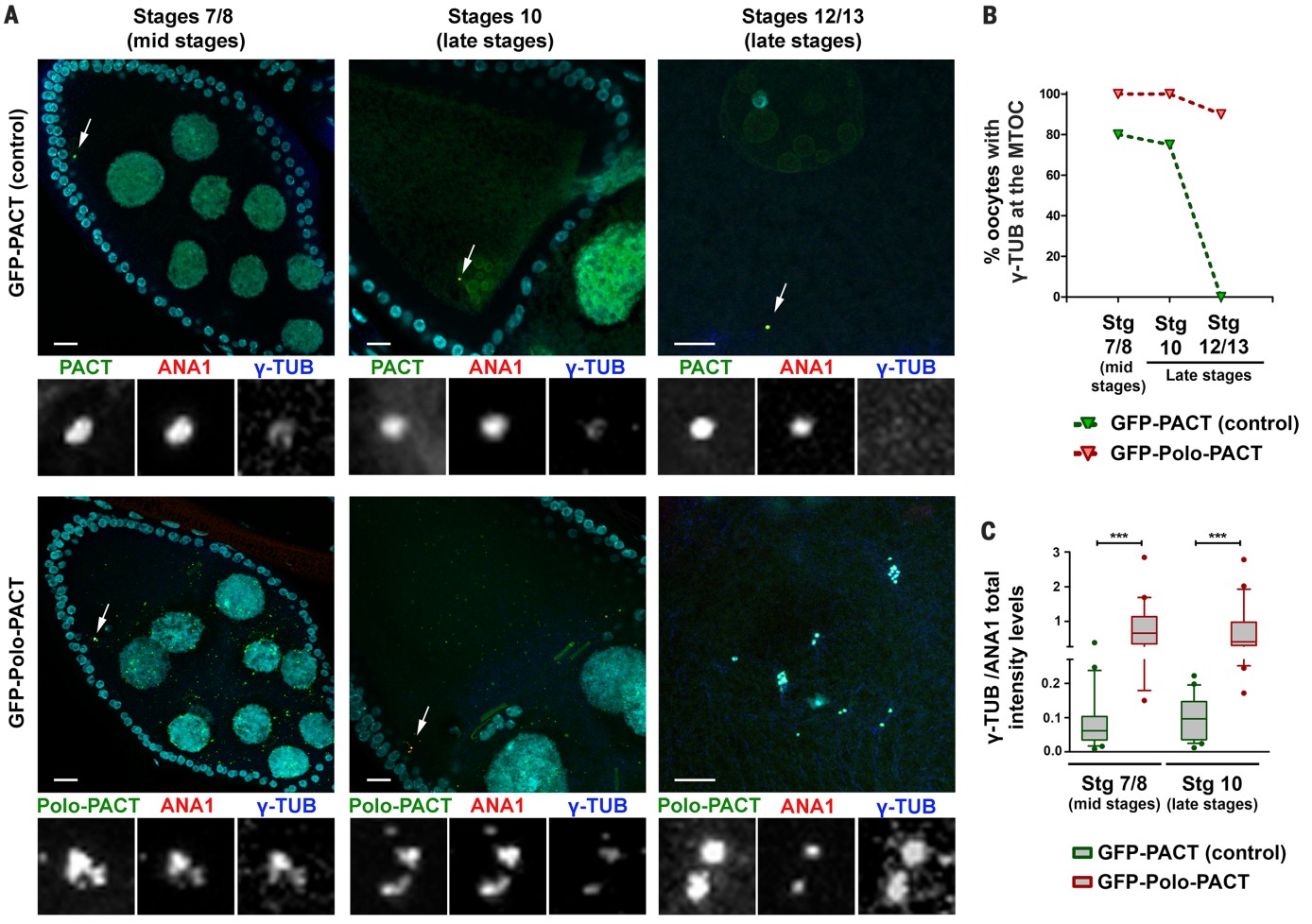

Fig. 4. Ectopic tethering of Polo to the centrioles prevents PCM loss. (**A**) Targeting Polo to the centrioles. GFP-PACT (control) and GFP-Polo-PACT were expressed in the germ line [PACT is the centriolar targeting domain of PLP (*37*)]. ANA1-tdTomato expression under endogenous promoter was used as a robust centriolar marker, and immunostaining for γ-tubulin (γ-TUB) as a PCM marker. Enlargements of the indicated areas (arrows) are shown. All images were acquired with same exposure. Scale bars, 10 μm. (**B**) Quantification of oocytes showing γ-TUB at the oocyte's MTOC (colocalization of γ-TUB, ANA1, and PACT). Note that expression of GFP-Polo-PACT retains γ-TUB at the MTOCs. Dashed lines are included to help infer general trends. More than 20 oocytes were analyzed per stage, per condition. (**C**) Quantification of the amount of γ-TUB per ANA1 at the centrioles. Expression of GFP-Polo-PACT led to approximately 3 times as much γ-TUB on centrioles. Box-and-whisker plot (10th to 90th percentiles) of the ratio between γ-TUB and ANA1 total integrated intensities. More than 20 oocytes were analyzed per stage, per condition. ***$P < 0.001$ (unpaired Mann-Whitney test).

of ovaries can validate the presence of normal centrioles by resolving the walls of the cylinder, a unique structure in the cell. We focused on stage 12, where normally most centrioles have been eliminated (Fig. 1J). Centriole barrels were clearly identified at stage 12 both in the control (GFP-PACT) and in GFP-Polo-PACT (Fig. 5E).

We then asked whether expression of GFP-Polo-PACT would also ensure centriole maintenance after meiotic nuclear envelope breakdown. Consistent with our initial characterization (Fig. 1F), in control oocytes (GFP-PACT) we were unable to identify centrioles at the spindle poles of meiosis I (stage 14) (Fig. 5, C and D, left panels). In GFP-Polo-PACT–expressing oocytes, we always observed centrioles (Fig. 5, C and D, right panels). Centrioles were mostly located at the anterior end of the immature egg, in the vicinity of the DNA and generally more scattered than in previous stages, forming on average 20 centriole clusters (Fig. 5, C and D, and fig. S5, A and B). In some eggs, centrioles were no longer clustered and their number could be resolved, with a maximum of 56 centrioles being observed in one egg (e.g., fig. S5A, right image). Moreover, we could observe the centriole barrel in this stage in GFP-Polo-PACT eggs in super-resolution micrographs (Fig. 5E, right panel). Those centrioles, in contrast to the remnant centrioles encountered in control eggs (fig. S1E), were able to nucleate MTs (fig. S5B). Thus, the majority of the centrioles were maintained as fully competent MTOCs.

Polo and its orthologs are known to have several functions mediated by catalysis. However, it has been speculated that some members of this family, in particular PLK5 can have noncatalytic functions (*39*, *40*). We asked whether Polo activity is critical for its function in centriole maintenance in both tissue culture cells and eggs. We generated a kinase-dead GFP-Polo-PACT (GFP-Polo-KD-PACT) as described (*38*). Expression of this construct at equal levels to GFP-Polo-PACT in ovaries did not fully rescue the centriole loss that normally occurs in stage 12 or 13, which suggests that Polo catalytic activity is indeed involved in centriole maintenance (fig. S6). Given that there was less centriole loss in GFP-Polo-KD-PACT than in controls, it is possible that Polo also has some noncatalytic function in centriole maintenance. Similar results were obtained in tissue culture cells (fig. S7). Thus, centriole elimination requires Polo loss from the centrioles.

Polo-dependent centriole maintenance leads to abnormal meiosis and aborted embryonic development

We then focused on the consequences of retaining centrioles for meiosis and embryo development. In GFP-Polo-PACT–expressing eggs, although a

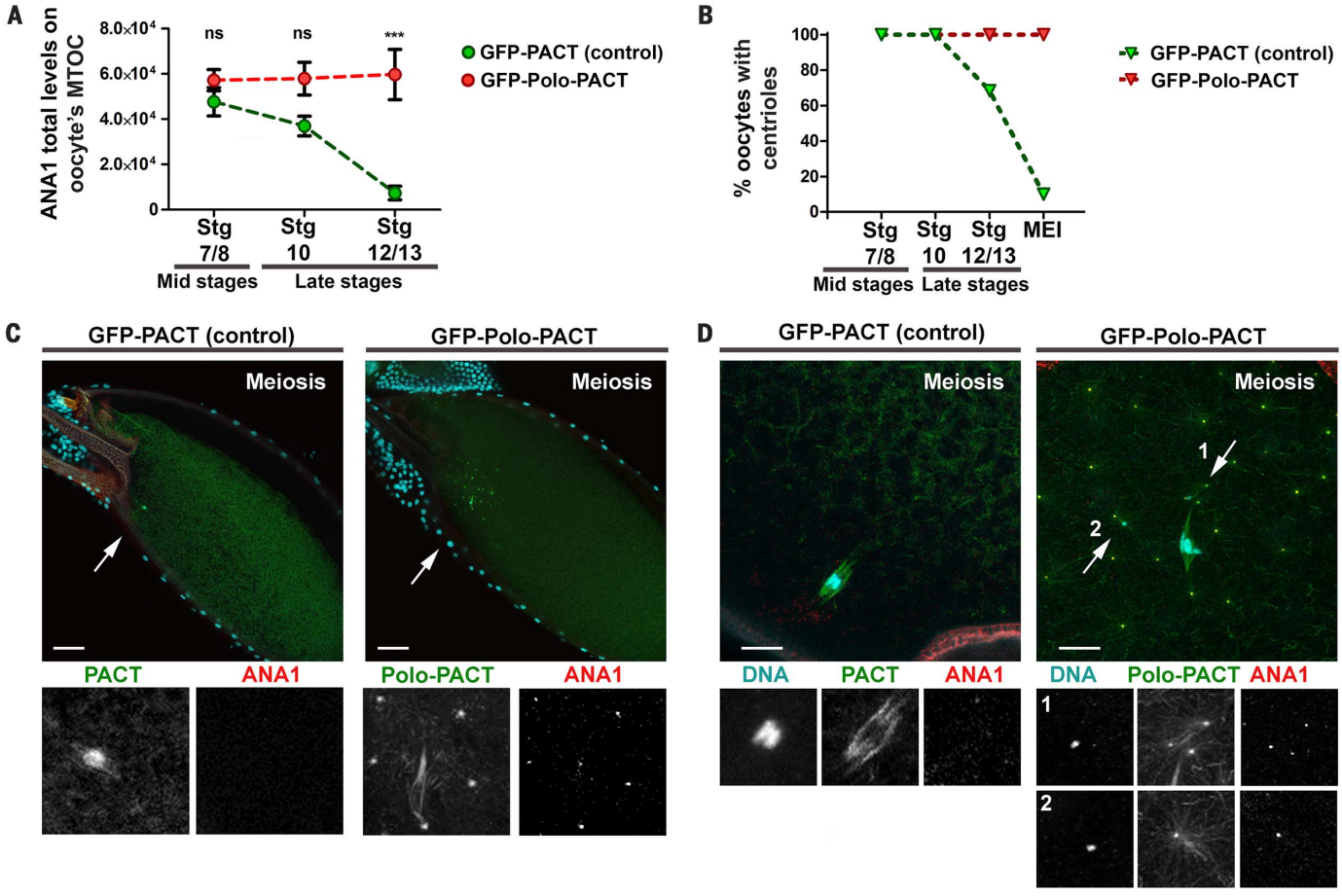

Fig. 5. Ectopic tethering of Polo to the centrioles prevents centriole loss leading to abnormal meiotic division. (**A**) Quantification of total ANA1-tdTomato levels (endogenous promoter) in mid and late oogenesis stages in GFP-PACT– and GFP-Polo-PACT–expressing oocytes. Note that ANA1 levels are constant throughout oogenesis upon GFP-Polo-PACT expression suggesting that centrioles are maintained. Dashed lines are included to help infer general trends. For stages 7/8 and 10, $n > 38$ oocytes per condition; for stages 12/13, $n > 18$ per condition. Data are means ± SEM. ***$P < 0.001$ (Kruskal-Wallis test). (**B**) Quantification of oocytes showing centrioles (oocytes with ANA1/total number of oocytes). Note that most meiosis I metaphases do not have centrioles in controls (GFP-PACT), while all oocytes expressing GFP-Polo-PACT show centrioles. For stages 7/8 and 10, $n > 38$ oocytes per condition. For stages 12/13 and meiosis, $n > 18$ per condition. (**C** and **D**) Different magnifications of stage 14 eggs expressing either GFP-PACT (control) or GFP-Polo-PACT. ANA1-tdTomato was used as a centriolar marker. (C) Eggs expressing GFP-Polo-PACT show the maintenance of centrioles at the anterior of the egg in the vicinity of the meiotic DNA. Enlargements of the indicated areas (arrows) are shown. Note that the nuclei surrounding the egg are from follicle cells. Scale bar, 40 μm. (D) Scattered DNA associates with maternal centrioles in meiosis in GFP-Polo-PACT-embryos. Enlargements of the indicated areas (arrows) are shown. Scale bar, 10 μm. (**E**) Representative super-resolution microscopy (i.e., structured illumination microscopy) images of centrioles in eggs expressing either GFP-PACT (control) or GFP-Polo-PACT in stage 12 and in meiotic divisions. Centrioles are very small (250 nm across); therefore, their barrel-like structure is only visible with super-resolution microscopy. ANA1-tdTomato was used to identify typical centriole barrel structures in stage 12 of both GFP-PACT– and GFP-Polo-PACT–expressing eggs. These structures were also present in meiotic divisions of GFP-Polo-PACT–expressing eggs; no structures were seen in control eggs at that stage (Fig. 1F). Enlargements of the indicated areas (arrows), focusing on a single centriole (cross section of the barrel), are shown. Scale bar, 1 μm.

few meioses looked normal upon centriole maintenance, centrioles often seemed to interact with the spindle, leading to abnormal meiosis, in many cases with scattered DNA (Fig. 5D, right panel, and fig. S5A). Thus, centriole elimination during late oogenesis requires Polo loss and consequent PCM loss. Moreover, non-eliminated centrioles can interfere with meiotic spindle assembly.

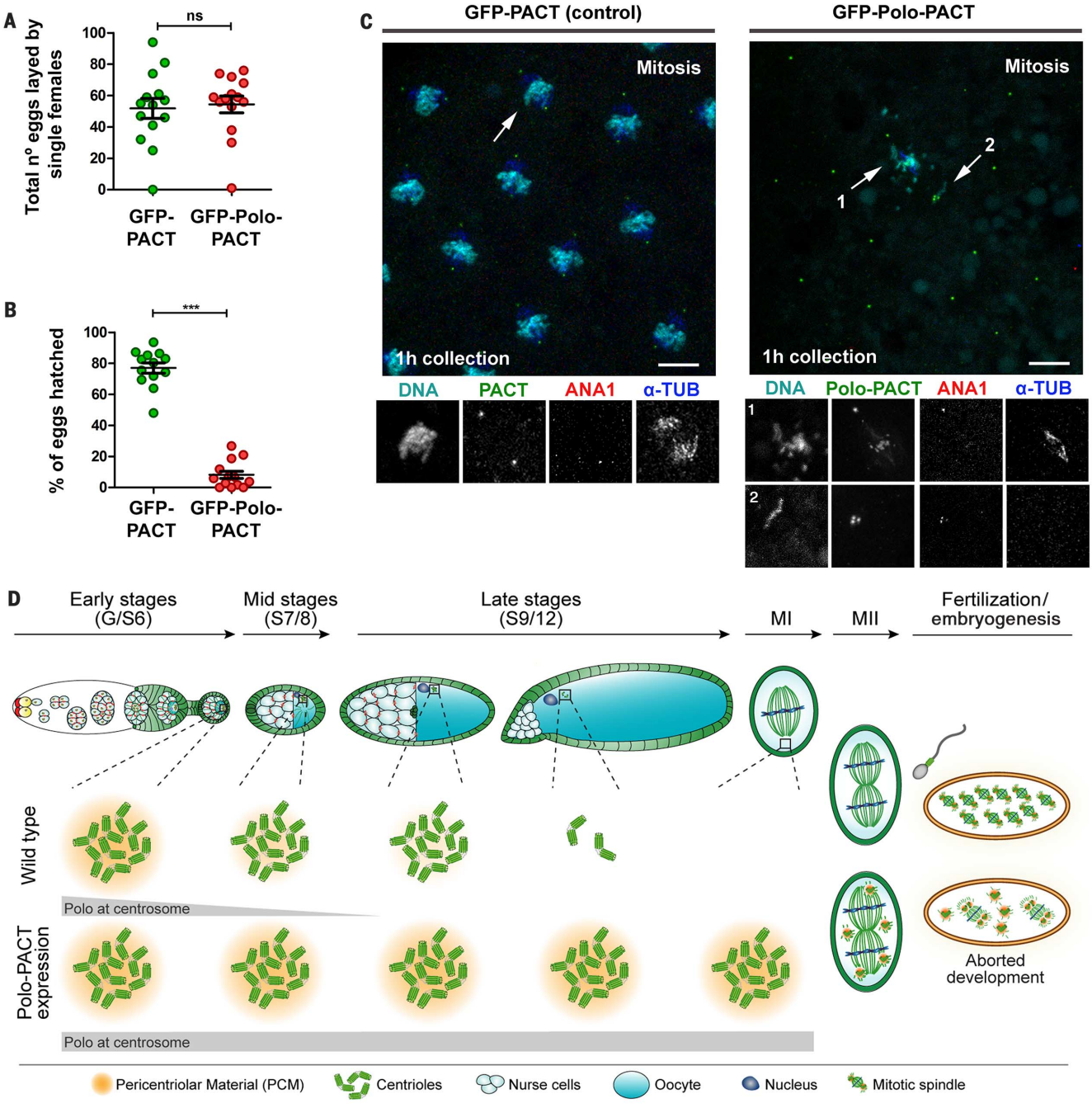

Fig. 6. Maintenance of centrioles in eggs leads to embryonic development arrest. (**A**) Expression of GFP-Polo-PACT does not affect egg laying. Quantification of the number of eggs laid by GFP-PACT and GFP-Polo-PACT females (14 females per condition). (**B**) The majority of GFP-Polo-PACT fertilized eggs do not hatch. Quantification of number of hatched eggs in GFP-PACT and GFP-Polo-PACT from (A). ***$P < 0.001$ (Mann-Whitney test). (**C**) GFP-Polo-PACT embryos show several mitotic defects and mitotic arrest. Embryos were collected 1 hour after fertilization. GFP-Polo-PACT embryos show supernumerary centrioles and few divisions with scattered DNA associated with centrioles. We observed that all embryos in GFP-Polo-PACT had not developed past cycle 2 ($n = 15$), whereas most GFP-PACT control embryos (16/19) had developed past that stage. The presence of centrioles in the embryos was analyzed by colabeling with ANA1 (centriolar marker under endogenous promoter, very weak in early embryos and likely to be accumulated in older centrioles) and PACT; α-tubulin (α-TUB, dark blue) was used to identify the spindle. Enlargements of the indicated areas (arrows) are shown. Scale bars, 10 μm. (**D**) Model of centriole elimination during oogenesis and the consequences of preventing centriolar Polo loss. Nearly all centrioles from the 16-cell cyst migrate to the oocyte in early oogenesis. In a wild-type fly, during oogenesis, there is both loss of expression and localization of Polo and PCM components on the oocytes centrioles, down-regulating a centriole maintenance program. In the absence of Polo and consequently PCM, the centrioles are not stable and are eliminated, ensuring their absence in meiosis, proper number of these structures upon fertilization, and successful embryonic development. By ectopically expressing and anchoring Polo to the maternal centrioles, the maintenance program is "on," so the PCM is maintained and centrioles are stable. Although the presence of active maternal centrioles does not preclude egg formation and fertilization, they lead to abnormal meiotic and mitotic divisions with consequently failed zygotic development.

We then asked what would be the consequences for reproduction of retaining centrioles in the egg. Eggs did not show any obvious morphological defects, and the dorsal appendages of the chorion (specialized structures in the *D. melanogaster* egg that ensure the breathing of the embryo), a hallmark of proper egg development, were well formed ($n > 450$ eggs in GFP-Polo-PACT and GFP-PACT),which suggests that ectopic centrosome presence during oogenesis did not induce major polarity defects. It is known that injection of centrioles in *Xenopus* eggs induces parthenogenic development (*7*). However, we did not observe parthenogenic offspring from unfertilized *Drosophila* eggs retaining centrosomes (GFP-Polo-PACT; $n = 50$ females). Fertilized eggs having both maternal (GFP-Polo-PACT–expressing eggs) and a paternal centrosome were laid in similar amounts relative to controls (Fig. 6A). However, eggs expressing GFP-Polo-PACT showed a very low egg hatching rate of 1%, compared to 75% in GFP-PACT controls (Fig. 6B) and 54% in Polo-Myc overexpression, where Polo was not tethered to centrioles (fig. S5D). Although eggs were fertilized (fig. S8A), embryogenesis was blocked very early in development (Fig. 6C). The majority of embryos from GFP-Polo-PACT–expressing mothers arrested in the first mitotic divisions, often with multiple centrosomes at each pole and scattered DNA associated with centrosomes (Fig. 6C), probably resulting from abnormal chromosome segregation. GFP-Polo-PACT expression per se, at the levels observed, is unlikely to have major detrimental effects in embryonic development, given the presence of normal escaper embryos (fig. S8B). Thus, maternal centrosome maintenance is detrimental for female meiosis and early embryonic development and has a negative impact on sexual reproduction.

Discussion

Asymmetric centriole inheritance is thought to be essential to sexual reproduction. How maternal centrioles are eliminated and the importance of this phenomenon for oogenesis progression, meiotic division, and embryogenesis has been a matter of extensive debate. Our results show that maternal *Drosophila* centriole elimination results from the shutdown of a novel centriole maintenance program relying on the presence of Polo kinase at the centrosome and consequent PCM retention (Fig. 6D). By artificially maintaining this program by tethering Polo to centrioles, we retained maternal centrosomes throughout all stages of oogenesis. Surprisingly, eggs with active centrosomes were well patterned and laid. However, the abnormal presence of centrosomes led to defective meiosis, abnormal mitosis after fertilization, and aborted early embryonic development (Fig. 6D).

Our findings are likely to extend to the female germ line of other animals, where centrioles are also eliminated during prophase I arrest. For example, in *Caenorhabditis elegans* oocytes, the PCM is also lost before centrioles are eliminated (*9*), and in *Xenopus* oocytes, the Polo ortholog Plx1 is also less expressed in early oogenesis (*41*, *42*). Echinoderms are an exception to centriole elimination in early prophase I arrest, because most centrioles are eliminated through extrusion within the polar bodies during both of the meiotic divisions, with a last centriole being eliminated after meiosis exit (*8*). Remarkably, echinoderm centrioles are surrounded by PCM (γ-tubulin and pericentrin) in all stages of oogenesis (*43*), which may protect them, further supporting the generality of a PCM-dependent centriole maintenance mechanism. It is also known that Polo substrate phosphorylation is important, both for their localization and to reinforce Polo's own localization at the centrosome, in a positive feedback loop (*26*). Recently, it was shown that both Polo and at least one of its PCM substrates, SPD2, are not transcribed at the beginning of late stages of *Drosophila* oogenesis (stages 9 and 10) (*35*). We propose that concomitant loss of expression of Polo and its PCM substrates leads to complete PCM loss from the oocyte MTOC and subsequent centriole loss. Moreover, physiological inhibitors of Polo (such as matrimony) (*34*) may contribute to further down-regulate its localization and activity at the centriole. Future work will focus on understanding which Polo substrates and binding proteins are important in this function.

To our knowledge, animal sexual reproduction is always associated with asymmetric centriole inheritance due to maternal centriole loss. Here, we tested the consequences of counteracting this process for meiosis and early embryonic development. We observed that oogenesis is robust to the presence of active centrioles (no major patterning defects). However, maternal centrioles interfere with meiotic and mitotic divisions in the embryo, leading to female sterility. Moreover, the presence of maternal centrioles is not sufficient to support parthenogenesis in *Drosophila*. In parthenogenic species, centrioles are still eliminated in oogenesis and appear de novo only after anaphase I (*44*). It is thus possible that the meiotic defects observed caused by the presence of maternal centrioles, or other unrelated requirements, preclude the induction of parthenogenesis.

Our study suggests that the widely accepted centriole stability is not an intrinsic property of those structures. Instead, centrioles are maintained by an interphase role of the major mitotic kinase Polo and by the PCM. We propose this to be a general feature of centrioles, because either Polo or PCM removal leads to centriole disappearance in *Drosophila* interphasic somatic cells arrested for a long time. Further studies are needed to address the role of PCM and Polo in centriole maintenance and the interplay of that role with centriole-stabilizing structural features (*2*, *45*–*47*). Finally, evidence of PCM's presence or loss from centrosomes in different tissues supports the idea that regulation of a centriole maintenance program is present and critical in many other cell types, such as cells that lose centrioles or their activity upon differentiation or disease (e.g., muscle, virus infection, cells with multiple centrosomes in cancer) and in cells that keep centrioles for a long time (e.g., cycling cells where centrioles go through many cell cycles and long-lived differentiated ciliated cells) (*6*, *48*–*52*).

REFERENCES AND NOTES

1. M. Sato, K. Sato, Dynamic regulation of autophagy and endocytosis for cell remodeling during early development. *Traffic* **14**, 479–486 (2013). doi: 10.1111/tra.12050; pmid: 23356349
2. D. A. Brito, S. M. Gouveia, M. Bettencourt-Dias, Deconstructing the centriole: Structure and number control. *Curr. Opin. Cell Biol.* **24**, 4–13 (2012). doi: 10.1016/j.ceb.2012.01.003; pmid: 22321829
3. M. Delattre, P. Gönczy, The arithmetic of centrosome biogenesis. *J. Cell Sci.* **117**, 1619–1630 (2004). doi: 10.1242/jcs.01128; pmid: 15075224
4. G. Manandhar, H. Schatten, P. Sutovsky, Centrosome reduction during gametogenesis and its significance. *Biol. Reprod.* **72**, 2–13 (2005). doi: 10.1095/biolreprod.104.031245; pmid: 15385423
5. A. Rodrigues-Martins, M. Riparbelli, G. Callaini, D. M. Glover, M. Bettencourt-Dias, From centriole biogenesis to cellular function: Centrioles are essential for cell division at critical developmental stages. *Cell Cycle* **7**, 11–16 (2008). doi: 10.4161/cc.7.1.5226; pmid: 18196975
6. I. Cunha-Ferreira, I. Bento, M. Bettencourt-Dias, From zero to many: Control of centriole number in development and disease. *Traffic* **10**, 482–498 (2009). doi: 10.1111/j.1600-0854.2009.00905.x; pmid: 19416494
7. F. Tournier, E. Karsenti, M. Bornens, Parthenogenesis in *Xenopus* eggs injected with centrosomes from synchronized human lymphoid cells. *Dev. Biol.* **136**, 321–329 (1989). doi: 10.1016/0012-1606(89)90259-5; pmid: 2583369
8. J. Borrego-Pinto *et al.*, Distinct mechanisms eliminate mother and daughter centrioles in meiosis of starfish oocytes. *J. Cell Biol.* **212**, 815–827 (2016). doi: 10.1083/jcb.201510083; pmid: 27002173
9. T. Mikeladze-Dvali *et al.*, Analysis of centriole elimination during *C. elegans* oogenesis. *Development* **139**, 1670–1679 (2012). doi: 10.1242/dev.075440; pmid: 22492357
10. A. F. Huettner, M. Rabinowitz, Demonstration of the central body in the living cell. *Science* **78**, 367–368 (1933). doi: 10.1126/science.78.2025.367-a; pmid: 17811080
11. A. P. Mahowald, J. M. Strassheim, Intercellular migration of centrioles in the germarium of Drosophila melanogaster. An electron microscopic study. *J. Cell Biol.* **45**, 306–320 (1970). doi: 10.1083/jcb.45.2.306; pmid: 4327572
12. J. Januschke *et al.*, The centrosome-nucleus complex and microtubule organization in the *Drosophila* oocyte. *Development* **133**, 129–139 (2006). doi: 10.1242/dev.02179; pmid: 16319114
13. S. Blachon *et al.*, *Drosophila* asterless and vertebrate Cep152 Are orthologs essential for centriole duplication. *Genetics* **180**, 2081–2094 (2008). doi: 10.1534/genetics.108.095141; pmid: 18854586
14. M. Martinez-Campos, R. Basto, J. Baker, M. Kernan, J. W. Raff, The *Drosophila* pericentrin-like protein is essential for cilia/flagella function, but appears to be dispensable for mitosis. *J. Cell Biol.* **165**, 673–683 (2004). doi: 10.1083/jcb.200402130; pmid: 15184400
15. E. P. Lucas, J. W. Raff, Maintaining the proper connection between the centrioles and the pericentriolar matrix requires *Drosophila* centrosomin. *J. Cell Biol.* **178**, 725–732 (2007). doi: 10.1083/jcb.200704081; pmid: 17709428
16. P. T. Conduit *et al.*, The centrosome-specific phosphorylation of Cnn by Polo/Plk1 drives Cnn scaffold assembly and centrosome maturation. *Dev. Cell* **28**, 659–669 (2014). doi: 10.1016/j.devcel.2014.02.013; pmid: 24656740
17. C. I. Dix, J. W. Raff, *Drosophila* Spd-2 recruits PCM to the sperm centriole, but is dispensable for centriole duplication. *Curr. Biol.* **17**, 1759–1764 (2007). doi: 10.1016/j.cub.2007.08.065; pmid: 17919907
18. M. G. Giansanti, E. Bucciarelli, S. Bonaccorsi, M. Gatti, *Drosophila* SPD-2 is an essential centriole component required for PCM recruitment and astral-microtubule nucleation. *Curr. Biol.* **18**, 303–309 (2008). doi: 10.1016/j.cub.2008.01.058; pmid: 18291647
19. J. Gopalakrishnan *et al.*, Sas-4 provides a scaffold for cytoplasmic complexes and tethers them in a centrosome. *Nat. Commun.* **2**, 359 (2011). doi: 10.1038/ncomms1367; pmid: 21694707
20. N. S. Dzhindzhev *et al.*, Asterless is a scaffold for the onset of centriole assembly. *Nature* **467**, 714–718 (2010). doi: 10.1038/nature09445; pmid: 20852615
21. J. B. Woodruff, O. Wueseke, A. A. Hyman, Pericentriolar material structure and dynamics. *Philos. Trans. R. Soc. London*

Ser. B **369**, 20130459 (2014). doi: 10.1098/rstb.2013.0459; pmid: 25047613
22. J. J. Moser, M. J. Fritzler, Y. Ou, J. B. Rattner, The PCM-basal body/primary cilium coalition. *Semin. Cell Dev. Biol.* **21**, 148–155 (2010). doi: 10.1016/j.semcdb.2009.06.006; pmid: 19591955
23. Y. Shang, B. Li, M. A. Gorovsky, *Tetrahymena thermophila* contains a conventional gamma-tubulin that is differentially required for the maintenance of different microtubule-organizing centers. *J. Cell Biol.* **158**, 1195–1206 (2002). doi: 10.1083/jcb.200205101; pmid: 12356864
24. J. Fu, D. M. Glover, Structured illumination of the interface between centriole and peri-centriolar material. *Open Biol.* **2**, 120104 (2012). pmid: 22977736
25. W.-J. Wang, R. K. Soni, K. Uryu, M.-F. B. Tsou, The conversion of centrioles to centrosomes: Essential coupling of duplication with segregation. *J. Cell Biol.* **193**, 727–739 (2011). doi: 10.1083/jcb.201101109; pmid: 21576395
26. S. Zitouni, C. Nabais, S. C. Jana, A. Guerrero, M. Bettencourt-Dias, Polo-like kinases: Structural variations lead to multiple functions. *Nat. Rev. Mol. Cell Biol.* **15**, 433–452 (2014). doi: 10.1038/nrm3819; pmid: 24954208
27. H. A. Lane, E. A. Nigg, Antibody microinjection reveals an essential role for human polo-like kinase 1 (Plk1) in the functional maturation of mitotic centrosomes. *J. Cell Biol.* **135**, 1701–1713 (1996). doi: 10.1083/jcb.135.6.1701; pmid: 8991084
28. L. Haren, T. Stearns, J. Lüders, Plk1-dependent recruitment of gamma-tubulin complexes to mitotic centrosomes involves multiple PCM components. *PLOS ONE* **4**, e5976 (2009). doi: 10.1371/journal.pone.0005976; pmid: 19543530
29. J. Dobbelaere *et al*., A genome-wide RNAi screen to dissect centriole duplication and centrosome maturation in *Drosophila*. *PLOS Biol.* **6**, e224 (2008). doi: 10.1371/journal.pbio.0060224; pmid: 18798690
30. K. Lee, K. Rhee, PLK1 phosphorylation of pericentrin initiates centrosome maturation at the onset of mitosis. *J. Cell Biol.* **195**, 1093–1101 (2011). pmid: 22184200
31. J. B. Woodruff *et al*., Regulated assembly of a supramolecular centrosome scaffold in vitro. *Science* **348**, 808–812 (2015). doi: 10.1126/science.aaa3923; pmid: 25977552
32. R. Mahen, A. D. Jeyasekharan, N. P. Barry, A. R. Venkitaraman, Continuous polo-like kinase 1 activity regulates diffusion to maintain centrosome self-organization during mitosis. *Proc. Natl. Acad. Sci. U.S.A.* **108**, 9310–9315 (2011). doi: 10.1073/pnas.1101112108; pmid: 21576470
33. V. Mirouse, E. Formstecher, J. L. Couderc, Interaction between Polo and BicD proteins links oocyte determination and meiosis control in *Drosophila*. *Development* **133**, 4005–4013 (2006). doi: 10.1242/dev.02565; pmid: 16971474
34. Y. Xiang *et al*., The inhibition of polo kinase by matrimony maintains G_2 arrest in the meiotic cell cycle. *PLOS Biol.* **5**, e323 (2007). doi: 10.1371/journal.pbio.0050323; pmid: 18052611
35. H. Jambor *et al*., Systematic imaging reveals features and changing localization of mRNAs in *Drosophila* development. *eLife* **4**, e05003 (2015). doi: 10.7554/eLife.05003; pmid: 25838129
36. C. E. Sunkel, D. M. Glover, Polo, a mitotic mutant of *Drosophila* displaying abnormal spindle poles. *J. Cell Sci.* **89**, 25–38 (1988). pmid: 3417791
37. A. K. Gillingham, S. Munro, The PACT domain, a conserved centrosomal targeting motif in the coiled-coil proteins AKAP450 and pericentrin. *EMBO Rep.* **1**, 524–529 (2000). doi: 10.1093/embo-reports/kvd105; pmid: 11263498
38. K. Kishi, M. A. van Vugt, K. Okamoto, Y. Hayashi, M. B. Yaffe, Functional dynamics of Polo-like kinase 1 at the centrosome. *Mol. Cell. Biol.* **29**, 3134–3150 (2009). doi: 10.1128/MCB.01663-08; pmid: 19307309
39. V. Archambault, G. Lépine, D. Kachaner, Understanding the Polo kinase machine. *Oncogene* **34**, 4799–4807 (2015). doi: 10.1038/onc.2014.451; pmid: 25619835
40. G. de Cárcer, G. Manning, M. Malumbres, From Plk1 to Plk5: Functional evolution of polo-like kinases. *Cell Cycle* **10**, 2255–2262 (2011). doi: 10.4161/cc.10.14.16494; pmid: 21654194
41. A. Karaiskou *et al*., Polo-like kinase confers MPF autoamplification competence to growing *Xenopus* oocytes. *Development* **131**, 1543–1552 (2004). doi: 10.1242/dev.01050; pmid: 14985258
42. D. L. Gard, D. Affleck, B. M. Error, Microtubule organization, acetylation, and nucleation in *Xenopus laevis* oocytes: II. A developmental transition in microtubule organization during early diplotene. *Dev. Biol.* **168**, 189–201 (1995). doi: 10.1006/dbio.1995.1071; pmid: 7883073
43. A. L. Egaña, J. A. Boyle, S. G. Ernst, *Strongylocentrotus drobachiensis* oocytes maintain a microtubule organizing center throughout oogenesis: Implications for the establishment of egg polarity in sea urchins. *Mol. Reprod. Dev.* **74**, 76–87 (2007). doi: 10.1002/mrd.20511; pmid: 16929525
44. M. G. Riparbelli, G. Callaini, *Drosophila* parthenogenesis: A model for de novo centrosome assembly. *Dev. Biol.* **260**, 298–313 (2003). doi: 10.1016/S0012-1606(03)00243-4; pmid: 12921733
45. P. Guichard *et al*., Native architecture of the centriole proximal region reveals features underlying its 9-fold radial symmetry. *Curr. Biol.* **23**, 1620–1628 (2013). doi: 10.1016/j.cub.2013.06.061; pmid: 23932403
46. D. Izquierdo, W. J. Wang, K. Uryu, M. F. Tsou, Stabilization of cartwheel-less centrioles for duplication requires CEP295-mediated centriole-to-centrosome conversion. *Cell Rep.* **8**, 957–965 (2014). doi: 10.1016/j.celrep.2014.07.022; pmid: 25131205
47. V. Mennella *et al*., Subdiffraction-resolution fluorescence microscopy reveals a domain of the centrosome critical for pericentriolar material organization. *Nat. Cell Biol.* **14**, 1159–1168 (2012). doi: 10.1038/ncb2597; pmid: 23086239
48. R. H. Warren, Microtubular organization in elongating myogenic cells. *J. Cell Biol.* **63**, 550–566 (1974). doi: 10.1083/jcb.63.2.550; pmid: 4547566
49. R. J. Przybylski, Occurrence of centrioles during skeletal and cardiac myogenesis. *J. Cell Biol.* **49**, 214–221 (1971). doi: 10.1083/jcb.49.1.214; pmid: 5555575
50. A. M. Tassin, B. Maro, M. Bornens, Fate of microtubule-organizing centers during myogenesis in vitro. *J. Cell Biol.* **100**, 35–46 (1985). doi: 10.1083/jcb.100.1.35; pmid: 3880758
51. J. A. Connolly, B. W. Kiosses, V. I. Kalnins, Centrioles are lost as embryonic myoblasts fuse into myotubes in vitro. *Eur. J. Cell Biol.* **39**, 341–345 (1986). pmid: 3514220
52. V. Brodu, A. D. Baffet, P. M. Le Droguen, J. Casanova, A. Guichet, A developmentally regulated two-step process generates a noncentrosomal microtubule network in *Drosophila* tracheal cells. *Dev. Cell* **18**, 790–801 (2010). doi: 10.1016/j.devcel.2010.03.015; pmid: 20493812
53. S. Blachon *et al*., A proximal centriole-like structure is present in *Drosophila* spermatids and can serve as a model to study centriole duplication. *Genetics* **182**, 133–144 (2009). doi: 10.1534/genetics.109.101709; pmid: 19293139
54. R. Basto *et al*., Flies without centrioles. *Cell* **125**, 1375–1386 (2006). doi: 10.1016/j.cell.2006.05.025; pmid: 16814722
55. P. T. Conduit, J. W. Raff, Cnn dynamics drive centrosome size asymmetry to ensure daughter centriole retention in *Drosophila* neuroblasts. *Curr. Biol.* **20**, 2187–2192 (2010). doi: 10.1016/j.cub.2010.11.055; pmid: 21145745
56. P. Sitaram, M. A. Anderson, J. N. Jodoin, E. Lee, L. A. Lee, Regulation of dynein localization and centrosome positioning by Lis-1 and asunder during *Drosophila* spermatogenesis. *Development* **139**, 2945–2954 (2012). doi: 10.1242/dev.077511; pmid: 22764052
57. P. Wang *et al*., Cell cycle regulation of Greatwall kinase nuclear localization facilitates mitotic progression. *J. Cell Biol.* **202**, 277–293 (2013). doi: 10.1083/jcb.201211141; pmid: 23857770
58. J. Q. Ni *et al*., A genome-scale shRNA resource for transgenic RNAi in *Drosophila*. *Nat. Methods* **8**, 405–407 (2011). pmid: 21460824
59. P. Prudêncio, L. G. Guilgur, Protein extraction from *Drosophila* embryos and ovaries. *Biol. Protoc.* **5**, e1459; www.bio-protocol.org/e1459 (2015).
60. M. Bettencourt-Dias *et al*., Genome-wide survey of protein kinases required for cell cycle progression. *Nature* **432**, 980–987 (2004). doi: 10.1038/nature03160; pmid: 15616552
61. G. C. Rogers, N. M. Rusan, D. M. Roberts, M. Peifer, S. L. Rogers, The SCF Slimb ubiquitin ligase regulates Plk4/Sak levels to block centriole reduplication. *J. Cell Biol.* **184**, 225–239 (2009). doi: 10.1083/jcb.200808049; pmid: 19171756
62. P. Rørth, Gal4 in the *Drosophila* female germline. *Mech. Dev.* **78**, 113–118 (1998). doi: 10.1016/S0925-4773(98)00157-9; pmid: 9858703
63. C. Q. Huynh, H. Zieler, Construction of modular and versatile plasmid vectors for the high-level expression of single or multiple genes in insects and insect cell lines. *J. Mol. Biol.* **288**, 13–20 (1999). doi: 10.1006/jmbi.1999.2674; pmid: 10329122
64. A. Rodrigues-Martins, M. Riparbelli, G. Callaini, D. M. Glover, M. Bettencourt-Dias, Revisiting the role of the mother centriole in centriole biogenesis. *Science* **316**, 1046–1050 (2007). doi: 10.1126/science.1142950; pmid: 17463247
65. M. Bettencourt-Dias *et al*., SAK/PLK4 is required for centriole duplication and flagella development. *Curr. Biol.* **15**, 2199–2207 (2005). doi: 10.1016/j.cub.2005.11.042; pmid: 16326102
66. V. Mottier-Pavie, T. L. Megraw, *Drosophila* bld10 is a centriolar protein that regulates centriole, basal body, and motile cilium assembly. *Mol. Biol. Cell* **20**, 2605–2614 (2009). doi: 10.1091/mbc.E08-11-1115; pmid: 19321663

ACKNOWLEDGMENTS

We thank M.-F. B. Tsou, R. Martinho, R. Oliveira, A. Dammermann, T. Schupbach, P. Lenart, J. Pinto, J. Januschke, V. Archambault, P. Prudêncio, M. Francia, M. Lince-Faria, J. Pereira-Leal, and E. Sucena for critical reading of the manuscript; all members of the M.B.-D. laboratory for discussions; H. Ohkura for sharing protocols; A. Carpenter and J. Dobbelaere for discussions and sharing unpublished data; T. Avidor-Reiss, J. Raff, D. St. Johnston, and V. Archambault for sharing tools; and G. Martins, S. Mendonça, and M. Pinho for help with experiments. Supported by Fundação Para a Ciência e Tecnologia (SFRH/BD/33565/2008; SFRH/BPD/79680/2011; SFRH/BPD/87479/2012; PTDC/SAU-BD/105616/2008; Ciencia2007 and FCT Investigator programmes), an EMBO Installation grant, and an ERC grant (ERC-2010-StG-261344).

SUPPLEMENTARY MATERIALS

www.sciencemag.org/content/353/6294/aaf4866/suppl/DC1
Materials and Methods
Figs. S1 to S8
Table S1
References (*53*–*66*)

16 February 2016; accepted 11 May 2016
Published online 26 May 2016
10.1126/science.aaf4866

RESEARCH ARTICLE

CHEMICAL BIOLOGY

Chemical genetic discovery of PARP targets reveals a role for PARP-1 in transcription elongation

Bryan A. Gibson,[1] Yajie Zhang,[2] Hong Jiang,[3]* Kristine M. Hussey,[4] Jonathan H. Shrimp,[3]† Hening Lin,[3] Frank Schwede,[5] Yonghao Yu,[2] W. Lee Kraus[1]‡

Poly[adenosine diphosphate (ADP)–ribose] polymerases (PARPs) are a family of enzymes that modulate diverse biological processes through covalent transfer of ADP-ribose from the oxidized form of nicotinamide adenine dinucleotide (NAD^+) onto substrate proteins. Here we report a robust NAD^+ analog–sensitive approach for PARPs, which allows PARP-specific ADP-ribosylation of substrates that is suitable for subsequent copper-catalyzed azide-alkyne cycloaddition reactions. Using this approach, we mapped hundreds of sites of ADP-ribosylation for PARPs 1, 2, and 3 across the proteome, as well as thousands of PARP-1–mediated ADP-ribosylation sites across the genome. We found that PARP-1 ADP-ribosylates and inhibits negative elongation factor (NELF), a protein complex that regulates promoter-proximal pausing by RNA polymerase II (Pol II). Depletion or inhibition of PARP-1 or mutation of the ADP-ribosylation sites on NELF-E promotes Pol II pausing, providing a clear functional link between PARP-1, ADP-ribosylation, and NELF. This analog-sensitive approach should be broadly applicable across the PARP family and has the potential to illuminate the ADP-ribosylated proteome and the molecular mechanisms used by individual PARPs to mediate their responses to cellular signals.

Adenosine diphosphate (ADP)–ribosylation of proteins is an important modulator of cellular processes, from the regulation of chromatin and transcription to protein translation and stability (*1*). Most of the 17 poly(ADP-ribose) polymerase (PARP) family members encoded in the human genome are enzymes with either mono- or poly(ADP-ribosyl) transferase activities, which covalently link ADP-ribose derived from the oxidized form of nicotinamide adenine dinucleotide (NAD^+) to their target proteins, primarily at glutamate, aspartate, and lysine residues (*2*). PARPs 1, 2, and 3, collectively referred to as the DNA-dependent PARPs, are a group of nuclear proteins with DNA-dependent mono- (PARP-3) or poly- (PARPs 1 and 2) ADP-ribosyl transferase activities involved in DNA repair, chromosome maintenance, chromatin regulation, and gene expression (*2*, *3*). Previous studies using immune-based enrichment, various affinity resins, or protein microarrays to identify the targets of ADP-ribosylation lacked specificity for individual PARP family members (*4*). A recent chemical genetics approach targeting a conserved residue in the nicotinamide binding site of the PARP catalytic domain was a technological advance but unfortunately ablated the poly(ADP-ribosyl) transferase activity of PARP enzymes, while preserving mono(ADP-ribosyl) transferase activity (*5*, *6*). A single chemical genetic approach that preserves the natural mono- and poly(ADP-ribosyl) transferase activities of PARP enzymes and is broadly applicable across the PARP family should be of great utility.

[1]The Laboratory of Signaling and Gene Expression, Cecil H. and Ida Green Center for Reproductive Biology Sciences and The Division of Basic Research, Department of Obstetrics and Gynecology, University of Texas Southwestern Medical Center, Dallas, TX 75390, USA. [2]Department of Biochemistry, University of Texas Southwestern Medical Center, Dallas, TX 75390, USA. [3]Howard Hughes Medical Institute and Department of Chemistry, Cornell University, Ithaca, NY 14850, USA. [4]Sarepta Therapeutics, Cambridge, MA 02142, USA. [5]Biolog Life Science Institute, D-28199 Bremen, Germany. *Present address: Interdisciplinary Research Center on Biology and Chemistry, Shanghai Institute of Organic Chemistry, Chinese Academy of Science, Shanghai 201203, China. †Present address: Chemical Biology Laboratory, Center for Cancer Research, National Cancer Institute, Frederick, MD 21702, USA. ‡Corresponding author. Email: lee.kraus@utsouthwestern.edu

An analog-sensitive PARP (asPARP) approach targeting the adenine moiety of NAD^+

Our previous studies indicated that the adenine moiety of NAD^+ is a useful target for chemical modification to alter the catalytic activity and chemistry of PARP family members (*7*). In this regard, we developed an adenine-focused, NAD^+ analog–sensitive approach for PARPs that preserves their poly(ADP-ribosyl) transferase activity (Fig. 1A and fig. S1A) and is capable of identifying the specific targets of individual PARP family members. Analog sensitivity is achieved by mutation of a large "gatekeeper" amino acid in the active site of a protein to a smaller residue, creating a pocket that fits a bulky R group on an engineered substrate, whereas interaction of the bulky R group with the wild-type (WT) enzyme would have been sterically blocked (*8*). We initially focused on PARP-1, an abundant and ubiquitously expressed PARP protein in metazoans. To identify a gatekeeper residue in PARP-1, we changed 10 large residues buried within the active site and facing the adenine ring of NAD^+ to glycine or alanine on the basis of a molecular model (Fig. 1A and figs. S1B and S2). We selected the eight position of the adenine ring of NAD^+ as the site for R group addition because its modification precludes ADP-ribosylation with WT PARP-1 (wtPARP-1) or other PARPs (*7*), a feature critical to the analog-sensitive approach. We then synthesized a library of 11 NAD^+ analogs, each with a different R group at position eight, from 8-methylamino-NAD^+ to 8-benzylamino-NAD^+ (Fig. 1B). In a screen of the 20 PARP-1 mutants versus the 11 NAD^+ analogs, we identified two different gatekeeper residues, L^{877} and I^{895} (*9*), whose mutation to alanine results in analog-sensitive activity in a PARP-1 automodification assay (Fig. 1C and figs. S1C and S3). Critically, both of these residues are buried within the active site of the enzyme; thus, their mutation is unlikely to affect protein-protein interactions that might influence substrate selectivity. Although L^{877} and I^{895} are separated by 18 amino acids in the PARP-1 linear sequence, they are adjacent to one another and proximal to the eight position of the adenine ring in three-dimensional (3D) space (Fig. 1D). These results support our molecular model of PARP-1 interactions with NAD^+ (figs. S1B and S2), as well as the structural basis for our asPARP approach.

To extend the utility of our asPARP approach, we functionalized the R group of 8-butylthio-NAD^+ (NAD^+ analog *6* in Fig. 1B) with an alkyne moiety to generate 8-Bu(3-yne)T-NAD^+ (Fig. 2A). 8-Bu(3-yne)T-NAD^+ is an NAD^+ analog with a single bifunctional R group at position 8, which facilitates asPARP-selective ADP-ribosylation. The R group also allows incorporation of alkynes into the posttranslationally modified substrates, for subsequent use in azide-alkyne cycloaddition ("click" chemistry) reactions to label or purify the PARP targets (Fig. 2B). asPARP-1 [$L^{877}\rightarrow A^{877}$ (L877A)] with 8-Bu(3-yne)T-NAD^+ acted similarly to the previously screened analogs, nearing WT enzyme kinetics when compared to PARP-1 and NAD^+ (fig. S4). Critically, this "clickable" NAD^+ analog also supports activity with asPARP-2 and asPARP-3 mutants (L443A and L394A, respectively, homologous to L^{877} of PARP-1) (Fig. 2C and fig. S5, A and B). The ability to transfer this analog-sensitive activity to the other PARPs by mutation of the conserved gatekeeper residue (Fig. 2C and fig. S5, C to G) suggests broad utility of this approach across the PARP family, for both mono- and poly(ADP-ribosyl) transferases.

Identification of site-specific nuclear substrates of PARPs 1, 2, and 3

We used the asPARP approach to identify site-specific ADP-ribosylation of glutamate and aspartate residues for nuclear substrates of PARPs 1, 2,

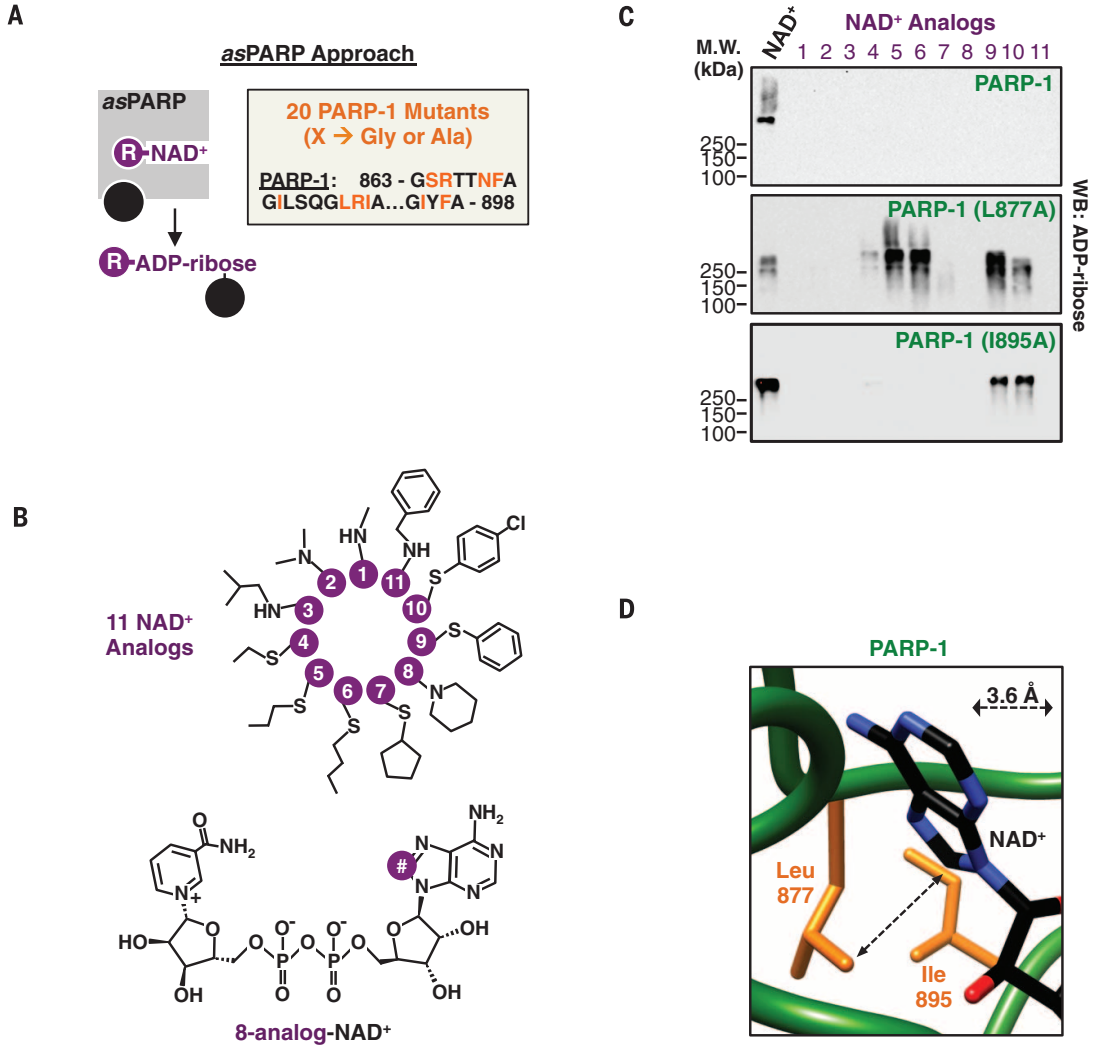

Fig. 1. Structure-based engineering of an asPARP-1 mutant. (**A**) (Left) Schematic illustrating NAD$^+$ analog sensitivity in PARP proteins. R, unnatural chemical moieties added to NAD$^+$. (Right) Residues in PARP-1 selected for mutation to glycine or alanine for discovery of gatekeeper residues. (**B**) Chemical structures of the 11 NAD$^+$ analogs used for screening for asPARP-1. (**C**) Western blot (WB) for ADP-ribose from automodification reactions containing PARP-1 or PARP-1 mutants (L877A and I895A) and NAD$^+$ or NAD$^+$ analogs. M.W., molecular weight. (**D**) Depiction of the spatial relationship between position eight of the adenine ring in NAD$^+$ and the gatekeeper residues.

and 3 (*10*). We incubated purified recombinant asPARPs 1, 2, or 3 with HeLa cell nuclear extract in the presence of 8-Bu(3-yne)T-NAD$^+$, which resulted in PARP-specific labeling of extract proteins (Fig. 3A). We then "clicked" the 8-Bu(3-yne) T-ADP-ribose–labeled proteins to azide-agarose, which led to their covalent attachment to the agarose resin, allowing extensive washing with denaturants, strong detergents, and organic solvents. We performed trypsin-based peptide identification of the ADP-ribosylated proteins by liquid chromatography–tandem mass spectrometry (LC-MS/MS) (protein ID), washed extensively again, and eluted the ADP-ribosylated peptides using hydroxylamine to identify the sites of ADP-ribosylation by LC-MS/MS (site ID) (*10*) (Fig. 3B). This approach revealed distinct and overlapping sites of PARP-1–, PARP-2–, and PARP-3–mediated ADP-ribosylation (Fig. 3C and fig. S6A). Ontological analyses of the target proteins revealed enrichment of terms related to transcription and DNA repair—consistent with the known biology of PARPs 1, 2, and 3—as well as additional terms, suggesting previously unknown functions (Fig. 3D and fig. S6B).

Motif analyses at the sites of PARP-1–, PARP-2–, and PARP-3–mediated ADP-ribosylation indicate some similarities in sequence preference among the three PARPs (e.g., glutamate residue proximal to the site of modification) but point out differences as well (fig. S6C). The sites of PARP-1–, PARP-2–, and PARP-3–mediated ADP-ribosylation that we identified herein partially overlapped and were more numerous than sites of ADP-ribosylation identified using other approaches (fig. S7), with excellent agreement for the specific sites of ADP-ribosylation in common targets when compared to a previous cell-based bulk ADP-ribosylation assay (*10*) (Fig. 3E). We also observed considerable overlap with an asPARP-1 data set that we generated from intact mouse embryonic fibroblast (MEF) nuclei (fig. S8). Collectively, these results show that our asPARP approach robustly and faithfully identifies sites of ADP-ribosylation mediated by a specific PARP family member.

Negative elongation factor (NELF) is ADP-ribosylated in a positive transcription elongation factor (P-TEFb)–dependent manner

Previous reports implicating the *Drosophila melanogaster* homolog of PARP-1 as a key modulator of RNA polymerase II (Pol II) pause release at heat shock loci (*11*, *12*), together with the identification of NELF-A and -E as ADP-ribosylated proteins (Fig. 4A and fig. S6B), led us to explore whether PARP-1 activity and ADP-ribosylation of the NELF complex might play a role in the control of transcription elongation. The negative elongation factor complex (NELF-A, -B,

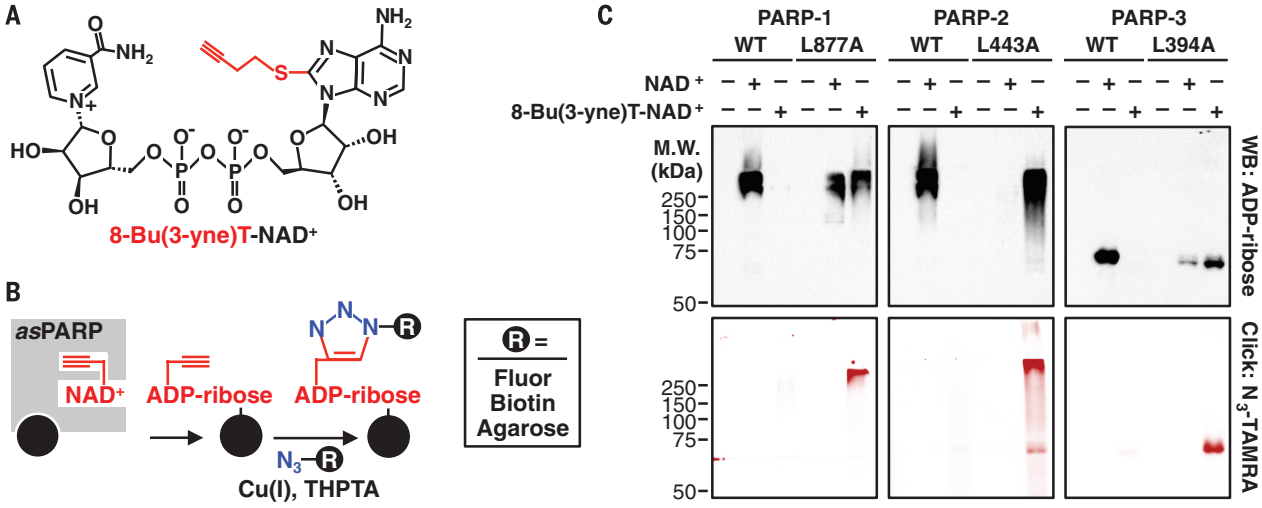

Fig. 2. Activity of asPARPs 1, 2, and 3 with a "clickable" NAD$^+$ analog. (**A**) Chemical structure of the bifunctional NAD$^+$ analog 8-Bu(3-yne)T-NAD$^+$ with the "clickable" analog sensitivity–inducing, alkyne-containing R group highlighted in red. (**B**) Schematic illustrating asPARP activity-dependent, click chemistry–mediated covalent attachment of fluorophores, biotin, or agarose resin to 8-Bu(3-yne)T-ADP-ribosylated proteins. THPTA, tris(3-hydroxypropyltriazolylmethyl)amine. (**C**) Automodification reactions with WT or analog-sensitive PARP-1, PARP-2, and PARP-3 analyzed by Western blotting for ADP-ribose (top) or click chemistry–based in-gel fluorescence (bottom). TAMRA, tetramethylrhodamine.

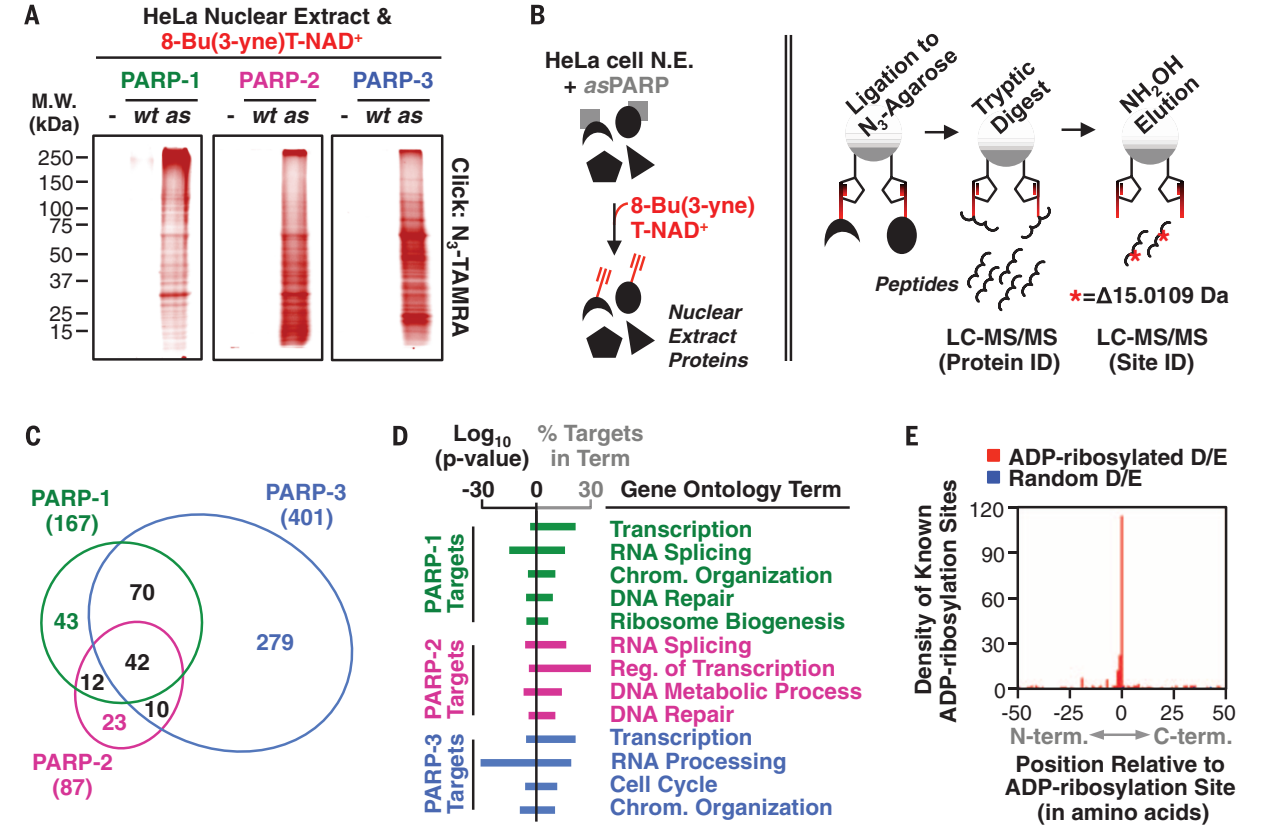

Fig. 3. Using asPARP mutants to unambiguously identify the ADP-ribosylation targets of DNA-dependent PARPs. (**A**) In-gel fluorescence of HeLa cell nuclear extract proteins conjugated to azido-TAMRA after reactions with 8-Bu(3-yne)T-NAD$^+$ in the presence of wild-type (*wt*) or analog-sensitive (*as*) PARP-1, PARP-2, or PARP-3. (**B**) Depiction of the strategy for LC-MS/MS detection of PARP-specific ADP-ribosylation sites. (Left) asPARP-dependent labeling of HeLa cell nuclear extract (N.E.) proteins (represented by various shapes) using 8-Bu(3-yne)T-NAD$^+$ (red). (Right) Postlabeling sample processing for LC-MS/MS. The 8-Bu(3-yne)T-ADP-ribosylated proteins are covalently linked to azide-agarose by copper-catalyzed cycloaddition (click chemistry; represented by pentagons), washed, and digested with trypsin to release peptides for protein identification. The remaining covalently linked peptides are eluted using hydroxyl amine (NH_2OH) with a mass shift of 15.0109 Da, which allows for identification of ADP-ribosylation sites. (**C**) Venn diagram depicting the overlap of the protein targets of PARP-1, PARP-2, and PARP-3. (**D**) Gene ontology terms enriched for the sets of PARP-1, PARP-2, and PARP-3 targets. (**E**) Histogram of the 2D relationship between previously identified ADP-ribosylation sites (*10*) with those identified herein. D/E, glutamate or aspartate residues.

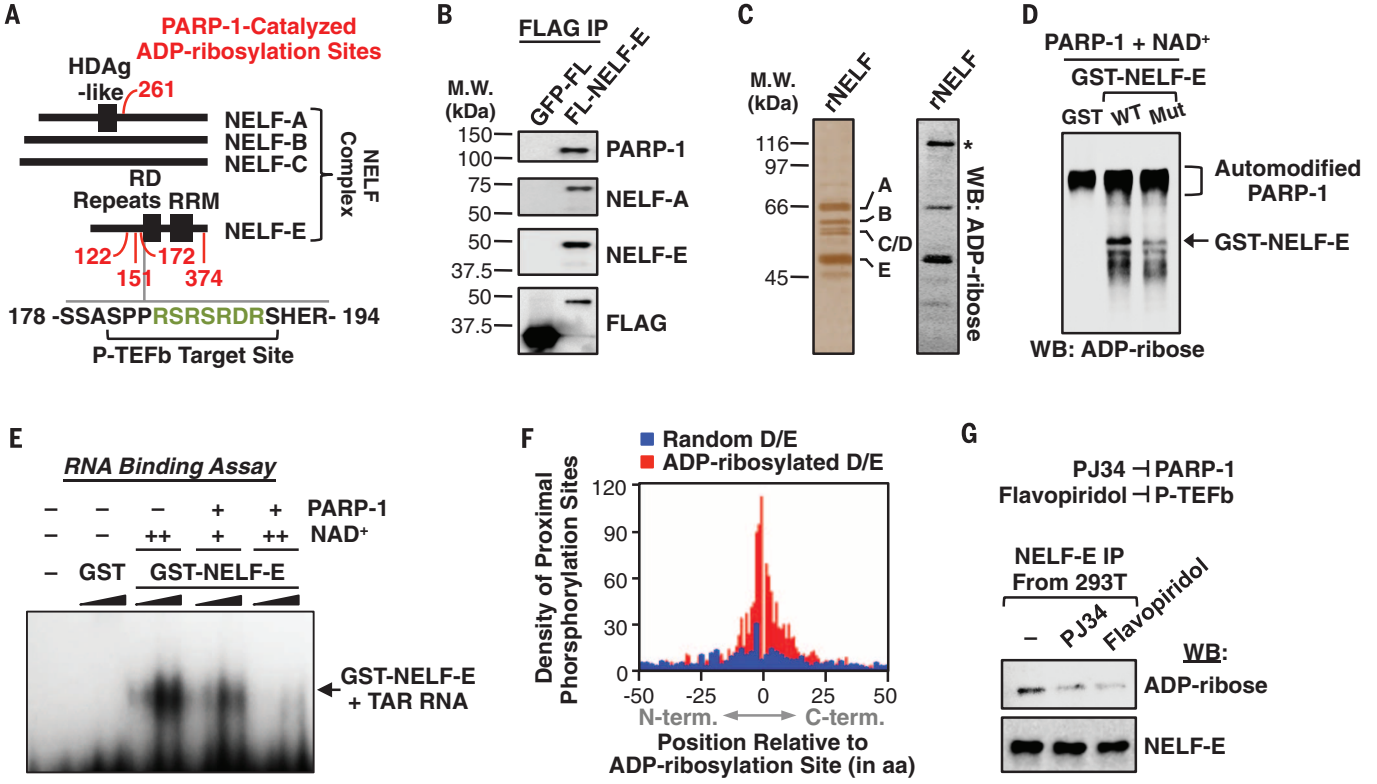

Fig. 4. P-TEFb-dependent ADP-ribosylation of NELF by PARP-1. (**A**) Schematic showing the distribution of PARP-1 ADP-ribosylation sites (red), P-TEFb phosphorylation sites, and a PARP target-enriched 7-nucleotide oligomer RSRSRDR (green) on proteins in the NELF complex. (**B**) Western blot analysis of immunoprecipitated FLAG-tagged NELF-E or GFP from 293T cells. (**C**) Silver-stained SDS-PAGE gel (left) and ADP-ribose Western blot (right) of the immunopurified NELF complex. The asterisk indicates automodified PARP-1. (**D**) Western blot for ADP-ribose of in vitro modification reactions containing glutathione *S*-transferase (GST), GST-tagged WT NELF-E, or GST-tagged ADP-ribosylation site point mutant NELF-E, PARP-1, and NAD^+ as indicated. (**E**) NELF-E/TAR RNA electrophoretic mobility shift assay with or without PARP-1–mediated ADP-ribosylation. GST or GST–NELF-E was titrated between 0.1 to 1.0 μM, and NAD^+ was added at 25 μM (+) or 100 μM (++) during the ADP-ribosylation reaction. (**F**) Histogram of the relationship between the ADP-ribosylation sites identified herein and the nearest incidence of known phosphorylation modifications on PARP target proteins. aa, amino acids. (**G**) Western blot analysis of immunoprecipitated FLAG-tagged NELF-E from 293T cells treated with vehicle, the PARPi PJ34, or the P-TEFb/CDK9 inhibitor flavopiridol.

-C or -D, and -E) functions to restrict transcriptional elongation and stimulate promoter-proximal pausing by Pol II (*13*). Immunoaffinity purification of NELF from mammalian cells expressing FLAG epitope–tagged NELF-E demonstrated that PARP-1 interacts with the NELF complex (Fig. 4B) and that NELF-E and NELF-A are ADP-ribosylated in mammalian cells (Fig. 4C). Mutation of the four NELF-E glutamate residues identified in our proteomic screen (E122, E151, E172, and E374) (Fig. 4A) to glutamines, a structurally similar residue refractory to ADP-ribosylation, resulted in a substantial reduction in NELF-E modification by PARP-1 (Fig. 4D). Finally, using an electrophoretic mobility shift assay with a model NELF-E–interacting RNA [i.e., HIV trans-activation response element (TAR)], we found that ADP-ribosylation of NELF-E ablates its ability to bind RNA, a function necessary for the establishment paused Pol II (*14*) (Fig. 4E and fig. S9).

We found that phosphorylation sites (Fig. 4F) and, to a lesser extent, sites of other post-translational modifications (fig. S10A) are frequently located at or near ADP-ribosylation sites across the proteome. This suggests a broad role for ADP-ribosylation as a modulator at hubs of regulatory activity, as well as a more specific regulatory role for ADP-ribosylation (and PARPs) in cooperation with phosphorylation (and kinases) across the proteome. In fact, using a PARP inhibitor (PARPi) (i.e., PJ34) and a cyclin-dependent kinase 9 (CDK9) inhibitor (i.e., flavopiridol), we observed that ADP-ribosylation of NELF-E in mammalian cells is dependent on phosphorylation by CDK9/P-TEFb (Fig. 4G), a kinase that phosphorylates Pol II, DSIF, and NELF-E (*15*). Furthermore, both inhibitors reduced the extent of serine-2 phosphorylation (Ser2P) in the C-terminal domain heptapeptide repeat of the Pol II RPB1 subunit in cells (fig. S10B). Because elevated Ser2P is associated with actively elongating Pol II (*15*), these results indicate a reduction in elongating Pol II upon inhibition of PARP-1 and CDK9. Interestingly, a 7-nucleotide oligomer amino acid sequence (RSRSRDR) enriched in targets of PARP-1 (fig. S10C) is located within the previously identified phosphorylation target site for P-TEFb in NELF-E, near a cluster of PARP-1–mediated ADP-ribosylation sites (Fig. 4A). Together, these results highlight the functional links between PARP-1–mediated ADP-ribosylation and transcription-related phosphorylation.

Identifying sites of PARP-1–mediated ADP-ribosylation across the genome

Although recent genomic approaches have facilitated the detection of sites of ADP-ribosylation genome-wide in the context of DNA damage (*16*), they have not allowed unambiguous assignment of genomic ADP-ribosylation events to a specific PARP family member in unstimulated cells. To unambiguously define sites of PARP-1–mediated ADP-ribosylation across the genome, we developed an assay, which we call "Click-ChIP-seq" (click chemistry–based chromatin isolation and precipitation with deep sequencing), using the asPARP-1 approach in nuclei. We expressed green fluorescent protein (GFP) (as a control), wtPARP-1, or asPARP-1 in *Parp1*$^{-/-}$ MEFs (fig. S11A). ADP-ribosylation after addition of 8-Bu(3-yne)T-NAD^+ was clearly evident in the nuclei of *Parp1*$^{-/-}$ MEFs expressing asPARP-1, but not wtPARP-1 (fig. S11B). We then collected 8-Bu(3-yne)T-NAD^+–treated nuclei, cross-linked them with formaldehyde, "clicked" the 8-Bu(3-yne)T-ADP-ribose to biotin,

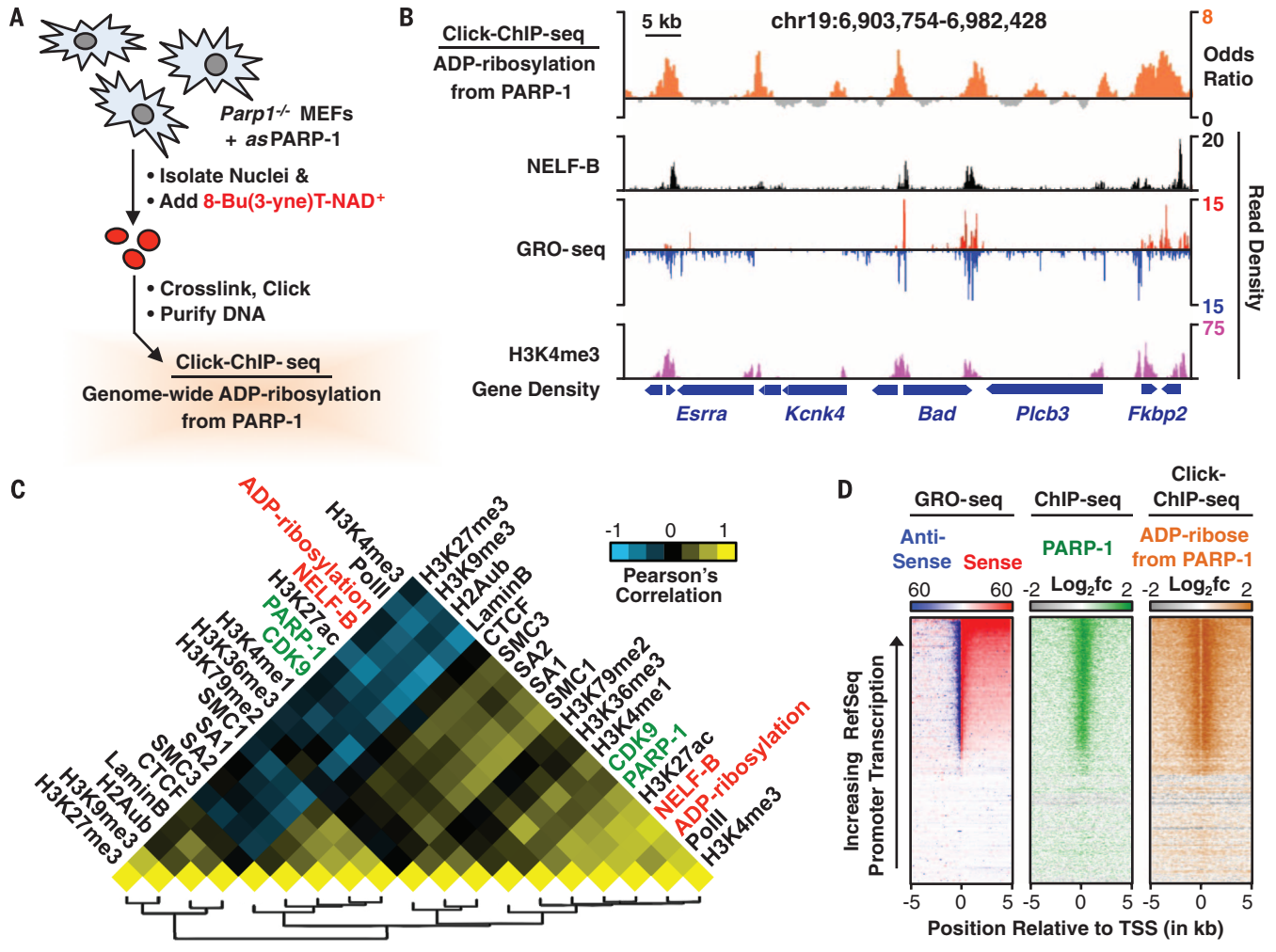

Fig. 5. Click-ChIP-seq, an asPARP-1–based method for identifying the genome-wide distribution of ADP-ribosylation events catalyzed by a specific PARP protein. (**A**) Schematic representation of Click-ChIP-seq. Nuclei are isolated from *Parp*$^{-/-}$ MEFs expressing asPARP-1, labeled with 8-Bu(3-yne)T-NAD$^+$, subjected to cross-linking with formaldehyde, and then processed for chromatin immunoprecipitation. The enriched DNA is subjected to deep sequencing. (**B**) Genome browser view of a multigene locus of the mouse genome showing PARP-1–catalyzed ADP-ribosylation (from Click-ChIP-seq) with other genomic features. (**C**) Heat map showing pairwise clustered correlations between genomic features and PARP-1–mediated ADP-ribosylation from Click-ChIP-seq. (**D**) Heat-map representations showing PARP-1–catalyzed ADP-ribosylation (from Click-ChIP-seq) in comparison to PARP-1 (from ChIP-seq) and transcription (from GRO-seq) at the promoters of all RefSeq genes. TSS, transcription start site.

and sheared the chromatin by sonication, finally subjecting the material to an assay analogous to chromatin immunoprecipitation (Fig. 5A and fig. S11C). A quantitative polymerase chain reaction–based assay of the enriched genomic DNA revealed asPARP-1–specific ADP-ribosylation at gene promoters in nuclei isolated from MEFs (fig. S11D).

Click-ChIP-seq revealed robust enrichment of PARP-1–mediated ADP-ribosylation at the promoters of transcriptionally active genes, which were defined by an enrichment of histone H3 lysine-4 trimethylation (H3K4me3, a mark of active promoters, from ChIP-seq) and actively transcribing Pol II [from global run-on sequencing (GRO-seq)] (Fig. 5B). This assay also revealed genomic loci with significant peaks of PARP-1 lacking enrichment of PARP-1–mediated ADP-ribosylation located in regions of repressed chromatin (fig. S12), which are difficult to discern in the absence of the specificity provided by the asPARP approach. Genome-wide correlation analyses between PARP-1–mediated ADP-ribosylation and a variety of other histone modifications and chromatin or transcription-related factors revealed strong clustering, as well as positive correlations with PARP-1 (correlation coefficient r = 0.606) and NELF-B (r = 0.754) (Fig. 5C). Heat-map representations of the genomic data highlight the relationships at gene promoters among PARP-1–mediated ADP-ribosylation; Pol II accumulation; and H3K4me3, NELF-B, and PARP-1 enrichment (Fig. 5D and fig. S13A). PARP-1–mediated ADP-ribosylation and CDK9 occupancy at promoters strongly correlated with low levels of Pol II pausing (fig. S13B). These results suggest that PARP-1–mediated ADP-ribosylation may act in a manner similar to CDK9/P-TEFb–mediated phosphorylation to promote the release of paused Pol II into productive elongation.

Role of PARP-1–mediated ADP-ribosylation of NELF in the release of paused Pol II

To determine the role of PARP-1 in the release of paused Pol II, we performed GRO-seq in MCF-7 breast cancer cells to monitor the effects of short hairpin RNA (shRNA)–mediated PARP-1 knockdown or treatment with the PARPi PJ34 on Pol II pausing. GRO-seq is a genomic assay that reveals the location of transcriptionally engaged RNA polymerases globally (*17*). We observed an accumulation of reads in the peaks of paused Pol II upon PARP-1 knockdown or treatment with PARPi [compared with an untreated luciferase knockdown control (Luc)] at gene promoters (fig. S14). This effect was evident genome-wide

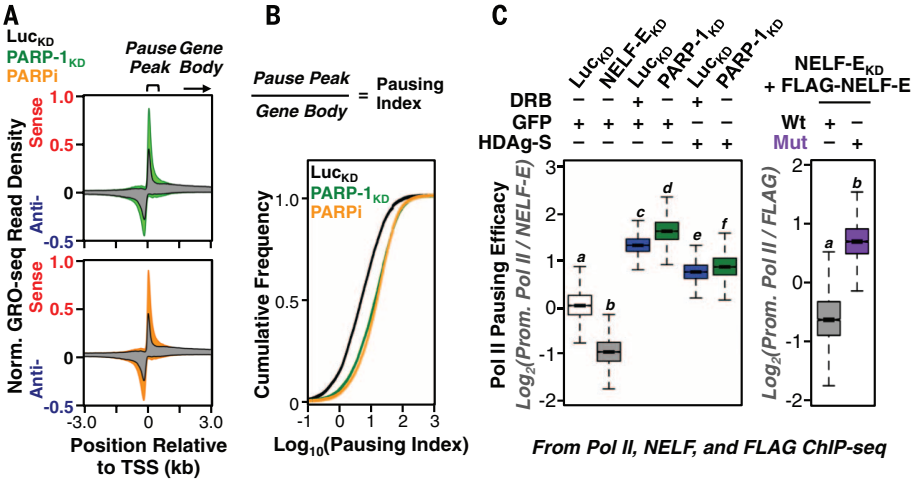

Fig. 6. Genome-wide functional links between PARP-1–catalyzed ADP-ribosylation, NELF binding, and Pol II pausing. (**A**) Metagenes of GRO-seq read density at the promoters of all expressed RefSeq genes from MCF-7 cells subjected to shRNA-mediated knockdown with either luciferase (control) or PARP-1 shRNAs (top) or treatment with the PARPi PJ34 (bottom). (**B**) Pol II pausing indices at the promoters of all transcribed RefSeq genes from MCF-7 cells subjected to shRNA-mediated knockdown with either luciferase (control) or PARP-1 shRNAs or treatment with PJ34. (**C**) Box plots of promoter proximal Pol II "pausing efficacy," as determined by Pol II and NELF ChIP-seq in MCF-7 cells under the different experimental conditions indicated for the top quartile of expressed RefSeq genes. Bars marked with different letters are significantly different ($P < 2.16 \times 10^{-16}$; *t* test).

(Fig. 6A), with a clear increase in global Pol II pausing indices upon PARP-1 depletion or inhibition (Fig. 6B). At active promoters with a significant accumulation of GRO-seq reads in the paused Pol II peak upon PARP-1 knockdown, we observed decreased GRO-seq reads in the gene bodies (fig. S15, see panel B for the gene body effects), which suggests that PARP-1 activity is necessary to achieve an efficient release of Pol II into productive elongation.

We showed that a large fraction of PARP-1–regulated genes (determined by PARP-1 knockdown) are also regulated by P-TEFb [determined by treatment with 5,6-dichloro-1-β-D-ribofuranosylbenzimidazole (DRB)] and NELF (determined by NELF knockdown), with respect to expression (by RNA-seq; fig. S16, A and B) and Pol II pausing (by Pol II ChIP-seq; fig. S16C). In addition, we found that the viral NELF inhibitor HDAg-S (*18*) reverses the inhibitory effects of both PARP-1 knockdown and DRB treatment on Pol II pausing, as determined from a ChIP-seq–based "Pol II pausing efficacy" assay (i.e., promoter proximal Pol II enrichment divided by NELF-E enrichment) (Fig. 6C and figs. S17 and S18). Finally, we showed that a NELF-E ADP-ribosylation site mutant (Mut) produces a NELF complex that is resistant to the inhibitory effects of PARP-1 and is a more potent inducer of Pol II pausing than the NELF complex containing WT NELF-E, in spite of lower cellular expression levels (Fig. 6C and figs. S18 and S19). Collectively, our data point to a functional link between CDK9-mediated phosphorylation, PARP-1–mediated ADP-ribosylation, and NELF-mediated Pol II pausing (fig. S20). Our results indicate that PARP-1–dependent ADP-ribosylation of NELF-E reinforces P-TEFb–mediated Pol II pause release and productive elongation for a subset of NELF-regulated genes, especially those with elevated NELF and Pol II loading, as well as H3K4me3 enrichment (fig. S21). Finally, these mechanisms are functional even at promoters where PARP-1 serves noncatalytic functions, such as the expulsion of the linker histone H1 from nucleosomes (*19*) (fig. S22).

Conclusions and perspectives

PARP proteins have gained considerable attention as therapeutic targets for the treatment of cancers and other diseases (*20*), although the broader biology of the PARP family remains largely unexplored. Understanding the biology of PARP proteins requires comprehension of the protein substrates that they modify. In this regard, we have developed an asPARP approach that preserves the natural mono- and poly(ADP-ribosyl) transferase activities of PARP enzymes, which can be coupled with protein mass spectrometry to identify the targets of specific PARP family members. We have also repurposed this asPARP technology for use in genomic assays to identify the genome-wide distribution of ADP-ribosylation events catalyzed by a specific PARP protein. Our studies focusing on NELF illustrate how an integrated approach based on asPARP technology can further the exploration of the biological functions for ADP-ribosylation. Our asPARP approach, which uses a conserved residue in the PARP catalytic domain, should be broadly applicable across the PARP family. This technique will facilitate the rapid, robust, and systematic identification of the molecular targets and mechanisms of action of the entire PARP family, with the potential to transform our understanding of PARP protein functions in physiology and disease.

REFERENCES AND NOTES

1. B. A. Gibson, W. L. Kraus, *Nat. Rev. Mol. Cell Biol.* **13**, 411–424 (2012).
2. S. Vyas *et al.*, *Nat. Commun.* **5**, 4426 (2014).
3. M. O. Hottiger, *Annu. Rev. Biochem.* **84**, 227–263 (2015).
4. C. M. Daniels, S.-E. Ong, A. K. L. Leung, *Mol. Cell* **58**, 911–924 (2015).
5. I. Carter-O'Connell, H. Jin, R. K. Morgan, L. L. David, M. S. Cohen, *J. Am. Chem. Soc.* **136**, 5201–5204 (2014).
6. I. Carter-O'Connell *et al.*, *Cell Rep.* **14**, 621–631 (2016).
7. H. Jiang, J. H. Kim, K. M. Frizzell, W. L. Kraus, H. Lin, *J. Am. Chem. Soc.* **132**, 9363–9372 (2010).
8. K. M. Specht, K. M. Shokat, *Curr. Opin. Cell Biol.* **14**, 155–159 (2002).
9. Single-letter abbreviations for the amino acid residues are as follows: A, Ala; C, Cys; D, Asp; E, Glu; F, Phe; G, Gly; H, His; I, Ile; K, Lys; L, Leu; M, Met; N, Asn; P, Pro; Q, Gln; R, Arg; S, Ser; T, Thr; V, Val; W, Trp; and Y, Tyr.
10. Y. Zhang, J. Wang, M. Ding, Y. Yu, *Nat. Methods* **10**, 981–984 (2013).
11. S. J. Petesch, J. T. Lis, *Cell* **134**, 74–84 (2008).
12. A. Tulin, A. Spradling, *Science* **299**, 560–562 (2003).
13. K. Adelman, J. T. Lis, *Nat. Rev. Genet.* **13**, 720–731 (2012).
14. Y. Yamaguchi, N. Inukai, T. Narita, T. Wada, H. Handa, *Mol. Cell. Biol.* **22**, 2918–2927 (2002).
15. J. Guo, D. H. Price, *Chem. Rev.* **113**, 8583–8603 (2013).
16. G. Bartolomei, M. Leutert, M. Manzo, T. Baubec, M. O. Hottiger, *Mol. Cell* **61**, 474–485 (2016).
17. L. J. Core, J. J. Waterfall, J. T. Lis, *Science* **322**, 1845–1848 (2008).
18. Y. Yamaguchi *et al.*, *Science* **293**, 124–127 (2001).
19. R. Krishnakumar *et al.*, *Science* **319**, 819–821 (2008).
20. N. J. Curtin, C. Szabo, *Mol. Aspects Med.* **34**, 1217–1256 (2013).

ACKNOWLEDGMENTS

We thank M. Chae, Q. Liang, J. DeBrabander, U. Havemann, and D. Imren for technical assistance and members of the Kraus laboratory for helpful discussions about this project. The asPARP expression constructs and the NAD^+ analogs can be obtained from University of Texas (UT) Southwestern Medical Center and Biolog Life Science Institute, respectively, under a material transfer agreement. W.L.K., B.A.G., F.S., and H.L. are inventors on U.S. patent application no. 62/144,711, filed by UT Southwestern Medical Center, related to the asPARP technology. W.L.K. and B.A.G. are inventors on U.S. patent application nos. 62/009,955 and PCT/US2015/034852, filed by UT Southwestern Medical Center, related to the ADP-ribose detection reagents. Y.Y. is an inventor on U.S. patent no. 8828672 B2, filed by UT Southwestern Medical Center, related to technology for the determination of D/E-ADP-ribosylation sites. This work was supported by a predoctoral fellowship from the American Heart Association to B.A.G.; grants from the Cancer Prevention and Research Institute of Texas (CPRIT R1103), the Welch Foundation (I-1800), and the UT Southwestern Endowed Scholars Program to Y.Y., who is the Virginia Murchison Linthicum Scholar in Medical Research and a CPRIT Scholar in Cancer Research; a grant from the NIH National Institute of General Medical Sciences (GM086703) to H.L.; and a grant from the NIH National Institute of Diabetes and Digestive and Kidney Diseases (DK069710) and support from the Cecil H. and Ida Green Center for Reproductive Biology Sciences Endowments to W.L.K. W.L.K. is a founder and consultant for Ribon Therapeutics. The genomic data sets from this study are available from the National Center for Biotechnology Information Gene Expression Omnibus database under accession numbers GSE74141 (ChIP-seq) and GSE74142 (GRO-seq and RNA-seq). The proteomic data sets generated for these studies are available in table S1. Author contributions: On the basis of (*7*), B.A.G. conceived the asPARP concept, with input from W.L.K. W.L.K. conceived the Click-ChIP-seq method, which was further developed by B.A.G. B.A.G. performed all experiments and computational analyses, except as follows: H.J., J.H.S., H.L., and F.S. synthesized all precursors and NAD^+ analogs used in this study. B.A.G. and H.J. performed the enzyme kinetics assays. B.A.G., Y.Z., and Y.Y. prepared the samples and ran the LC-MS/MS analysis. K.M.H. made the PARP-1 knockdown MCF-7 cells and prepared the GRO-seq samples. W.L.K. secured funding to support this project and provided intellectual support for all aspects of the work. B.A.G. and W.L.K. prepared the figures and wrote the paper.

SUPPLEMENTARY MATERIALS

www.sciencemag.org/content/353/6294/45/suppl/DC1
Materials and Methods
Figs. S1 to S22
Tables S1 and S2
References (*21–49*)

30 March 2016; accepted 19 May 2016
Published online 2 June 2016
10.1126/science.aaf7865

REPORTS

ORGANIC CHEMISTRY

Catalytic, asymmetric difluorination of alkenes to generate difluoromethylated stereocenters

Steven M. Banik, Jonathan William Medley, Eric N. Jacobsen*

Difluoromethyl groups possess specific steric and electronic properties that invite their use as chemically inert surrogates of alcohols, thiols, and other polar functional groups important in a wide assortment of molecular recognition processes. We report here a method for the catalytic, asymmetric, migratory geminal difluorination of β-substituted styrenes to access a variety of products bearing difluoromethylated tertiary or quaternary stereocenters. The reaction uses commercially available reagents (*m*-chloroperbenzoic acid and hydrogen fluoride pyridine) and a simple chiral aryl iodide catalyst and is carried out readily on a gram scale. Substituent effects and temperature-dependent variations in enantioselectivity suggest that cation-π interactions play an important role in stereodifferentiation by the catalyst.

The effect of fluoroalkyl groups on the physical and biological properties of molecules (*1*–*4*) has inspired substantial research effort aimed toward identifying general methods for the controlled introduction of these motifs into organic compounds (*5*–*7*). Particular focus on the geminal or 1,1-difluoro group, motivated by its facile synthesis from simple carbonyl compounds, has showcased its useful properties as a chemically inert isostere of a variety of polar functional groups (*8*). The difluoromethyl group (CHF_2) has the additional feature of bearing a slightly acidic C–H bond, allowing it to act as a lipophilic hydrogen-bond donor (*9*) and, by extension, as a bioisostere for alcohols and thiols (Fig. 1A) (*8*). Difluoromethyl group incorporation into molecules can therefore confer the advantageous effects of fluorination, such as modulated bioavailability, metabolic stability, and lipophilicity, while also introducing or retaining a key recognition element for biologic targets.

Stereochemically defined hydrogen-bond donors are often critical contributors to specific interactions of bioactive small molecules with chiral receptors (e.g., enzymes and proteins). For difluoromethylated compounds to be fully exploited as bioisosteres of protic functional groups, practical methods for their stereocontrolled preparation are needed. However, no broadly effective strategy for the construction of enantioenriched tertiary and quaternary centers bearing CHF_2 groups has emerged. To date, elaboration of prochiral electrophiles bearing pre-installed CHF_2 groups has been the most widely studied strategy for generating enantioenriched CHF_2-containing small molecules (Fig. 1B) (*10*–*13*). Deoxyfluorination of aldehydes (*14*–*16*) is a conceptually straightforward approach to constructing CHF_2 groups, but α-branched chiral tertiary aldehydes are prone to epimerization and other decomposition pathways (*15*, *17*, *18*), whereas α-quaternary aldehydes are susceptible to rearrangement reactions (*14*, *19*–*21*) (Fig. 1C). Other established methods for *gem*-difluorination, such as fluorodesulfurization of dithianes or dithiolanes, have not been widely applied to the synthesis of compounds bearing CHF_2 groups bound to defined stereogenic centers (*22*, *23*). Although moderate progress has been achieved in the development of enantioselective methods targeting C_{sp^3}–C_{CHF_2} bond construction, these approaches generally require the use of a CHF_2 equivalent that must be unmasked in a separate

Department of Chemistry and Chemical Biology, Harvard University, Cambridge, MA 02138, USA.
*Corresponding author. Email: jacobsen@chemistry.harvard.edu

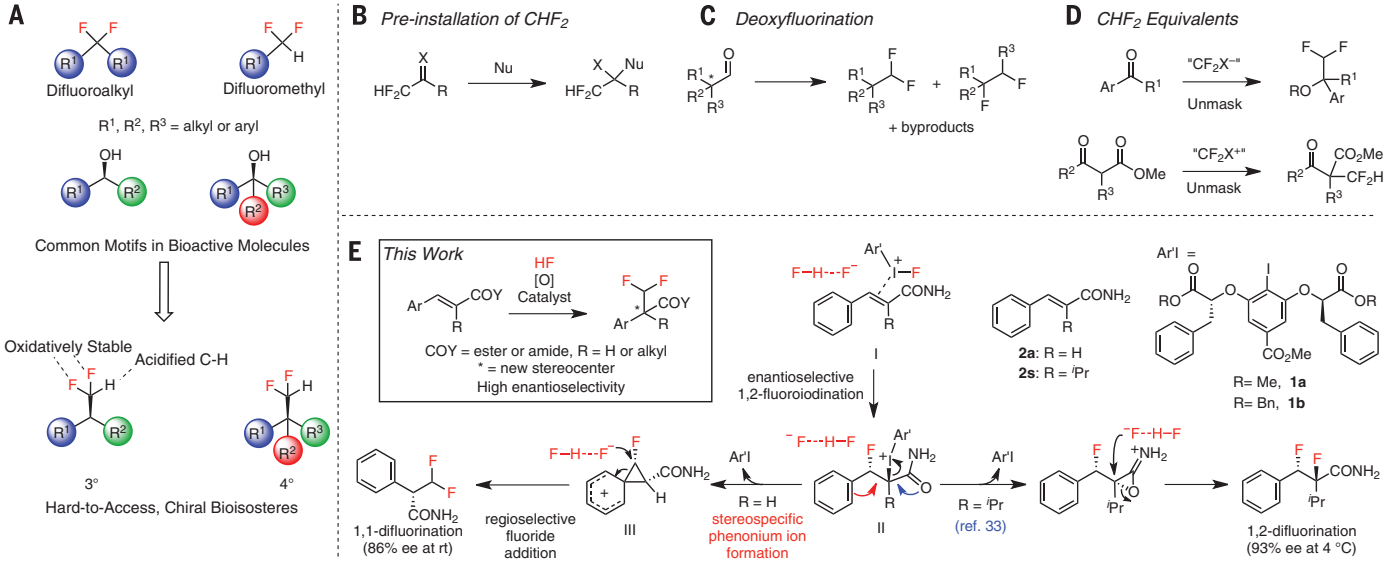

Fig. 1. Previous and current approaches to difluoromethylation. (**A**) The difluoromethyl group is a bioisostere for alcohols and other protic functionality. (**B** to **D**) Reported strategies for the preparation of enantioenriched difluoromethylated products. (**E**) Aryl iodide–catalyzed enantioselective difluorination of cinnamate derivatives. 1,2-Difluorination occurs via anchimeric assistance by the carbonyl group, whereas 1,1-difluorination is achieved through skeletal rearrangement via a phenonium ion intermediate.

operation (Fig. 1D) (*24*–*26*). A straightforward and general approach to enantioenriched difluoromethyl group–bearing building blocks from simple starting materials would facilitate the preparation of a wide array of molecular architectures containing the CHF_2 bioisostere. We report here the direct, catalytic, and highly enantioselective conversion of styrenes to versatile chiral building blocks containing difluoromethyl groups.

Direct difluorination of alkenes provides a nonobvious, but potentially powerful, approach to the stereoselective synthesis of difluoromethylated compounds. In particular, hypervalent iodoarenes have been demonstrated to mediate the 1,1-difluorinative rearrangement of both cyclic (*27*) and acyclic (*28*–*31*) alkyl-substituted styrenes through the intermediacy of phenonium ion intermediates (e.g., **III**) (Fig. 1E), and Kitamura and co-workers have reported a catalytic protocol for the conversion of unfunctionalized, terminal styrenes to achiral difluorinated products (*32*). We considered that invention of an enantioselective catalytic difluorinative rearrangement reaction could provide an attractive means to access useful chiral building blocks bearing difluoromethyl groups, particularly if it could be extended to styrene derivatives possessing useful functional handles (Fig. 1E).

We chose to examine cinnamic acid derivatives as candidate substrates because their difluorinative rearrangement would generate synthetically versatile, chiral aryl propionic acid derivatives as products. In this manner, we discovered that two distinct pathways are available in the difluorination of cinnamamides catalyzed by aryl iodides. We have reported recently that the trisubstituted cinnamamide derivative **2s** undergoes enantioselective and diastereospecific 1,2-difluorination with HF•pyridine and *m*-chloroperbenzoic acid (*m*CPBA) in the presence of chiral aryl iodide catalyst **1a** (*33*, *34*). However, if aryl migration via a phenonium ion intermediate (**III**) is favorable relative to anchimeric assistance by the neighboring amide group, then the rearrangement pathway dominates and the 1,1-difluorination product is obtained. The latter reactivity is observed in the reaction of the disubstituted cinnamamide **2a**, which undergoes the desired rearrangement reaction in the presence of catalyst **1a** to afford difluoromethylated phenyl propionamide **3a** (Fig. 1E). Remarkably, no 1,2-product was observed in the difluorination of **2a**, nor was 1,1-product detected in the difluorination of **2s**; recovered starting material and unidentified by-products accounted for the mass balance of the reactions, and no products resulting from direct oxidation with *m*CPBA were identified.

Resorcinol-based frameworks related to **1a** have been used extensively as effective templates in a range of hypervalent iodine-mediated asymmetric alkene difunctionalization reactions (*35*–*39*). In the difluorination of cinnamamide derivatives (Fig. 1E), we observed that the presence of benzylic substituents at the catalyst stereogenic centers as in **1a** is essential for obtaining high enantioselectivity. As discussed below, we propose that the polarizable aromatic groups enhance stereodifferentiation through specific attractive noncovalent interactions. Introduction of benzylic groups at the ester position as in **1b** did not have an analogous beneficial effect on enantioselectivity but led to an increase in reactivity, allowing reactions to be conducted at reduced temperatures with concomitant improvements in enantiomeric excess (e.e.) (see table S1). Under optimized conditions, the conversion of cinnamamide **2a** to **3a** could be accomplished on a gram scale with high (>90%) enantioselectivity.

In an examination of the scope of the difluorinative rearrangement reaction catalyzed by **1b**, high enantioselectivities and good yields were obtained with a variety of cinnamamide derivatives (Fig. 2). The low temperatures required to attain optimal e.e.'s (–20° to –50°C, depending on the substrate) were maintained conveniently using commercial circulatory baths. Primary, secondary, and tertiary cinnamamides all underwent highly enantioselective reactions, although lower yields and higher levels of byproduct formation were observed with the tertiary amides. Cinnamate esters were also oxidized successfully to the difluoromethyl-containing rearrangement products (**3k** to **3n**), albeit with slightly diminished yields and enantioselectivities compared with the corresponding primary cinnamamides. Simple styrene and stilbene derivatives lacking conjugation to carbonyl groups also underwent oxidative rearrangement successfully, although the resulting noncrystalline products **3o** to **3r** were obtained with more modest (64 to 77%) enantioselectivities.

Engagement of β,β-disubstituted styrene substrates in the rearrangement reaction would allow construction of quaternary difluoromethylated

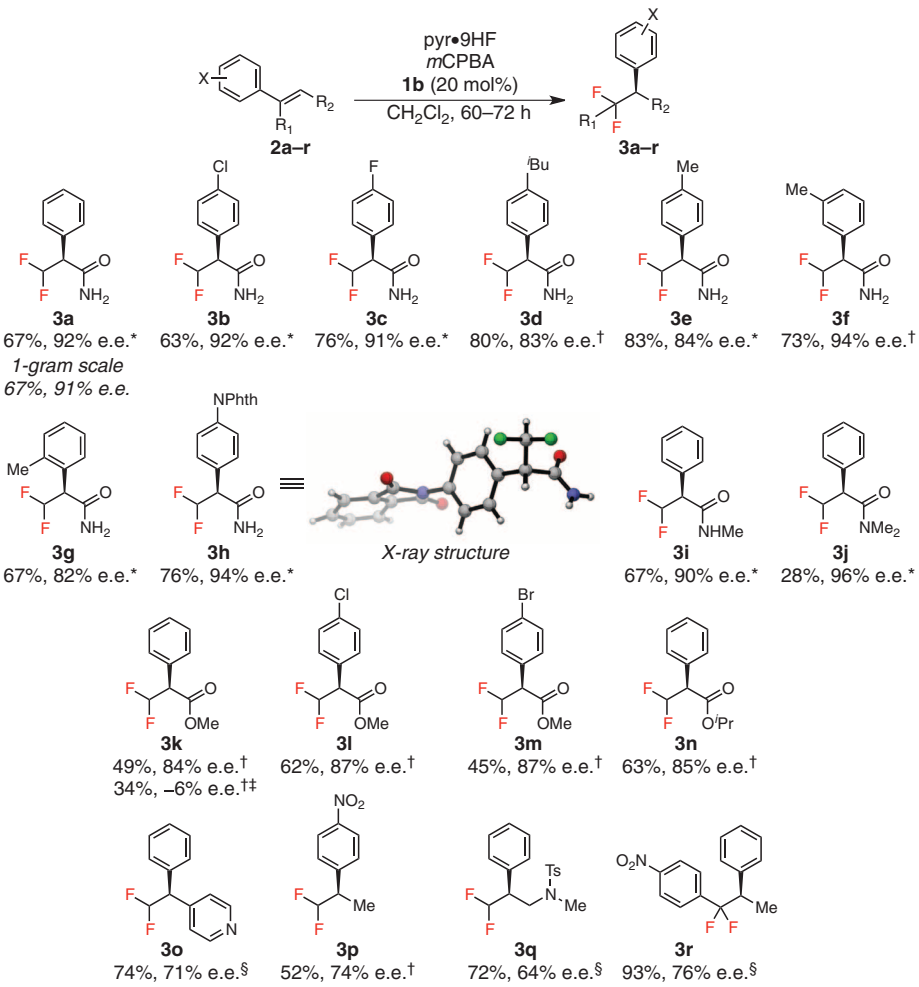

Fig. 2. Substrate scope with β-monosubstituted styrenes. Reactions were conducted on a 1.04-mmol scale with 1.1 to 1.3 equivalents of *m*CPBA and 11.1 equivalents of pyr•9HF (pyr is pyridine); isolated yields are reported. The absolute configuration of **3h** was assigned by x-ray crystallography (structure shown), and the configuration of all other products was assigned by analogy. *, Reaction conducted at –20°C; †, reaction conducted at –40°C; ‡, reaction conducted with (*Z*)-methyl cinnamate, §, reaction conducted at –50°C.

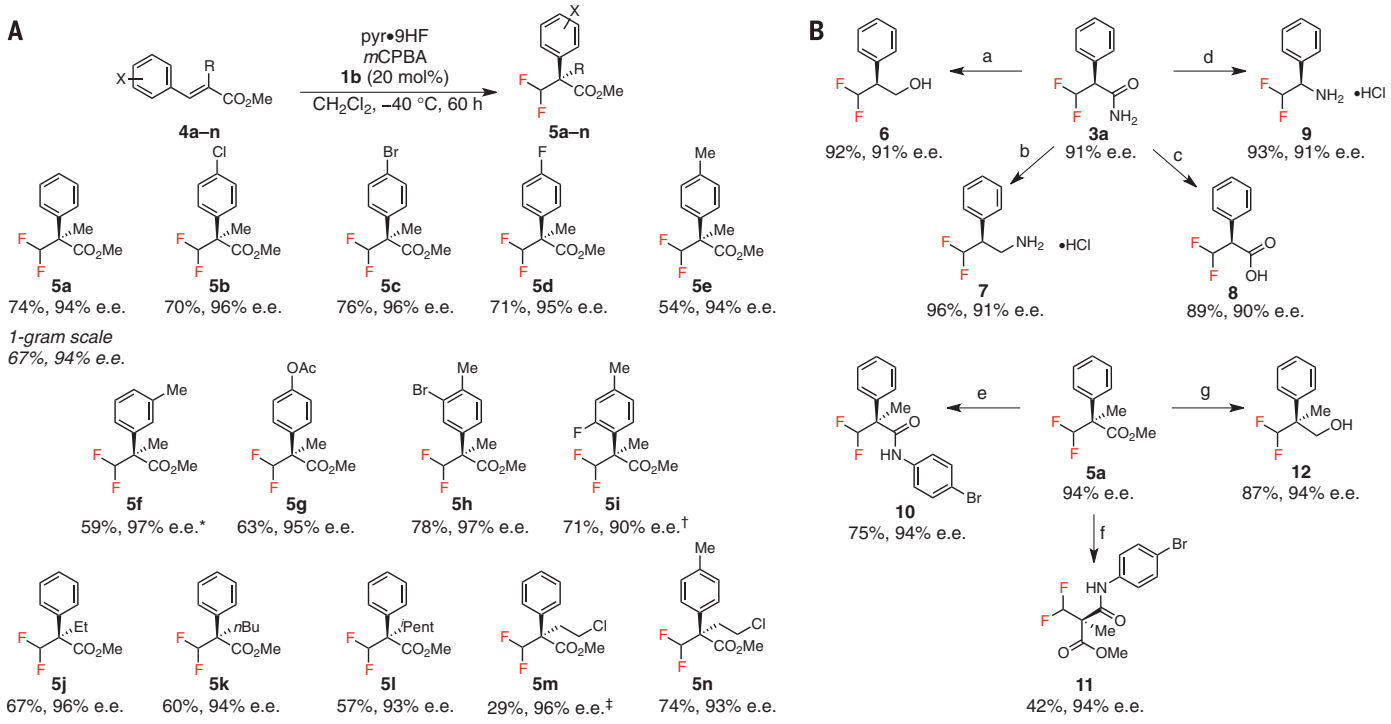

Fig. 3. Substrate scope with trisubstituted cinnamate ester derivatives and product elaboration. (**A**) Reactions were conducted on a 1.04-mmol scale with 1.3 equivalents of *m*CPBA and 11.1 equivalents of pyr•9HF; isolated yields are reported. *, Reaction conducted for 168 hours; †, reaction conducted at –50°C; ‡, reaction conducted on 0.68-mmol scale. (**B**) Diversification of difluoromethyl-containing products. Conditions: **a**, SmI_2 in tetrahydrofuran (THF) for 5 min followed by Et_3N and H_2O at room temperature. **b**, BH_3•dimethyl sulfide in THF at 65°C for 16 hours, then HCl. **c**, *t*-butyl nitrite in MeCN and H_2O at 80°C for 48 hours. **d**, [bis(trifluoroacetoxy)iodo]benzene (PIFA) in MeCN and H_2O for 36 hours at room temperature, then HCl. **e**, i. NaOH in H_2O, THF, and MeOH for 12 hours at room temperature; ii. $(COCl)_2$, *N,N*-dimethylformamide (DMF, catalyst) in CH_2Cl_2 for 6 hours at 0°C; iii. 4-bromoaniline, *N,N*-dimethylaminopyridine (DMAP) in CH_2Cl_2 for 24 hours at room temperature. **f**, i. $RuCl_3$ (catalyst), $NaIO_4$ in MeCN and H_2O for 24 hours at room temperature; ii. 4-bromoaniline, (1-cyano-2-ethoxy-2-oxoethylidenaminooxy)dimethylamino-morpholino-carbenium hexafluorophosphate (COMU), and diisopropylethylamine (DIPEA) in DMF for 72 hours at room temperature. **g**, diisobutylaluminum hydride (DIBAL) in THF for 1.5 hours at 0°C.

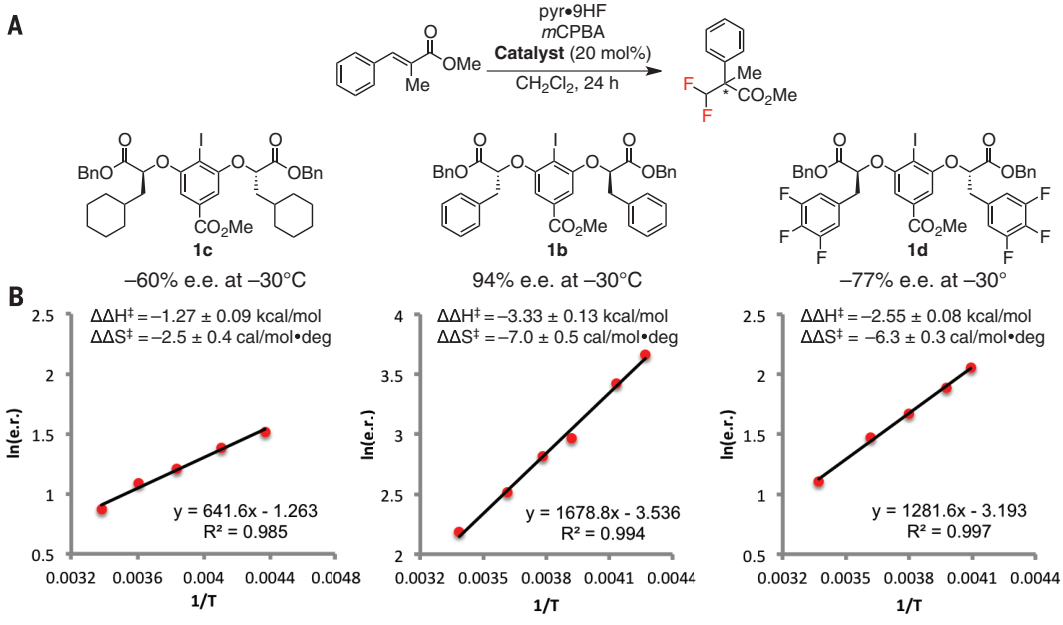

Fig. 4. Catalyst substituent effects on enantioselectivity. (**A**) Catalyst comparison revealing that the enantioselectivity in the conversion of **4a** to **5a** is correlated with the π-donor properties of the catalyst substituents. (**B**) Eyring analysis. The differential activation parameters were calculated using the following relationship: $\ln(e.r.) = -\Delta\Delta H^{\ddagger}/RT + \Delta\Delta S^{\ddagger}/R$ [where R = 1.986 cal/(mol•K), T is temperature in Kelvin, and e.r. is enantiomeric ratio].

stereocenters. However, trisubstituted cinnamamide derivatives undergo selective anchimeric assistance by the amide group en route to 1,2-difluorination products (i.e., **2s**) (*33*). According to the mechanism outlined in Fig. 1E, decomposition of intermediate **II** via the phenonium ion rearrangement should be favored by the use of cinnamate derivatives bearing less nucleophilic carbonyl groups. Indeed, trisubstituted methyl cinnamate derivatives were found to be excellent substrates for enantioselective oxidative rearrangement catalyzed by **1b** (Fig. 3). As illustrated with **4a**, comparable results were obtained on both 1-mmol and gram scale in good yields. Although electron-rich arenes such as phenols are incompatible with the oxidative hypervalent iodine conditions due to dearomatization pathways (*40*), suitably protected derivatives such as the acetate **4g** were found to undergo the desired difluorination to produce **5g** in high enantioselectivity and yield. The α-alkyl substituent of the cinnamate ester could also be varied without detrimental effect on reaction outcome (**5j** to **5l**), further underlining the utility of this rearrangement approach for the synthesis of sterically congested stereocenters. Low reactivity was observed in the difluorinative rearrangement of 3-chloropropyl–substituted **4m**, suggesting that relatively long-range inductive effects can influence the susceptibility of the alkene to the oxidation reaction. This deactivating effect is offset, however, by introduction of an electron-donating group on the aromatic ring of the substrate as in **4n**.

The products of this asymmetric reaction can be elaborated through a variety of synthetic manipulations without compromise of enantiomeric integrity (Fig. 3B). Cinnamamide-derived **3a** was reduced in high yield to alcohol **6** or primary amine **7**. Although erosion of stereochemical purity was observed in the hydrolysis of **3a** under acidic conditions, diazotization with *tert*-butylnitrite and hydrolysis under neutral conditions provided **8** with retention of e.e. Hoffman degradation of **3a** provided **9** in excellent yield and complete preservation of optical purity. Quaternary difluoromethyl-containing building block **5a** lacks an acidic α-proton and is therefore not prone to epimerization under saponification conditions. The resulting carboxylic acid was converted easily to amide **10** via the acid chloride. Ruthenium-catalyzed oxidation of the arene and subsequent amide bond formation provided **11** with preservation of stereochemical purity. This reaction sequence allows for the synthesis of synthetically versatile, chiral malonate derivatives bearing difluoromethylated quaternary stereocenters.

As noted above, pronounced enhancement in enantioselectivity is observed in difluorinative rearrangements using catalysts bearing benzylic (i.e., **1a** and **1b**) versus aliphatic substituents (see table S1). We hypothesized that attractive cation-π interactions might play a role in the selective stabilization of high-energy cationic intermediates and/or transition structures in the hypervalent iodine-catalyzed reaction, and we sought to evaluate this possibility by tuning the π-donating ability of the catalysts. The incorporation of more electron-rich or polarizable aromatic substituents into the catalyst was not a viable approach because these groups are incompatible with the strongly oxidizing reaction medium. However, the more electron-deficient 3,4,5-trifluorophenyl analog **1d** (Fig. 4B) could be evaluated and was found to be markedly less enantioselective than **1b**, as expected if cation-π interactions play a productive role in modulating stereocontrol (*41*). Eyring analysis in the 23° to −45°C temperature range of catalysts **1b**, **1c**, and **1d** for reaction of substrate **4a** was performed in order to glean additional insight into the basis for enantioinduction (Fig. 4B). For each catalyst, enantioselectivity was found to be enthalpically controlled, with a relatively small entropic compensation. The significant difference in the differential enthalpy of activation ($\Delta\Delta H^{\ddagger}$) between **1b** and **1c** is difficult to ascribe to steric effects alone, and it suggests instead a selective stabilizing interaction with **1b** in the transition state leading to the major enantiomer (*42*). To the extent that it exists, this stabilization is lost with weaker π-donating catalyst **1d**, as reflected in a $\Delta\Delta H^{\ddagger}$ value more similar to that of **1c**. This analysis is consistent with a more electron-donating π surface contributing to the high enantioselectivity in the 1,1-difluorination reaction, and it raises the intriguing possibility that cation-π interactions might be used to modulate enantioselectivity in other hypervalent iodine-mediated alkene oxidations.

REFERENCES AND NOTES

1. S. Purser, P. R. Moore, S. Swallow, V. Gouverneur, *Chem. Soc. Rev.* **37**, 320–330 (2008).
2. W. K. Hagmann, *J. Med. Chem.* **51**, 4359–4369 (2008).
3. J. Wang *et al.*, *Chem. Rev.* **114**, 2432–2506 (2014).
4. E. P. Gillis, K. J. Eastman, M. D. Hill, D. J. Donnelly, N. A. Meanwell, *J. Med. Chem.* **58**, 8315–8359 (2015).
5. X. Yang, T. Wu, R. J. Phipps, F. D. Toste, *Chem. Rev.* **115**, 826–870 (2015).
6. T. Liang, C. N. Neumann, T. Ritter, *Angew. Chem. Int. Ed.* **52**, 8214–8264 (2013).
7. J. Hu, W. Zhang, F. Wang, *Chem. Commun.* **2009** (48): 7465–7478 (2009).
8. N. A. Meanwell, *J. Med. Chem.* **54**, 2529–2591 (2011).
9. J. A. Erickson, J. I. McLoughlin, *J. Org. Chem.* **60**, 1626–1631 (1995).
10. K. Aikawa, S. Yoshida, D. Kondo, Y. Asai, K. Mikami, *Org. Lett.* **17**, 5108–5111 (2015).
11. D. Grassi, H. Li, A. Alexakis, *Chem. Commun.* **48**, 11404–11406 (2012).
12. Y.-L. Liu *et al.*, *Org. Lett.* **13**, 3826–3829 (2011).
13. R. Smits, C. D. Cadicamo, K. Burger, B. Koksch, *Chem. Soc. Rev.* **37**, 1727–1739 (2008).
14. W. J. Middleton, *J. Org. Chem.* **40**, 574–578 (1975).
15. M. Hudlický, in *Organic Reactions* (Wiley, New York, 1988), vol. 35, pp. 513–637.
16. R. P. Singh, J. M. Shreeve, *Synthesis* **17**, 2561–2578 (2002).
17. J. S. Sabol, N. W. Brake, I. A. McDonald, *Tetrahedron Lett.* **35**, 1821–1824 (1994).
18. W. Dmowski, *J. Fluor. Chem.* **32**, 255–282 (1986).
19. J. Mann, B. Pietrzak, *J. Chem. Soc., Perkin Trans. 1* **1987**, 385–388 (1987).
20. M. G. B. Drew, J. Mann, B. Pietrzak, *J. Chem. Soc. Chem. Commun.* **1985** (17): 1191–1192 (1985).
21. A. P. Truong *et al.*, *Bioorg. Med. Chem. Lett.* **20**, 6231–6236 (2010).
22. S. Rozen, *Acc. Chem. Res.* **38**, 803–812 (2005).
23. V. Hugenberg, G. Haufe, *J. Fluor. Chem.* **143**, 238–262 (2012).
24. N. Shibata, S. Mizuta, H. Kawai, *Tetrahedron Asymmetry* **19**, 2633–2644 (2008).
25. C. Ni, F. Wang, J. Hu, *Beilstein J. Org. Chem.* **4**, 21 (2008).
26. Y. Zhao, W. Huang, J. Zheng, J. Hu, *Org. Lett.* **13**, 5342–5345 (2011).
27. S. Hara, J. Nakahigashi, K. Ishi-I, T. Fukuhara, N. Yoneda, *Tetrahedron Lett.* **39**, 2589–2592 (1998).
28. W. Carpenter, *J. Org. Chem.* **31**, 2688–2689 (1966).
29. T. B. Patrick, J. J. Scheibel, W. E. Hall, Y. H. Lee, *J. Org. Chem.* **45**, 4492–4494 (1980).
30. M. Zupan, A. Pollak, *J. Chem. Soc. Chem. Commun.* **1975** (17): 715–716 (1975).
31. N. O. Ilchenko, B. O. A. Tasch, K. J. Szabó, *Angew. Chem. Int. Ed.* **53**, 12897–12901 (2014).
32. T. Kitamura, K. Muta, J. Oyamada, *J. Org. Chem.* **80**, 10431–10436 (2015).
33. S. M. Banik, J. W. Medley, E. N. Jacobsen, *J. Am. Chem. Soc.* **138**, 5000–5003 (2016).
34. I. G. Molnár, R. Gilmour, *J. Am. Chem. Soc.* **138**, 5004–5007 (2016).
35. M. Uyanik, T. Yasui, K. Ishihara, *Angew. Chem. Int. Ed.* **49**, 2175–2177 (2010).
36. M. Uyanik, T. Yasui, K. Ishihara, *Angew. Chem. Int. Ed.* **52**, 9215–9218 (2013).
37. R. M. Romero, T. H. Wöste, K. Muñiz, *Chem. Asian J.* **9**, 972–983 (2014).
38. U. Farid, F. Malmedy, R. Claveau, L. Albers, T. Wirth, *Angew. Chem. Int. Ed.* **52**, 7018–7022 (2013).
39. A. Yoshimura, V. V. Zhdankin, *Chem. Rev.* **116**, 3328–3435 (2016).
40. Y. Kita *et al.*, *J. Am. Chem. Soc.* **116**, 3684–3691 (1994).
41. C. Uyeda, E. N. Jacobsen, *J. Am. Chem. Soc.* **133**, 5062–5075 (2011).
42. R. R. Knowles, E. N. Jacobsen, *Proc. Natl. Acad. Sci. U.S.A.* **107**, 20678–20685 (2010).

ACKNOWLEDGMENTS

Complete experimental and characterization data are provided in the supplementary materials. This work was supported by NIH (GM043214), by an NSF predoctoral fellowship to S.M.B., and by an NIH postdoctoral fellowship to J.W.M. We thank S.-L. Zheng (Harvard) for determination of the x-ray crystal structures of **3h** and **10**. Metrical parameters are available free of charge from the Cambridge Crystallographic Data Centre under reference numbers CCDC-1480097 and CCDC-1480098.

SUPPLEMENTARY MATERIALS

www.sciencemag.org/content/353/6294/51/suppl/DC1
Materials and Methods
Figs. S1 to S4
Schemes S1 and S2
Tables S1 to S7
References (*43*–*76*)

1 April 2016; accepted 31 May 2016
10.1126/science.aaf8078

MARTIAN GEOLOGY

Large wind ripples on Mars: A record of atmospheric evolution

M. G. A. Lapotre,[1]* R. C. Ewing,[2] M. P. Lamb,[1] W. W. Fischer,[1] J. P. Grotzinger,[1] D. M. Rubin,[3] K. W. Lewis,[4] M. J. Ballard,[2] M. Day,[5] S. Gupta,[6] S. G. Banham,[6] N. T. Bridges,[7] D. J. Des Marais,[8] A. A. Fraeman,[1,9] J. A. Grant,[10] K. E. Herkenhoff,[11] D. W. Ming,[12] M. A. Mischna,[9] M. S. Rice,[13] D. A. Sumner,[14] A. R. Vasavada,[9] R. A. Yingst[15]

Wind blowing over sand on Earth produces decimeter-wavelength ripples and hundred-meter– to kilometer-wavelength dunes: bedforms of two distinct size modes. Observations from the Mars Science Laboratory Curiosity rover and the Mars Reconnaissance Orbiter reveal that Mars hosts a third stable wind-driven bedform, with meter-scale wavelengths. These bedforms are spatially uniform in size and typically have asymmetric profiles with angle-of-repose lee slopes and sinuous crest lines, making them unlike terrestrial wind ripples. Rather, these structures resemble fluid-drag ripples, which on Earth include water-worked current ripples, but on Mars instead form by wind because of the higher kinematic viscosity of the low-density atmosphere. A reevaluation of the wind-deposited strata in the Burns formation (about 3.7 billion years old or younger) identifies potential wind-drag ripple stratification formed under a thin atmosphere.

Bedforms are repeating topographic forms on a granular surface that arise because of interactions between the sediment bed, sediment transport, and fluid flow (*1*). Bedforms typically manifest as ripples or dunes made of sand mobilized by air or water. They create spatial patterns that are recognizable on the surfaces of Venus, Earth, Mars, Titan, and comet 67P (*2, 3*) and leave stratified sedimentary deposits. Because their morphology depends on formation mechanisms (*4*–*6*), bedforms are a primary means to reconstruct active and ancient atmospheric and hydrologic conditions.

Wind-driven (eolian) bedforms on Earth display two distinct scales: decimeter-wavelength sand ripples and hundred-meter– to kilometer-wavelength dunes (*4, 7*) (Fig. 1A). Grain-impact processes are thought to dominate the formation of wind ripples, whereas dune formation involves an aerodynamic instability (*6*). Orbital observations of Mars also show the superposition of two distinct scales of active bedforms (Fig. 1B and fig. S3) (*8*). Martian dunes form at a similar wavelength as on Earth; however, those dunes are ubiquitously mantled with bedforms 1 to 5 m in wavelength (hereafter referred to as large martian ripples) (*9*).

Large martian ripples were thought to have a similar origin to decimeter-wavelength eolian impact ripples on Earth, but to be larger on Mars because of differences in saltation (ballistic hopping of grains) (*6*). An implicit assumption under this hypothesis is that small wind ripples should not coexist with large martian ripples. Until recently, the spatial coexistence of three scales of bedforms could not be tested because the resolution of orbital imagery was too coarse [25 to 50 cm per pixel in

[1]Division of Geological and Planetary Science, California Institute of Technology, Pasadena, CA 91125, USA. [2]Department of Geology and Geophysics, Texas A&M University, College Station, TX 77843, USA. [3]Department of Earth and Planetary Sciences, University of California Santa Cruz, Santa Cruz, CA 95064, USA. [4]Department of Earth and Planetary Sciences, Johns Hopkins University, Baltimore, MD 21218, USA. [5]Jackson School of Geosciences, University of Texas at Austin, Austin, TX 78712, USA. [6]Department of Earth Science and Engineering, Imperial College London, London SW7 2AZ, UK. [7]Applied Physics Laboratory, Johns Hopkins University, Laurel, MD 20723, USA. [8]NASA Ames Research Center, Moffett Field, CA 94035, USA. [9]Jet Propulsion Laboratory, California Institute of Technology, Pasadena, CA 91109, USA. [10]National Air and Space Museum, Smithsonian Institution, Washington, DC 20560, USA. [11]Astrogeology Science Center, U.S. Geological Survey, Flagstaff, AZ 86001-1698, USA. [12]NASA Johnson Space Center, Houston, TX 77058, USA. [13]Geology Department, Western Washington University, Bellingham, WA 98225-9080, USA. [14]Department of Earth and Planetary Sciences, University of California, Davis, CA 95616, USA. [15]Planetary Science Institute, Tucson, AZ 85719, USA.
*Corresponding author. Email: mlapotre@caltech.edu

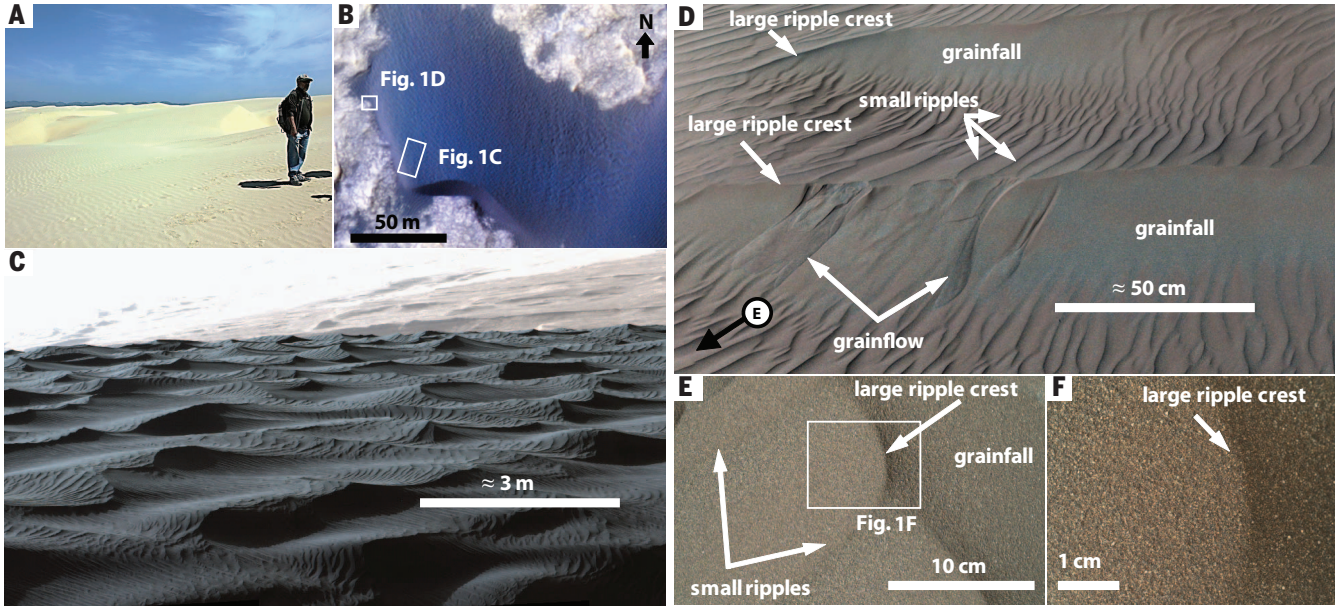

Fig. 1. Eolian bedforms on Earth and Mars. (**A**) Dunes and ripples at Oceano Dunes, California, United States (35.094960°N, –120.623476°E). (B) to (F) Dune in the Bagnold dune field, Gale crater, Mars, as shown from (**B**) a HiRISE image (ESP_035917_1755) and [(C) to (F)] the Curiosity rover. (**C**) Mastcam mosaic (mcam05410, sol 1192) showing small and large ripples on the dune. (**D**) Mastcam image (mcam05600, sol 1221) of large ripples with superimposed small ripples. (**E**) MAHLI 25-cm standoff image (1223MH0005550010403094C00, sol 1223), ~1 m off frame of (D) in the direction of the black circle and arrow. (**F**) 5-cm standoff image (1223MH0005560010403097C00, sol 1223) of the crest of a large ripple.

High Resolution Imaging Experiment (HiRISE) images (*10*)] to detect decimeter-scale ripples, and rovers had not visited active dune fields, only sand sheets and coarse-grained ripples (*11, 12, 13*). Observations made by the Curiosity rover (*14*) at an active dune field (the Bagnold dune field) (*15*) in Gale crater now show that large martian ripples are not simply larger versions of the decimeter-scale wind ripples seen on Earth. Rather, we observe decimeter-scale ripples superimposed on larger, meter-scale ripples, which are in turn superimposed on dunes (Fig. 1 and fig. S2). Thus, two stable ripple-scale bedforms coexist on Mars and both are superimposed on dunes, in contrast to the single scale of superimposed terrestrial ripples.

Mast Camera [Mastcam (*14*)] images collected by Curiosity indicate that large martian ripples have morphologies unlike those of eolian impact ripples. Terrestrial impact ripples have straight crestlines created by lateral grain splash (*16*), and relatively subdued profiles (*17*). In contrast, the large ripples of the Bagnold dune field have sinuous crest lines and asymmetric topographic profiles with distinct upwind (stoss) and downwind (lee) slope angles. Furthermore, the stoss slopes of the large ripples are mantled by small-scale ripples with a wavelength range of ~5 to 12 cm, which, based on their straight crestlines, we interpret as impact ripples similar to those of Earth (Fig. 1, C and D). This interpretation is consistent with recent numerical modeling that predicts that martian impact ripples should have decimeter-scale wavelengths (*18*). In contrast, the crests of the large ripples are sharp and give way downslope to angle-of-repose slip faces (slopes dipping ~30° downwind; fig. S5A) marked by the presence of grainflows [small avalanche deposits (Fig. 1D)], indicating recent activity. The presence of grainfall (i.e., sand that settles out on the lee slope) and deflected impact ripples on the lee slope indicates the aerodynamic influence of the large ripples contemporaneous with small-ripple migration (Fig. 1D).

We compiled a comprehensive multiscale data set of eolian bedform wavelengths on Mars by combining remote measurements from 11 martian sites (fig. S1 and tables S1 and S2), with rover measurements from stereo imagery in Gale crater (fig. S5) (*7*). Our statistical analysis confirms that Mars has an additional bedform-wavelength mode and that meter-scale ripples are absent in terrestrial eolian landscapes (Fig. 2 and table S3) (*7*).

Large martian ripples are not simply small dunes, because they maintain a stable size, whereas meter-wavelength dunes, which are rare on Earth, grow as they translate downwind (*6*) (fig. S3 versus fig. S4). Large martian ripples mantled with impact ripples also cannot be explained as large versions of terrestrial impact ripples forming by large saltation (*18*, *19*); no existing model can reproduce the coexistence and coevolution of two scales of impact ripples (*20*) (supplementary online text). Moreover, the large-ripple morphology differs significantly from that of impact ripples. An alternative interpretation of the large ripples is that they are coarse-grained ripples (*21*). However, images from the Mars Hand Lens Imager [MAHLI (*14*)] show well-sorted large ripples up the dune's stoss slopes (Fig. 1E), with very fine to medium sand and no significant grain-size differences between the small and large ripples (Fig. 1, E and F). Thus, neither the impact nor the coarse-grained hypothesis readily explains the coexistence of two distinct equilibrium scales of active ripples composed of sediments of similar size.

Their stable size, sinuous crests, and asymmetric profiles with avalanche faces make the large martian ripples morphologically similar to terrestrial subaqueous current ripples (fig. S6), also called fluid-drag ripples (*22*) (supplementary text). If the large martian ripples form aerodynamically [i.e., wind-drag ripples (*4*, *23*)], then theory developed for current ripples should predict their scale once adjusted for martian conditions. Decades of flume experiments (*24*, *25*) have led to

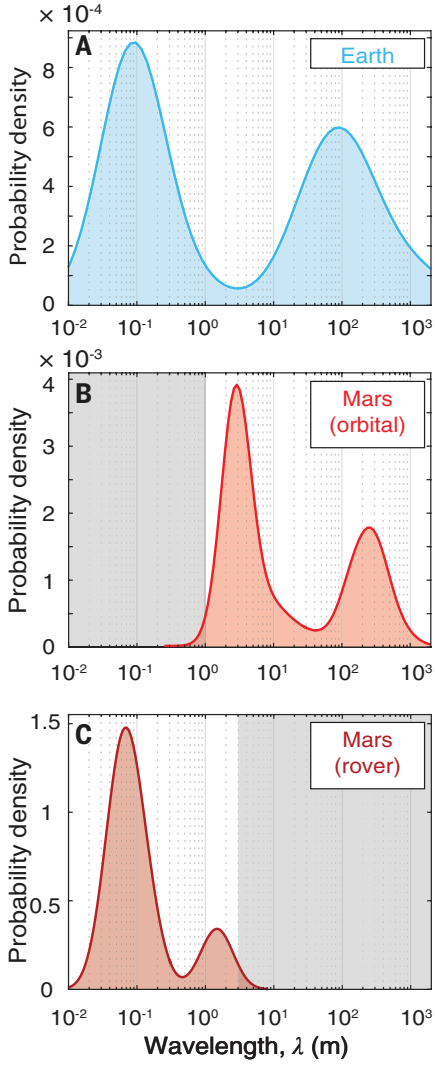

Fig. 2. Distinct modes of eolian bedforms on Earth and Mars. Bedform wavelength distribution on (**A**) Earth (n = 1473 bedforms), (**B**) Mars from orbit (n = 2430 bedforms; the shaded area is below the limit of detection), and (**C**) the Curiosity rover (n = 44 bedforms; the shaded area is constrained by perspective from the ground) (*7*).

scaling relations for current ripples (*25*, *26*). Following the theoretical framework of (*25*), we cast ripple size data in terms of the dimensionless current ripple wavelength, $\lambda^* = \frac{u_*}{\nu}\lambda$ [where λ is ripple wavelength, ν is kinematic fluid viscosity, u_* is bed shear velocity, and ν/u_* is proportional to the viscous sublayer thickness (*25*)], which is a function of the parameter $\mathrm{Re_p}\sqrt{\tau_*}$ [where $\mathrm{Re_p}$ is particle Reynolds number and τ_* is Shields stress (fig. S7 and supplementary text)]. These dimensionless variables provide a complete description of ripple-size scaling that accounts for fluid and grain properties and for gravity. A large database of current ripple wavelengths (*25*), updated here to include results from high-viscosity fluids (*24*), illustrates that

$$\lambda^* = 2453(\mathrm{Re_p}\sqrt{\tau_*})^{1/3} \quad (1)$$

(Fig. 3). To compare the predictions of fluid-drag ripple wavelengths to the large martian ripples, we calculated $\mathrm{Re_p}\sqrt{\tau_*}$ and λ^* for all compiled martian bedforms (*7*) (supplementary text). Results show that wind-drag ripples on Mars are predicted to be much larger than the decimeter-scale impact ripples because of the high kinematic viscosity in Mars' low-density atmosphere; furthermore, the wavelength of the large martian ripples is consistent with fluid-drag theory (Fig. 3) across a range of elevations with different atmospheric density (fig. S10).

Because wind-drag ripples are predicted to be smaller in thicker atmospheres, identification of these bedforms in ancient sedimentary rocks (*27*) offers the potential to reconstruct atmospheric loss and the global drying of Mars (*28*). The migration of bedforms produces cross-stratification in sedimentary rocks, which can be used to determine their original three-dimensional geometry. Based on morphology and scale, and using a kinematic model (*29*) (Fig. 4), we expect sinuous wind-drag ripples formed under present-day martian atmospheric conditions (*30*) to form decimeter-thick trough cross-sets, grouped into larger sets formed by overall migration of the dune (supplementary text). Large-ripple stratification should be distinct from that of compound wind dunes or coarse-grained ripples, because compound dunes do not maintain a persistently stable size in the down-dip direction (fig. S3 versus fig. S4) and typically form thicker cross-sets, and coarse-grained ripples leave recognizable coarse-grained lags. Stratification from the large ripples might also resemble that of subaqueous ripples and dunes. However, identification of distinctive wind-ripple strata [inversely graded millimeter-thick continuous layers (*31*)] coexisting with both decimeter-scale cross-sets and meter-scale dune troughs would enable the definitive interpretation of an eolian origin, whereas other contextual support, such as fluvial bar sets, desiccation cracks, and soft-sediment deformation, would characterize wet environments (*27*).

Candidate wind-drag ripples were observed by the Opportunity rover at Cape St. Mary, Victoria crater, in the Burns formation (Fig. 4 and supplementary text) (*32*) and were recognized as

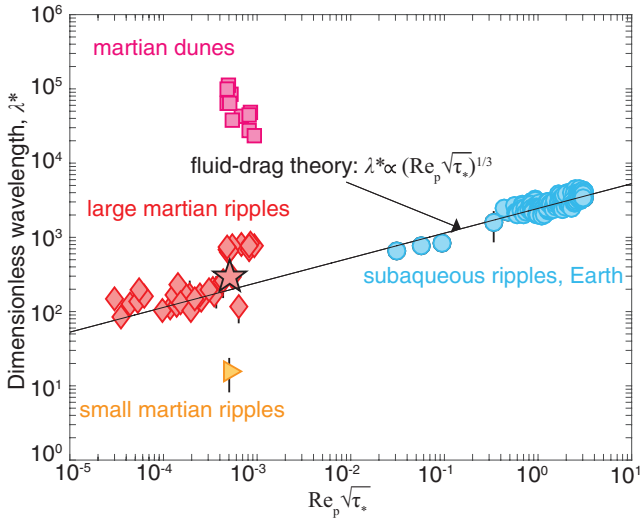

Fig. 3. Scaling of fluid-drag ripples. Dimensionless bedform wavelength as a function of particle Reynolds number, Re_p, and Shields stress, τ_*, quantities that control fluid-drag ripple size (*25*) (current ripples, blue circles; theory, black line). In contrast to martian dunes (pink squares) and small martian ripples (orange triangles), large martian ripples [red diamonds, n = 7280 bedforms, measured over 36 locations globally, including our measurements (*7*) and those of (*38*); the red star indicates rover measurements at Gale crater] match fluid-drag ripple theory. Symbols are means and error bars represent standard deviations at a given measurement site; error bars are smaller than marker size where not shown.

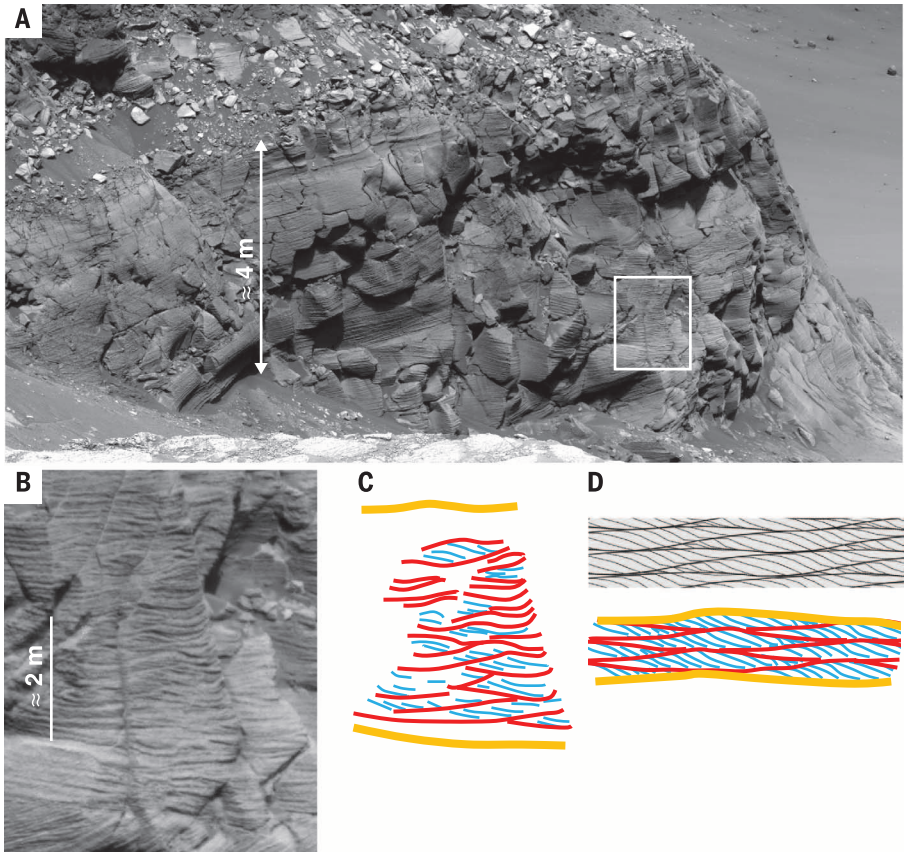

Fig. 4. Candidate wind-drag ripple stratification on Mars. (**A**) Mars Exploration Rover Panoramic Camera (*39*) image (P2441, sol 1212) of Cape St. Mary outcrop, Victoria crater, Mars. The white box shows the location of (**B**) decimeter-scale trough cross-strata and (**C**) an interpretation of stratal features from (B). (**D**) Uninterpreted (top) and interpreted (bottom) stratification produced by kinematic modeling of compound bedforms (*29*). Yellow lines represent surfaces scoured by dune troughs, red lines represent erosional surfaces produced by the migration of wind-drag ripples, and blue lines indicate wind-drag ripple cross-stratification.

abnormally sinuous and large eolian ripples at the time. There, repeated 10- to 20-cm-thick trough cross-sets are bounded by meter-scale dune troughs. The morphology, scale, contextual relationship to distinctly larger bounding surfaces, and apparent high deposition rate (*32*) all support the hypothesis that this stratification was formed by wind-drag ripples. The wind-drag ripple hypothesis therefore indicates a substantially thinned martian atmosphere during deposition of the Late Noachian–Early Hesperian Burns formation (fig. S10) (*33*). This interpretation supports models of atmospheric loss based on carbon isotope calculations (*28*). It is also consistent with centimeter-scale trough cross-strata in sulfate-rich sands in the lower Burns formation (*27*) that indicate subaqueous flows discharged from melt- or groundwater as brines of high ionic strength, rather than meteoric precipitation, due to the highly soluble sand rains (*26*, *34*, *35*). Although the relative ages are highly uncertain, our analysis suggests that ancient lakes in Gale crater (*36*) might predate the inferred low-density atmosphere associated with the lower Burns formation. Thus, whereas aqueous activity can be local and sourced from the subsurface (*37*), widespread shifts in wind-drag ripple size can indicate global changes in atmospheric density, and should prove an important geological indicator of the drying of Mars (figs. S8 and S9).

REFERENCES AND NOTES

1. G. V. Middleton, J. B. Southard, *Mechanics of Sediment Movement* (SEPM Society for Sedimentary Geology, Tulsa, OK, ed. 2, 1984).
2. J. Grotzinger, A. Hayes, M. Lamb, S. McLennan, in *Comparative Climatology of Terrestrial Planets*, S. Mackwell, M. Bullock, J. Harder, Eds. (Univ. of Arizona Press, 2013), pp. 439–472.
3. N. Thomas *et al.*, *Science* **347**, aaa0440 (2015).
4. I. G. Wilson, *Sedimentology* **19**, 173–210 (1972).
5. D. Rubin, D. McCulloch, *Sediment. Geol.* **26**, 207–231 (1980).
6. J. F. Kok, E. J. Parteli, T. I. Michaels, D. B. Karam, *Rep. Prog. Phys.* **75**, 106901 (2012).
7. Materials and methods are available as supplementary materials on *Science* Online.
8. N. T. Bridges *et al.*, *Geology* **40**, 31–34 (2011).
9. N. Bridges *et al.*, *Geophys. Res. Lett.* **34**, L23205 (2007).
10. A. S. McEwen *et al.*, *J. Geophys. Res. Planets* **112**, E05S02 (2007).
11. R. Sullivan *et al.*, *Nature* **436**, 58–61 (2005).
12. D. J. Jerolmack, D. Mohrig, J. P. Grotzinger, D. A. Fike, W. A. Watters, *J. Geophys. Res. Planets* **111**, E12S02 (2006).
13. D. F. Blake *et al.*, MSL Science Team, *Science* **341**, 1239505 (2013).
14. J. P. Grotzinger *et al.*, *Space Sci. Rev.* **170**, 5 (2012).
15. S. Silvestro *et al.*, *Geology* **41**, 483–486 (2013).
16. D. M. Rubin, *Earth Sci. Rev.* **113**, 176–185 (2012).
17. B. Werner, P. Haff, R. Livi, R. Anderson, *Geology* **14**, 743 (1986).
18. H. Yizhaq, J. Kok, I. Katra, *Icarus* **230**, 143–150 (2014).
19. O. Durán, P. Claudin, B. Andreotti, *Proc. Natl. Acad. Sci. U.S.A.* **111**, 15665–15668 (2014).
20. B. Andreotti, P. Claudin, O. Pouliquen, *Phys. Rev. Lett.* **96**, 028001 (2006).
21. S. de Silva, M. Spagnuolo, N. Bridges, J. Zimbelman, *Geol. Soc. Am. Bull.* **125**, 1912–1929 (2013).
22. J. B. Southard, L. A. Boguchwal, *J. Sediment. Res.* **60**, 658–679 (1990).
23. R. Bagnold, *The Physics of Blown Sand and Desert Dunes* (Methuen and Co., London, 1941), vol. 10.
24. R. A. Grazer, *Experimental Study of Current Ripples Using Medium Silt* (Massachusetts Institute of Technology, 1982).
25. M. S. Yalin, *J. Hydraul. Eng.* **111**, 1148–1155 (1985).

26. M. P. Lamb, J. P. Grotzinger, J. B. Southard, N. J. Tosca, *Sedimentary Geol. Mars* **102**, 139 (2012).
27. J. P. Grotzinger *et al.*, *Earth Planet. Sci. Lett.* **240**, 11–72 (2005).
28. R. Hu, D. M. Kass, B. L. Ehlmann, Y. L. Yung, *Nat. Commun.* **6**, 10003 (2015).
29. D. M. Rubin, C. L. Carter, *Bedforms 4.0: MATLAB Code for Simulating Bedforms and Cross-Bedding* (Open-File Report 2005-1272 of the U.S. Geological Survey, 2005).
30. P. Withers, M. D. Smith, *Icarus* **185**, 133–142 (2006).
31. R. E. Hunter, *Sedimentology* **24**, 361–387 (1977).
32. A. Hayes *et al.*, *J. Geophys. Res. Planets* **116**, E00F21 (2011).
33. R. Arvidson *et al.*, *J. Geophys. Res. Planets* **111**, E02S01 (2006).
34. N. J. Tosca *et al.*, *Earth Planet. Sci. Lett.* **240**, 122–148 (2005).
35. N. J. Tosca, S. M. McLennan, M. P. Lamb, J. P. Grotzinger, *J. Geophys. Res. Planets* **116**, E05004 (2011).
36. P. R. Mahaffy *et al.*, *Science* **347**, 412–414 (2015).
37. L. Ojha *et al.*, *Nat. Geosci.* **8**, 829–832 (2015).
38. R. D. Lorenz, N. T. Bridges, A. A. Rosenthal, E. Donkor, *Icarus* **230**, 77–80 (2014).
39. J. Bell III *et al.*, *J. Geophys. Res. Planets* **108**, E12, 8063 (2003).

ACKNOWLEDGMENTS

We thank the MSL engineering and science teams; the Mastcam team; Malin Space Science Systems, who made the rover observations possible; and B. Ehlmann and K. Edgett for insightful comments. Data presented in this paper are archived in the Planetary Data System (https://pds.nasa.gov/), and our compilation is available in the supplementary materials (data tables S1 and S2). Part of this research was carried out at the Jet Propulsion Laboratory–Caltech, under a contract with NASA. Work in the United Kingdom was funded by the UK Space Agency. D.M.R. was funded by the NASA MSL Participating Scientist program, and A.A.F. by a KISS Prize Postdoctoral Fellowship and a Caltech GPS Division Texaco Prize Postdoctoral Fellowship.

SUPPLEMENTARY MATERIALS

www.sciencemag.org/content/353/6294/55/suppl/DC1
Materials and Methods
Supplementary Text
Figs. S1 to S10
Tables S1 to S3
References (*40*–*89*)
Data Tables S1 and S2

25 January 2016; accepted 31 May 2016
10.1126/science.aaf3206

SOLAR CELLS

A vacuum flash–assisted solution process for high-efficiency large-area perovskite solar cells

Xiong Li,[1]* Dongqin Bi,[2]* Chenyi Yi,[1]* Jean-David Décoppet,[1] Jingshan Luo,[1] Shaik Mohammed Zakeeruddin,[1] Anders Hagfeldt,[2] Michael Grätzel[1]†

Metal halide perovskite solar cells (PSCs) currently attract enormous research interest because of their high solar-to-electric power conversion efficiency (PCE) and low fabrication costs, but their practical development is hampered by difficulties in achieving high performance with large-size devices. We devised a simple vacuum flash–assisted solution processing method to obtain shiny, smooth, crystalline perovskite films of high electronic quality over large areas. This enabled us to fabricate solar cells with an aperture area exceeding 1 square centimeter, a maximum efficiency of 20.5%, and a certified PCE of 19.6%. By contrast, the best certified PCE to date is 15.6% for PSCs of similar size. We demonstrate that the reproducibility of the method is excellent and that the cells show virtually no hysteresis. Our approach enables the realization of highly efficient large-area PSCs for practical deployment.

In the span of a few years, the power conversion efficiency (PCE) of perovskite solar cells (PSCs) has risen from 3.8% (*1*) to 22.10% (*2*), which is unprecedented in the field of photovoltaics. However, such high efficiencies have been achieved only with cells of very small size—between 0.04 and 0.2 cm^2—and few investigators have attempted to fabricate larger-area cells (*3*–*10*). The use of small-area devices has raised some doubts on the remarkable progress of the PSC field because the measurement errors tend to increase as the active cell area becomes smaller. Thus, the development of PSCs with a mandatory minimum active area of >1 cm^2 is required for the evaluation of this new photovoltaic (PV) technology (*3*, *8*). At present, the best certified PCE of a cell with a size exceeding the critical threshold of 1 cm^2 is 15.6% (*11*) because of the limitations of current preparation methods (*12*–*15*). Top-performing PSCs often are made with an anti-solvent such as chlorobenzene to precipitate the perovskite or its intermediate from its solution, which typically contains a solvent mixture of γ-butyrolactone (GBL), dimethylformamide (DMF), and dimethylsulfoxide (DMSO) (*3*, *7*, *8*, *14*, *16*–*19*). The antisolvent induces oversaturation of the perovskite solution, but because the antisolvent is usually dripped in the center of the film during spin-coating, the result is a radial gradient in oversaturation; the spatially inhomogeneous nucleation of the perovskite or its intermediate ultimately leads to defects in the perovskite film (*3*, *20*). In addition, the antisolvents currently used are toxic and harmful to the environment, hampering their large-scale application (*8*, *14*). Thus, alternative procedures for preparing large-area PSCs are warranted if their performance on a large device area is to be competitive with that of inorganic thin-film photovoltaics.

We developed a simple and effective method to produce high-quality perovskite films for large-area PSCs by applying a vacuum-flash treatment during the solution processing of the perovskite. Our approach differs from previous studies that used high-vacuum methods for vapor deposition of the perovskite (*13*, *15*) or for removal of reaction products (i.e., methylammonium chloride) by sublimation during the thermal annealing of the films (*21*). Vacuum flash–assisted solution processing (VASP) is a method that enables the sudden and well-controlled removal of solvent, thereby boosting rapid crystallization of a fibrous material that consists of a Lewis acid-base–type adduct representing the perovskite precursor phase (*19*). Upon thermal annealing, the precursor phase produces highly oriented, crystalline perovskite films of excellent electronic quality that can be grown on a variety of substrates (*17*–*19*). Furthermore, VASP allows deposition of the perovskite films on large substrate sizes and can be turned into a continuous process.

We achieved a maximum PCE of 20.5% and a certified PCE of 19.6% for large cells with square aperture areas greater than 1 cm^2, which is commensurate with the 21.0% reached by today's best thin-film copper indium gallium selenide (CIGS) and CdTe devices of similar size (*11*). Our method also eliminates the hysteresis in the current-voltage (*J-V*) curves, a notorious problem with PSCs (*22*). We tested the method with state-of-the-art perovskites using formamidinium (FA) and methylammonium (MA) mixed-cation and iodide-bromide mixed-anion perovskite formulations (*16*, *23*) of composition $FA_{0.81}MA_{0.15}PbI_{2.51}Br_{0.45}$. To demonstrate the versatility of the method, we also prepared the emerging cesium (Cs^+) and FA mixed-cation perovskite $FA_xCs_{1-x}PbI_yBr_{3-y}$ formulations (*24*–*26*). The VASP method is also readily scalable to the industrial level.

The basic steps of perovskite film fabrication by the VASP method are shown in Fig. 1A. The perovskite precursor solution, of composition $FA_{0.81}MA_{0.15}PbI_{2.51}Br_{0.45}$ containing DMSO with a nominal 1:1 ratio of lead to DMSO, was first spin-coated on top of a mesoporous TiO_2 film prepared as described (*16*). The film was then placed for a few seconds into a vacuum chamber to boost rapid crystallization of the perovskite intermediate phase by removing most of the residual solvents, consisting mainly of GBL and DMF. We observed that the pressure applied

[1]Laboratory of Photonics and Interfaces, Department of Chemistry and Chemical Engineering, École Polytechnique Fédérale de Lausanne, Lausanne CH-1015, Switzerland. [2]Laboratory of Photomolecular Science, Department of Chemistry and Chemical Engineering, École Polytechnique Fédérale de Lausanne, Lausanne CH-1015, Switzerland.
*These authors contributed equally to this work. †Corresponding author. Email: michael.graetzel@epfl.ch

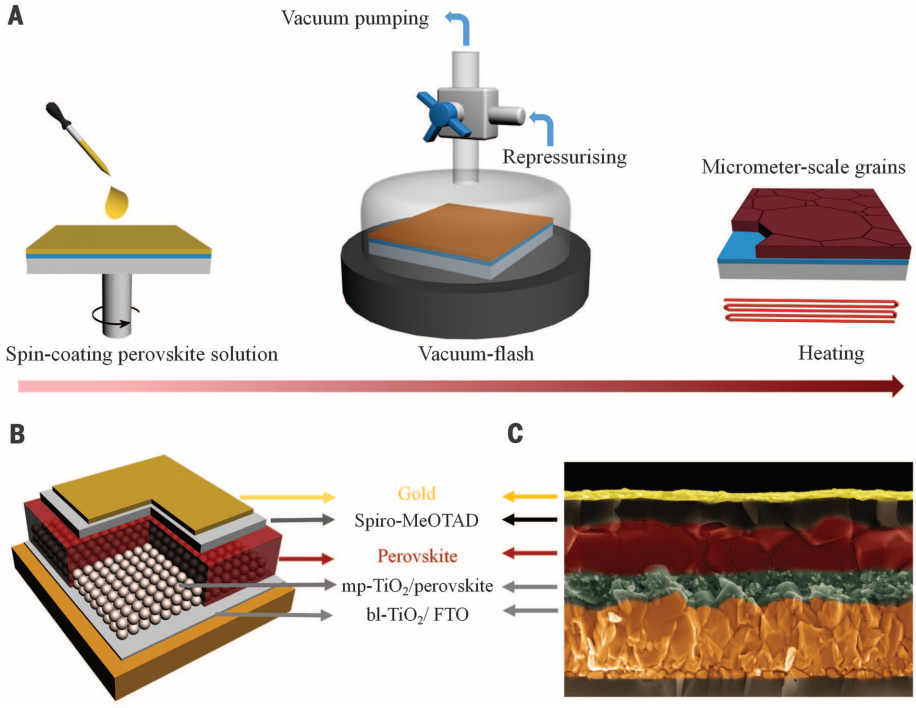

Fig. 1. Perovskite film deposition and device structure. (**A**) Schematic illustration of nucleation and crystallization procedures during the formation of perovskite film via vacuum flash–assisted solution processing (VASP). (**B**) Schematic illustration of the perovskite solar cell configuration, where a smooth and compact perovskite capping layer fully covers the mesoporous TiO_2 layer (mp-TiO_2) infiltrated with perovskite. bl-TiO_2, TiO_2 compact layer. (**C**) A high-resolution cross-sectional SEM image of a complete solar cell fabricated by VASP.

during the vacuum-flash process has considerable influence on the perovskite film formation. We obtained optimal results with a pressure of 20 Pa and used this condition during further studies (fig. S1). The film darkened slightly after the VASP treatment and formed a transparent orange layer of the perovskite precursor. We confirmed the presence of DMSO in this transparent orange film with Fourier transform infrared spectroscopy (fig. S2). Thus, the intermediate phase represents a Lewis acid-base adduct of DMSO with the likely composition DMSO-$PbI_{1.7}Br_{0.3}$-$(FAI)_{0.85}(MABr)_{0.15}$ (*14*, *17*–*19*). Further analysis by scanning electron microscopy (SEM) showed that this intermediate product consisted of nanofibrous aggregates (fig. S3), which upon annealing for 30 min at 100°C transformed into the shiny, smooth, and highly crystalline perovskite layer.

We spin-coated a hole-transporting layer onto the perovskite film [2,29,7,79-tetrakis(*N*,*N*-di-*p*-methoxyphenylamine)-9,9-spirobifluorene (spiro-OMeTAD) containing *tert*-butyl-pyridine (*t*-BP) and lithium bis(trifluoromethylsulfonyl) imide (LiTFSI) as an additive] (*16*). Finally, an 80-nm gold layer was evaporated on the hole transport layer to produce the full device. We illustrate the mesoscopic-planar bilayer device architecture in Fig. 1B and show a cross-sectional SEM image of this embodiment in Fig. 1C.

SEM images reveal stark differences between the $FA_{0.81}MA_{0.15}PbI_{2.51}Br_{0.45}$ perovskite films without and with vacuum-flash treatment (Fig. 2, A and B). The top view (Fig. 2A) of a film prepared by the conventional single-step solution deposition process without the vacuum-flash step (abbreviated as CP) (*27*) shows that the mesoporous TiO_2 was not fully covered by the perovskite. Pigment aggregates formed islands surrounded by numerous pinholes, apparently because the film dewetted during the formation of the perovskite (*28*). The VASP method yielded homogeneous films without pinholes; the TiO_2 was fully covered by the perovskite grains with sizes between 400 and 1000 nm, which greatly exceeds the grain size of films prepared by the CP method. This is illustrated by the top-view SEM image shown in fig. S1B. The cross-sectional SEM images (Fig. 2B) confirm the difference in morphology between films subjected and not subjected to VASP.

Without vacuum-flash treatment, a large fraction of the TiO_2 remained exposed and only a part was covered by the perovskite, but if VASP was applied, the perovskite was well infiltrated into the mesoporous TiO_2 film and formed a continuous TiO_2-perovskite nanocomposite that was covered by a contiguous and compact capping layer ~400 nm thick. The size of most of the perovskite crystallites in the capping layer was commensurate with its thickness, and most of the grain boundaries were perpendicular to the substrate to minimize the grain boundary energy (*29*). Hence, very few grain boundaries are visible within the plane of the capping layer. As shown below, the small amount of grain boundaries retarded nonradiative charge carrier recombination, which enhanced the open-circuit voltage (V_{oc}) of the cell (*16*).

To further scrutinize the uniformity of the VASP-treated $FA_{0.81}MA_{0.15}PbI_{2.51}Br_{0.45}$ perovskite film over large areas, we performed atomic force microscopy (AFM) to assess the surface roughness of nine square-shaped spots (each 10 μm × 10 μm in size) that were uniformly distributed over a film surface area of 1 cm^2. A typical AFM topography of one of the spots is illustrated in the left panel of Fig. 2C. The apparent grain size observed in the AFM image is consistent with that seen in the SEM image in Fig. 2A. Furthermore, all nine spots showed about the same root mean square roughness value of 30 ± 5 nm, reflecting a promising scalability of the VASP technique with respect to morphological control of perovskite thin films.

The SEM top view of the fresh film treated by VASP (fig. S3) holds vital clues about the formation of the high-quality perovskite polycrystalline film from the intermediate phase. The image reveals the presence of particles consisting of agglomerated nanofibers. The nanofibers are likely a perovskite adduct with the DMSO solvent, of composition DMSO-$PbI_{1.7}Br_{0.3}$-$(FAI)_{0.85}(MABr)_{0.15}$ (fig. S1). Besides the nanofibers, a few bright particles were observed that probably represent perovskite grains. Upon annealing at 100°C, the fibrous intermediates rearranged and coalesced via the Ostwald ripening process to minimize surface energy, which led to a homogeneous polycrystalline film with large perovskite grains and an optimized crystal orientation (*17*). This mechanism agrees well with the cross-sectional SEM image of the VASP-treated perovskite film. During the conventional deposition process, the spin-coating of the perovskite precursor solution resulted in a metastable film containing residual solvent (such as GBL or DMF). The subsequent annealing of the film above its glass transition temperature increased the mobility of the perovskite precursor, which resulted in dewetting and uncontrolled morphological variations as well as a wide range of grain size distribution (*28*, *30*). The VASP treatment prevented dewetting because flash evaporation of the solvent augmented the viscosity and glass transition temperature of the fluid thin film (apart from oversaturating the solution) and produced a burst of perovskite precursor crystals. The intermediate formation of the DMSO adduct retarded the crystal growth and increased the perovskite grain size during subsequent annealing (*19*).

The x-ray diffraction (XRD) spectra of the $FA_{0.81}MA_{0.15}PbI_{2.51}Br_{0.45}$ perovskite films (Fig. 3A) prepared by both methods show that for films prepared by the VASP method, the perovskite reflection at 2θ = 14.15° was 6.4 times as intense as the intensity of the peak from the fluorine-doped tin oxide (FTO) at 2θ = 37.73°, whereas for films prepared by CP, the ratio was only 1.4. This difference arises from the much superior shielding of the FTO serving as electron collector (Fig. 1A) by the contiguous and compact character of the perovskite capping layer formed via the VASP method. The CP reference sample lacked homogeneity, which is apparent from the photographs of the two films (Fig. 3B, inset). From the XRD spectra, we inferred that the vacuum-flash

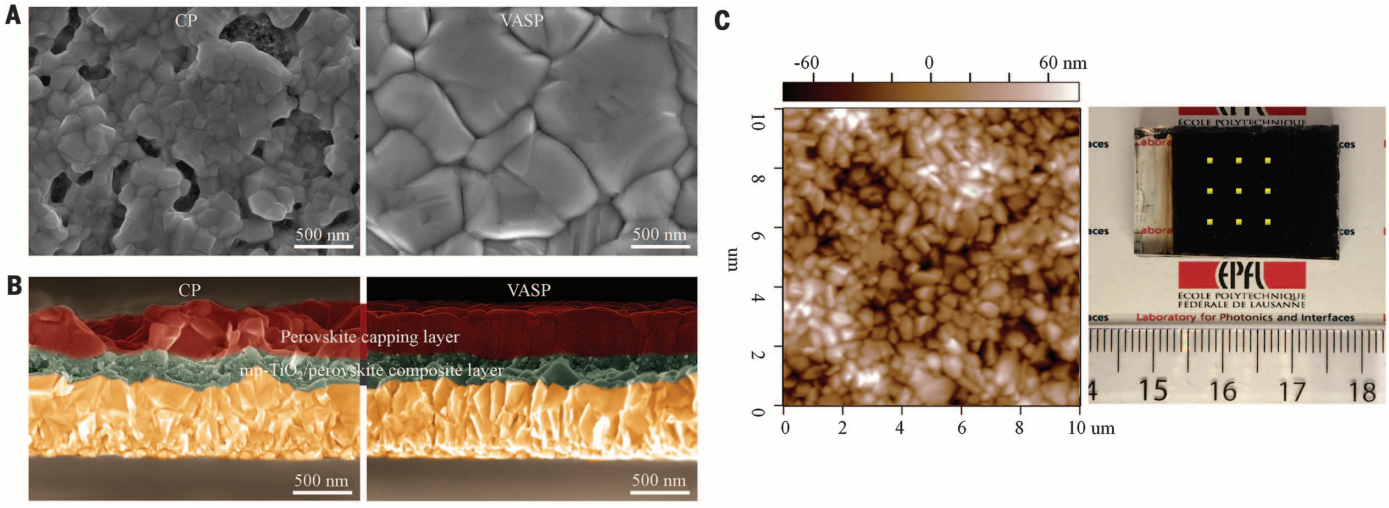

Fig. 2. Microscope images. (**A** and **B**) Surface (A) and cross-sectional (B) SEM images of the perovskite films fabricated by the conventional process (CP) and VASP. (**C**) Left: Typical AFM image of VASP-treated perovskite film taken from one of the nine square-shaped spots, each 10 μm × 10 μm. Right: Optical image of the whole square-inch-size perovskite film. The yellow squares mark the locations of the nine spots on the surface of the perovskite layer examined by AFM.

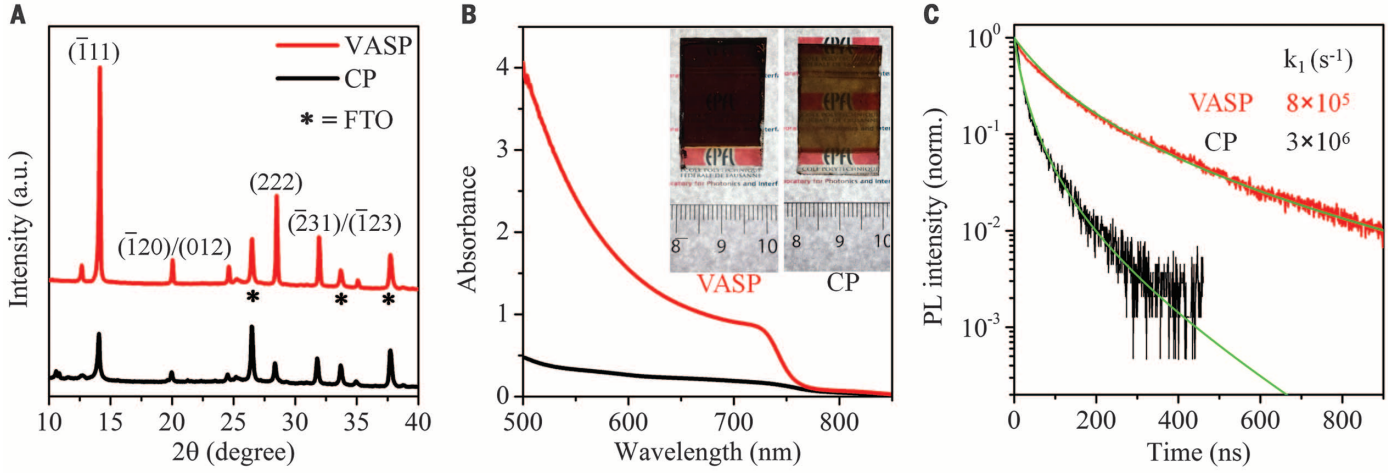

Fig. 3. Additional analyses of perovskite films prepared by the CP and VASP methods. (**A** to **C**) XRD patterns (A), UV-vis spectra (B), and time-resolved photoluminescence (PL) decay (C) of representative perovskite films deposited on FTO covered by a compact blocking layer and a mesoscopic scaffold of TiO_2 using VASP (red trace) or CP (black trace). Time-resolved photoluminescence dynamics was performed by monitoring the photoluminescence from the bulk perovskite (excited from the side of the capping layer) at 760 nm; the green lines are fits to Eq. 2.

treatment also affects the crystal orientation. Thus, the ratio of relative intensity of $(\bar{1}11)$ to $(\bar{1}20)/(012)$ diffraction peaks (*31*) increased from 5.0 for the CP-deposited film to 9.3 for the VASP-treated film. The peaks are stronger and sharper for the films treated by VASP; the full width at half maximum (FWHM) of the $(\bar{1}11)$ peak decreased from 0.16° for CP to 0.11° for VASP, reflecting the expansion of the mean size of perovskite crystallites from 68 to 109 nm. These results indicate that the vacuum-flash treatment can simultaneously improve perovskite crystallinity and grain size.

Figure 3B shows ultraviolet-visible (UV-vis) absorption for the perovskite films. The smooth, compact morphology of the VASP perovskite films led to a much stronger absorbance than the CP reference sample in the 500- to 800-nm range. Time-resolved photoluminescence decay measurements (Fig. 3C) of the perovskite band-gap emission at 760 nm allowed us to derive quantitative information on the dynamics of charge carrier recombination in the perovskite films. Much faster photoluminescence decay was seen for the CP reference than for the VASP-treated film. Neglecting Auger-type recombination, we describe the kinetics of charge carrier recombination by the differential rate law,

$$-\frac{dn}{dt} = k_1 n + k_2 n^2 \qquad (1)$$

where k_1 and k_2 are the first- and second-order rate constants for nonradiative (trap-controlled) and bimolecular radiative recombination of charge carriers, respectively. Integration of Eq. 1 yields Eq. 2, where n^0 and n denote the concentration of charge carriers at time 0 and t:

$$n(t) = \frac{k_1}{k_2}\left[\exp(k_1 t)\left(\frac{k_1}{n^0 k_2} + 1\right) - 1\right]^{-1} \qquad (2)$$

From fitting the luminescence decays in Fig. 3C to this rate equation, drawn as solid line through the data points, we obtain the values of the rate constants for the nonradiative decay processes: $k_1 = 3 \times 10^6\ s^{-1}$ and $k_1 = 8 \times 10^5\ s^{-1}$ for the CP and VASP films, respectively. These values imply that the nonradiative recombination was slower by a factor of ~4 in the VASP-treated film. The slower nonradiative recombination arising from the lower defect concentration should entail an

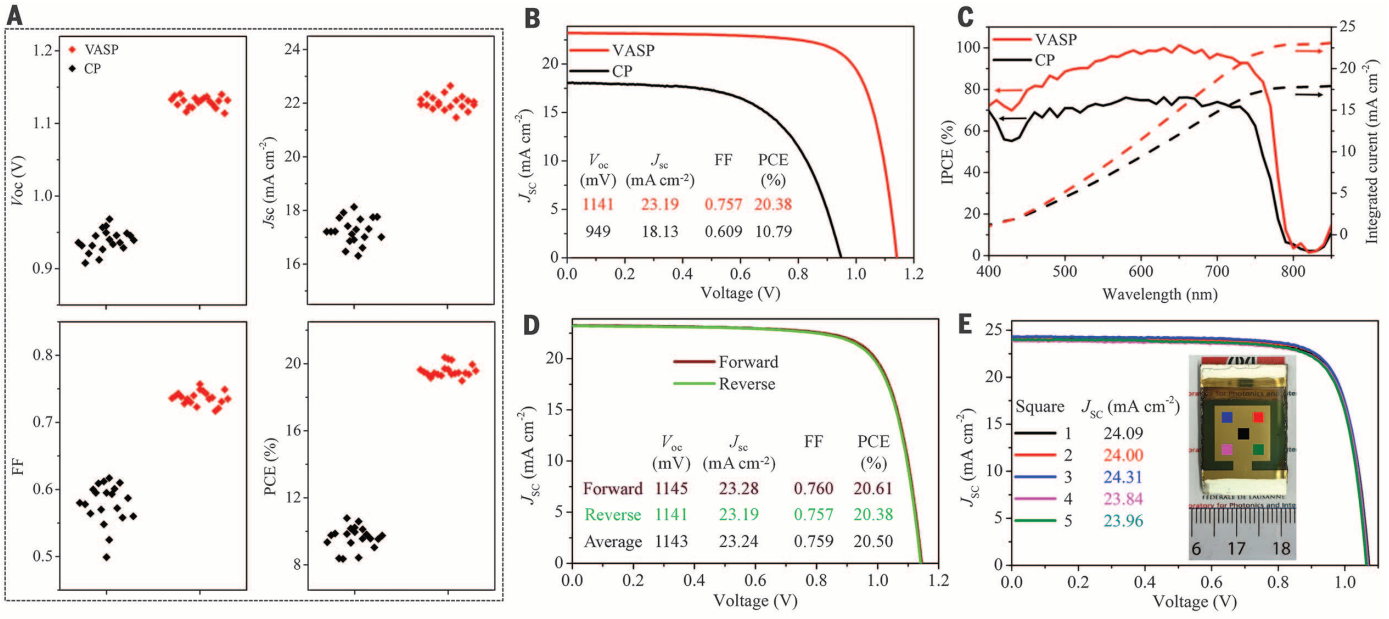

Fig. 4. Photovoltaic characterization. (**A**) PV metrics for 20 devices fabricated by the CP and VASP methods. (**B**) Current-voltage (*J-V*) curves for the best performing devices using perovskite films prepared by the CP (black) or VASP (red) method, measured under standard AM1.5 solar radiation. (**C**) Solid lines are IPCE curves of cells fabricated by the CP (black) or VASP (red) method. Measurements were taken with chopped monochromatic light under a white light bias corresponding to 5% solar intensity. Dashed lines show J_{sc} calculated from the overlap integral of the IPCE spectra with the standard AM1.5 solar emission. (**D**) *J-V* curves for the best cell fabricated by VASP, recorded in reverse (from V_{oc} to J_{sc}) and forward (from J_{sc} to V_{oc}) scanning directions. Inset: PV metrics derived from the two *J-V* curves as well as their average PCEs. (**E**) PV parameters for a representative $FA_{0.81}MA_{0.15}PbI_{2.51}Br_{0.45}$-based perovskite device fabricated by VASP measured from five different spots with an aperture area of 0.16 cm^2 selected from the total active area of 1.2 cm × 1.2 cm under standard AM1.5 illumination. All *J-V* curves were recorded at a scanning rate of 50 mV s^{-1} in the reverse direction unless stated otherwise.

increase in V_{oc}, and the average V_{oc} of the perovskite cells prepared by VASP was 192 mV larger than that of the reference (Fig. 4A) (*16*).

We fabricated mesoscopic-planar PSCs using perovskite thin films of composition $FA_{0.81}MA_{0.15}PbI_{2.51}Br_{0.45}$ as light harvesters and evaluated the PV metrics of the devices by measuring their photocurrent density versus voltage (*J-V*) curves and their incident photon-to-current conversion efficiency (IPCE). We also tested their stabilized maximum power output. We covered devices with an active area of 1.44 cm^2 by a black mask with an aperture area of 1.0 cm × 1.0 cm. Tables S1 and S2 provide statistical data on the PV metrics of the PSCs. As shown in Fig. 4A, VASP greatly improved device performance and reproducibility relative to the CP method. The average PCE for 20 control PSCs fabricated by CP was 9.62 ± 0.67%, with an average short-circuit photocurrent density (J_{sc}) = 17.25 ± 0.49 mA cm^{-2}, V_{oc} = 938 ± 15 mV, and fill factor (FF) = 0.58 ± 0.03. For the VASP films, the average PCE more than doubled to 19.58 ± 0.37%, with an average J_{sc} = 23.12 ± 0.28 mA cm^{-2}, V_{oc} = 1130 ± 8 mV, and FF = 0.74 ± 0.01. *J-V* curves are shown for the best cells in Fig. 4B. The substantial performance improvement induced by VASP is reflected in the values for all the PV metrics. The best cell produced by CP gave a PEC of 10.79%, corresponding to J_{sc} = 15.60 mA cm^{-2}, V_{oc} = 949 mV, and FF = 0.61. The values for the VASP perovskite film were J_{sc} = 23.19 mA cm^{-2}, V_{oc} = 1141 mV, and FF = 0.76, reaching a PCE of 20.38% under standard AM1.5 solar illumination. Figure 4C shows IPCE over the spectral range from 400 to 800 nm. The VASP technique achieved much higher IPCE values than the CP method, matching the difference in device photocurrents obtained from these two procedures. Integration of the IPCE spectrum over the solar emission yields AM1.5 photocurrents of 23.2 and 17.8 mA/cm^2 for the VASP and CP reference devices, respectively, in excellent agreement with the measured J_{sc} values; this finding indicates that the spectral mismatch between our simulator and the true AM1.5 solar emission is negligibly small.

We used different *J-V* scan directions to examine the hysteresis of our cells fabricated by VASP (Fig. 4D). The PCE difference between the forward and reverse scan was as small as 1% in absolute PCE values, reflecting negligible hysteresis. The enlarged perovskite crystal size and improved crystalline quality eliminated hysteresis, likely by reducing the overall bulk defect density and suppressing charge trapping during solar cell operation (*32*, *33*). A 20.32% stabilized PCE output with a photocurrent density of 21.25 mA cm^{-2} was achieved for the same large-area device in Fig. 4D (fig. S4), indicating that the PCEs obtained in forward and reverse scans at a routine scanning condition are near the real performance. We also measured *J-V* curves at five different small spots (each 0.4 cm × 0.4 cm) located at the center and the four corners of the device active area (Fig. 4E). All the PV metrics including J_{sc}, extracted from these five curves by a black mask with a square aperture area of 0.16 cm^2, were almost identical (table S3); the values of J_{sc} show very small variation when the square aperture area of the mask is increased up to 1 cm^2 (fig. S5), attesting to the uniformity of the perovskite film over the square-centimeter scale. One of our 1.0 cm × 1.0 cm devices was tested by an accredited PV test laboratory (Newport Corporation PV Lab, Bozeman, MT, USA), which certified its PCE to be 19.6%, with J_{sc} = 22.60 mA cm^{-2}, V_{oc} = 1.143 V, and FF = 0.76 (fig. S6). A preliminary stability investigation showed that the devices are stable in ambient conditions, their final PCE even increasing slightly after 39 days (fig. S7 and table S4). Figure S8 compares the stability of two typical devices prepared by the VASP and CP methods under light soaking with AM1.5 light of 100 W/m^2 intensity. After 100 hours of continuous illumination, the VASP device and CP standard retained 90% and 70% of their initial performance, respectively, showing the superior light resistance of the VASP-based cell.

We also produced PSCs of 1 cm^2 size using the antisolvent method as described (*16*) and measured their PV performance. Data on 10 cells are shown in table S5. The average PCE was 16.99 ± 0.71%, which is obviously lower and exhibits a larger standard deviation than that of 19.58 ± 0.37% for the devices prepared by VASP.

We found the VASP method to be versatile with respect to variations of precursor components and perovskite composition. As a demonstration, we tested it with the emerging perovskite material

$FA_xCs_{1-x}PbI_yBr_{3-y}$ (*24*–*26*). We obtained an excellent PCE of close to 18.0% in the initial trial; detailed PV metrics are listed in table S6.

REFERENCES AND NOTES

1. A. Kojima, K. Teshima, Y. Shirai, T. Miyasaka, *J. Am. Chem. Soc.* **131**, 6050–6051 (2009).
2. NREL chart, www.nrel.gov/ncpv/images/efficiency_chart.jpg.
3. W. Chen *et al.*, *Science* **350**, 944–948 (2015).
4. Z. Yang *et al.*, *Nano Energy* **15**, 670–678 (2015).
5. J. Seo *et al.*, *Energy Environ. Sci.* **7**, 2642–2646 (2014).
6. S. Razza *et al.*, *J. Power Sources* **277**, 286–291 (2015).
7. H. Minemawari *et al.*, *Nature* **475**, 364–367 (2011).
8. M. Yang *et al.*, *Adv. Mater.* **27**, 6363–6370 (2015).
9. O. Malinkiewicz *et al.*, *Adv. Energy Mater.* **4**, 1400345 (2014).
10. L. K. Ono, S. H. Wang, Y. Kato, S. R. Raga, Y. B. Qi, *Energy Environ. Sci.* **7**, 3989–3993 (2014).
11. M. A. Green, K. Emery, Y. Hishikawa, W. Warta, E. D. Dunlop, *Prog. Photovolt. Res. Appl.* **24**, 3–11 (2016).
12. J. Burschka *et al.*, *Nature* **499**, 316–319 (2013).
13. M. Liu, M. B. Johnston, H. J. Snaith, *Nature* **501**, 395–398 (2013).
14. N. J. Jeon *et al.*, *Nat. Mater.* **13**, 897–903 (2014).
15. C. W. Chen *et al.*, *Adv. Mater.* **26**, 6647–6652 (2014).
16. D. Bi *et al.*, *Sci. Adv.* **2**, e1501170 (2016).
17. Y. Guo *et al.*, *J. Am. Chem. Soc.* **137**, 15907–15914 (2015).
18. N. Ahn *et al.*, *J. Am. Chem. Soc.* **137**, 8696–8699 (2015).
19. J.-W. Lee, H.-S. Kim, N.-G. Park, *Acc. Chem. Res.* **49**, 311–319 (2016).
20. L. Wengeler, in *Coating and Drying Processes for Functional Films in Polymer Solar Cells* (Karlsruher Institut für Technologie Scientific Publishing, Karlsruhe, Germany, 2014), pp. 78–80.
21. F. X. Xie *et al.*, *ACS Nano* **9**, 639–646 (2015).
22. M. Grätzel, *Nat. Mater.* **13**, 838–842 (2014).
23. N. J. Jeon *et al.*, *Nature* **517**, 476–480 (2015).
24. J. W. Lee *et al.*, *Adv. Energy Mater.* **5**, 150131 (2015).
25. C. Y. Yi *et al.*, *Energy Environ. Sci.* **9**, 656–662 (2016).
26. D. P. McMeekin *et al.*, *Science* **351**, 151–155 (2016).
27. H.-S. Kim *et al.*, *Sci. Rep.* **2**, 591 (2012).
28. M. D. McGehee, *Nat. Mater.* **13**, 845–846 (2014).
29. S. Auer, D. Frenkel, *Nature* **413**, 711–713 (2001).
30. G. Reiter, *Phys. Rev. Lett.* **68**, 75–78 (1992).
31. S. O. Pang *et al.*, *Chem. Mater.* **26**, 1485–1491 (2014).
32. S. Meloni *et al.*, *Nat. Commun.* **7**, 10334 (2016).
33. H. Cho *et al.*, *Science* **350**, 1222–1225 (2015).

ACKNOWLEDGMENTS

Supported by King Abdulaziz City for Science and Technology (M.G. and S.M.Z.), an EPFL Fellowship co-funded by a Marie Curie stipend from the European Union's Seventh Framework Programme (no. 291771) (J.L.), the Swiss National Science Foundation, NRP 70 "Energy Turnaround," SNF-NanoTera (SYNERGY), and the Swiss Federal Office of Energy. We thank F. Zhang for experimental aid with the preparation of some perovskite solutions and TiO_2 films, I. Dar and G. J. Jacopin for assistance with the photoluminescence experiments, and W. Tress for help with the curve fitting. X.L., D.B., C.Y., S.M.Z., A.H., and M.G. have applied for a European patent for the VASP process.

SUPPLEMENTARY MATERIALS

www.sciencemag.org/content/353/6294/58/suppl/DC1
Materials and Methods
Supplementary Text
Figs. S1 to S8
Tables S1 to S6

2 April 2016; accepted 25 May 2016
Published online 9 June 2016
10.1126/science.aaf8060

ULTRAFAST DYNAMICS

Direct time-domain observation of attosecond final-state lifetimes in photoemission from solids

Zhensheng Tao,[1]*† Cong Chen,[1]*† Tibor Szilvási,[2] Mark Keller,[3] Manos Mavrikakis,[2] Henry Kapteyn,[1] Margaret Murnane[1]

Attosecond spectroscopic techniques have made it possible to measure differences in transport times for photoelectrons from localized core levels and delocalized valence bands in solids. We report the application of attosecond pulse trains to directly and unambiguously measure the difference in lifetimes between photoelectrons born into free electron–like states and those excited into unoccupied excited states in the band structure of nickel (111). An enormous increase in lifetime of 212 ± 30 attoseconds occurs when the final state coincides with a short-lived excited state. Moreover, a strong dependence of this lifetime on emission angle is directly related to the final-state band dispersion as a function of electron transverse momentum. This finding underscores the importance of the material band structure in determining photoelectron lifetimes and corresponding electron escape depths.

The electronic band structure of materials consists of occupied and unoccupied bands that emerge as the electron wave functions of adjacent atoms in the lattice overlap with each other. In general, valence bands will have more wave function overlap and will therefore be wider than, for example, the core levels. The periodicity of a crystal lattice imposes an energy-momentum relation that is described as the dispersion relationship for electrons in each band, making the electronic structure of solids quite complex. Fortunately, angle-resolved photoemission spectroscopy (ARPES) can resolve both the energy and momentum of photoelectrons by probing photoemission from materials at well-defined angles. This information is related to the energy and momentum of electrons populating distinct bands, providing a direct measurement of the band dispersion and the Fermi surface (*1*). When combined with ultrafast lasers, time-resolved ARPES makes it possible to capture fast changes in the band structure of materials near the center of the Brillouin zone (i.e., low electron momenta) on picosecond and femtosecond time scales (*2*). More recently, advances in tabletop high-harmonic generation (HHG) (*3*, *4*) have resulted in coherent extreme ultraviolet (EUV) and soft x-ray beams that are ideally suited for ARPES, opening up time-resolved studies over the entire Brillouin zone (*5*, *6*). HHG is emitted as a series of attosecond pulse trains with unique characteristics of good energy resolution (~100 to 300 meV) combined with sub-femtosecond time resolution. These capabilities have made it possible to observe and control the fastest electron dynamics in molecular and material systems (*7*, *8*). Recent work probed how fast a material can change its magnetic state or transition from insulating to metallic (*5*, *9*), uncovering which microscopic mechanisms were responsible for driving fast phase or state transitions in materials. Other work probed the ~7-fs lifetime of core-excited states of adsorbates on surfaces (*10*).

HHG has also been used to probe the time delay associated with the photoemission process itself in isolated atoms and materials (*11*–*17*) by taking advantage of laser-assisted photoemission (*18*). Although some discrepancy remains between experiment and theory (*17*, *19*), it is generally agreed that the photoemission time delay from isolated atoms arises from convolution of a Wigner time delay due to scattering of photoelectrons in the atomic potential and a measurement-induced delay due to propagation of the photoelectrons in the laser field (*20*). Unlike the case of isolated atoms, interpreting photoemission time delays from solids requires consideration of complex band structures and various many-body interactions that photoelectrons can experience as they approach the surface. Previous attosecond-streaking studies of a transition-metal W(110) surface revealed a considerable time delay (~110 as) between photoemission from core-level and valence-band states (*11*). In contrast, no delay was measured for the free-electron metal Mg, although a time delay similar to that of W was expected (*13*). Various theoretical models have been proposed to explain the photoemission time delay from solids in terms of transport time (*21*, *22*), degrees of initial-state localization (*21*, *23*), and band-structure effects (*24*, *25*). The use of isolated attosecond pulses in these experiments was necessarily accompanied by a broad EUV bandwidth, which then gave rise to an integrated broadband photoemission feature comprising multiple valence bands (*11*, *13*, *14*). Other recent work used synchrotron sources to measure the final-state linewidths of photoemission from Cu, finding pronounced variations in the ARPES spectra with small changes in photon energy that could not be assigned to a free-electron final state. This work identified the direct transitions and

[1]Department of Physics and JILA, University of Colorado and NIST, Boulder, CO 80309, USA. [2]Department of Chemical and Biological Engineering, University of Wisconsin, Madison, WI 53706, USA. [3]National Institute of Standards and Technology (NIST), Boulder, CO 80305, USA.
***Corresponding author. Email: zhensheng.tao@jila.colorado.edu (Z.T.); cong.chen@colorado.edu (C.C.)** †These authors contributed equally to this work.

measured very broad linewidths of >3 eV for unoccupied excited final states in the band structure within the photon energy range 20 to 150 eV (*26*).

Here, we directly and unambiguously measured the influence of the band structure of a material on the lifetime of photoelectrons. To accomplish this, we used attosecond pulse trains of well-defined harmonics to measure the photoemission time delays for free-electron final states as well as final states corresponding to the unoccupied bulk bands of the transition metal Ni(111). We were able to distinguish photoelectron lifetimes from individual valence bands and final states in Ni(111), with additional help from selection rules for photoemission for EUV fields with different polarizations (*1*, *27*). Our results show that when the final state corresponds to an unoccupied excited state in the Ni band structure, photoelectrons experience an abrupt delay of ~212 ± 30 as. This delay corresponds to the lifetime of the excited state and can be interpreted physically as a variation of the attenuation length of the final-state wave function inside the crystal. Therefore, through a direct time-domain measurement of attosecond photoelectron dynamics, our results provide insights into the fundamental concepts of photoelectron lifetime, inelastic mean free path (IMFP), and group velocity. Moreover, we observed large angle-dependent (i.e., momentum-dependent) variations in photoemission time delay, which are directly related to the final-state band dispersion.

The basic principle underlying our experiments is illustrated in Fig. 1A. Linearly polarized high harmonics are focused collinearly with infrared laser pulses (~26 fs, 780 nm) onto an atomically clean Ni(111) surface. The HHG spectra consist of multiple harmonic orders (11th to 41st) spanning from 17 to 66 eV, which are generated using different noble gases (Xe, Kr, Ar, and Ne). The corresponding HHG pulse train comprises EUV bursts with durations of ~200 as [full width at half maximum (FWHM)] within a ~15-fs (FWHM) envelope (*28*) in the time domain. Photoelectrons with sufficiently large momenta along the surface-normal direction escape the surface and are detected by a hemispherical electron analyzer. In the angle-resolved photoelectron spectrum, the same initial Bloch wave packet is excited to multiple final states with different kinetic energies, manifesting as a ladder of direct photoemission bands, each separated by twice the fundamental photon energy $\hbar\omega_L$ (where $\hbar$ is the Planck constant divided by 2π and ω_L is the frequency of the fundamental driving laser) (Fig. 1B). Laser-assisted photoemission in the presence of the phase-locked infrared (IR) laser field (3×10^{11} W/cm^2) modulates the photoelectron spectra as a function of τ_d, the relative delay between the EUV pump and IR probe fields. This allows us to extract photoelectron dynamics on attosecond time scales and angstrom length scales by analyzing the attosecond beating due to the interference of two-photon quantum pathways that lead to the same final photoelectron energy (in a technique called RABBITT) (*16*, *28*). RABBITT and attosecond streaking have been shown to yield the same temporal information about the photoemission process (*19*, *20*).

We first probed the electronic band structure of Ni(111) by studying the dependence of the static photoelectron spectra on the EUV photon energy and polarization (Fig. 2A). Striking differences can be observed for photoemission excited by s- and p-polarized EUV fields, which can be understood in terms of the selection rules for direct interband transitions (*1*, *27*). Taking these selection rules into account and considering our experimental geometry (45° angle of incidence of the HHG beam), we can unambiguously assign the two photoemission peaks in Fig. 2A that are excited by s-polarized light to the two valence bands with Λ_3 symmetry (Λ_3^α and Λ_3^β, with respective binding energies of ~0.6 eV and ~1.25 eV). The additional spectral weight observed for p-polarized light is from the Λ_1 initial band (~1.7 eV) (Fig. 2B). Both s- and p-polarized photoemission exhibit peak shifts when excited by different photon energies; this is clear evidence of contributions from bulk band transitions. Assuming direct transitions to a free electron–like final state, we can map the electron momentum in the surface-normal direction $\mathbf{k}_\perp$ for different photon energies (*1*, *29*, *30*). The extracted band structure is plotted in Fig. 2B. The good agreement of our photoelectron spectra with previous studies using synchrotron light covering a similar energy range (*30*) (Fig. 2B) verifies that high harmonics are ideal for capturing electron and band structure dynamics with subfemtosecond time resolution, good energy resolution (100 to 300 meV), easy manipulation of the photon energy and polarization (*31*), and perfect synchronization to the driving laser. Note that the valence bands calculated using density functional theory (DFT) are ~0.7 eV deeper than experiment because of the presence of strong correlations for Ni 3d electrons (*30*, *32*).

The most pronounced feature of Fig. 2A is the enhancement in the intensity of the low-energy spectral peak (~ –1.25 eV) upon excitation by ~24-eV HHG photons (15th order). This resonant feature clearly appears in the spectra that emerge from excitation by an s-polarized EUV field, indicating that the Λ_3^β band is the initial band. Considering the band structure of Ni(111) along the Γ-L direction, we can assign this spectral resonance to direct interband transitions from the Λ_3^β initial band to the high-energy unoccupied Λ_1^B final band located at ~24 eV above the Fermi level, as indicated by the blue arrow in Fig. 2B.

In photoemission theory, the matrix element responsible for photoelectron spectra can be written as $M_{fi} = \langle f|H^{int}|i\rangle$, where $|i\rangle$ is the initial state, $|f\rangle$ is the final state, and $H^{int} = \mathbf{A}_X \cdot \mathbf{p} + \mathbf{p} \cdot \mathbf{A}_X$

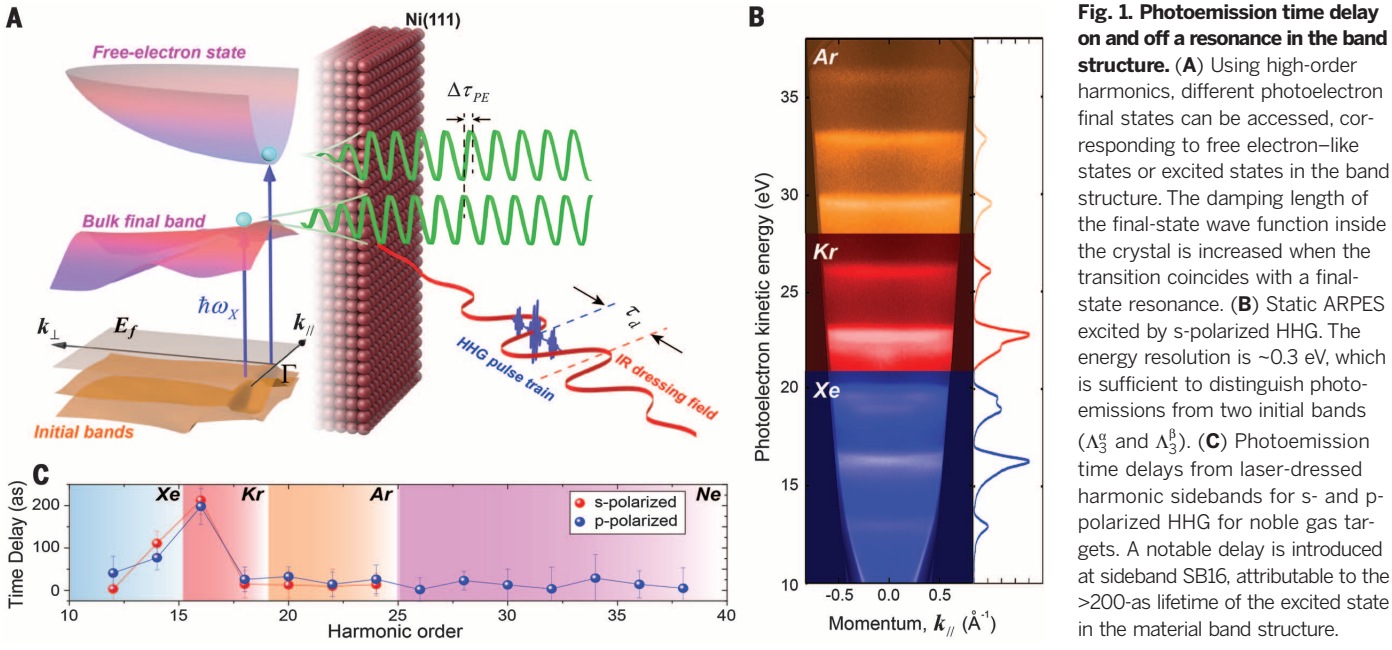

Fig. 1. Photoemission time delay on and off a resonance in the band structure. (**A**) Using high-order harmonics, different photoelectron final states can be accessed, corresponding to free electron–like states or excited states in the band structure. The damping length of the final-state wave function inside the crystal is increased when the transition coincides with a final-state resonance. (**B**) Static ARPES excited by s-polarized HHG. The energy resolution is ~0.3 eV, which is sufficient to distinguish photoemissions from two initial bands (Λ_3^α and Λ_3^β). (**C**) Photoemission time delays from laser-dressed harmonic sidebands for s- and p-polarized HHG for noble gas targets. A notable delay is introduced at sideband SB16, attributable to the >200-as lifetime of the excited state in the material band structure.

represents the interaction Hamiltonian between an electron and EUV electromagnetic radiation with vector potential $\mathbf{A}_X$. The final-state wave function can be represented as a time-reversed low-energy electron diffraction (LEED) state, composed of a free-electron wave arriving at the detector and a damped Bloch wave inside the crystal (*1*, *33*), with a characteristic damping length directly related to the IMFP and photoelectron lifetime. The increase in photoemission intensity as a result of this final-state resonance can be attributed to an increase in photoelectron lifetime, with associated elongation of the characteristic damping length of the final-state wave function, which strongly enhances the spatial overlap between the initial and final-state wave functions, and hence the transition probability. The energy-dependent photoemission intensity of the Λ_3^β band is summarized in Fig. 3B, together with a fit to a Lorentzian function with width $\gamma = 3.68 \pm 0.88$ eV and centered at 24.40 eV, which is consistent with previous studies (*26*). Thus, the characteristic lifetime of this final state can be extracted from $\tau_{spec} = \hbar/\gamma = 179 \pm 43$ as.

To directly measure the difference in photoelectron lifetimes between electrons excited into high-energy final bands (i.e., on resonance) and those excited into free-electron final states located in the band-gap region (*1*, *33*), we introduced an IR laser field to dress the photoelectrons. In the presence of the dressing laser field, there are two distinct quantum paths from an initial state to the same sideband, namely (i) absorption $\hbar\omega_{2n-1} + \hbar\omega_L$ and (ii) emission $\hbar\omega_{2n+1} - \hbar\omega_L$ of an IR photon (fig. S1B). When the relative time delay τ_d between the HHG pump and the IR probe is changed, the intensity of sidebands from a given initial band is modulated as a result of quantum-path interferences (*16*, *28*):

$$S_{2n}(\tau_d) = A_0 \sin[2\omega_L(\tau_d - \tau_X - \tau_{PE})] \quad (1)$$

where A_0 is the intensity of modulation, $\tau_X = (\phi_{2n+1} - \phi_{2n-1})/2\omega_L$ represents a time delay contributed by the phase chirp between neighboring harmonics ($\phi_{2n+1} - \phi_{2n-1}$), and τ_{PE} is the photoemission delay. Simultaneous measurement of two photoelectron wave packets excited by the same harmonic orders allows us to cancel the influence of attochirp (τ_X). This method was first implemented and validated for isolated atoms (*16*). In our experiments, we use the nonresonant photoemission from the Λ_3^α band as the timing reference and determine the relative photoemission delay of the resonant $\tau_{PE}(\Lambda_3^\beta) - \tau_{PE}(\Lambda_3^\alpha)$ and nonresonant $\tau_{PE}(\Lambda_1) - \tau_{PE}(\Lambda_3^\alpha)$. This allows us to compare time delays for comparable photoelectron energies and to cancel effects arising from the attochirp- or dressing field–induced phase delays.

We first measured the time delay $\tau_{PE}(\Lambda_3^\beta) - \tau_{PE}(\Lambda_3^\alpha)$ using s-polarized HHG fields. In Fig. 3C, we plot a set of experimental RABBITT interferograms for τ_d in the range –2 to 2 fs. The interferograms were obtained by integrating the photoelectron spectra over ±2.5° around the Γ point and subtracting the background spectrum obtained well before time zero. We intentionally selected a small angular region in the analysis to avoid the ambiguities resulting from angle-dependent photoemission time delay (see below). Figure 3C clearly shows that photoelectrons from the Λ_3^β band are notably delayed for sideband SB16 (corresponding to a photon energy of 25.6 eV), which manifests as a large offset in oscillations in the interferograms. This time delay gradually vanishes at increasing and decreasing photon energies, showing a nonmonotonic change of $\tau_{PE}(\Lambda_3^\beta) - \tau_{PE}(\Lambda_3^\alpha)$ as a function of photon energies. One-dimensional (1D) lineouts corresponding to the Λ_3^α and Λ_3^β bands in the sideband region are extracted in the panel on the right side of Fig. 3C, making it possible to determine the precise values of $\tau_{PE}(\Lambda_3^\beta) - \tau_{PE}(\Lambda_3^\alpha)$ as a function of energy. The results are summarized in Fig. 3A (see supplementary materials for detailed analysis). By comparing this relative photoemission delay with the spectral resonance (Fig. 3B), we find that the observed maximum in time delay coincides with the spectral resonance at the same photon energy, strongly indicating that the observed photoemission time delay originates from the excited-state band structure of Ni(111). Most important, the time delay measured using laser-assisted photoemission, $\tau_{chron} = 212 \pm 30$ as, agrees (within error bars) with the value from the spectral resonance, $\tau_{spec} = 179 \pm 43$ as.

To extract the photoemission time delay $\tau_{PE}(\Lambda_1) - \tau_{PE}(\Lambda_3^\alpha)$, we used p-polarized EUV fields for photoemission (Fig. 1C). We note that in this situation, the low-energy sideband intensity of the RABBITT oscillations has contributions from both Λ_1 and Λ_3^β bands. With the knowledge of the intensity contributions from these two initial bands, the time delay $\tau_{PE}(\Lambda_1) - \tau_{PE}(\Lambda_3^\alpha)$ can be extracted (see supplementary materials), as shown in Fig. 3A. In strong contrast to the Λ_3^β band, photoemission from the Λ_1 band exhibits a very small time delay relative to that from the Λ_3^α band and varies smoothly across the photon energy range.

In photoemission theory, the photoelectron lifetime can be understood as the time taken for the wave function to evolve from a Bloch wave inside the material into a free-electron wave function outside the solid. Semiclassically, this is also the time the photoelectron spends moving a distance corresponding to an IMFP (*33*, *34*). As we show below, the on-resonance time delay measured in our experiments can be directly related to the lifetime of the final-state high-energy band. The fact that our measured time delay agrees well with the lifetime extracted from the spectral linewidth indicates that the lifetimes of photoelectrons originating from the initial Λ_3^α band are very small (within experimental error, ~ ±53 as). At the same time, the photoelectron lifetimes corresponding to the Λ_1 band are longer by ~50 as (Fig. 3A). Because both bands exhibit a smooth variation in photoemission cross section over the photon energy range used here (see supplementary materials), it is reasonable to assume that their photoelectron lifetimes are slowly varying as a function of photon energies. Thus, the results shown in Fig. 3A can be interpreted as an abrupt increase of ~212 as in photoelectron lifetime from the Λ_3^β band when the direct transition approaches a bulk final band (Λ_1^B), resulting in a final-state resonance.

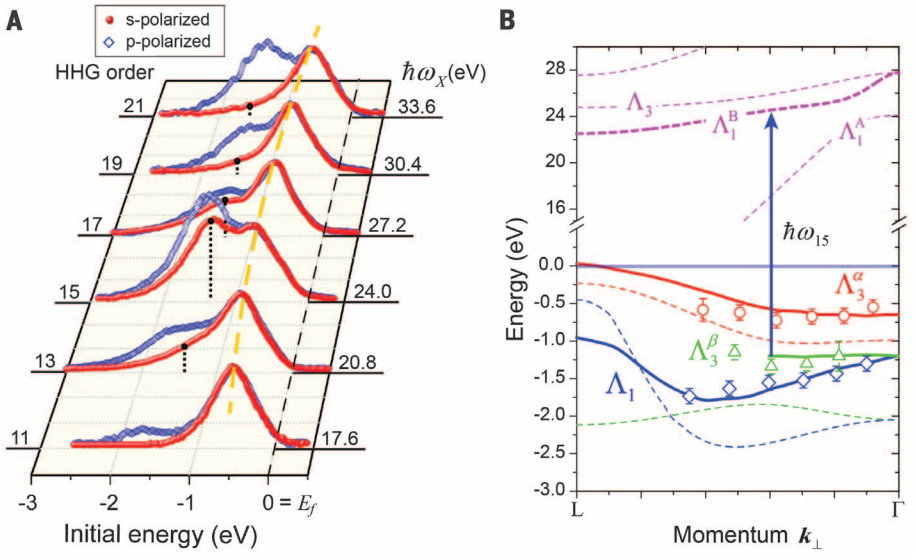

Fig. 2. Final-state resonance in photoemission from Ni(111). (**A**) EDC curves excited by s- (red) and p-polarized (blue) HHG in a normal emission geometry (integrated ~ ±2° around the Γ point). The position of the Fermi level (black dashed line) is determined from the laser photon energy (~1.6 eV) and analyzer work function (4.25 eV). The orange dashed line shows the shift of the high-energy peak with HHG photon energy, emphasizing the contribution of bulk band transitions. The intensity of the Λ_3^β band clearly shows a spectral resonance at ~24 eV. (**B**) Band structure along the Γ-L direction (normal to the surface) extracted from our data (open symbols) compared with results of previous experiments (*30*) (solid lines) and DFT calculations (dashed lines). A free-electron final state in a constant inner potential (*30*) is assumed and is used to map the electron momentum normal to the sample surface $\mathbf{k}_\perp$. The final-state resonance observed in (A) corresponds to a direct transition from the Λ_3^β initial band to the Λ_1^B final band, as highlighted by the blue arrow.

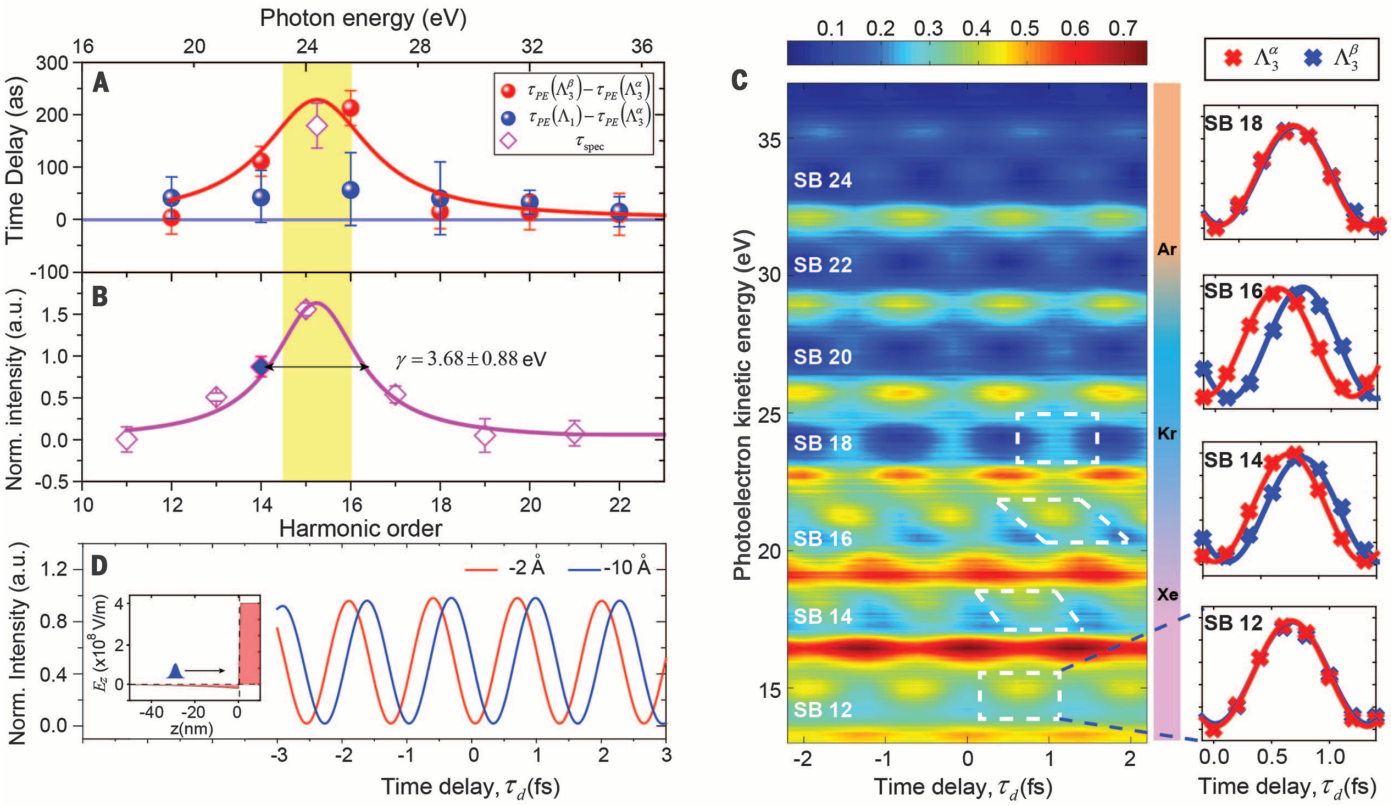

Fig. 3. Direct time-domain measurement of the final-state lifetime. (**A**) Photoemission time delays $\tau_{PE}(\Lambda_3^\beta) - \tau_{PE}(\Lambda_3^\alpha)$ and $\tau_{PE}(\Lambda_1) - \tau_{PE}(\Lambda_3^\alpha)$ as a function of photon energy, clearly showing an increase in lifetime (by 212 ± 30 as) when the final state corresponds to a short-lived excited state in the band structure. Error bars represent SD of time delays extracted from more than 200 individual scans. The red solid line is a Lorentzian curve with the same linewidth as in (B). (**B**) Spectral intensity of the Λ_3^β initial band as a function of photon energy. The blue point (14th order) is obtained from HHG driven by 390-nm laser field. Error bars represent the fitting uncertainties of the photoelectron yield from individual photoelectron spectra that were used to extract each point (see supplementary materials). The pink line represents a Lorentzian fit, yielding a linewidth of γ = 3.68 eV. (**C**) Two-dimensional map of photoelectron yields as a function of photoelectron energy and pump-probe time delay τ_d, excited by s-polarized HHG. To enhance the color contrast, 90% of the ground-state spectrum is subtracted to visualize the interferogram. The relative delays between photoelectrons from the Λ_3^α and Λ_3^β initial bands are manifested as a large offset in oscillations in the sidebands (white dashed boxes). A zoom-in view in both energy and time delay at the resonant energy is plotted in fig. S5D. Right panel: 1D lineouts for Λ_3^α and Λ_3^β initial bands in the corresponding regions. (**D**) Results of 1D semiclassical simulations. Relative to photoelectrons emitted from 2 Å below the surface, those emitted from 10 Å below the surface are delayed by 267 as. Inset: Profile of the dressing field strength normal to the surface (E_z) across the interface.

To physically interpret our measurements, we used a 1D semiclassical model (*35*) to calculate the RABBITT interferograms of photoelectrons with the same final energy but emitted from different depths (e.g., 2 Å and 10 Å) below the surface to simulate photoelectrons with different IMFPs. This model considers the quantum phases accumulated as the photoelectrons scatter from the IR dressing field and crystal potential (see supplementary materials). The IR dressing field inside the metal is mostly screened (see supplementary materials and inset of Fig. 3D) and has negligible influence on photoelectrons as they travel to the surface (*36*). One-dimensional lineouts of the RABBITT oscillations are plotted in Fig. 3D for photoelectrons with a free-electron velocity corresponding to an energy of 25.5 eV inside the crystal. We find that the RABBITT oscillation traces of photoelectrons emitted 10 Å below the surface are delayed by 267 as relative to those corresponding to photoelectrons originating 2 Å below the surface; this is consistent with the measured lifetime difference between them. In turn, this allows us to directly relate our time-domain measurements to the lifetimes and IMFPs of photoelectrons, which determine the surface and bulk contributions (*1*, *33*).

Determining the IMFP involves selecting a photoelectron velocity to be used in calculating it. In a periodic crystal lattice, the elastic interaction with atoms strongly modifies the electron energy-momentum relationship, giving rise to the electronic band structure. It is generally believed that the velocity of photoelectrons can be represented by the group velocity of the corresponding final bands, which is given by the derivative of the energy with respect to the momentum wave vector $\mathbf{k}_\perp$ (*11*, *13*, *14*). To determine the final-state group velocity, we used an ab initio calculation for the bulk band structure of Ni along the Γ-L direction, including the high-energy valence bands (~24 eV). We found that the final band involved in the resonant transition (highlighted in Fig. 2B) has a narrow bandwidth (~4 eV), consistent with our experimental spectra. The corresponding group velocity is given by $|\partial E_{fin}/\partial(\hbar\mathbf{k}_\perp)| \approx 3.0$ eVÅ/ħ, which is much smaller than the velocity of a free electron with the same kinetic energy (~19.1 eVÅ/ħ). Using the calculated group velocity, we obtain an IMFP of at most 1 Å, which is much smaller than values reported in other studies (*37*, *38*). We believe that this discrepancy arises because the group velocity is not the transport velocity for high-energy photoelectrons. As pointed out in previous studies (*34*), high-energy (>20 eV) photoelectrons leave the crystal before they are subject to the influence of the crystal lattice, so they behave more like plane waves with a free-electron dispersion. By using the corresponding free-electron velocity in our analysis, we extract an IMFP of ~6 Å for photoelectrons that are emitted on resonance, consistent with previous studies (*29*). In contrast, the IMFPs of photoelectrons from the Λ_3^α and Λ_1 bands, as well as those from the Λ_3^β band away from the spectral resonance, are estimated to be ~3 Å, manifesting their surface-emission nature.

Other important evidence that the band structure of the material strongly influences the photoemission lifetime can be seen from the angle

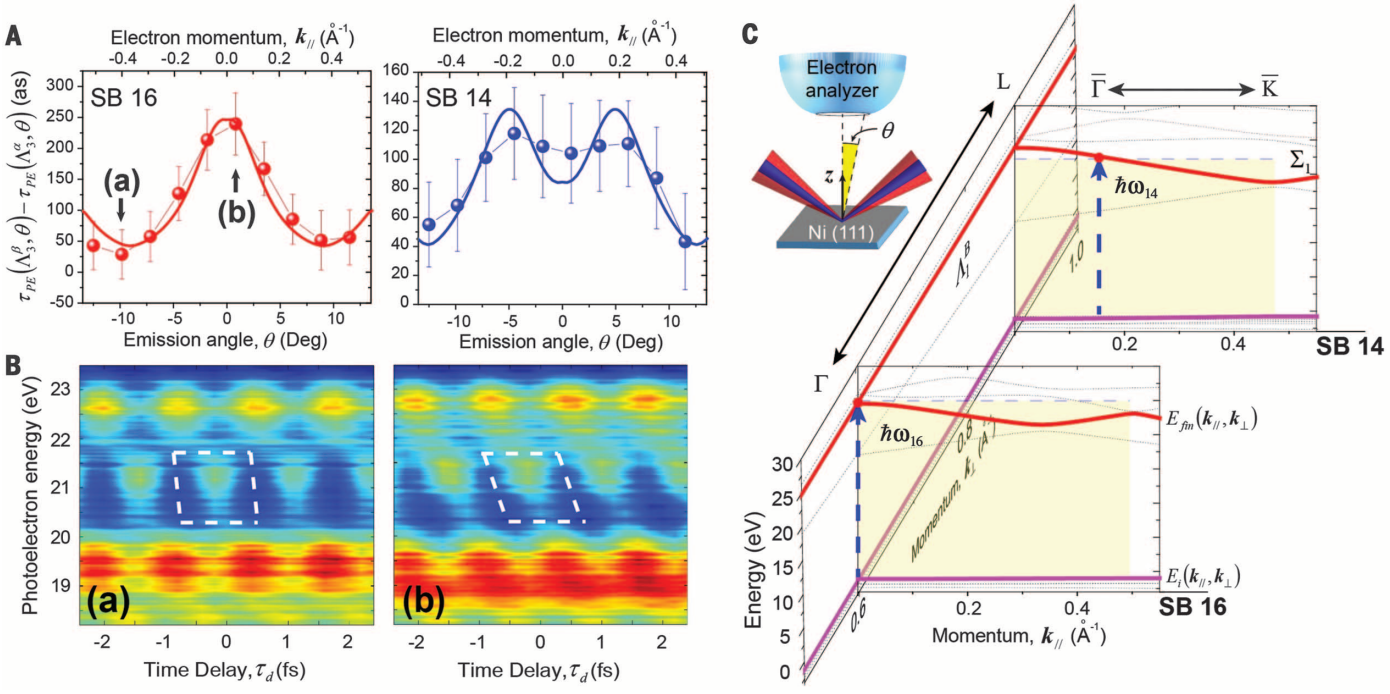

Fig. 4. Angle-dependent photoemission time delays. (**A**) Angle-dependent photoemission time delay $\tau_{PE}(\Lambda_3^\beta,\theta) - \tau_{PE}(\Lambda_3^\alpha,\theta)$ for SB16 and SB14 obtained using s-polarized HHG. The experimental data are points; the solid lines are a fit to the final-state band structure obtained from our model and DFT calculations (see supplementary materials). Error bars represent SD of the time delays extracted from more than 200 individual scans. (**B**) Typical RABBITT interferograms for SB16 with emission angles [(a) and (b)] labeled in (A). The offset in oscillations is highlighted with white dashed boxes. (**C**) Illustration of direct transitions in the $\overline{\Gamma}$–$\overline{K}$ direction for SB14 and SB16. Because different photon energies are used for these two sidebands, different $\mathbf{k}_\perp$ along the Γ-L direction are assigned according to the band-mapping results in Fig. 2B. The initial and final bands are highlighted by thick solid lines; the binding energy of the initial band (purple) is corrected according to the binding energy obtained in our experiments. Transitions corresponding to sideband photon energies are labeled as dashed arrows. Inset: Experimental geometry. IR and HHG beams are focused onto a Ni(111) surface at a 45° incident angle; θ is assigned to the emission angle of photoelectrons relative to the sample normal direction (**z**) along the $\overline{\Gamma}$–$\overline{K}$ direction.

dependence of the lifetime as a function of electron transverse momentum $\mathbf{k}_{//}$. To cancel any time delays imposed by the incident and reflected laser fields (*35*, *36*) and to extract the contribution due to band-structure effects, we used the RABBITT oscillations from the Λ_3^α band as the timing reference at different emission angles (θ) for each sideband (see supplementary materials). The angle-dependent results of $\tau_{PE}(\Lambda_3^\beta,\theta) - \tau_{PE}(\Lambda_3^\alpha,\theta)$ are summarized in Fig. 4A for SB16 and SB14 (near the resonance). As shown in Fig. 4A, the time delay $\tau_{PE}(\Lambda_3^\beta,\theta) - \tau_{PE}(\Lambda_3^\alpha,\theta)$ at SB16 reaches its maximum value of ~220 as at $\overline{\Gamma}$ point (θ = 0), whereas it reduces to ~30 as when the emission angle approaches θ = ±15°. The overall trend is symmetric around the $\overline{\Gamma}$ point, which strongly suggests the band-structure origin of this angle-dependent photoemission time delay. The most interesting feature is that $\tau_{PE}(\Lambda_3^\beta,\theta) - \tau_{PE}(\Lambda_3^\alpha,\theta)$ exhibits a double-peak shape at SB14 (Fig. 4A) as the time delay increases to its maximum on-resonance value at θ ≈ ±6° and then decreases for larger emission angles.

To quantitatively interpret this angle-dependent photoemission lifetime, we compared the predicted time delays associated with our model and DFT calculations (see supplementary materials) with the experimental data (Fig. 4A). Our results show that for SB16, the HHG photon energy closely matches the resonant excited state at the $\overline{\Gamma}$ point, yielding a maximum time delay for θ = 0. Moreover, the time delay monotonically decreases at larger emission angles, since final-state band dispersion causes the transition to be off resonance. On the other hand, for SB14, in which the photon energy is ~3.2 eV lower, the resonant transition is not accessible at the $\overline{\Gamma}$ point, but is on resonance and yields a maximum time delay at a ~6° emission angle (Fig. 4C). The key factor for this agreement is the dispersion of the Σ_1 final band along the $\overline{\Gamma}$–$\overline{K}$ direction (with a group velocity of ~ –14 eVÅ/ħ), which determines the slope of the time delay as a function of θ.

Our results highlight the importance of the material band structure in determining photoemission time delays, which must also be taken into account even at higher photon energies. In the future, this approach can be used to experimentally access quasi-particle lifetimes, electron mean free paths, electron-electron scattering, and dynamical screening, all of which represent grand challenges for condensed matter theory. Moreover, other effects, including Cooper minima (*39*) and Fano resonances (*40*), could also lead to notable delays, making attosecond studies of metal valence bands a challenging but also a rich and interesting problem.

REFERENCES AND NOTES

1. S. Hüfner, *Photoelectron Spectroscopy: Principles and Applications* (Springer-Verlag, ed. 3, 2003).
2. F. Schmitt *et al.*, *Science* **321**, 1649–1652 (2008).
3. A. Rundquist *et al.*, *Science* **280**, 1412–1415 (1998).
4. D. Popmintchev *et al.*, *Science* **350**, 1225–1231 (2015).
5. S. Hellmann *et al.*, *Nat. Commun.* **3**, 1069 (2012).
6. S. Eich *et al.*, *J. Electron Spectrosc. Relat. Phenom.* **195**, 231–236 (2014).
7. W. Li *et al.*, *Proc. Natl. Acad. Sci. U.S.A.* **107**, 20219–20222 (2010).
8. S. Mathias *et al.*, *Proc. Natl. Acad. Sci. U.S.A.* **109**, 4792–4797 (2012).
9. E. Turgut *et al.*, *Phys. Rev. Lett.* **110**, 197201 (2013).
10. L. Miaja-Avila *et al.*, *Phys. Rev. Lett.* **101**, 046101 (2008).
11. A. L. Cavalieri *et al.*, *Nature* **449**, 1029–1032 (2007).
12. R. Locher *et al.*, *Optica* **2**, 405–410 (2015).
13. S. Neppl *et al.*, *Phys. Rev. Lett.* **109**, 087401 (2012).
14. S. Neppl *et al.*, *Nature* **517**, 342–346 (2015).
15. R. Pazourek, S. Nagele, J. Burgdörfer, *Rev. Mod. Phys.* **87**, 765–802 (2015).
16. K. Klünder *et al.*, *Phys. Rev. Lett.* **106**, 143002 (2011).
17. M. Schultze *et al.*, *Science* **328**, 1658–1662 (2010).
18. L. Miaja-Avila *et al.*, *Phys. Rev. Lett.* **97**, 113604 (2006).
19. C.-H. Zhang, U. Thumm, *Phys. Rev. A* **82**, 043405 (2010).
20. J. M. Dahlström *et al.*, *Chem. Phys.* **414**, 53–64 (2013).
21. C.-H. Zhang, U. Thumm, *Phys. Rev. Lett.* **102**, 123601 (2009).
22. C. Lemell, B. Solleder, K. Tokési, J. Burgdörfer, *Phys. Rev. A* **79**, 062901 (2009).
23. A. K. Kazansky, P. M. Echenique, *Phys. Rev. Lett.* **102**, 177401 (2009).
24. E. E. Krasovskii, *Phys. Rev. B* **84**, 195106 (2011).
25. A. G. Borisov, D. Sánchez-Portal, A. K. Kazansky, P. M. Echenique, *Phys. Rev. B* **87**, 121110(R) (2013).
26. F. Roth, C. Lupulescu, E. Darlatt, A. Gottwald, W. Eberhardt, *J. Electron Spectrosc. Relat. Phenom.* **208**, 2–10 (2016).
27. J. Hermanson, *Solid State Commun.* **22**, 9–11 (1977).
28. P. M. Paul *et al.*, *Science* **292**, 1689–1692 (2001).
29. J. A. Knapp, F. J. Himpsel, D. E. Eastman, *Phys. Rev. B* **19**, 4952–4964 (1979).

30. F. J. Himpsel, J. A. Knapp, D. E. Eastman, *Phys. Rev. B* **19**, 2919–2927 (1979).
31. C. Chen *et al.*, *Sci. Adv.* **2**, e1501333 (2016).
32. A. Liebsch, *Phys. Rev. Lett.* **43**, 1431–1434 (1979).
33. B. Feuerbacher, R. F. Willis, *J. Phys. C* **9**, 169–216 (1976).
34. J. S. Dolado, V. M. Silkin, M. A. Cazalilla, A. Rubio, P. M. Echenique, *Phys. Rev. B* **64**, 195128 (2001).
35. M. Lucchini, A. Ludwig, L. Kasmi, L. Gallmann, U. Keller, *Opt. Express* **23**, 8867–8879 (2015).
36. M. Lucchini *et al.*, *Phys. Rev. Lett.* **115**, 137401 (2015).
37. C. J. Powell, *Surf. Sci.* **44**, 29–46 (1974).
38. D. E. Eastman, J. A. Knapp, F. J. Himpsel, *Phys. Rev. Lett.* **41**, 825–828 (1978).
39. G. Rossi, I. Lindau, L. Braicovich, I. Abbati, *Phys. Rev. B* **28**, 3031–3042 (1983).
40. C. Guillot *et al.*, *Phys. Rev. Lett.* **39**, 1632–1635 (1977).

ACKNOWLEDGMENTS

We thank A. Carr, P. Matyba, G. D. Mahan, G. B. Arnold, G. F. Mancini, H. X. Li, Z. Zhu and Y. Cao for helpful discussions. This work was done at JILA. The JILA authors gratefully acknowledge support from the National Science Foundation through the JILA Physics Frontiers Centers Program and a Gordon and Betty Moore Foundation EPiQS Award through grant GBMF4538. T.S. and M.Ma. gratefully acknowledge support from Air Force Office of Scientific Research under a Basic Research Initiative grant (AFOSR FA9550-12-1-0481) and DOE-BES, the Division of Chemical Sciences (grant DE-FG02-05ER15731). The authors declare that they have no competing interests. H.K. and M.Mu. have a financial interest in a laser company, KMLabs.

SUPPLEMENTARY MATERIALS

www.sciencemag.org/content/353/6294/62/suppl/DC1
Supplementary Text
Figs. S1 to S9
References (*41*–*72*)

13 March 2016; accepted 11 May 2016
Published online 2 June 2016
10.1126/science.aaf6793

MALARIA MOSQUITOES

A maleness gene in the malaria mosquito *Anopheles gambiae*

Elzbieta Krzywinska,[1]* Nathan J. Dennison,[2,3]* Gareth J. Lycett,[2] Jaroslaw Krzywinski[1,2]†

The molecular pathways controlling gender are highly variable and have been identified in only a few nonmammalian model species. In many insects, maleness is conferred by a Y chromosome–linked M factor of unknown nature. We have isolated and characterized a gene, *Yob*, for the M factor in the malaria mosquito *Anopheles gambiae*. *Yob*, activated at the beginning of zygotic transcription and expressed throughout a male's life, controls male-specific splicing of the *doublesex* gene. Silencing embryonic *Yob* expression is male-lethal, whereas ectopic embryonic delivery of *Yob* transcripts yields male-only broods. This female-killing property may be an invaluable tool for creation of conditional male-only transgenic *Anopheles* strains for malaria control programs.

Animals have evolved a variety of mechanisms for sex determination. In insects, a common pattern requires a primary sex-determining signal that in early embryos activates a short cascade of sex-specifically spliced genes. The products of these genes modulate differentiation of an individual into either male or female, depending on the sex determination system (*1*). In the absence of the primary signal, a default pattern of gene splicing leads to the development of the opposite sex. Only the final element of the cascade, the *doublesex* gene, is well conserved, whereas upstream genes are highly evolutionarily labile (*2*) and are difficult to identify with comparative genomics tools.

Drosophila melanogaster has an XX/XY chromosomal sex determination system, in which a double dose of X chromosome–linked signal elements (XSE) represents the primary signal that initiates female-specific pre-mRNA splicing in a cascade of subordinate genes *sex lethal* (*Sxl*), *transformer* (*tra*), and *doublesex* (*dsx*) (*3*, *4*). The resulting transcripts yield functional female-specific proteins, of which SXL regulates splicing of *tra*, and TRA, along with its cofactor TRA2, promotes splicing of *dsx*. In males, a single dose of XSE is insufficient to initiate this female-specific cascade, and the three genes are spliced by a default male-specific mode, with only *dsx* encoding a functional protein. The male and female forms of DSX regulate sex-specific morphologies by modulating the expression of genes involved in downstream sexual differentiation processes.

The dipterans *Ceratitis capitata*, *Lucilia cuprina*, and *Musca domestica*, and the beetle *Tribolium castaneum*, also possess an XX/XY chromosomal system. However, in these insects an unidentified Y chromosome–linked M factor constitutes a primary signal that determines maleness (*5*–*8*). In none of these species is *Sxl* involved in sex determination. Instead, maternal *tra* mRNA is sufficient to direct default female development in the absence of the Y-linked factor, whereas in males the M may be preventing establishment of *tra* function by an unknown mechanism (*9*–*12*). The XX/XY system incorporating a dominant Y-linked M factor is common in many insect groups (*13*–*15*). However, with the exception of *Nix* (a homolog of *tra2*) from a mosquito *Aedes aegypti* (*16*), genes encoding M factor have remained enigmatic.

In anopheline mosquitoes, the only described element of the (morphological) sex determination cascade is *dsx* (*17*). To elucidate the initial steps of sex determination in the African malaria mosquito, *Anopheles gambiae*, we analyzed transcriptomes of male and female embryos (*18*), whose sexual identity was determined by polymerase chain reaction (PCR) (fig. S1). Separate pools of mRNA were sequenced, yielding ~500,000 Roche 454 reads from each sex. From the male pool, 21 reads uniquely mapped to the previously characterized scaffold AAAB01008227 derived from the *A. gambiae* Y chromosome (*19*).

The corresponding gene (hereafter called *Yob*) consists of three exons and produces transcripts differing in size because of intron retention (fig. S2). *Yob* likely represents the same gene as *gYG2* (*20*), which partially overlaps *Yob*, but its annotation lacks over half of the *Yob* gene sequence. Among the *A. gambiae* Y-linked genes, only the *Yob*/*gYG2* locus is Y-linked across the examined species from the *A. gambiae* complex (*21*), indicative of an important sexual identity function. Consistent with the chromosomal location, transcription of *Yob* is limited to males. Transcription begins in embryos between 2 and 2.5 hours after oviposition, before blastoderm formation (*22*) and expression of other Y-chromosome genes (*20*, *21*), and continues throughout the life of the mosquito (Fig. 1A and fig. S3A). Onset of the *Yob* transcription is nearly contemporaneous with that of orthologs of *even skipped* (AGAP010279) and *hunchback* (AGAP010777) (fig. S3B), whose transcripts mark the beginning of zygotic expression in *Drosophila (23, 24)*. We

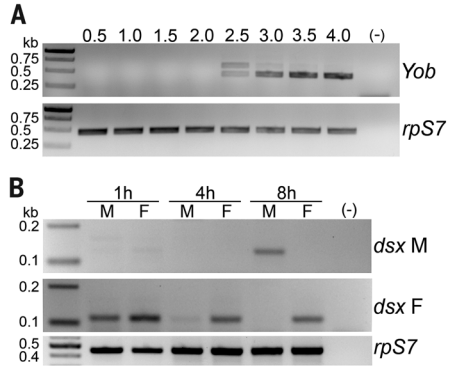

Fig. 1. Transcription of *Yob* and *dsx* in *A. gambiae* early embryos. (**A**) Onset of zygotic *Yob* transcription. (**B**) Establishment of the sex-specific expression pattern of *dsx*. Time of RNA sample collection (in hours after oviposition) are shown above gel images; (-) negative control; ribosomal protein *S7* (*rpS7*) transcript levels were used as a gel loading control.

[1]The Pirbright Institute, Ash Road, Pirbright, Surrey, GU24 0NF, UK. [2]Vector Biology Department, Liverpool School of Tropical Medicine, Pembroke Place, Liverpool L3 5QA, UK. [3]Department of Life Sciences, Imperial College, South Kensington Campus, London SW7 2AZ, UK.
*These authors contributed equally to this work. †Corresponding author: Email: jaroslaw.krzywinski@pirbright.ac.uk

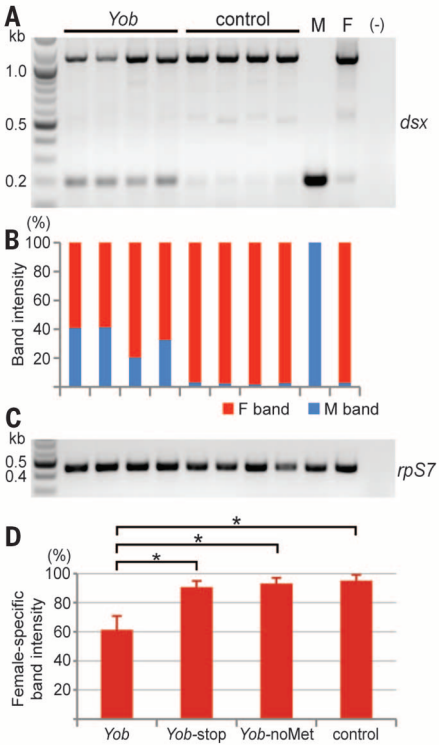

Fig. 2. *Yob* is a protein-coding sex determination gene controlling *dsx* splicing. (**A**) Reverse transcription (RT)–PCR analysis of *dsx* splicing pattern in the *A. gambiae* Sua5.1 cells transfected with in vitro–synthesized *Yob* mRNA, as compared with control nontransfected cells. M and F, *A. gambiae* male and female pupae; (-) negative control. Similar results were obtained in three independent experiments. (**B**) Digital representation of the relative amounts of *dsx* splice forms shown in (A). (**C**) RT-PCR analysis of ribosomal protein *S7* transcript levels used as a sample loading control. (**D**) Splicing pattern of *dsx* in Sua5.1 cells transfected with native *Yob* transcripts; nonproductive forms of *Yob*, either lacking the methionine start codon, or containing a premature stop codon; and in nontransfected control cells. The data shown are mean + SD. *$P < 0.001$, one-sided Mann-Whitney test.

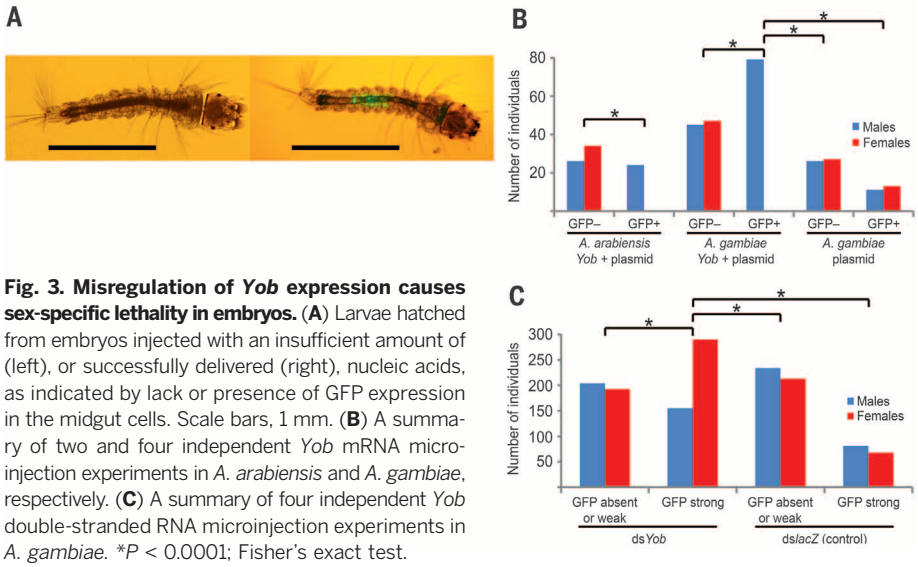

Fig. 3. Misregulation of *Yob* expression causes sex-specific lethality in embryos. (**A**) Larvae hatched from embryos injected with an insufficient amount of (left), or successfully delivered (right), nucleic acids, as indicated by lack or presence of GFP expression in the midgut cells. Scale bars, 1 mm. (**B**) A summary of two and four independent *Yob* mRNA microinjection experiments in *A. arabiensis* and *A. gambiae*, respectively. (**C**) A summary of four independent *Yob* double-stranded RNA microinjection experiments in *A. gambiae*. *$P < 0.0001$; Fisher's exact test.

determined that *Yob* activation precedes establishment of sex-specific splicing of *dsx* by up to 6 hours. The female isoform of *dsx* is maternally deposited, but largely degraded in male embryos within 4 hours of oviposition, and only after complete degradation of the female isoform in males is a persistent pattern of sex-specific *dsx* splicing established (Fig. 1B). These findings are consistent with *Yob* acting upstream of *dsx* in the sex-determining hierarchy. If true, introduction of *Yob* transcripts into female cells should cause an alteration of *dsx* splicing pattern.

We investigated the effect of in vitro–synthesized mRNA corresponding to the shortest, presumably mature *A. gambiae Yob* transcript isoform on *dsx* splicing in the *A. gambiae* Sua5.1 cell line, which lacks the Y chromosome and *Yob* expression (fig. S4). We observed a significant loss of the female and gain of the male *dsx* transcript isoforms in cells transfected with *Yob* mRNA, as compared with control nontransfected cells (Fig. 2, A, B, and D), or cells transfected with nonproductive forms of *Yob* (see below; Fig. 2D). Transfection experiments in larvae suggest that *Yob* exerts the same effect on *dsx* in vivo (fig. S5). This confirms that *Yob* is involved in the sex determination pathway as a direct or an indirect upstream regulator of *dsx* splicing.

In the vast majority of protein-coding genes, different evolutionary constraints on individual codon positions result in synonymous substitutions observed with much higher frequency than the nonsynonymous ones (*25*). Based on this principle, we evaluated the protein-coding potential of *Yob* by comparing its sequence to PCR-isolated orthologous sequences from *Anopheles arabiensis* and *Anopheles quadriannulatus*, two members of the *Anopheles gambiae* complex. The analyzed region encompasses two open reading frames (ORFs) longer than 50 codons, of which only the shorter ORF bears a substitution pattern indicative of purifying selection (fig. S6). Guided by these results, we experimentally tested for the protein-coding potential of the shorter ORF. We transfected the Sua5.1 cells with two modified *Yob* transcripts containing putative nonsynonymous point mutations r.1A>C and [r.5U>A; 6U>G] and investigated the effects of the deduced amino acid changes $Met^1 \rightarrow Leu$ and $Phe^2 \rightarrow Stop$, respectively, on *dsx* splicing. No shift in *dsx* splicing pattern was observed in cells transfected with transcripts either lacking an initiation codon or containing a premature stop codon, unlike the positive control cells transfected in parallel with the wild-type *Yob* transcripts (Fig. 2D and fig. S7). These results indicate that *Yob* encodes a short, 56–amino acid protein that may contain a helix-loop-helix motif (fig. S8). A protein with the same length and similar secondary structure, but nonconserved primary sequence, was proposed to be encoded by an early zygotically expressed Y-linked gene, *GUY1*, potentially involved in sex determination in *Anopheles stephensi* (*26*).

We injected *Yob* mRNA into nonsexed preblastoderm embryos of *A. gambiae* and its sibling species *A. arabiensis* to assess whether ectopic *Yob* transcripts affect mosquito sex ratios. To control for successful injection, we coinjected a plasmid with a green fluorescent protein (GFP) expression cassette (embryos that receive sufficient nucleic acids develop into larvae transiently expressing GFP; fig. S9). Surviving individuals were sorted at the larval stage into a GFP-positive and a GFP-negative group (Fig. 3A), and at the pupal stage mosquitoes were sexed. In both species, all the GFP-positive individuals developed as phenotypic males, whereas in the GFP-negative group and in the control group of *A. gambiae* embryos injected with GFP plasmid only, the sex ratio was unbiased (Fig. 3B). The GFP-positive males had the XY karyotype, as indicated by PCR; moreover, they had normally developed reproductive organs, produced motile sperm, and were fertile (table S1). Thus, ectopic delivery of *Yob* mRNA is lethal to genetic female embryos, but has no discernible effect on the sexual development of genetic males.

In *D. melanogaster*, female-specific embryonic lethality is caused by loss-of-function mutations in genes located at the top of the sex determination cascade and invariably results from a misregulation of dosage compensation (*3*, *27*–*29*). The dosage compensation mechanism in that species equalizes X-linked gene products in XX and XY individuals by up-regulation of transcription from the male X chromosome (*30*). The process is tightly linked to the sex determination through female-specific repression by SXL (*31*, *32*). Mutations in *Sxl*, or in genes involved in *Sxl* regulation, cause overexpression of X-linked genes and female death during embryogenesis (*3*, *27*–*29*). In females of *T. castaneum*, in which *Sxl* has no sex-determining role, TRA has been proposed to inhibit dosage compensation (*12*). In a lepidopteran, *Bombyx mori*, in which females are heterogametic (ZW) and males homogametic (ZZ), male embryo lethality, observed after a knockdown

of a sex determination gene, *Masculinizer* (responsible for male-specific splicing of *dsx* and repression of transcription from Z chromosomes), has been similarly attributed to misregulation of dosage compensation (*33*).

Dosage compensation in *A. gambiae* also relies on hyperactivation of the X-chromosome genes in males (*34*). Therefore, in the presence of YOB, dosage compensation may be directly or indirectly induced in the XX embryos, leading to their death as a result of abnormal overtranscription from both X chromosomes (fig. S10). Conversely, in the absence of YOB, lack of dosage compensation and concomitant insufficient transcription from the X chromosome should be male-lethal, rather than leading to feminization of the XY individuals. Indeed, we observed highly significant male deficiency in mosquitoes surviving transient knockdown of *Yob* in nonsexed embryos (Fig. 3C). All tested female survivors had the XX karyotype.

Involvement of the Y chromosome factor in sex determination in *Anopheles* was first supported by the finding of a single, triploid *Anopheles culicifacies* male with the XXY sex chromosomes (*15*). Such a karyotype, apparently extremely rare and not reported elsewhere in numerous mutational and cytogenetic studies in *Anopheles*, seems to counter overtranscription of the X-chromosome genes as a cause of female embryo lethality observed in our study. However, the genetic background of this male must have been severely compromised through the mutagenic effects of irradiation on his parents (*15*). It thus seems likely that the XXY male may have carried multiple mutations, including those causing loss of function of dosage compensation machinery that allowed his survival to adulthood despite possessing two X chromosomes.

A. gambiae and *A. arabiensis* are the most important African vectors of human malaria. Control of the disease depends heavily on the use of insecticides, but emergence of resistance in mosquito populations severely threatens the effectiveness of these approaches (*35*). The sterile insect technique and other genetic control methods have been proposed to complement current efforts to suppress mosquito populations (*36*, *37*). Such programs must incorporate male-only releases, because released females would contribute to pathogen transmission. However, no effective methods to sex the large number of *Anopheles* needed for releases currently exist. The fitness and mating competitiveness of adults is highly dependent on larval density; therefore, removing females from the release generation during the embryonic stage would drastically decrease the costs of rearing of high-quality males (*38*). *Yob* represents an excellent tool to be used in transgenic technology to conditionally eliminate female embryos and efficiently produce male-only generations of both malaria-transmitting *Anopheles* species (*37*).

REFERENCES AND NOTES

1. T. Gempe, M. Beye, *BioEssays* **33**, 52–60 (2011).
2. A. S. Wilkins, *BioEssays* **17**, 71–77 (1995).
3. T. W. Cline, B. J. Meyer, *Annu. Rev. Genet.* **30**, 637–702 (1996).
4. J. W. Erickson, J. J. Quintero, *PLOS Biol.* **5**, e332 (2007).
5. T. Hiroyoshi, *Genetics* **50**, 373–385 (1964).
6. D. Bedo, G. Foster, *Chromosoma* **92**, 344–350 (1985).
7. U. Willhoeft, G. Franz, *Genetics* **144**, 737–745 (1996).
8. J. J. Stuart, G. Mocelin, *Genome* **38**, 673–680 (1995).
9. A. Pane, M. Salvemini, P. Delli Bovi, C. Polito, G. Saccone, *Development* **129**, 3715–3725 (2002).
10. C. Concha, M. J. Scott, *Genetics* **182**, 785–798 (2009).
11. M. Hediger *et al.*, *Genetics* **184**, 155–170 (2010).
12. J. N. Shukla, S. R. Palli, *Sci. Rep.* **2**, 602 (2012).
13. I. Marín, B. S. Baker, *Science* **281**, 1990–1994 (1998).
14. M. J. D. White, *Animal Cytology and Evolution* (Cambridge Univ. Press, Cambridge, ed. 3., 1973).
15. R. H. Baker, R. K. Sakai, *J. Hered.* **70**, 345–346 (1979).
16. A. B. Hall *et al.*, *Science* **348**, 1268–1270 (2015).
17. C. Scali, F. Catteruccia, Q. Li, A. Crisanti, *J. Exp. Biol.* **208**, 3701–3709 (2005).
18. Materials and methods are available on *Science* Online.
19. J. Krzywinski, D. R. Nusskern, M. K. Kern, N. J. Besansky, *Genetics* **166**, 1291–1302 (2004).
20. A. B. Hall *et al.*, *BMC Genomics* **14**, 273 (2013).
21. A. B. Hall *et al.*, *Proc. Natl. Acad. Sci. U.S.A.* **113**, E2114–E2123 (2016).
22. J. Juhn, A. A. James, *Insect Mol. Biol.* **15**, 363–372 (2006).
23. D. Tautz *et al.*, *Nature* **327**, 383–389 (1987).
24. D. K. Pritchard, G. Schubiger, *Genes Dev.* **10**, 1131–1142 (1996).
25. W. H. Li, in *Molecular Evolution*, W. H. Li, Ed. (Sinauer, Sunderland, MA, 1997), pp. 177–214.
26. F. Criscione, Y. Qi, R. Saunders, B. Hall, Z. Tu, *Insect Mol. Biol.* **22**, 433–441 (2013).
27. J. C. Lucchesi, T. Skripsky, *Chromosoma* **82**, 217–227 (1981).
28. J. P. Gergen, *Genetics* **117**, 477–485 (1987).
29. A. Hilfiker, H. Amrein, A. Dübendorfer, R. Schneiter, R. Nöthiger, *Development* **121**, 4017–4026 (1995).
30. J. C. Lucchesi, W. G. Kelly, B. Panning, *Annu. Rev. Genet.* **39**, 615–651 (2005).
31. M. E. Gelbart, M. I. Kuroda, *Development* **136**, 1399–1410 (2009).
32. G. J. Bashaw, B. S. Baker, *Cell* **89**, 789–798 (1997).
33. T. Kiuchi *et al.*, *Nature* **509**, 633–636 (2014).
34. G. Rose *et al.*, *Genome Biol. Evol.* **8**, 411–425 (2016).
35. J. Hemingway *et al.*, *Lancet* **387**, 1785–1788 (2016).
36. E. F. Knipling, *Science* **130**, 902–904 (1959).
37. L. Alphey, *Annu. Rev. Entomol.* **59**, 205–224 (2014).
38. P. A. Papathanos *et al.*, *Malar. J.* **8** (suppl. 2), S5 (2009).

ACKNOWLEDGMENTS

We thank H. Ranson, A. Wilson, and anonymous reviewers for comments and L. Revuelta for technical assistance. This study was supported by funds from the Liverpool School of Tropical Medicine (LSTM), an MRC-LSTM Research Studentship, Wellcome Trust grant 089045/Z/09/Z (J.K. and G.J.L.), and funds from the Pirbright Institute (J.K.). Transgenic mosquitoes used for sexing were developed with Biotechnology and Biological Sciences Research Council grant BB/F021933/1 (G.J.L.). J.K. was partly supported by a subcontract CRSC120816JKUND of the NIH contract HHSN272200900039C. The RNA-sequencing data have been deposited in the Sequence Read Archive repository under the accession numbers SRR953486.1 and SRR953487.1.

SUPPLEMENTARY MATERIALS

www.sciencemag.org/content/353/6294/67/suppl/DC1
Materials and Methods
Figs. S1 to S10
Tables S1 to S3
References (*39*–*48*)

28 February 2016; accepted 1 June 2016
10.1126/science.aaf5605

CLIMATE CHANGE

Sex-specific responses to climate change in plants alter population sex ratio and performance

William K. Petry,[1,2]*† Judith D. Soule,[2] Amy M. Iler,[2,3] Ana Chicas-Mosier,[2,4] David W. Inouye,[2,5] Tom E. X. Miller,[6] Kailen A. Mooney[1,2]

Males and females are ecologically distinct in many species, but whether responses to climate change are sex-specific is unknown. We document sex-specific responses to climate change in the plant *Valeriana edulis* (valerian) over four decades and across its 1800-meter elevation range. Increased elevation was associated with increased water availability and female frequency, likely owing to sex-specific water use efficiency and survival. Recent aridification caused male frequency to move upslope at 175 meters per decade, a rate of trait shift outpacing reported species' range shifts by an order of magnitude. This increase in male frequency reduced pollen limitation and increased seedset. Coupled with previous studies reporting sex-specific arthropod communities, these results underscore the importance of ecological differences between the sexes in mediating biological responses to climate change.

Differences between the sexes in morphology and physiology can result in sex-specific responses to the environment (*1*–*3*). Given this, climate change may affect the sexes differently, potentially creating an imbalance in the frequency of males and females and altering patterns of fertility and population dynamics (*4*–*6*). In so doing, climate change might ameliorate or exaggerate existing sex ratio biases, alternatively driving population growth or decline (*4*, *7*) and affecting the ability of species' ranges to track shifting climate envelopes (*8*, *9*).

We investigated whether climatic variation differentially affects the performance of the sexes and whether these differences are sufficient to bias population sex ratios. We studied *Valeriana edulis* (valerian, Caprifoliaceae), a dioecious herb with fixed, genetically based sex expression (*10*, *11*), over its entire elevation range from arid low-elevation scrublands to mesic alpine tundra (2000 to 3790 m) and in response to 33 years of climate change. We assessed (i) sex ratio change along these two complementary axes of climate variation, (ii) the sex-specific mechanisms underlying this change, and (iii) how biased sex ratios influence individual fitness.

Climate varies considerably across the elevation range of *V. edulis* (fig. S1, A to D, and

table S2). Contemporary climate data for our study area in the Rocky Mountains of Colorado (fig. S2 and table S1) showed that increasing elevation is accompanied by a decrease in mean growing season (June–August) temperature (−0.59°C per 100 m), an increase in growing season precipitation (1.5 mm per 100 m), a delay in the date of snowmelt (4.1 days later per 100 m), and a marginally significant trend for increasing growing season soil moisture (1.09% per 100 m). Collectively, these changes produce a gradient of decreasing aridity with increasing elevation.

We surveyed population operational sex ratios (OSRs; the proportion of flowering individuals that are male) across this elevation gradient to test whether elevational variation in climate was accompanied by parallel variation in *V. edulis* population OSR. Surveys of 31 *V. edulis* populations across the species' elevation range in 2011 showed that males decrease in frequency with increasing elevation (linear regression, $F_{1, 29} = 10.33$, $P = 0.003$, $R^2 = 0.26$) (Fig. 1A), falling from 50.0% of flowering individuals at the lowest elevation population to 22.7% at the highest population, for an average change of −0.88% per 100 m of elevation. Spatial climatic variation thus affects *V. edulis* OSR, suggesting that similar shifts may occur in response to climate change over time.

Recent climate change has warmed and dried our study area, driving climatic isoclines up in elevation and providing a temporal axis of climate variation that parallels that which occurs over the elevation gradient (fig. S1, E to H, and table S2). Data collected during the growing season over the past four decades (1978–2014) show that mean temperature increased 0.21°C/decade, precipitation decreased 1.91 mm/decade, and soil moisture decreased 1.5%/decade, whereas snowmelt date marginally advanced 2.9 days/decade (tables S1 and S2). This change over time is equivalent to an upslope shift in the isoclines for growing season mean temperature, precipitation, advancement of snowmelt, and soil moisture at rates of 36 ± 8, 133 ± 26, 72 ± 40, and 195 ± 523 m/decade (±SEM), respectively. Climate change over the past four decades has advanced the onset of flowering in *V. edulis* by 3.1 days/decade (linear regression, $P = 0.062$, $R^2 = 0.091$) (fig. S3), likely because of an advancing date of snowmelt, which is strongly associated with flowering phenology in this species (linear regression, $P < 0.0001$, $R^2 = 0.47$) (*12*). Regional climatic projections suggest that climate will continue to change (*13*).

Recent climate change has in turn significantly shifted *V. edulis* OSR in a manner consistent with the upslope shift in climate. Surveys of OSR from nine populations in both 1978 and 2011 showed that males have become more frequent across the species' elevation range at a rate of 1.28%/decade (paired *t* test, $t_9 = 2.29$, $P = 0.047$) (Fig. 1B). Comparing this temporal shift with the independent, parallel pattern of OSR variation over space shows that OSR isoclines are moving upslope at a rate of 175 m/decade (lower SE = 87 m/decade, upper SEM = 316 m/decade), mirroring the rates at which precipitation and soil moisture have changed. The parallel changes in OSR over elevation and time implicate climate as the driver of OSR variation but do not reveal the processes by which this occurs.

To explore the mechanisms underlying sex-specific responses to climate change, we quantified life history differences between the sexes in four populations spanning 1167 m of elevation (2470 to 3637 m) and varying 22% in OSR (48 to 26% male). We used sex- and size-structured rates of annual growth and mortality collected from 1978–1980 to calculate male and female life expectancy upon reaching reproductive maturity in each population. This metric integrates sex differences in demographic performance across the life span and reflects the average duration during which a plant contributes to OSR. Sex differences in reproductive life expectancy were concordant with population OSR, so that female-biased OSRs were associated with longer reproductive life spans than those of males (fig. S4) and suggesting that sex-specific effects of climate on life history drive population variation in OSR.

We sought to determine the proximate, physiological basis for the sex-specific effects of climate by focusing on water, a key resource. A plant's water use efficiency (WUE; carbon assimilation per unit of water transpiration) mediates its ability to acquire energy within the short, water-limited growing season (fig. S5). We hypothesized that sex differences in WUE—a trait known to differ between the sexes in many plant species, likely resulting from higher costs of reproduction in females (*14*)—underlie sex differences in plant performance and drive patterns in OSR. We measured the integrated WUE of each sex as indicated by leaf carbon isotope ratios collected from eight populations varying in OSR (*15*). Sex differences in WUE strongly predicted population OSR (Deming regression, $t_6 = 2.06$, $P = 0.043$) (Fig. 2); females had higher WUE than that of males in strongly female-biased populations (low OSR), but males had higher WUE than that of females in populations with a higher proportion of males (higher OSR). Although these findings do not directly link WUE to differential performance of the sexes, in other species this trait drives sex differences in performance that produce intrapopulation variation in OSR among arid and mesic microsites (*16*).

Variation in OSR may feed back to affect population growth by altering pollen availability and seedset rates (*7*, *17*). We measured the response of female seedset to an index of pollen availability

[1]Department of Ecology and Evolutionary Biology, University of California, Irvine, CA 92697-2525, USA. [2]Rocky Mountain Biological Laboratory, Crested Butte, CO 81224, USA. [3]Aarhus Institute of Advanced Studies, Aarhus University, Høegh-Guldbergs Gade 6B, DK-8000 Aarhus C, Denmark. [4]Department of Integrative Biology, Oklahoma State University, Stillwater, OK 74078, USA. [5]Department of Biology, University of Maryland, College Park, MD 20742, USA. [6]Department of BioSciences, Program in Ecology and Evolutionary Biology, Rice University, Houston, TX 77005, USA.
*Corresponding author. Email: william.petry@usys.ethz.ch
†Present address: Institute of Integrative Biology, ETH Zürich (Swiss Federal Institute of Technology), Universitätstrasse 16, Zürich, Switzerland.

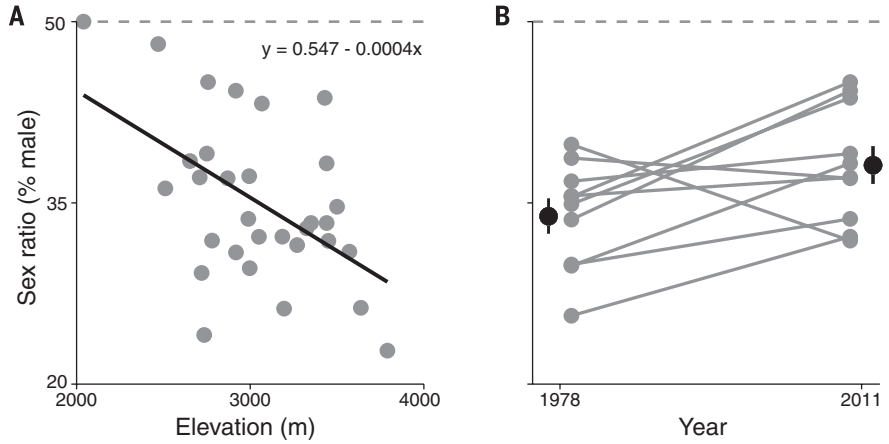

Fig. 1. OSR of *V. edulis* populations declines with climatic variation over elevation and increases in response to climate change. (**A**) OSR becomes significantly more female-biased with increasing elevation across the species elevation range in contemporary surveys (2011). (**B**) Males have significantly increased in frequency with climate change between 1978 and 2011 by an average of 5.5% (black points ± SEM) representing nine resurveyed populations (linked gray time points). A mean of 294 plants were surveyed in each population; populations with <100 flowering plants were censused completely.

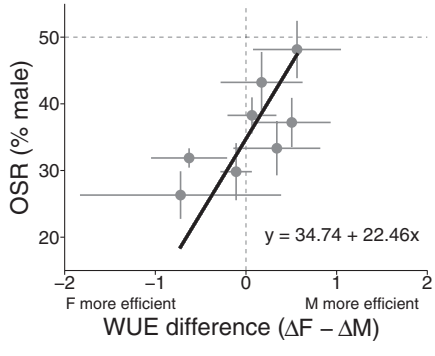

Fig. 2. Sex differences in WUE predict OSR. Each point represents a single population ($n = 8$ populations; 2470 to 3637 m). WUE is inferred from ^{13}C fractionation (Δ), and positive differences between the sexes (ΔF − ΔM) indicate that WUE of females is lower than that of males and vice versa. Data are means ± SEM.

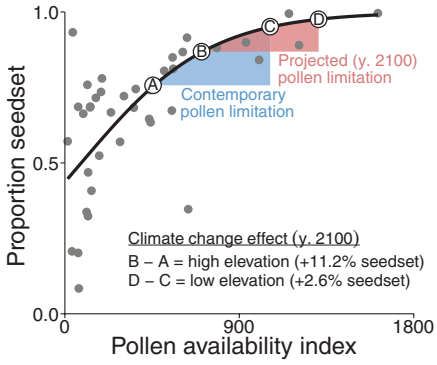

Fig. 3. Pollen availability limits female reproductive success. Each point represents one focal female controlling for competition with neighboring females for pollen. Estimated mean pollen availability for the range of contemporary OSRs observed across the *V. edulis* elevation range and expected OSRs in the year 2100 are indicated by the shaded regions where labeled points ("A" to "D") graphically show the expected change in pollen availability and seedset at the species' range margins. A linear model was fit to logit-transformed data; the back-transformed model fit is shown (*12*).

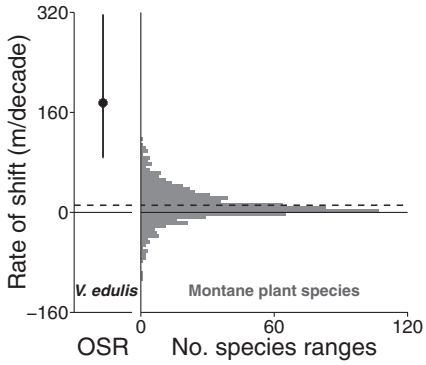

Fig. 4. Elevation range shifts of montane plant species are on average an order of magnitude slower than the rate of *V. edulis* OSR change. (**Left**) The black point ± SEM indicates the pace of OSR shift in *V. edulis*. (**Right**) A histogram shows the observed distribution of range shifts (677 observations encompassing 643 species reported in the literature), and the mean range shift (dashed black line) is indicated.

within the range of pollen movement (*12*). The majority (~90%) of pollen was received from males within 10 m of focal females (fig. S6). Female seedset in turn increased with pollen availability in this mating neighborhood (Fig. 3), rising from 39.3 to 99% of flowers producing seed across the observed range of neighborhood pollen availability. Simulating the effect of population OSR on seedset across the range of observed OSRs (Fig. 1A and supplementary materials, materials and methods), we found that the observed spatial variation in OSR was sufficient to alter female fitness. The low frequency of males at high elevation (22.8%) reduced median pollen availability by 55% compared with low-elevation populations with balanced OSR, corresponding to a reduction in seedset from 95 to 76% (Fig. 3). The demographic consequences of these effects are unclear because population growth rate in long-lived species is often relatively insensitive to changes in seed production (*18*). Nevertheless, *V. edulis* disperses only by seed, and climate effects on seedset may thus have important consequences for range shifts.

A mechanistic understanding of OSR dynamics in this system enables projections of the future state of *V. edulis* populations. Assuming the rate of increase in male frequency continues (1.28%/decade) (Fig. 1B), pollen limitation of reproduction at high-elevation populations could be halved by the year 2100 (a median seedset increase of 11.2%) (Fig. 3), facilitating the upslope range expansion of this species. In contrast, increasing male frequency at low elevation could have little effect on seedset (+2.6%) because females in those populations are pollen-saturated under contemporary, balanced OSRs (Fig. 3). Instead, increasingly male-biased OSRs at low elevation may threaten population viability by replacing females with males and thus reducing population-level seed production (*7*). Moreover, our previous work shows that female *V. edulis* support dramatically higher densities of arthropods than do males, including several specialist herbivores that depend exclusively on *V. edulis* (*19*, *20*). Accordingly, the effects of a climate-driven decline in female frequency may extend to higher levels of ecological organization.

Our data are distinctive in that they provide a pace of trait change (the upslope shift in plant sex distributions), whereas past studies of distribution responses to climate change have focused on species range shifts. Although trait changes are predicted to occur more rapidly than range shifts (*21*, *22*), the magnitude of such differences is hitherto unknown. Previously reported rates of species range shifts in montane plants show a mean upslope shift of 11.1 m/decade (*12*), which is dramatically slower than the 175 m/decade upslope pace of OSR change in *V. edulis* (Fig. 4). The pace of species range shifts frequently lags behind the pace of climate change (*12*), and such range disequilibria are frequently attributed to dispersal limitation (*23*). In contrast, shifts in traits within species ranges may track climate change more closely because they are based on differential performance of genetically based types that often already exist in many populations across the range. Here, we show that the pace of OSR change in *V. edulis* tracked climate change; it has kept pace with shifts in precipitation and soil moisture and has exceeded those of temperature and snowmelt (fig. S1).

We have demonstrated the occurrence of a potentially widespread form of biological response to climate change. We show that sex specificity of these responses can be exceptionally rapid, with broad effects across multiple scales of ecological organization. Within populations, sex-specific responses to climate change can skew sex ratios—through sex differences in physiology and performance or otherwise (*5*, *9*, *24*)—and the resulting sex ratio biases may, by mediating reproduction, affect population growth rate, the risk of population extinction, and the rate of adaptation to changing climate by altering the effective population size (*25*, *26*). In so doing, climate-driven changes in sex ratio may also control the tempo of species range shifts by mediating mate limitation at the leading or trailing range margins (*8*, *9*). Accordingly, a full understanding of biological responses to climate change requires a multiscale approach that integrates the underlying, but often cryptic, changes in intraspecific traits that give rise to higher-order patterns.

REFERENCES AND NOTES

1. M. A. Geber, T. E. Dawson, L. F. Delph, *Gender and Sexual Dimorphism in Flowering Plants* (Springer, 1999).
2. R. Lande, *Evolution* **34**, 292–305 (1980).
3. R. Shine, *Q. Rev. Biol.* **64**, 419–461 (1989).
4. J.-F. Le Galliard, P. S. Fitze, R. Ferrière, J. Clobert, *Proc. Natl. Acad. Sci. U.S.A.* **102**, 18231–18236 (2005).
5. J. M. Calabrese *et al.*, *J. Anim. Ecol.* **77**, 746–756 (2008).
6. A. O. Shelton, *Ecology* **89**, 3020–3029 (2008).
7. H. Caswell, D. E. Weeks, *Am. Nat.* **128**, 707–735 (1986).
8. T. E. X. Miller, B. D. Inouye, *Ecol. Lett.* **16**, 354–361 (2013).
9. T. E. X. Miller, A. K. Shaw, B. D. Inouye, M. G. Neubert, *Am. Nat.* **177**, 549–561 (2011).
10. O. Meurman, *Soc. Sci. Fennica. Commentationes Biologicae II* **2**, 1–104 (1925).
11. J. D. Soule, thesis, Michigan State University, East Lansing (1981).
12. Materials and methods are available as supplementary materials on *Science* Online.
13. E. P. Maurer, L. Brekke, T. Pruitt, P. B. Duffy, *Eos Trans. AGU* **88**, 504–504 (2007).
14. T. E. Dawson, M. A. Geber, in *Gender and Sexual Dimorphism in Flowering Plants*, M. A. Geber, T. E. Dawson, L. F. Delph, Eds. (Springer, 1999), pp. 175–216.
15. G. D. Farquhar, J. R. Ehleringer, K. T. Hubick, *Annu. Rev. Plant Physiol. Plant Mol. Biol.* **40**, 503–537 (1989).
16. K. R. Hultine, S. E. Bush, A. G. West, J. R. Ehleringer, *Oecologia* **154**, 85–93 (2007).
17. T. M. Knight *et al.*, *Annu. Rev. Ecol. Evol. Syst.* **36**, 467–497 (2005).
18. M. Franco, J. Silvertown, *Ecology* **85**, 531–538 (2004).
19. W. K. Petry *et al.*, *Ecology* **94**, 2055–2065 (2013).
20. K. A. Mooney, A. Fremgen, W. K. Petry, *Arthropod-Plant Interact.* **6**, 553–560 (2012).
21. J. Thompson *et al.*, *Proc. Natl. Acad. Sci. U.S.A.* **110**, 2893–2897 (2013).
22. J. R. Etterson, R. G. Shaw, *Science* **294**, 151–154 (2001).
23. J. P. Sexton, P. J. McIntyre, A. L. Angert, K. J. Rice, *Annu. Rev. Ecol. Evol. Syst.* **40**, 415–436 (2009).
24. Y. E. Morbey, R. C. Ydenberg, *Ecol. Lett.* **4**, 663–673 (2001).
25. B. Charlesworth, *Nat. Rev. Genet.* **10**, 195–205 (2009).
26. D. J. Rankin, H. Kokko, *Oikos* **116**, 335–348 (2007).

ACKNOWLEDGMENTS

We are grateful to the Rocky Mountain Biological Laboratory for facilitating this research over several decades. We are indebted to K. Perry and numerous field and laboratory assistants for data collection and processing; to b. barr, J. Thomson, and J. Harte for snowmelt data; to N. Morueta-Holme for species range data; to T. Huxman for assistance with stable isotope analyses; and to P. CaraDonna for his invaluable comments on a previous draft. Funding sources for this multidecade research are listed in the supplementary materials. Data for this study have been deposited in Dryad (DOI: 10.5061/dryad.1cf8p).

SUPPLEMENTARY MATERIALS

www.sciencemag.org/content/353/6294/69/suppl/DC1
Materials and Methods
Supplementary Text
Figs. S1 to S8
Tables S1 to S5
References (*27*–*60*)

14 January 2016; accepted 16 May 2016
10.1126/science.aaf2588

CARBON CYCLE

Mycorrhizal association as a primary control of the CO_2 fertilization effect

César Terrer,[1]* Sara Vicca,[2] Bruce A. Hungate,[3,4] Richard P. Phillips,[5] I. Colin Prentice[1,6]

Plants buffer increasing atmospheric carbon dioxide (CO_2) concentrations through enhanced growth, but the question whether nitrogen availability constrains the magnitude of this ecosystem service remains unresolved. Synthesizing experiments from around the world, we show that CO_2 fertilization is best explained by a simple interaction between nitrogen availability and mycorrhizal association. Plant species that associate with ectomycorrhizal fungi show a strong biomass increase (30 ± 3%, $P < 0.001$) in response to elevated CO_2 regardless of nitrogen availability, whereas low nitrogen availability limits CO_2 fertilization (0 ± 5%, $P = 0.946$) in plants that associate with arbuscular mycorrhizal fungi. The incorporation of mycorrhizae in global carbon cycle models is feasible, and crucial if we are to accurately project ecosystem responses and feedbacks to climate change.

Terrestrial ecosystems sequester annually about a quarter of anthropogenic carbon dioxide (CO_2) emissions (*1*), slowing climate change. Will this effect persist? Two contradictory hypotheses have been offered: The first is that CO_2 will continue to enhance plant growth, partially mitigating anthropogenic CO_2 emissions (*1*, *2*), whereas the second is that nitrogen (N) availability will limit the CO_2 fertilization effect (*3*, *4*), reducing future CO_2 uptake by the terrestrial biosphere (*5*–*7*). Plants experimentally exposed to elevated levels of CO_2 (eCO_2) show a range of responses in biomass—from large and persistent (*8*, *9*), to transient (*6*), to nonexistent (*10*)—leaving the question of CO_2 fertilization open. Differences might be driven by different levels of plant N availability across experiments (*11*), but N availability alone cannot explain contrasting results based on available evidence (*7*, *12*). For instance, among two of the most studied free-air CO_2 enrichment (FACE) experiments with trees, eCO_2 enhanced biomass production only during the first few years at Oak Ridge National Laboratory (ORNL)–FACE (*6*), whereas trees in the Duke University FACE experiment showed a sustained enhancement during the course of the experiment (*8*), despite N limitation. In addition to N limitation, other factors have been suggested as potential drivers of the response of plant biomass to eCO_2: age of the vegetation (*13*), water limitation (*14*), temperature (*15*), type of vegetation (*12*), or even the eCO_2 fumigation technology used (*11*). Although these factors may explain some observations, none has been found to be general, explaining the range of observations globally.

About 94% of plant species form associations with mycorrhizal fungi, an ancient mutualism thought to have facilitated the colonization of land by early plants (*16*). In this mutualism, the fungus transfers nutrients and water to the plant in exchange for carbohydrates, which are necessary for fungal growth. Mycorrhizal fungi are critical for terrestrial C cycling (*17*); are known to influence plant growth (*18*), nutrient cycling (*19*, *20*), and soil carbon storage (*21*); and respond strongly to elevated CO_2 (*22*, *23*). Yet, their impact on the N-dependence of the CO_2 fertilization effect has not been tested, despite the increasing evidence that N limitation constrains the CO_2 fertilization effect (*5*). Arbuscular mycorrhizae (AM) and ectomycorrhizae (ECM) are by far the most widespread types of mycorrhizae (*24*): AM-plants predominate in deserts, grasslands, shrublands, and tropical forest ecosystems, whereas ECM-fungi predominate in boreal and many temperate forests (for example, those dominated by *Pinus*). ECM can transfer N to the host plant under eCO_2 to sustain CO_2 fertilization (*25*), whereas the symbiotic effects of AM fungi in N-limited systems can range from beneficial to parasitic (*19*). Hence, the association of *Liquidambar styraciflua* with AM-fungi at ORNL-FACE, and *Pinus taeda* with ECM-fungi at Duke-FACE, might explain why only trees in the latter could increase N-uptake and take advantage of eCO_2 to grow faster for a sustained period (*20*, *25*). We tested the hypothesis that the differences in the nutrient economies of ECM and AM fungi influence global patterns of the magnitude of plant biomass responses to elevated CO_2.

We synthesized data (overview is provided in table S1) on total plant biomass (grams per square meter) from 83 eCO_2 experiments (fig. S1), separating responses into aboveground biomass ($n = 83$) (fig. S2) and belowground biomass ($n = 82$) (fig. S3) in a mixed-effects meta-analysis. As potential drivers of the plant biomass response, we considered the increase in atmospheric CO_2 concentration (ΔCO_2), mean annual precipitation (MAP), mean annual temperature (MAT), age of the vegetation at the start of the experiment, vegetation type (such as grassland or forest), CO_2 fumigation technology (such as FACE or growth chamber), length of the study (years), dominant mycorrhizal type (AM or ECM), and N-status [high or low N availability, considering soil characteristics and occasional fertilizer treatments, following the approach by Vicca *et al.* (*17*) and assigning all experiments with indications for some degree of N limitation to the "low N" class and experiments that were unlikely N limited to the "high N" class] (supplementary materials, materials and methods, and table S2).

Model selection analysis, based on corrected Akaike Information Criterion (AICc), showed that the most parsimonious model within two AICc units included N-status, mycorrhizal type, and ΔCO_2 ($P < 0.001$). The relative importance of the predictors (Fig. 1) supported the removal of climate variables, length of the experiment, age of the vegetation, fumigation technology, and system type. Some predictors reduced the CO_2 effect on biomass (such as age of the vegetation), whereas others were associated with an increased CO_2 effect (such as ECM, ΔCO_2, and high N availability) (fig. S4).

The response of total biomass to an increase of CO_2 from 400 to 650 μmol mol^{-1} was larger ($P < 0.001$) in ECM (30 ± 3%, $P < 0.001$) than in AM-dominated (7 ± 4%, $P = 0.089$) ecosystems (mean ± SE, mixed effects metaregression). The overall response of total biomass was 20 ± 3% ($P < 0.001$), which is similar to previous meta-analyses (*15*), with a larger effect under high (27 ± 4%, $P < 0.001$) than low N availability (15 ± 4%, $P < 0.001$), as expected (*5*, *7*, *11*). Furthermore, we found a strong interaction between mycorrhizal type and N-status ($P < 0.001$); under low N availability, eCO_2 had no effect on total biomass of AM-dominated species (0 ± 5%, $P = 0.946$) but increased biomass by 28 ± 5% in ECM-dominated species ($P < 0.001$) (Fig. 2A). Under

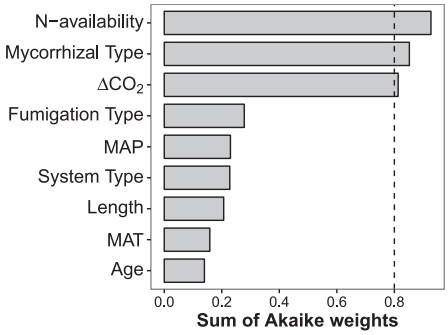

Fig. 1. Model-averaged importance of the predictors of the CO_2 fertilization effect on total biomass. The importance is based on the sum of Akaike weights derived from model selection using AICc (Akaike's Information Criteria corrected for small samples). Cutoff is set at 0.8 (dashed line) in order to differentiate among the most important predictors.

[1]AXA Chair Programme in Biosphere and Climate Impacts, Department of Life Sciences, Silwood Park Campus, Ascot, Imperial College London, UK. [2]Centre of Excellence PLECO (Plant and Vegetation Ecology), Department of Biology, University of Antwerp, 2610 Wilrijk, Belgium. [3]Center for Ecosystem Science and Society, Northern Arizona University, Flagstaff, AZ 86011, USA. [4]Department of Biological Sciences, Northern Arizona University, Flagstaff, AZ 86011, USA. [5]Department of Biology, Indiana University, Bloomington, IN 47405, USA. [6]Department of Biological Sciences, Macquarie University, North Ryde, New South Wales 2109, Australia.
*Corresponding author. Email: c.terrer@imperial.ac.uk

high N availability, the CO_2 effect on total biomass in both AM- and ECM-dominated species was significant: 20 ± 6% (P = 0.002) for AM and 33 ± 4% (P < 0.001) for ECM (Fig. 2A), with no significant differences between the two groups (P = 0.139). Hence, high N availability significantly increased the CO_2 effect in AM [post-hoc, Tukey's honestly significant difference (HSD): adj-P = 0.038] but not in ECM-associated species (adj-P = 0.999).

The patterns observed for total biomass were reflected in both aboveground and belowground biomass. Under low N availability, eCO_2 stimulated aboveground biomass significantly in ECM plants (P < 0.001), with no effect in AM plants (P = 0.584) (Fig. 2B). Similarly, eCO_2 enhanced belowground biomass in ECM plants at low N (P = 0.003) but not in AM plants (P = 0.907) (Fig. 2C).

We conducted a sensitivity analysis to ensure that the findings were robust. First, we added an intermediate level of N availability (table S2) by assigning some ecosystems that were initially classified as "low" to a "medium" class (for example, Duke, Aspen, and ORNL) (fig. S5). This enabled testing whether the large CO_2 stimulation in ECM plants was driven by experiments with intermediate N availability. Second, we weighted individual experiments by the inverse of the mixed-model variance (fig. S6) so as to ensure that the weights of the meta-analysis did not affect the outcome. Third, we ran a separate meta-analysis with the subset of experiments with trees only (fig. S7). Previous meta-analyses have reported that trees are more responsive to eCO_2 than are grasslands (*12*); as such, our findings could reflect differences of plant growth form rather than mycorrhizal association per se. Because trees are the only type of vegetation that can associate with ECM and AM (or both), an analysis of tree responses to eCO_2 can thus be used to isolate the influence of mycorrhizal type from that of vegetation growth form. These three sensitivity analyses confirmed that the CO_2 stimulation of total and aboveground plant biomass was significant and large in ECM plants regardless of N availability, whereas the effect was not significant in AM plants under low N availability. The trend was consistent for belowground biomass in ECM plants, although with high variance and low sample size, the effect was not significant (P = 0.244) under low N when the "medium" class was included.

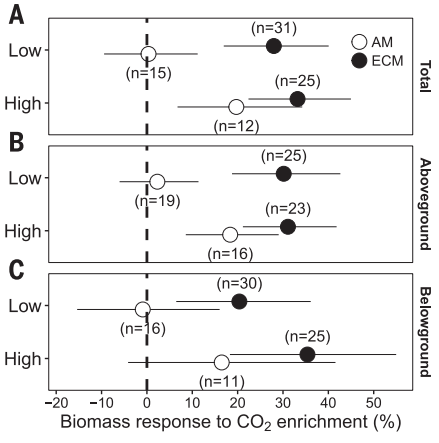

Fig. 2. Overall effects of CO_2 on plant biomass. (**A** to **C**) Effects on (A) total, (B) aboveground, and (C) belowground biomass for two types of mycorrhizal plants species (AM and ECM) in N-limited experiments (low N) or experiments that are unlikely N-limited (high N). Overall means and 95% confidence intervals are given; we interpret CO_2 effects when the zero line is not crossed.

Plant N uptake can be enhanced through mycorrhizal associations or through associations with N-fixing microbes. Some of the CO_2 experiments in our study contained N-fixing species, which might have increased N availability (table S3). eCO_2 stimulated aboveground biomass in AM species under low N by 8 ± 3% (P = 0.019) in this subgroup of experiments that included N-fixing species, whereas the remaining AM experiments under low N availability showed no biomass response to eCO_2 (1 ± 10%, P = 0.893). But even with the additional N input from N_2 fixation, the 8% biomass increase in AM plants under low N was considerably smaller than the 28 ± 5% increase found for ECM plants.

Most CO_2 experiments have been carried out in the Northern Hemisphere (fig. S8), where N, rather than phosphorus (P), is limiting. AM fungi transfer large quantities of P to the plant and hence are more likely mutualistic in P-limited ecosystems (*19*). Tropical forests are typically associated with P limitations and dominated by AM-fungi and could potentially show enhanced biomass under eCO_2. The role of nutrients on the CO_2 fertilization effect in these P-limited forests has yet to be explored (*26*).

Responses of plants to rising CO_2 are thus well explained by a simple interaction between N and microbial mutualists: When N availability is limited, only plant species that associate with ECM-fungi show an overall biomass increase due to eCO_2. Several mechanisms could explain these responses. First, ECM-associated plants typically allocate more C to support mycorrhizae than do AM plants, particularly under eCO_2 (*23*). Moreover, because ECM fungi, unlike AM fungi, produce extracellular enzymes that degrade organic N compounds (*27*), increased allocation to ECM fungi under eCO_2 may supply host plants with the N needed to sustain their growth response to eCO_2. This may explain why eCO_2 often stimulates priming effects in ECM-dominated ecosystems (*28*, *29*). Second, differences in litter quality between ECM and AM plants may influence how much N is available to be primed or decomposed. Several studies have reported that AM plants produce litters that decompose faster than those of ECM plants (*20*, *30*). Given emerging evidence that fast decomposing litters promote the formation of stable mineral-associated organic matter (*31*, *32*), much of the organic N in AM-dominated ecosystems may be inaccessible to AM plants or their associated mycorrhizae (*20*). And whereas slow-degrading ECM litters may reduce N availability in the short term, most of the N exists in particulate forms, which should be accessible to most microbes (including ECM fungi). Therefore, AM fungi are equipped with less specialized enzymes for N acquisition than are ECM and occur in soils in which N is more tightly protected. Both factors would presumably limit the enhancement of AM plant growth in response to eCO_2.

Mycorrhizal symbioses are not accounted for in most global vegetation models (*24*). Thus, the projected CO_2 fertilization effect by "carbon-only models" (*1*) is likely overestimated for AM-dominated ecosystems, which cover ~65% of the global vegetated area (*24*), albeit only when N-limited. On the other hand, global models that consider N limitation to constrain the CO_2 fertilization effect (*4*) likely underestimate responses of ECM plants to eCO_2, an area that encompasses ~35% of the vegetated area of the earth (*24*), most of which is considered N-limited by these models. Our framework reconciles the apparent discrepancy between widespread N limitation (*3*), which is assumed to limit C sequestration on land (*4*), and the observed increase over time of the terrestrial C sink (*1*, *2*), which is thought to be driven primarily by CO_2 fertilization (*33*). These results may also partly explain past findings that forests (commonly ECM) show stronger responses to eCO_2 as compared with grasslands (AM) (*12*). We propose that the CO_2 fertilization effect be quantified on the basis of mycorrhizal type and soil nitrogen status, and that large-scale ecosystem models incorporate mycorrhizal types to account for the differences in biomass enhancement by eCO_2. Mycorrhizae are ubiquitous and sort predictably with plant functional type (*24*, *34*), making feasible their inclusion in models to capture this microbial influence on global biogeochemistry. Accounting for the influence of mycorrhizae will improve representation of the CO_2 fertilization effect in vegetation models, which is critical for projecting ecosystem responses and feedbacks to climate change.

REFERENCES AND NOTES

1. P. Ciais *et al.*, in *Climate Change 2013: The Physical Science Basis. Contribution of Working Group I to the Fifth Assessment Report of the Intergovernmental Panel on Climate Change*, T. F. Stocker *et al.*, Eds. (Cambridge Univ. Press, 2013), pp. 465–570.
2. C. Le Quéré *et al.*, *Earth Syst. Sci. Data* **7**, 349–396 (2015).
3. B. A. Hungate, J. S. Dukes, M. R. Shaw, Y. Luo, C. B. Field, *Science* **302**, 1512–1513 (2003).
4. W. R. Wieder, C. C. Cleveland, W. K. Smith, K. Todd-Brown, *Nat. Geosci.* **8**, 441–444 (2015).
5. P. B. Reich, S. E. Hobbie, *Nat. Clim. Change* **3**, 278–282 (2013).
6. R. J. Norby, J. M. Warren, C. M. Iversen, B. E. Medlyn, R. E. McMurtrie, *Proc. Natl. Acad. Sci. U.S.A.* **107**, 19368–19373 (2010).
7. P. B. Reich, B. A. Hungate, Y. Luo, *Annu. Rev. Ecol. Evol. Syst.* **37**, 611–636 (2006).
8. H. R. McCarthy *et al.*, *New Phytol.* **185**, 514–528 (2010).
9. A. F. Talhelm *et al.*, *Glob. Change Biol.* **20**, 2492–2504 (2014).
10. B. A. Newingham *et al.*, *Glob. Change Biol.* **19**, 2168–2181 (2013).
11. M.-A. de Graaff, K. J. van Groenigen, J. Six, B. Hungate, C. van Kessel, *Glob. Change Biol.* **12**, 2077–2091 (2006).
12. E. A. Ainsworth, S. P. Long, *New Phytol.* **165**, 351–372 (2005).
13. C. Körner *et al.*, *Science* **309**, 1360–1362 (2005).
14. M. J. Hovenden, P. C. D. Newton, K. E. Wills, *Nature* **511**, 583–586 (2014).
15. S. Baig, B. E. Medlyn, L. M. Mercado, S. Zaehle, *Glob. Change Biol.* **21**, 4303–4319 (2015).

16. M. C. Brundrett, *New Phytol.* **154**, 275–304 (2002).
17. S. Vicca *et al.*, *Ecol. Lett.* **15**, 520–526 (2012).
18. M. G. A. van der Heijden *et al.*, *Nature* **396**, 69–72 (1998).
19. N. C. Johnson, G. W. T. Wilson, J. A. Wilson, R. M. Miller, M. A. Bowker, *New Phytol.* **205**, 1473–1484 (2015).
20. R. P. Phillips, E. Brzostek, M. G. Midgley, *New Phytol.* **199**, 41–51 (2013).
21. C. Averill, B. L. Turner, A. C. Finzi, *Nature* **505**, 543–545 (2014).
22. K. K. Treseder, *New Phytol.* **164**, 347–355 (2004).
23. O. Alberton, T. W. Kuyper, A. Gorissen, *New Phytol.* **167**, 859–868 (2005).
24. M. Shi, J. B. Fisher, E. R. Brzostek, R. P. Phillips, *Glob. Change Biol.* **22**, 1299–1314 (2016).
25. J. E. Drake *et al.*, *Ecol. Lett.* **14**, 349–357 (2011).
26. R. J. Norby *et al.*, *New Phytol.* **209**, 17–28 (2016).
27. J. Perez-Moreno, D. J. Read, *New Phytol.* **145**, 301–309 (2000).
28. R. P. Phillips, A. C. Finzi, E. S. Bernhardt, *Ecol. Lett.* **14**, 187–194 (2011).
29. B. A. Hungate *et al.*, *New Phytol.* **200**, 767–777 (2013).
30. J. Cornelissen, R. Aerts, B. Cerabolini, M. Werger, M. van der Heijden, *Oecologia* **129**, 611–619 (2001).
31. M. F. Cotrufo *et al.*, *Nat. Geosci.* **8**, 776–779 (2015).
32. B. N. Sulman, R. P. Phillips, A. C. Oishi, E. Shevliakova, S. W. Pacala, *Nat. Clim. Change* **4**, 1099–1102 (2014).
33. Z. Zhu *et al.*, *Nat. Clim. Change* 10.1038/nclimate3004 (2016).
34. V. B. Chaudhary *et al.*, *Sci. Data* **3**, 160028 (2016).

ACKNOWLEDGMENTS

We thank A. Talhelm, A. Finzi, L. Andresen, I. Kappel, C. Calfapietra, B. Sigurdsson, J. Dukes, P. Newton, D. Blumenthal, B. Kimball, J. Heath, P. Reich, R. Norby, C. Körner, N. Chiariello, C. Field, and M. Schneider, who provided additional data and advice. This research is a contribution to the Imperial College initiative Grand Challenges in Ecosystems and the Environment and the AXA Chair Programme in Biosphere and Climate Impacts. C.T. is supported by an Imperial College Ph.D. studentship within this program. C.T. and S.V. acknowledge support of ClimMani COST Action (ES1308). S.V. is a postdoctoral fellow of the Research Foundation–Flanders (FWO) and acknowledges support from the European Research Council grant ERC-SyG-610028 IMBALANCE-P. B.A.H. was supported by the Biological and Environmental Research program, Office of Science, U.S. Department of Energy (DOE) grant DE SC0008270. R.P. acknowledges support from NSF (Ecosystem Studies Program 1153401) and DOE (Environmental System Science Program). R.P. and C.T. thank the Royal Netherlands Academy of Arts and Sciences, DOE, INTERFACE, and the New Phytologist trust for funding the Workshop "Climate models revisited: the biogeochemical consequences of mycorrhizal dynamics." The data reported in this paper are available online as supplementary materials. C.T. conceived the initial idea, collected the data, and conducted the data synthesis and meta-analysis. S.V. developed the nitrogen classification. B.A.H. refined model selection, meta-analysis, and framework. All authors contributed to the development of the conceptual framework and to the writing of the manuscript.

SUPPLEMENTARY MATERIALS

www.sciencemag.org/content/353/6294/72/suppl/DC1
Materials and Methods
Figs. S1 to S8
Tables S1 to S4
References (*35*–*139*)

11 February 2016; accepted 6 June 2016
10.1126/science.aaf4610

BIRD FLIGHT

Frigate birds track atmospheric conditions over months-long transoceanic flights

Henri Weimerskirch,[1,2]* Charles Bishop,[3] Tiphaine Jeanniard-du-Dot,[4] Aurélien Prudor,[1,2] Gottfried Sachs[5]

Understanding how animals respond to atmospheric conditions across space is critical for understanding the evolution of flight strategies and long-distance migrations. We studied the three-dimensional movements and energetics of great frigate birds (*Fregata minor*) and showed that they can stay aloft for months during transoceanic flights. To do this, birds track the edge of the doldrums to take advantage of favorable winds and strong convection. Locally, they use a roller-coaster flight, relying on thermals and wind to soar within a 50- to 600-meter altitude band under cumulus clouds and then glide over kilometers at low energy costs. To deal with the local scarcity of clouds and gain longer gliding distances, birds regularly soar inside cumulus clouds to use their strong updraft, and they can reach altitudes of 4000 meters, where freezing conditions occur.

The movement of animals is driven by processes that act across multiple spatial and temporal scales. Long-distance movements such as the migrations of birds have evolved in response to large-scale environmental gradients (*1*). In particular, atmospheric conditions play a large role in determining the efficiency of migratory routes, whose consistency over years has allowed evolutionary processes to act at population levels (*2*). At smaller time and spatial scales, long-range movements have to constantly be adjusted to local conditions, in particular to minimize energy expenditure (*3*, *4*). These long movements or migrations can be done over inhospitable areas as different as deserts, high mountains, or oceans, which come with specific environmental constraints to which birds need to behaviorally and physiologically adapt their flight strategies (*5*, *6*). How these long restless flights can be energetically achieved has attracted much interest, but remains largely unknown because of the inherent difficulties of studying such behaviors in situ.

Biologists have long been attracted to locomotor extremes because they provide clear examples from which information about structure-function relationships can be drawn (*7*). Among birds, frigate birds are extreme in many aspects of their life history, including having the lowest wing loading, with a specialized capacity for soaring flight (*8*). They are also unusual seabirds because their feathers are not waterproof and their legs are small, so they are unable to land on the sea surface even though they feed exclusively at sea. They deal with these conflicting constraints by staying aloft for days when they are foraging from their nest when breeding (*9*). Probably as a consequence of these extreme attributes, frigate birds have the longest period of parental care in birds, suggesting a long period of learning to acquire flight and foraging abilities in early life (*10*). Their ability to remain airborne continuously for days is probably possible because of the capability of frigate birds to use thermals over the sea as a main energy source for soaring (*11*, *12*).

We asked how frigate birds can perform long migrations over oceans without landing and whether oceanic thermals are reliable enough in space and time to allow birds to stay airborne over long periods. To address these questions, we investigated the movement of frigate birds at several spatial scales with regard to (i) how frigate birds make use of large-scale weather systems to perform long-range movements, and (ii) how flight dynamics and energetics at a finer scale contribute to these long ranges.

We studied the three-dimensional movements and energetics of frigate birds on Europa Island (Fig. 1) between 2011 and 2015 (*13*). To study large-scale migratory movements, 24 adults and 25 juvenile birds were equipped with solar-powered Argos transmitters (*13*). To study the relationship between heart rate, activity (flapping frequency), and behavior (ascent rates and horizontal speed), 11 adult females were equipped with external custom-designed loggers measuring triaxial acceleration and electrocardiography and a Global Positioning System (GPS) device (*13*). To study movements, activity, and ambient temperature, 37 adult females and males were equipped with solar-powered GPS accelerometers, whose data were recovered regularly by an automatic recording station (*13*).

During the southwest Indian monsoon from June to October, strong trade winds occur in the southern Indian Ocean and cross the equator to form southwest winds in the northern Indian Ocean (*14*) (Fig. 1). During this season, adult frigate birds finishing the breeding season left Europa and migrated northward to take advantage of the southerly winds. They settled on roosting sites in

[1]Centre d'Etudes Biologiques de Chizé, CNRS, 79360 Villiers en Bois, France. [2]UMR 9220 ENTROPIE, Université de la Réunion, Saint Denis, La Réunion. [3]School of Biological Sciences, Bangor University, Bangor, Gwynedd, UK. [4]Department of Zoology, University of British Columbia, Vancouver, Canada. [5]Institute of Flight System Dynamics, Technische Universität München, Garching, Germany.
***Corresponding author. Email: henriw@cebc.cnrs.fr**

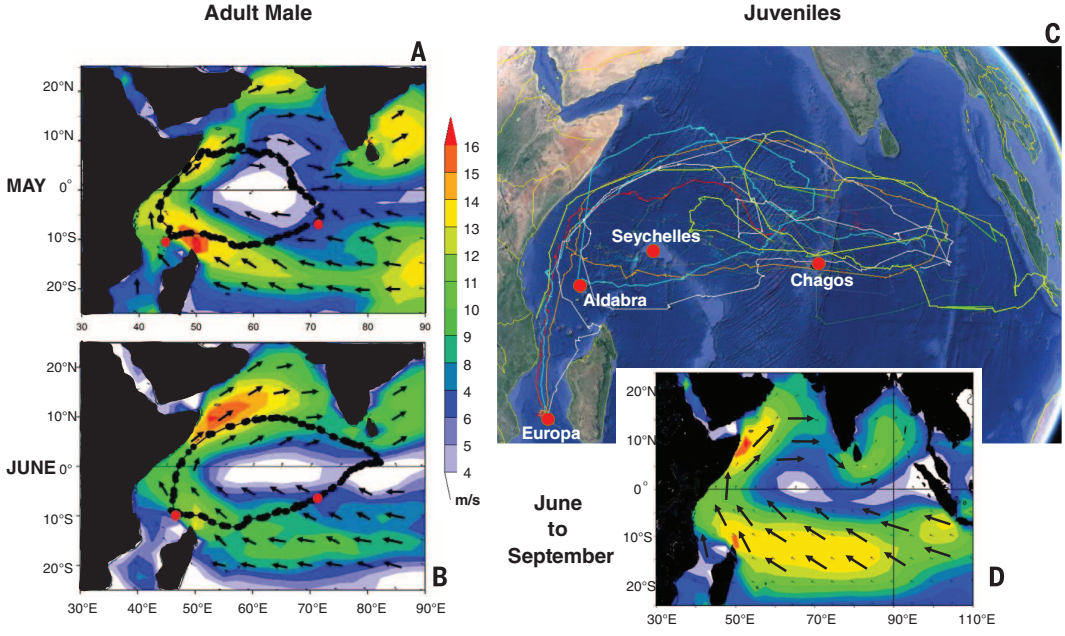

Fig. 1. Movements of adult and juvenile frigate birds in relation to wind conditions in the Indian Ocean. (Left) Two successive clockwise movements from Aldabra Island (Seychelles) of an adult male great frigate bird (no. 138502) in relation to wind strength (in meters per second, color scale) and direction (arrows). (**A**) In May 2015, a 24-day foraging trip around the doldrums (shown by the absence of wind, in white), with 1 day of rest in Chagos. (**B**) In June 2015, a 28-day foraging trip, with a 36-hour rest in Chagos. (**C**) Movements between June and September 2015 of six young frigate birds fledged from Europa Island, moving around the doldrums zone. (**D**) Climatology of wind speed and direction (average values over 4 months) in June to September 2015, showing the average position of the doldrums (white) on the equator.

the Seychelles from where they foraged for months. Some adults performed long looping movements around the equator, where a belt of converging air and wind occurs, with no wind in the center, named the doldrums zone by ancient mariners (Fig. 1). On successive loops, adults closely followed the edges of the doldrums, which oscillate longitudinally (Fig. 1, A and B). Birds stayed continuously on the wing for periods lasting up to 48 days and traveled on average 420 ± 220 km daily.

Young frigate birds left their birthplace at the same time as adults, but independently of their parents. They crossed the equator and turned eastward to enter into a circular transoceanic movement into the wind belt around the doldrums (Fig. 1, C and D). During these dispersive movements, juvenile birds stayed continuously aloft for flights lasting up to 2.1 months (average maximum time spent aloft, 41.2 ± 15.1 days, n = 8 birds). They travelled on average 450 ± 220 km daily. They episodically stopped on isolated islands such as Chagos, islets off Indonesia, or on islets of the Seychelles archipelago for very short rests (8 to 48 hours) before continuing their large-scale wandering movement tracking the edge of the doldrums (Fig. 1C and fig. S1). They flew at altitudes ranging between the sea surface and 3000 m, but mainly between 0 and 600 m (fig. S2).

To understand how frigate birds are able to stay aloft for such long periods, we studied their flight dynamics and energetics during 2- to 15-day foraging trips from Europa. Breeding frigate birds travelled on average 410 ± 142 km per day (n = 18 birds), mainly during the daytime, traveling over shorter distances at night (Fig. 2). Two clear behavioral modes were identified during movements at sea. Traveling occurred with high ground speeds and low wing beat frequencies (82 ± 9% of travelling time with no or rare wing beats), with birds remaining at altitudes ranging from 30 to 2000 m, reaching up to 4120 m. Foraging can only occur when birds descend close to the sea surface (altitudes 0 to 30 m), and during these periods they are very active, flapping during 75 ± 18% of the foraging phase (Fig. 2). Active foraging occurred only episodically (10 ± 7% of time at sea), indicating rare feeding opportunities, mainly during the day (86.4% of bouts of active foraging occurred during the daytime).

When in flight at sea, heart rate was on average 203 ± 84 beats min^{-1} but varied extensively (Fig. 2 and figs. S3 and S4), occasionally attaining values as low as when resting on the nest (71 ± 25 beats min^{-1}, range 57 to 215). Heart rate and dynamic body acceleration were generally well correlated (*13*) (figs. S3 and S4); therefore, we used dynamic body acceleration, measured on all individuals, as the main proxy for energy expenditure. Whereas active foraging is very costly for frigate birds, requiring high dynamic body acceleration and heart rates, traveling periods have a remarkably low energy expenditure, with few wingbeats (Fig. 2 and fig. S3), suggesting that overall field metabolic rate during months at sea is likely to be exceptionally low (*13*) (figs. S5 and S6). Excluding periods of active foraging close to the surface, dynamic body acceleration was the lowest at altitudes between 300 and 600 m (fig. S7), indicating an optimal altitude for traveling at low cost.

Traveling at low cost is achieved by successive climbs, mainly through soaring with no or few wing flaps and low heart rate, and descents, by gliding (Figs. 2 and 3). A close examination of flight paths shows that when soaring, birds move with the wind (fig. S8), using circling movements to soar (Fig. 3C) in thermals below cumulus clouds where rising air creates updrafts (*15*). Because of the strong trade winds, they drift with the wind while climbing (Fig. 3), resulting in "wind-drift circling soaring." Conversely, when gliding, they preferentially fly with side winds and achieve the highest ground speeds (Figs. 2 and 3 and fig. S8). The resulting movement is a complex zig-zagging, roller-coaster movement, with an average altitude xgain of 59.1 ± 43.8 m per kilometer covered (ground distance); i.e., 15.4 ± 3.0 km climbed daily. These vertical movements take place generally up to 600 to 700 m, corresponding to the base of the cumulus clouds that is relatively constant throughout the trade wind zone (*16*).

However, birds regularly climbed up to 1000 to 2000 m, with a maximum of 4120 m (fig. S9). The frequency of climbs at altitudes higher than 700 m increased throughout the day to peak during the first hours of night (fig. S10). Climbing to high altitudes can be separated into a phase of slow climb up to the base of the cumulus clouds at 600 to 700 m, followed by a more rapid climb to 1600 m (Fig. 2D) or higher. This second phase of the ascent is performed without flapping the wings (Fig. 2D); i.e., in pure soaring flight and with climb rates reaching 4 to 5 m s^{-1} at 2000 to 3000 m (fig. S11). Ascent to high altitude can only take place inside cumulus clouds, where updrafts reach 5 m s^{-1} and

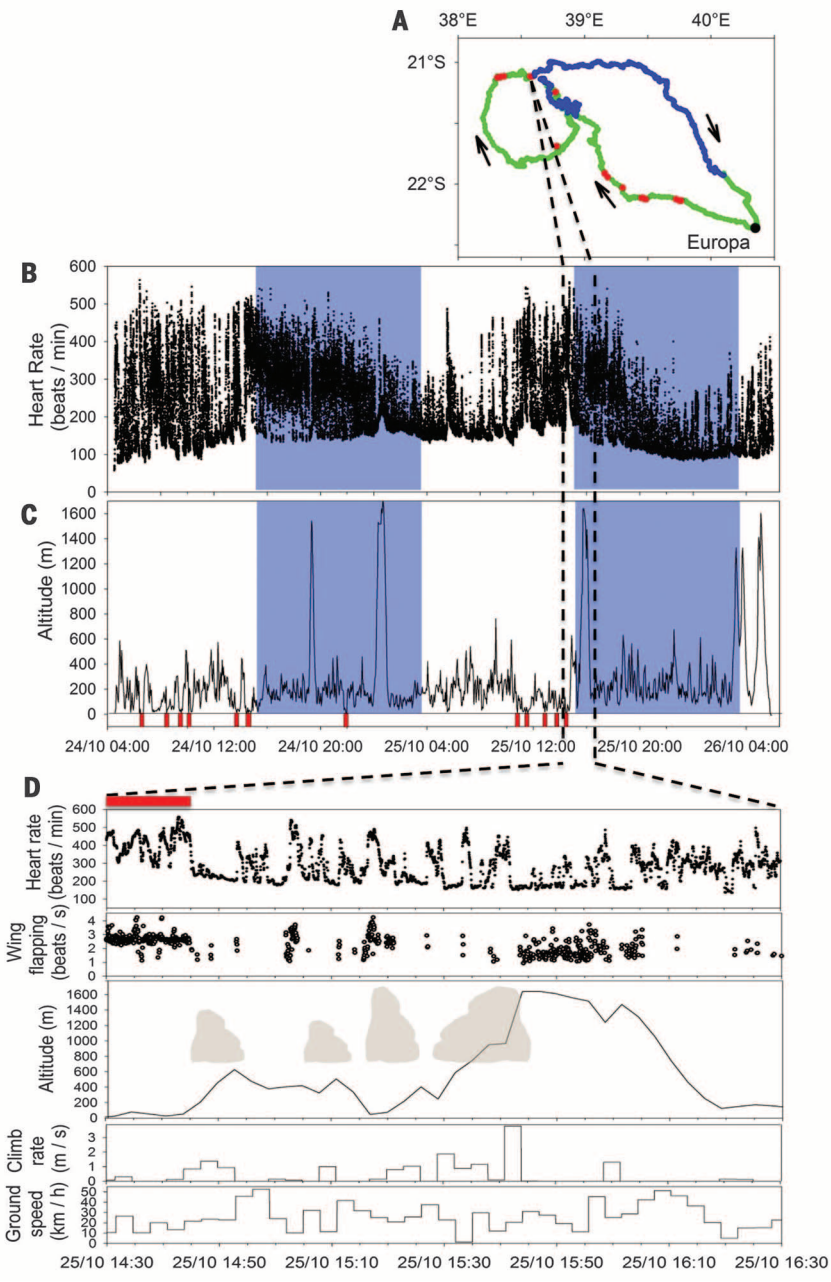

Fig. 2. Movement, changes in altitude, heart rate, and flight parameters during a 2-day trip at sea. (**A**) 1130-km-long movement from Europa during the daytime (green) and night (blue) with foraging bouts in red, with recorded (**B**) heart rate and (**C**) altitude. Shaded blue areas represent nighttime, and red blocks represent foraging bouts. (**D**) A 2-hour period during the trip at sea, with an active foraging phase followed by a traveling phase, showing the changes in altitude and corresponding heart rate, wing-flapping rate, climb rate, and ground speed. On the altitude panel, the predicted presence of cumulus clouds is indicated (gray).

are strong enough to provide such climb rates (*15*). During the gliding phase made outside the clouds, the minimum sink rate was 23.6 ± 19.1 m of ground distance covered per meter lost between 500- to 700-m altitudes, compared to 14.3 ± 11.7 m at higher altitudes ($F_{1,7}$ = 8.4, P = 0.045).

Our study shows that frigate birds can remain almost indefinitely on the wing by tracking, at a basin-wide scale, the wind belt around the doldrums, an atmospheric feature whose location is predictable. Locally, they display a specific flight strategy based on an energy-efficient use of convection and wind. By using wind-drift circling soaring and long periods of gliding, frigate birds are able to simultaneously use convection and wind as energy sources and move over extensive distances at low energy costs. They favor altitudes between 50 and 600 m, where atmospheric conditions are optimal for low-cost flight; i.e., steady winds and updrafts from convection under clouds (Fig. 4). These altitudes are also convenient to spot feeding opportunities from long distances away during the daytime; birds then descend close to the surface to forage actively when feeding opportunities have been detected (*9*).

Although birds are not thought to carry out intentional, sustained cloud climbs (*17*, *18*), our study shows the ability of frigate birds to frequently ascend to very high altitudes inside clouds. At an altitude of 4000 m, air temperatures are negative and air density and oxygen availability are almost half of those at sea level (*17*), suggesting that this tropical bird encounters extreme conditions at such altitudes. Cumulus clouds and cloud fields are considered to be randomly distributed in space in the trade wind zone (*16*). In these conditions, climbing higher than 1000 m presents a fundamental advantage by allowing frigate birds to cover much longer distances by gliding to reach the next updraft under clouds; for example, >60 km of glide from 4000 m as compared to 17 km when starting a glide just at the base of cumulus clouds. Therefore, when clouds are sparsely distributed, birds can adjust their gliding distance by climbing higher to avoid the risk of switching to costly flapping flight. Juvenile individuals are able to master the flight strategy of adults as soon as they become independent. When they leave their birthplace, they all head north to reach the equator and circle the entire Indian Ocean. This stereotyped movement suggests a genetically encoded behavior that brings young individuals directly to a predictable, favorable, and large-scale atmospheric feature located thousands of kilometers from their birthplace.

Great frigate birds are the only birds other than swifts (*19*) to be able to stay aloft for months. Long periods in continuous flight are interrupted by very short periods of rest on land, suggesting that frigate birds might sleep while airborne (*20*). Periods of low activity (no flapping) occur mainly during soaring episodes and may allow sleep. However, periods of completely motionless (no flapping at all) flight, potentially corresponding to periods of sleep, are relatively short, (~2 min, never exceeding 12 min). Animals such as frigate birds may have evolved the ability to dispense with sleep when ecological demands favor wakefulness such as during extended flights (*21*), but studies are needed to determine how they sleep during much longer-lasting flights

Frigate birds clearly encounter several atmospheric challenges during their movements at sea, such as low temperatures, low air density and oxygen levels during high climbs, and the unpredictable distribution of cumulus clouds at small scale, together with the presence of powerful cyclones in their optimal range. This dependence on atmospheric systems could make them particularly sensitive to future climate changes, along with some other seabirds (*22*). Climate models for the tropical ocean forecast an increase in the intensity of tropical storms and of convections around the equator, where the doldrums and strong convections occur (*23*). More variable atmospheric

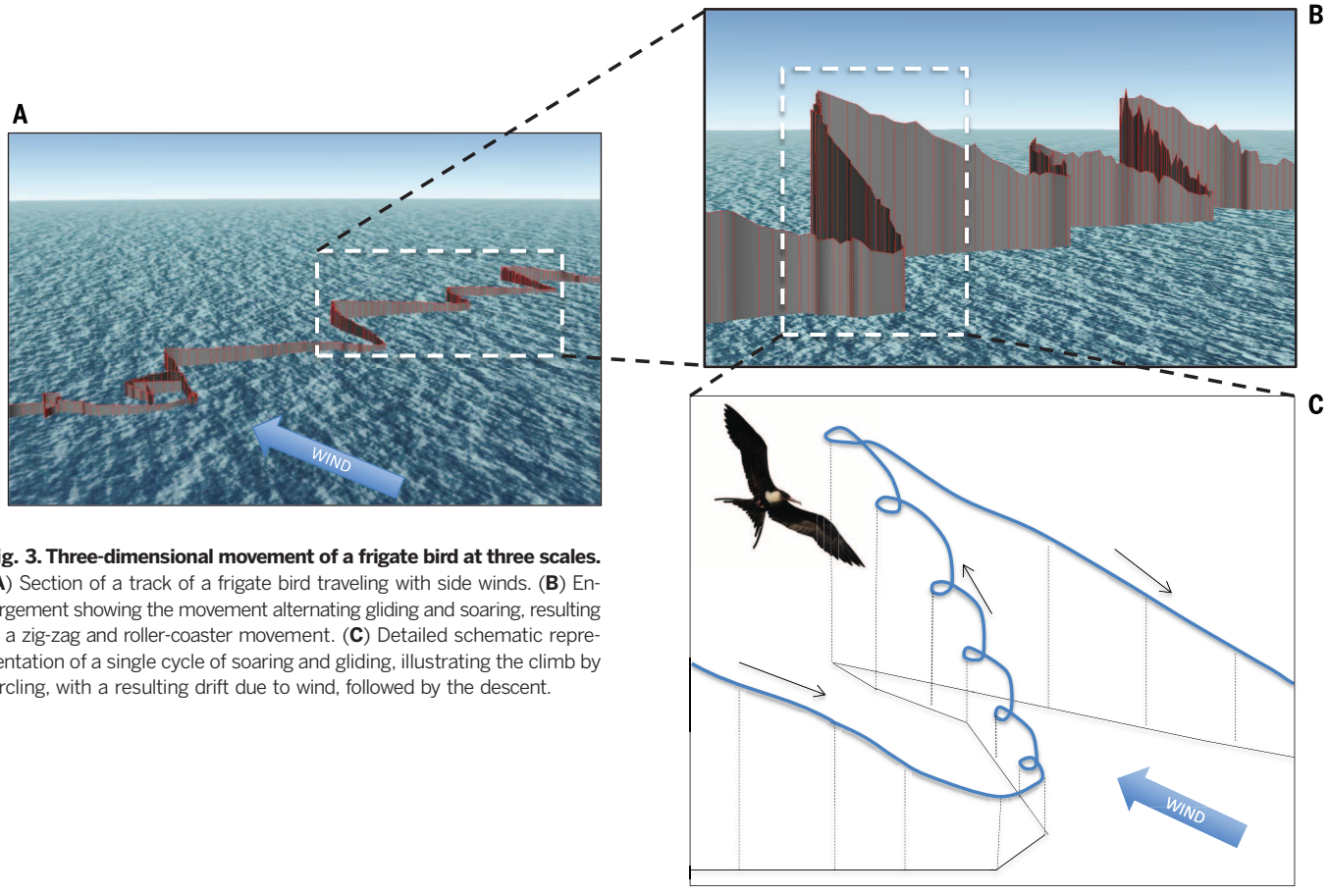

Fig. 3. Three-dimensional movement of a frigate bird at three scales. (**A**) Section of a track of a frigate bird traveling with side winds. (**B**) Enlargement showing the movement alternating gliding and soaring, resulting in a zig-zag and roller-coaster movement. (**C**) Detailed schematic representation of a single cycle of soaring and gliding, illustrating the climb by circling, with a resulting drift due to wind, followed by the descent.

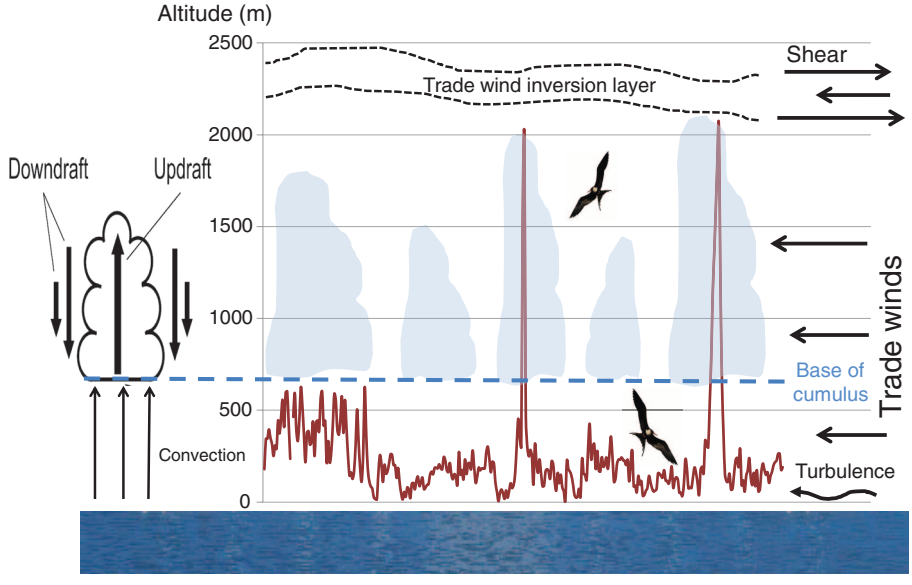

Fig. 4. Altitudinal movement of a frigate bird in relation to potential atmospheric conditions. The traveling flight is performed between 30 and 600 to 700 m altitude in a band with regular winds, avoiding the turbulence close to the surface. The bird occasionally climbs to 2000 m within cumulus clouds that form by convection, whose base is at 600 to 700 m and whose vertical extension is limited by the inversion layer where strong shear occurs. A schematic presentation of the updrafts and downdrafts characteristic of cumulus clouds is shown at left (*24*).

conditions in the future may become too challenging for a species that already seems to encounter extreme conditions during its lifetime movements.

REFERENCES AND NOTES

1. G.-R. Walther *et al.*, *Nature* **416**, 389–395 (2002).
2. B. Kranstauber, R. Weinzierl, M. Wikelski, K. Safi, *Ecol. Lett.* **18**, 1338–1345 (2015).
3. T. Alerstam, Ã. Lindström, in *Bird Migration: Physiology and Ecophysiology*, E. Gwinner, Ed. (Springer, 1990), pp. 331–351.
4. J. Rayner, performance, in *Bird Migration: Physiology and Ecophysiology*, E. Gwinner, Ed. (Springer, 1990), pp. 283–299.
5. C. M. Bishop *et al.*, *Science* **347**, 250–254 (2015).
6. R. E. Gill *et al.*, *Proc. Biol. Sci.* **276**, 447–457 (2009).
7. M. H. Dickinson *et al.*, *Science* **288**, 100–106 (2000).
8. C. Pennycuick, *Bird Flight Performance: A Practical Calculation Manual* (Oxford Univ. Press, Oxford, 1989).
9. H. Weimerskirch, M. Le Corre, S. Jaquemet, M. Potier, F. Marsac, *Mar. Ecol. Prog. Ser.* **275**, 297–308 (2004).
10. J. B. Nelson, *The Living Bird* **14**, 113–155 (1976).
11. C. J. Pennycuick, *J. Exp. Biol.* **102**, 307–325 (1983).
12. H. Weimerskirch, O. Chastel, C. Barbraud, O. Tostain, *Nature* **421**, 333–334 (2003).
13. See the supplementary materials on *Science* Online.
14. A. Laing, J. M. Evans, *Introduction to Tropical Meteorology: A Comprehensive Online & Print Textbook*, Comet Program, A. Laing, Ed. (University Corporation for Atmospheric Research, Boulder, CO, 2011).
15. J. S. Malkus, *J. Meteorol.* **11**, 220–237 (1954).
16. U. Nair, R. Weger, K. Kuo, R. Welch, *J. Geophys. Res. Atmos.* **103**, 11363–11380 (1998).
17. C. J. Pennycuick, *Modelling the Flying Bird* (Elsevier, 2008).

18. T. Alerstam, D. Christie, A. Ulfstrand, *Bird Migration* (Cambridge Univ. Press, 1993).
19. F. Liechti, W. Witvliet, R. Weber, E. Bächler, *Nat. Commun.* **4**, 2554 (2013).
20. N. C. Rattenborg, *Naturwissenschaften* **93**, 413–425 (2006).
21. J. A. Lesku *et al.*, *Science* **337**, 1654–1658 (2012).
22. H. Weimerskirch, M. Louzao, S. de Grissac, K. Delord, *Science* **335**, 211–214 (2012).
23. U. C. Mohanty, M. Mohapatra, O. P. Singh, B. K. Bandyopadhyay, L. S. Rathore, *Monitoring and Prediction of Tropical Cyclones in the Indian Ocean and Climate Change* (Springer, Dordrecht, Netherlands, 2014).
24. H. J. J. Jonker, T. Heus, P. P. Sullivan, *Geophys. Res. Lett.* **35**, L07810 (2008).

ACKNOWLEDGMENTS

The tracking data presented in the paper are available from the Dryad Digital Repository. We thank the Forces Armées de la Zone Sud de l'Océan Indien for transport and logistical support on Europa Island and the TAAF Administration for allowing us to work on Europa Island. We thank the fieldworkers involved in the study on Europa, in particular J. B. Pons and R. Weimerskirch; R. Spivey for help with preparing the electrocardiogram and acceleration tags and for the data processing of the heart rate recording; and A. Corbeau for help with data analyses. The study is a contribution to the Program EARLYLIFE funded by a European Research Council Advanced Grant under the European Community's Seven Framework Program FP7/2007–2013 (grant agreement ERC-2012-ADG_20120314 to H.W.). We thank Y. Ropert-Coudert, Y. Cherel, and two anonymous reviewers for helpful comments on earlier versions of the manuscript.

SUPPLEMENTARY MATERIALS

www.sciencemag.org/content/353/6294/74/suppl/DC1
Materials and Methods
Supplementary Text
Figs. S1 to S10
Table S1
References (*25*–*34*)

11 February 2016; accepted 20 May 2016
10.1126/science.aaf4374

TRANSCRIPTION

Visualization and analysis of gene expression in tissue sections by spatial transcriptomics

Patrik L. Ståhl,[1,2]* Fredrik Salmén,[2]* Sanja Vickovic,[2]† Anna Lundmark,[2,3]† José Fernández Navarro,[1,2] Jens Magnusson,[1] Stefania Giacomello,[2] Michaela Asp,[2] Jakub O. Westholm,[4] Mikael Huss,[4] Annelie Mollbrink,[2] Sten Linnarsson,[5] Simone Codeluppi,[5,6] Åke Borg,[7] Fredrik Pontén,[8] Paul Igor Costea,[2] Pelin Sahlén,[2] Jan Mulder,[9] Olaf Bergmann,[1] Joakim Lundeberg,[2]‡ Jonas Frisén[1]

Analysis of the pattern of proteins or messenger RNAs (mRNAs) in histological tissue sections is a cornerstone in biomedical research and diagnostics. This typically involves the visualization of a few proteins or expressed genes at a time. We have devised a strategy, which we call "spatial transcriptomics," that allows visualization and quantitative analysis of the transcriptome with spatial resolution in individual tissue sections. By positioning histological sections on arrayed reverse transcription primers with unique positional barcodes, we demonstrate high-quality RNA-sequencing data with maintained two-dimensional positional information from the mouse brain and human breast cancer. Spatial transcriptomics provides quantitative gene expression data and visualization of the distribution of mRNAs within tissue sections and enables novel types of bioinformatics analyses, valuable in research and diagnostics.

Tissue transcriptomes are typically studied by RNA-sequencing (RNA-seq) (*1*) of homogenized biopsies, which results in an averaged transcriptome and loss of spatial information. The positional context of gene expression is of key importance to understanding tissue functionality and pathological changes. Several strategies have recently been developed with this aim (*2*–*5*), but they have limitations in the number of transcripts that can be analyzed, rely on rich preexisting data sets, and/or are costly and labor-intensive, and none of them are operational in the standard research and diagnostic setting of regular histological tissue sections.

We asked whether it would be possible to introduce positional molecular barcodes in the complementary DNA (cDNA) synthesis reaction within the context of an intact tissue section before RNA-seq. We first assessed whether it was feasible to generate cDNA from messenger RNA (mRNA) in tissue sections on a surface. We immobilized reverse-transcription oligo(dT) primers on glass slides and placed on the slides sections of adult mouse olfactory bulb, a brain region with clear histological landmarks and ample gene-expression reference data. The tissue was fixed, stained, and imaged (Fig. 1A) (*6*).

After permeabilization, we added reverse-transcription reagents on top of the tissue. We used fluorescently labeled nucleotides to visualize the synthesized cDNA (Fig. 1A and fig. S1). The tissue was then enzymatically removed, which left cDNA coupled to the arrayed oligonucleotides on the slide (*6*). The fluorescent cDNA showed a pattern in detail corresponding to the tissue structure revealed by the general histology (Fig. 1, B and C), and the cDNA was strictly localized directly under individual cells (Fig. 1, D to G′). By comparing the hematoxylin-and-eosin and fluorescent signals, we could measure the average distance of diffusion outside the border of a cell to 1.7 ± 2 μm (mean ± SD) (fig. S1, E to H).

The realization that it is possible to capture mRNA in tissue sections with minimal diffusion and maintained positional representation motivated us to array oligonucleotides with positional barcodes (Fig. 2A), and we denoted this strategy "spatial transcriptomics." We deposited ~200 million oligonucleotides in each of 1007 features, with a diameter of 100 μm and a center-to-center distance of 200 μm, over an area of 6.2 mm by 6.6 mm (fig. S2).

After capturing and reverse-transcribing mRNA, we generated sequencing libraries based on amplification by in vitro transcription (fig. S3, A and B) (*7*, *8*). Comparison with data from RNA extracted and fragmented in solution revealed that ~95% of the genes found with one of the methods was also found with the other (fig. S3C). The correlation between the surface and in-solution libraries was r = 0.94, with even representation of genes having high or low expression (fig. S3D). Replicates of surface-based experiments of adjacent tissue sections showed a correlation of r = 0.97 (fig. S3E). Thus, cDNA synthesis from tissue with arrayed oligonucleotides on a surface is efficient and does not introduce bias compared with in-solution protocols (fig. S3F and table S1).

We sorted the RNA-seq data to its corresponding array features by using the spatial barcodes and aligned the tissue image with the features of the array, which enabled visualization and analyses. Examples of gene-expression patterns revealed by spatial transcriptomics and validation by in situ hybridization are shown in Fig. 2B and fig. S4, A to C. Transcripts expressed at very low levels, such as olfactory receptor mRNAs (*9*), were also detected with spatial transcriptomics (fig. S4D).

The number of genes (*10*) (Fig. 2C) and unique transcripts (fig. S5A) per individual feature varied between cell layers with different cell density (Fig. 2D and table S2). For the vast majority of genes, the coefficient of variation decreased as the average expression increased (fig. S5B). The number of

[1]Department of Cell and Molecular Biology, Karolinska Institute, SE-171 77 Stockholm, Sweden. [2]Science for Life Laboratory, Division of Gene Technology, KTH Royal Institute of Technology, SE-106 91 Stockholm, Sweden. [3]Department of Dental Medicine, Division of Periodontology, Karolinska Institute, SE-141 04 Huddinge, Sweden. [4]Science for Life Laboratory, Department of Biochemistry and Biophysics, Stockholm University, Box 1031, SE-171 21 Solna, Sweden. [5]Division of Molecular Neuroscience, Department of Medical Biochemistry and Biophysics, Karolinska Institute, SE-17177 Stockholm, Sweden. [6]Department of Physiology and Pharmacology, Karolinska Institute, SE-17177 Stockholm, Sweden. [7]Division of Oncology and Pathology, Department of Clinical Sciences Lund, Lund University, SE-223 81 Lund, Sweden. [8]Department of Immunology, Genetics and Pathology, Uppsala University, SE-751 85 Uppsala, Sweden. [9]Science for Life Laboratory, Department of Neuroscience, Karolinska Institute, SE-171 77 Stockholm, Sweden.
*These authors contributed equally to this work. †These authors contributed equally to this work. ‡Corresponding author. Email: joakim.lundeberg@scilifelab.se

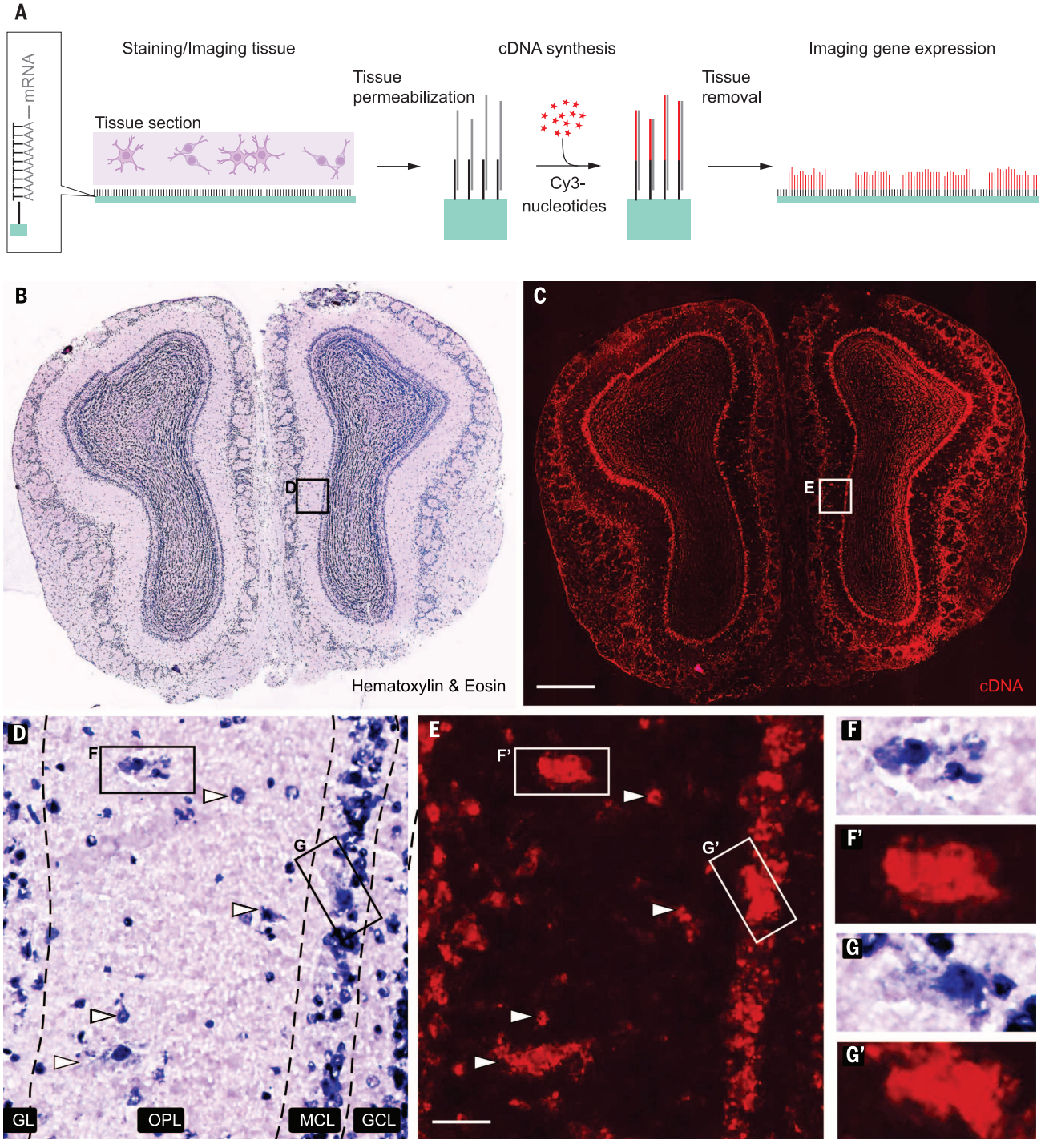

Fig. 1. Spatially localized cDNA synthesis. (**A**) The tissue is sectioned, placed onto oligo(dT) primers, stained, and imaged. cDNA synthesis with Cy3-labeled nucleotides reveals fluorescent cDNA after tissue removal. (**B**) Hematoxylin-and-eosin staining of olfactory bulbs and (**C**) fluorescent cDNA after tissue removal. Scale bar, 500 μm. (**D** and **E**) Magnification of boxes in (B) and (C). Cell layers: GL; OPL, outer plexiform layer; MCL; and GCL. Arrowheads and boxes indicate individual cells and corresponding cDNA with overlapping positions. Scale bar, 40 μm. (**F** to **G'**) Cells in (D) and (E) magnified showing cytoplasm and corresponding cDNA.

genes and transcripts captured was at least twice as high as when using laser capture microdissection (*11*), and spatial transcriptomics detected almost twice as many genes as examination by in situ hybridization in the Allen Brain Atlas (fig. S5, C and D). Furthermore, we compared spatial transcriptomics with the near-100% sensitivity of single-molecule fluorescent in situ hybridization in adjacent tissue sections. The sensitivity of spatial transcriptomics was 6.9 ± 1.5% of single-molecule fluorescent in situ hybridization (fig. S6). By comparison, single-cell RNA sequencing has been reported to have about 5 to 40% sensitivity (*12*).

To further assess the potential lateral diffusion of transcripts, we investigated the distribution of the expression of 10 different genes with highly enriched expression in the mitral cell layer (MCL),

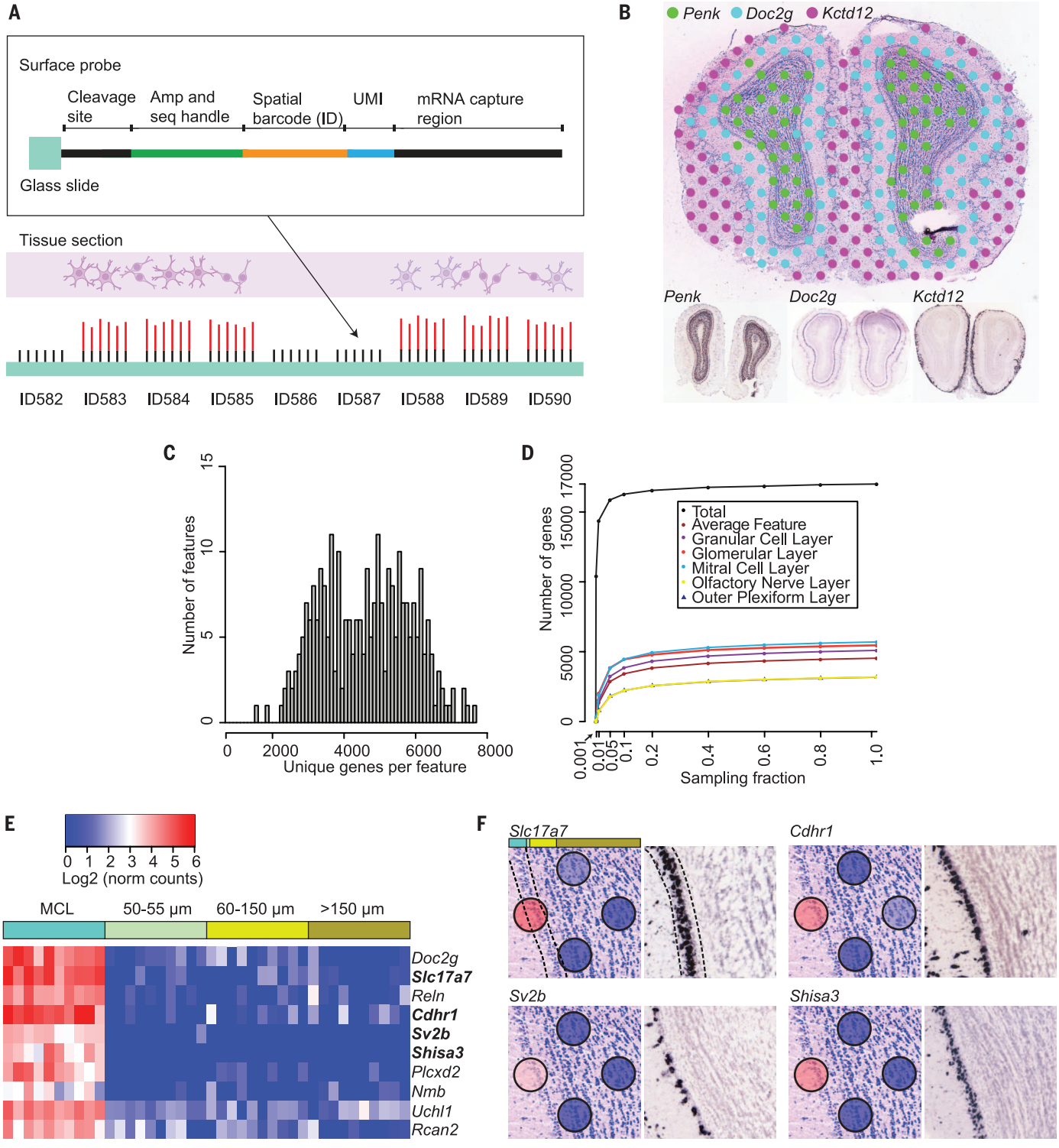

Fig. 2. Spatially resolved gene expression. (**A**) Each array feature contains unique DNA-barcoded probes containing a cleavage site, a T7 amplification and sequencing handle, a spatial barcode, a unique molecular identifier (UMI), and an oligo(dT) VN-capture region, where V is anything but T and where N is any nucleotide. cDNA (red) is generated from captured mRNA by reverse transcription. (**B**) Visualization of the expression of three genes by spatial transcriptomics (top) and in situ hybridization (bottom). *Penk* and *Kctd12* in situ images are from the Allen Institute. Cutoff normalized counts, *Penk*, 8; *Doc2g*, 13; and *Kctd12*, 19. (**C**) Distribution of unique genes per feature under the tissue. (**D**) Number of genes detected for different layers and entire tissue over sequencing depth. (**E**) Lateral diffusion of transcripts from genes enriched in MCL. The genes are expressed in MCL features but are not separable from the background in features adjacent to the MCL. (**F**) Spatial expression and in situ hybridization of four genes in (E). The leftmost feature overlaps the MCL, and the three rightmost features are situated in the GCL. The colored bar depicts the distances from feature center in (E).

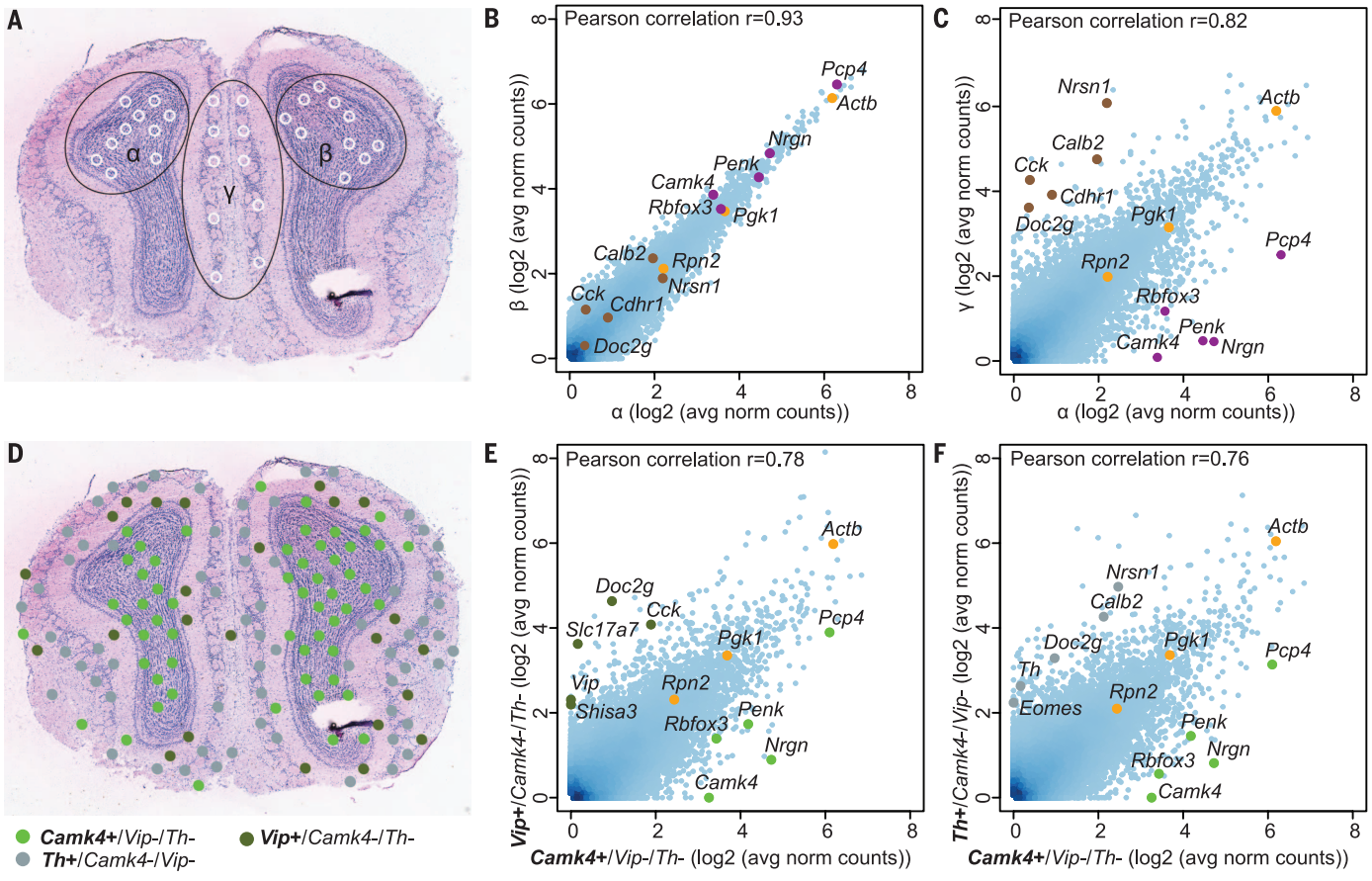

Fig. 3. Visualization and bioinformatics analyses of tissue domains defined by morphology or gene expression profile. (**A**) Ten selected features in areas α (GCL), β (GCL), or γ (GL) are indicated. (**B**) Scatterplot of gene expression in areas α and β shows similar expression of layer-specific genes. Examples of genes are indicated with purple and brown dots. Housekeeping genes are orange. (**C**) Scatterplot of gene expression in areas α and γ shows a difference in gene expression. Examples from the 170 differentially expressed genes are labeled. (**D**) The spatial expression of three interneuron-marker–gene profiles. Ten features with the different expression profiles were randomly selected for differential expression analysis. (**E**) Comparing the 10 *Camk4*$^+$/*Vip*$^-$/*Th*$^-$ features with the 10 *Vip*$^+$/*Camk4*$^-$/*Th*$^-$ features. Examples, out of the 196 differentially expressed genes, are labeled. (**F**) Comparing the 10 *Camk4*$^+$/*Vip*$^-$/*Th*$^-$ features with the 10 *Th*$^+$/*Camk4*$^-$/*Vip*$^-$ features. Examples from the 328 differentially expressed genes are labeled.

and we asked whether they could be detected in the adjacent granular cell layer (GCL). All these genes were confirmed to be highly expressed in the MCL by spatial transcriptomics, but they were undetectable or detected at very low levels within the GCL, even with the border of the feature 0 to 5 μm and the center of the feature 50 to 55 μm from the MCL (Fig. 2, E and F, and fig. S7A). Furthermore, we compared the distribution of transcripts between areas obtained with laser capture microdissection (*6*) where there is no diffusion of transcripts and with spatial transcriptomics features, and we did not find evidence for a difference between these methods in terms of mRNA diffusion (fig. S7, B and C).

A common goal of gene expression analysis of tissues is to define the transcriptome of specific areas. Analysis between homologous regions revealed very similar expression profiles (Fig. 3, A and B, and fig. S8), with no differentially expressed genes. In contrast, comparison of different domains revealed different gene expression profiles (Fig. 3, A and C, and fig. S8). This included genes with previously known restricted expression, such as *Doc2g* in the glomerular layer (GL) and *Penk* in the GCL (*13*), as well as novel layer-specific gene expression profiles (Fig. 3C).

It is valuable to explore the gene expression pattern of populations of cells or tissue domains that can be defined by a combination of markers. Spatial transcriptomics offers an alternative approach that circumvents multiplex labeling and cell isolation. Any combination of presence or absence of expression for a set of genes can be used to define a marker profile of interest for further analysis. Features were selected on the basis of the presence and/or absence of the three interneuron-marker genes *Camk4*, *Th*, and *Vip*. The distribution of features, where one of the genes is expressed alone, is shown in Fig. 3D. Comparing gene expression revealed specific transcriptomes defined by these interneuron-marker profiles (Fig. 3, E and F, and fig. S8).

To further explore gene expression profiles in spatially defined domains within the olfactory bulb, we used principal component analysis (fig. S9) or the t-distributed stochastic neighbor embedding (t-SNE) (*14*, *15*) machine-learning algorithm for dimensionality reduction, followed by hierarchical clustering (Fig. 4A). When placing back the clustered features on the tissue images, it was apparent that each cluster of features largely corresponded to well-defined morphological layers (Fig. 4B). The clusters were then compared with each other, which allowed the identification and visualization of cluster-specific marker genes (fig. S10, A and B). This proved to be an efficient, unbiased way to identify genes with expression enriched in the cell layers of interest. Furthermore, we investigated the gene expression pattern in 10 sections from a total of five animals, as well as the feature-to-feature correlation at the same location in two adjacent sections (fig. S10, C to E).

Analysis of the histology and a set of markers are routine in cancer diagnostics, although analysis of the expression of panels of genes has started to enter the clinic. We asked whether adding a spatial dimension to gene expression analysis may add information in cancer diagnostics and applied spatial transcriptomics to breast cancer biopsies. In Fig. 4, C and D (see also fig. S11, A and B), an area with invasive ductal

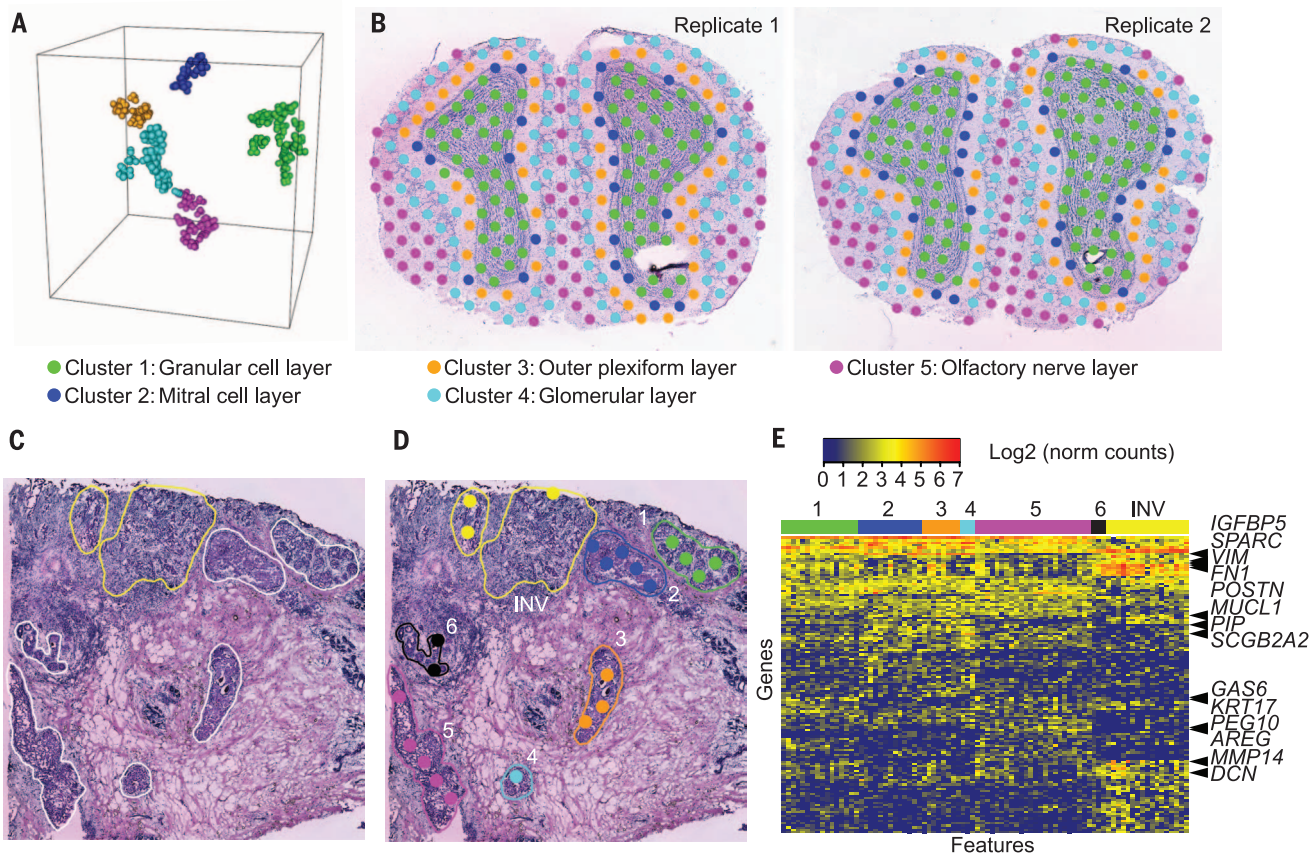

Fig. 4. Comparative analyses of tissue domains. (**A**) t-SNE analysis and hierarchical clustering of 551 features from two replicates creates five distinct clusters. (**B**) The features placed back onto the two tissue images. (**C** and **D**) Histological section of a breast cancer biopsy (C) containing invasive ductal cancer (INV) and six separate areas of ductal cancer in situ (1 to 6), with analyzed spatial transcriptomics features in (D). INV areas without, or with minimal, stromal infiltration were selected. (**E**) Gene expression heat map over the different areas in four adjacent sections (D) and (fig. S11).

cancer, as well as six separate areas of ductal cancer in situ, were identified on the basis of morphological criteria. Spatial transcriptomics analysis of the invasive component revealed high expression of extracellular matrix–associated genes (Fig. 4E). Analysis of the ductal cancer in situ areas revealed a surprisingly high degree of heterogeneity in gene expression between these regions, probably reflecting different subclones, with varying expression of several genes implicated in cancer progression (Fig. 4E and fig. S11C). For example, expression of *KRT17* and *GAS6*, implicated in epithelial-to-mesenchymal transition (*16*, *17*), was high only in areas 1 and 5 (Fig. 4, C to E, and fig S11). Thus, spatial transcriptomics revealed unexpected heterogeneity within a biopsy, which would not be possible to detect with regular transcriptome analysis and which may give more detailed prognostic information.

Spatial transcriptomics calls for only a few extra steps compared with RNA-seq analysis of homogenized tissue, with the benefit of providing spatial information enabling additional levels of analysis. In contrast to standard methods, different domains of the tissue are processed in the same reaction in spatial transcriptomics, which removes technical variation between samples. A unique feature of spatial transcriptomics is that any gene expression profile can be selected to specify a molecularly defined domain for further analysis. Finally, in contrast to when different regions of a tissue are dissected for analysis, the information for the whole section is maintained; hence, the analysis is not limited to the initially selected regions. An individual spatial transcriptomics experiment thus serves as a permanent resource to investigate gene expression patterns for future research questions.

REFERENCES AND NOTES

1. Z. Wang, M. Gerstein, M. Snyder, *Nat. Rev. Genet.* **10**, 57–63 (2009).
2. N. Crosetto, M. Bienko, A. van Oudenaarden, *Nat. Rev. Genet.* **16**, 57–66 (2015).
3. R. Satija, J. A. Farrell, D. Gennert, A. F. Schier, A. Regev, *Nat. Biotechnol.* **33**, 495–502 (2015).
4. P. A. Combs, M. B. Eisen, *PLOS ONE* **8**, e71820 (2013).
5. K. Achim *et al.*, *Nat. Biotechnol.* **33**, 503–509 (2015).
6. Materials and methods are available as supplementary materials on *Science* Online.
7. T. Hashimshony, F. Wagner, N. Sher, I. Yanai, *Cell Reports* **2**, 666–673 (2012).
8. R. N. Van Gelder *et al.*, *Proc. Natl. Acad. Sci. U.S.A.* **87**, 1663–1667 (1990).
9. R. Vassar *et al.*, *Cell* **79**, 981–991 (1994).
10. K. D. Pruitt *et al.*, *Nucleic Acids Res.* **42** (D1), D756–D763 (2014).
11. S. Zechel, P. Zajac, P. Lönnerberg, C. F. Ibáñez, S. Linnarsson, *Genome Biol.* **15**, 486 (2014).
12. D. Grün, A. van Oudenaarden, *Cell* **163**, 799–810 (2015).
13. E. S. Lein *et al.*, *Nature* **445**, 168–176 (2007).
14. A. Mahfouz *et al.*, *Methods* **73**, 79–89 (2015).
15. L. J. P. van der Maaten, G. E. Hinton, *J. Mach. Learn. Res.* **9**, 2579–2605 (2008).
16. M. Kittaneh, A. J. Montero, S. Glück, *Biomarkers Cancer* **5**, 61–70 (2013).
17. C. Gjerdrum *et al.*, *Proc. Natl. Acad. Sci. U.S.A.* **107**, 1124–1129 (2010).

ACKNOWLEDGMENTS

We thank K. Meletis and M. Nilsson for discussions. This study was supported by Knut och Alice Wallenberg Foundation, the Swedish Foundation for Strategic Research, the Swedish Research Council, the Swedish Cancer Society, the Karolinska Institute, Tobias Stiftelsen, Torsten Söderbergs Stiftelse, Ragnar Söderbergs Stiftelse, StratRegen, Åke Wiberg Foundation, and the Jeansson Foundations. P.L.S. was supported by a postdoctoral fellowship from the Swedish Research Council. We thank the Swedish National Genomics Infrastructure hosted at SciLifeLab, as well as the Swedish National Infrastructure for Computing–Uppsala Multidisciplinary Center for Advanced Computational Science and Bioinformatics Long-Term Support for providing sequencing and computational assistance and infrastructure. The sequencing data are deposited at the National Center for Biotechnology Information, NIH, with BioProject ID PRJNA316587. Gene counts and scripts can be downloaded from www.spatialtranscriptomicsresearch.org. P.L.S., F.S., J.L., and J.F. are authors on patents applied for by Spatial Transcriptomics AB covering the technology.

SUPPLEMENTARY MATERIALS

www.sciencemag.org/content/353/6294/78/suppl/DC1
Materials and Methods
Figs. S1 to 11
Tables S1 and S2
References (*18*–*25*)

12 January 2016; accepted 31 May 2016
10.1126/science.aaf2403

STRUCTURAL BIOLOGY

Elucidation of AMPA receptor–stargazin complexes by cryo–electron microscopy

Edward C. Twomey,[1,2] Maria V. Yelshanskaya,[1] Robert A. Grassucci,[1,4] Joachim Frank,[1,3,4]* Alexander I. Sobolevsky[1]*

AMPA-subtype ionotropic glutamate receptors (AMPARs) mediate fast excitatory neurotransmission and contribute to high cognitive processes such as learning and memory. In the brain, AMPAR trafficking, gating, and pharmacology is tightly controlled by transmembrane AMPAR regulatory proteins (TARPs). Here, we used cryo–electron microscopy to elucidate the structural basis of AMPAR regulation by one of these auxiliary proteins, TARP γ2, or stargazin (STZ). Our structures illuminate the variable interaction stoichiometry of the AMPAR-TARP complex, with one or two TARP molecules binding one tetrameric AMPAR. Analysis of the AMPAR-STZ binding interfaces suggests that electrostatic interactions between the extracellular domains of AMPAR and STZ play an important role in modulating AMPAR function through contact surfaces that are conserved across AMPARs and TARPs. We propose a model explaining how TARPs stabilize the activated state of AMPARs and how the interactions between AMPARs and their auxiliary proteins control fast excitatory synaptic transmission.

Excitatory neurotransmission is mediated predominantly by ionotropic glutamate receptors (iGluRs) (*1*). iGluRs are tetrameric ligand-gated ion channels found in the postsynaptic densities of neurons and are typically activated by glutamate released from presynaptic terminals, resulting in ion flux and postsynaptic depolarization (*1*, *2*). The AMPA subtype iGluRs exhibit kinetics at the millisecond time scale and mediate fast neurotransmission in excitatory synapses, directly affecting synaptic plasticity, learning, and memory (*1*). Aberrations in AMPAR function are implicated in a wide range of diseases, from developmental diseases such as fragile X syndrome (*3*) to psychiatric disorders (*1*), acute trauma in ischemic stroke (*4*, *5*), epileptic seizures (*6*, *7*), and chronic neurodegenerative disorders such as Parkinson's and Alzheimer's diseases (*1*).

Structural studies have revealed the three-layer architecture of AMPARs—which includes a two-layer extracellular domain (ECD) composed of two amino-terminal domain (ATD) and ligand-binding domain (LBD) dimers and a channel-forming transmembrane domain (TMD)—and have provided insights into the gating mechanism through models obtained by crystallography (*8*–*11*) and cryo–electron microscopy (cryo-EM) (*12*). However, in cells, AMPARs exist as complexes with various soluble and membrane proteins that alter their function (*13*–*15*). The prototypical transmembrane AMPAR regulatory protein (TARP) γ2, or stargazin (STZ), controls AMPAR synaptic targeting, gating, and pharmacology (*16*–*18*). TARPs are linked to the pathophysiology of several neurological and psychiatric disorders (*19*, *20*), making TARPs and TARP-AMPAR complexes targets for a variety of human diseases. However, despite negative-stain EM studies showing that STZ contributes to the TMD of native AMPAR complexes (*21*), detailed structural information on the AMPAR-TARP interactions, including stoichiometry (*22*–*24*), remains elusive—a key barrier to informed therapeutic design.

Here, we used cryo-EM to elucidate the structural basis for STZ modulation of GluA2 function. To form the complex between GluA2 and STZ, we used a tandem construct, GluA2-STZ, where the N terminus of STZ was fused to the C terminus of GluA2 by a glycine-threonine (GT) linker (Fig. 1A) (*25*). Purified GluA2-STZ eluted from the size-exclusion column as a monodisperse peak, shifted leftward compared with nonfused GluA2 (Fig. 1B), and ran as a higher

[1]Department of Biochemistry and Molecular Biophysics, Columbia University, 650 West 168th Street, New York, NY 10032, USA. [2]Integrated Program in Cellular, Molecular, and Biomedical Studies, Columbia University, 650 West 168th Street, New York, NY 10032, USA. [3]Department of Biological Sciences, Columbia University, 650 West 168th Street, New York, NY 10032, USA. [4]Howard Hughes Medical Institute, 650 West 168th Street, New York, NY 10032, USA.
*Corresponding author. Email: as4005@cumc.columbia.edu (A.I.S.); jf2192@cumc.columbia.edu (J.F.)

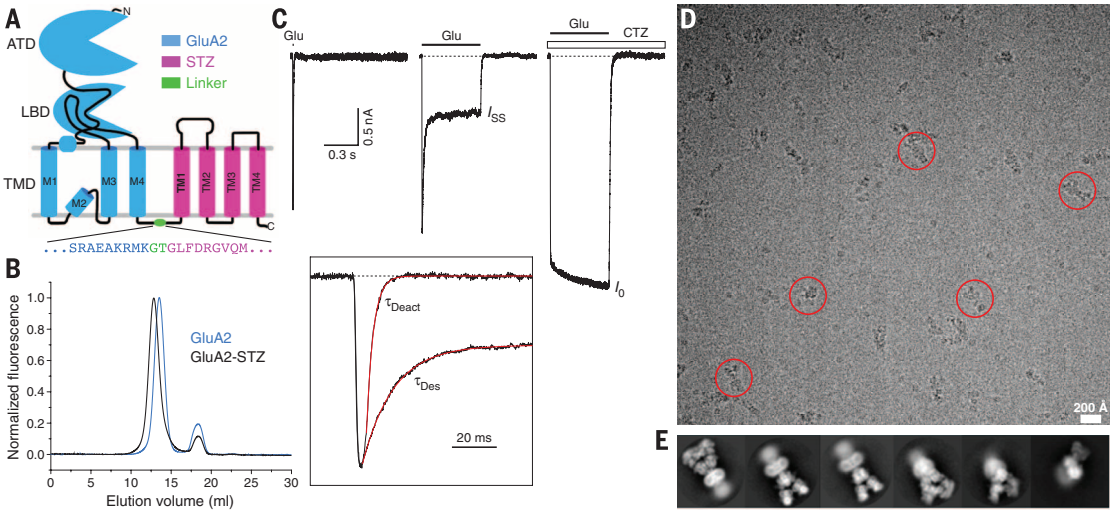

Fig. 1. Design, function, and cryo-EM characterization of GluA2-STZ. (**A**) Topology of the GluA2-STZ construct with GluA2 (blue) and STZ (magenta) connected by a glycine-threonine linker (green). Expanded is the amino acid sequence encompassing the linker region. (**B**) Fluorescence-detection size-exclusion chromatography profiles of purified GluA2-STZ (black) and GluA2 (blue) followed by tryptophan fluorescence. (**C**) Representative whole-cell currents recorded at −60 mV membrane potential from a human embryonic kidney–293 cell expressing GluA2-STZ in response to 2- or 500-ms applications of 3 mM glutamate (Glu) alone or application of Glu in the continuous presence of 30 μM cyclothiazide (CTZ). Inset shows normalized currents in response to 2- and 500-ms applications of Glu alone, fitted using single exponentials with the time constants τ_{Deact} and τ_{Des} (Deact, deactivation; Des, desensitization). (**D**) Drift-corrected cryo-EM micrograph of GluA2-STZ, with example particles highlighted by red circles. (**E**) Representative 2D class averages.

molecular-weight band on SDS–polyacrylamide gel electrophoresis (fig. S1). To assess functionality, we recorded glutamate-activated GluA2-STZ currents using patch-clamp electrophysiology. Compared with wild-type GluA2, GluA2-STZ showed reduced desensitization and slower rates of deactivation, desensitization, and recovery from desensitization (Fig. 1C and fig. S2), as expected (*26*–*30*). Thus, the presence of the GT linker between GluA2 and STZ in our GluA2-STZ construct did not significantly affect modulation of GluA2 function by STZ.

Cryo-EM micrographs of purified GluA2-STZ bound to antagonist ZK200775 gave initial insight into the particle details (Fig. 1D), and initial views of GluA2-STZ from two-dimensional (2D) classes suggested high data quality, with visible linkers between the LBD and TMD, clear secondary structure features in both the ECD and TMD, and diverse particle orientations (Fig. 1E). However, atypical for the GluA2 three-layer topology (fig. S3, A and B), GluA2-STZ showed a four-layer architecture, where below the TMD layer is a fourth layer (Fig. 1D) that appears disordered (Fig. 1E). A closer look at the GluA2-STZ particles (*25*) suggested that the disordered fourth layer under the TMD is likely composed of unbound STZ and is a result of the tandem construct design, which defines the protomer ratio but not interaction stoichiometry.

We identified multiple STZ-bound states of the GluA2-STZ complex through additional image processing (fig. S4). One state resembles the map for GluA2 alone (fig. S3C) and shows no STZ bound (GluA2-0xSTZ) (Fig. 2A). A second state shows a single STZ assembled around GluA2, which we call GluA2-1xSTZ (Fig. 2B). We also identified a third state of the GluA2-STZ particles, where two STZ molecules are assembled around the GluA2 core, termed GluA2-2xSTZ (Fig. 2C). For all three states, we observed no preferred particle orientation in the refined maps (fig. S5), with most particles contributing to the single-bound STZ state (fig. S6). A closer look through 2D slices of the 3D refined cryo-EM density maps in the TMD and LBD-TMD linkers highlights the differences in stoichiometry, where zero (Fig. 2A), one (Fig. 2B), or two (Fig. 2C) STZ TMDs and ECDs are visible around the GluA2 core and periphery, respectively. Correspondingly, the disordered fourth layer (Fig. 1E) in these three stoichiometric states presumably has four, three, and two STZ molecules from the tandem construct that are not bound around the GluA2 core (*25*). Based on our density maps (Fig. 2), we propose that the preferred stoichiometry of the GluA2-STZ interaction is one or two STZ protomers to one tetramer of GluA2. The existence of multiple stoichiometric states suggests that STZ expression levels could have a profound effect on AMPAR-mediated neurotransmission.

To gain further insight into the AMPAR-TARP interaction, we built a structural model of the GluA2-1xSTZ state. Guided by the two-fold symmetry of the ECD (*8*–*12*), we used the corresponding portion of the GluA2-1xSTZ map refined with C2 symmetry to 5.6 Å resolution (fig. S6) (*25*) to fit GluA2 ATDs and LBDs (*8*) and to build ATD-LBD linkers. We further used the 6.4 Å map obtained from refinement without symmetry restraints (fig. S7) to fit the GluA2 TMD region (*8*) and to build LBD-TMD linkers (fig. S8). We then took advantage of amino acid sequence conservation between TARP family and Claudin family proteins (fig. S9) and built a Claudin-19–based homology model of STZ. This model was fitted into the GluA2-1xSTZ density (*25*) (fig. S8B), confirming the similar overall fold of TARPs and Claudins (*31*, *32*) (fig. S9). The STZ and GluA2 protomers from the GluA2-1xSTZ structure were also fitted into the GluA2-2xSTZ map to generate a structure of the corresponding complex (Fig. 3, A and B).

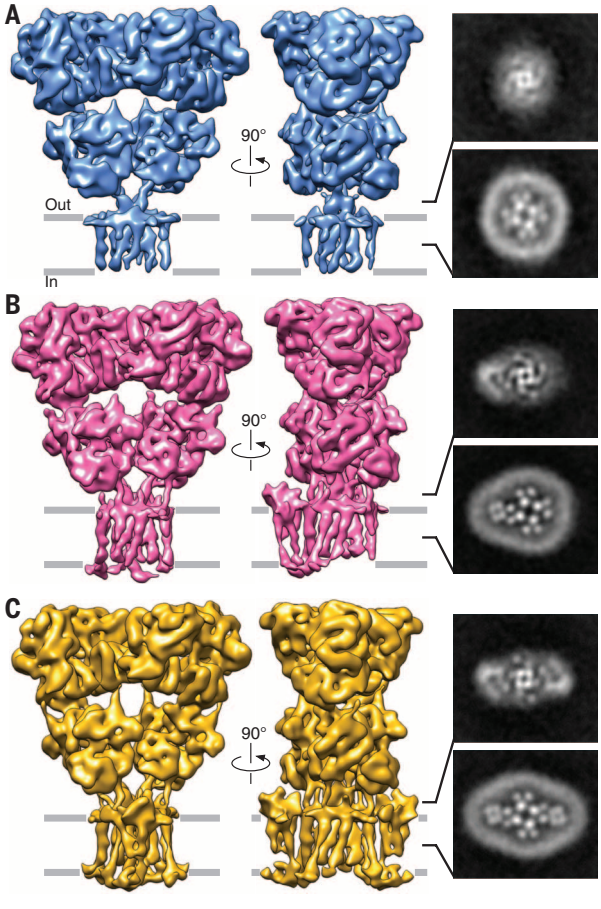

Fig. 2. Stoichiometric states of GluA2-STZ. On the left, cryo-EM density maps of (**A**) STZ-unbound, (**B**) single STZ-bound, and (**C**) double STZ-bound states of GluA2-STZ filtered to 8.7 Å, 6.4 Å, and 7.8 Å resolution, respectively. For each state, 2D slices made parallel to the membrane through the refined, nonfiltered map are shown on the right: one through the middle of GluA2 LBD-TMD linker region and another through the middle of GluA2 TMD. (Details of collection and refinement are included in fig. S6.)

The structure of STZ includes a TMD that represents a bundle of four transmembrane helices, TM1 to TM4, and an extracellular head domain that sits atop the TMD (Fig. 3C). The main interaction between STZ and AMPAR is mediated by a substantial interface between transmembrane helices TM3 and TM4 of STZ and M1 and M4 of GluA2 (Fig. 3D). STZ TM1 and TM2 have no direct contact to the AMPAR core and face the lipid membrane. The STZ head domain is composed of two extracellular polypeptide segments between TM1 and TM2 and between TM3 and TM4 (Fig. 3C). Most of the head domain is a β sheet that includes strands β1 to β4 formed by the N-terminal portion of the TM1-TM2 segment and β5 formed by the C-terminal portion of the TM3-TM4 segment. The remaining portions of the extracellular segments, the TM3-β5 loop and the β4-TM2 loop in particular, are conveniently positioned in close proximity to the LBD and LBD-TMD linkers to play a key role in regulation of AMPAR function.

The GluA2-STZ structures indicate that the TM3-β5 and β4-TM2 loops of STZ can only interact with GluA2 subunits B and D but not A and C (Fig. 3B). At the level of the LBD, B and D represent the distal subunits (fig. S10A) that play a more important role in iGluR gating than the proximal subunits A and C (*9*, *33*, *34*). STZ molecules are thus optimally positioned in the GluA2-STZ complex to maximally affect GluA2 gating. The most likely regions of GluA2 subunits B and D to interact with STZ loops TM3-β5 and β4-TM2 are the adjacent S1-M1 linker and the LBD loop between helix H and the β stand 10 (Fig. 4A). The S1-M1 linker contains four positively charged residues (K505, K506, K509, and K511), in addition to four positively charged residues in the helix H-β strand 10 loop (R692, K695, K697, and K699), that form an electropositive patch on the surface of GluA2 facing STZ (Fig. 4, B and C). In contrast, six negatively charged residues in the β4-TM2 loop of STZ (E84, D85, D87, E89, D91, and E94) form an electronegative patch on the surface of the STZ head domain facing GluA2.

Confirming a key role of the electrostatic interactions in regulation of AMPAR function by STZ, recent mutagenesis experiments on a similar GluA2-STZ tandem construct showed that the aspartate substitution of a KGK motif, which is highly conserved in AMPARs and includes K697 and K699 residues in the helix H-β strand 10 loop, almost completely abolished the effects of STZ on GluA2 receptor function (*29*). In addition, the electronegative motif in the STZ β4-TM2 loop is highly conserved across type I TARPs (*19*), including γ2 (STZ), γ3, γ4, and γ8 (fig. S9). Similar to STZ, γ3, γ4, and γ8 slow AMPAR deactivation and desensitization kinetics (*19*). In contrast, type II TARPs γ5 and γ7 do not have the conserved electronegative

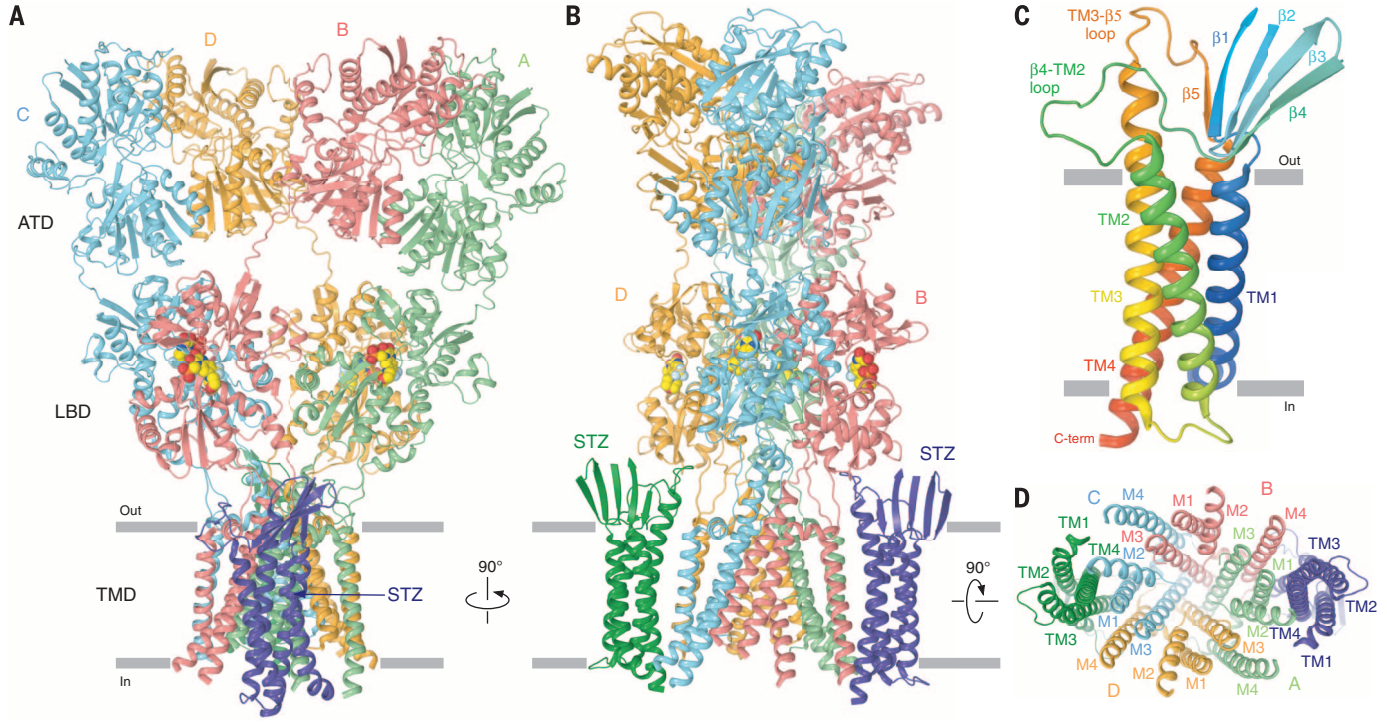

Fig. 3. Architecture of the GluA2-STZ complex. (**A**, **B**, and **D**) Model of GluA2-2xSTZ viewed parallel to [(A) and (B)] or from the intracellular side of (D) the membrane. The four GluA2 subunits (A to D) are colored mint (A), coral (B), light-blue (C), and gold (D), and the STZ molecules are in green and purple; TMD secondary structure elements are labeled in (D). (**C**) Rainbow-colored homology model (from blue N terminus to red C terminus) of STZ with the secondary structure elements labeled. In (A) and (B), the antagonist ZK200775 is shown as a space-filling model.

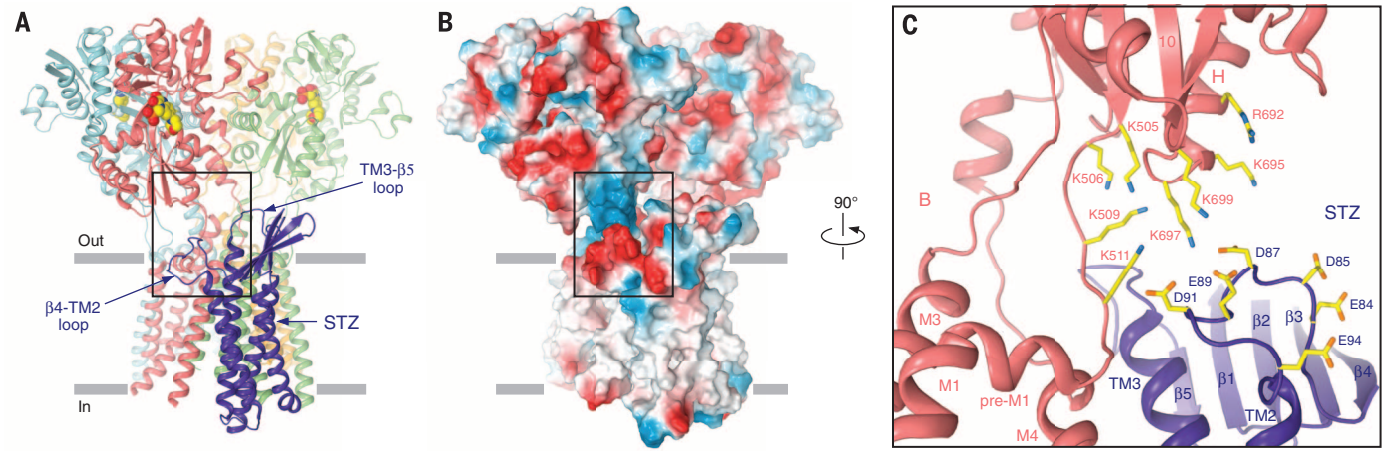

Fig. 4. Electrostatic interactions between the STZ head domain and GluA2. (**A**) Side view of GluA2-1xSTZ with GluA2 ATDs omitted and STZ β4-TM2 and TM3-β5 loops labeled. (**B**) Electrostatic surface of the molecule in (A) with highly electronegative regions shown in red and highly electropositive regions shown in blue. (**C**) Close-up orthogonal view of the region boxed in (A) and (B). Charged residues in the S1-M1 linker and LBD lower lobe of GluA2, and the β4-TM2 loop of STZ are shown as sticks.

motif in the β4-TM2 loop (fig. S9) and likely use different mechanisms to alter AMPAR gating and pharmacology (*19*, *35*). Indeed, substitution of the TM1-TM2 extracellular stretch in STZ with that of γ5 dramatically reduced the effect of STZ on AMPAR gating and agonist efficacy to nearly the levels of AMPAR alone (*27*).

We hypothesize that the overall compression of AMPARs upon activation (*9*–*12*, *36*) brings the negative patch on the STZ surface closer to the positive patch on the surface of GluA2 (fig. S10B), thus enhancing their electrostatic attraction. This additional force would account for STZ-stabilization of the open conformation of AMPARs (*37*) and correspondingly make deactivated and desensitized states less favorable.

REFERENCES AND NOTES

1. S. F. Traynelis *et al.*, *Pharmacol. Rev.* **62**, 405–496 (2010).
2. J. Kumar, M. L. Mayer, *Annu. Rev. Physiol.* **75**, 313–337 (2013).

3. G. Uzunova, E. Hollander, J. Shepherd, *Curr. Neuropharmacol.* **12**, 71–98 (2014).
4. C. N. Morrell *et al.*, *J. Exp. Med.* **205**, 575–584 (2008).
5. F. Zhang, A. Guo, C. Liu, M. Comb, B. Hu, *Stroke* **44**, 170–176 (2013).
6. A. G. Chapman, *J. Nutr.* **130** (suppl.), 1043S–1045S (2000).
7. M. A. Rogawski, *Acta Neurol. Scand. Suppl.* **127**, 9–18 (2013).
8. A. I. Sobolevsky, M. P. Rosconi, E. Gouaux, *Nature* **462**, 745–756 (2009).
9. L. Chen, K. L. Dürr, E. Gouaux, *Science* **345**, 1021–1026 (2014).
10. K. L. Dürr *et al.*, *Cell* **158**, 778–792 (2014).
11. M. V. Yelshanskaya, M. Li, A. I. Sobolevsky, *Science* **345**, 1070–1074 (2014).
12. J. R. Meyerson *et al.*, *Nature* **514**, 328–334 (2014).
13. D. S. Bredt, R. A. Nicoll, *Neuron* **40**, 361–379 (2003).
14. J. R. Howe, *J. Physiol.* **593**, 61–72 (2015).
15. J. Schwenk *et al.*, *Neuron* **74**, 621–633 (2012).
16. L. Chen *et al.*, *Nature* **408**, 936–943 (2000).
17. A. C. Jackson, R. A. Nicoll, *J. Neurosci.* **31**, 3939–3952 (2011).
18. W. Vandenberghe, R. A. Nicoll, D. S. Bredt, *Proc. Natl. Acad. Sci. U.S.A.* **102**, 485–490 (2005).
19. A. S. Kato, M. B. Gill, H. Yu, E. S. Nisenbaum, D. S. Bredt, *Trends Neurosci.* **33**, 241–248 (2010).
20. A. C. Jackson, R. A. Nicoll, *Neuron* **70**, 178–199 (2011).
21. T. Nakagawa, Y. Cheng, E. Ramm, M. Sheng, T. Walz, *Nature* **433**, 545–549 (2005).
22. P. Hastie *et al.*, *Proc. Natl. Acad. Sci. U.S.A.* **110**, 5163–5168 (2013).
23. K. S. Kim, D. Yan, S. Tomita, *J. Neurosci.* **30**, 1064–1072 (2010).
24. Y. Shi, W. Lu, A. D. Milstein, R. A. Nicoll, *Neuron* **62**, 633–640 (2009).
25. Materials and methods are available as supplementary materials on *Science* Online.
26. A. Priel *et al.*, *J. Neurosci.* **25**, 2682–2686 (2005).
27. S. Tomita *et al.*, *Nature* **435**, 1052–1058 (2005).
28. A. L. Carbone, A. J. Plested, *Nat. Commun.* **7**, 10178 (2016).
29. G. B. Dawe *et al.*, *Neuron* **89**, 1264–1276 (2016).
30. W. Zhang, S. P. Devi, S. Tomita, J. R. Howe, *Eur. J. Neurosci.* **39**, 1138–1147 (2014).
31. H. Suzuki *et al.*, *Science* **344**, 304–307 (2014).
32. Y. Saitoh *et al.*, *Science* **347**, 775–778 (2015).
33. H. Dong, H. X. Zhou, *Nat. Commun.* **2**, 354 (2011).
34. R. Kazi, J. Dai, C. Sweeney, H. X. Zhou, L. P. Wollmuth, *Nat. Neurosci.* **17**, 914–922 (2014).
35. A. S. Kato, E. R. Siuda, E. S. Nisenbaum, D. S. Bredt, *Neuron* **59**, 986–996 (2008).
36. A. I. Sobolevsky, *J. Physiol.* **593**, 29–38 (2015).
37. D. M. MacLean, S. S. Ramaswamy, M. Du, J. R. Howe, V. Jayaraman, *J. Gen. Physiol.* **144**, 503–512 (2014).

ACKNOWLEDGMENTS

We thank Z. H. Yu, C. Hong, and R. Huang for assistance with data collection at the Howard Hughes Medical Institute Janelia Research Campus, M. Fislage (J.F. laboratory) for assistance with the initial cryo-EM preparation and critical reading of the manuscript, and H. Kao (J.F. laboratory) for computational support. We are grateful for manuscript edits and comments provided by K. Saotome and A. K. Singh (A.I.S. laboratory) and advice on image processing provided by I. S. Fernandez (Columbia), Z. Liu (J.F. laboratory), O.B. Clarke (Hendrickson laboratory, Columbia), A. des Georges (City University of New York), and members of J.F.'s laboratory. E.C.T. was supported by NIH training grants T32 GM008224 and GM008281. A.I.S. was supported by NIH (R01 NS083660), the Pew Scholar Award in Biomedical Sciences, the Schaefer Research Scholar Award, the Klingenstein Fellowship Award in the Neurosciences, and the Irma T. Hirschl Career Scientist Award. J.F. was supported by the Howard Hughes Medical Institute and NIH (R01 GM029169). Cryo-EM density maps have been deposited in the EM Data Bank under accession numbers EMD-8229 (GluA2-0xSTZ), EMD-8230 (GluA2-1xSTZ), EMD-8231 (GluA2-2xSTZ), and EMD-8232 (GluA2). Model coordinates have been deposited in the Protein Data Bank under accession numbers 5KBS (GluA2-0xSTZ), 5KBT (GluA2-1xSTZ), 5KBU (GluA2-2xSTZ), and 5KBV (GluA2).

SUPPLEMENTARY MATERIALS

www.sciencemag.org/content/353/6294/83/suppl/DC1
Materials and Methods
Figs. S1 to S10
References (*38*–*58*)

7 April 2016; accepted 8 June 2016
10.1126/science.aaf8411

THE NORWEGIAN ACADEMY OF SCIENCE AND LETTERS

ANNOUNCES THE 2016 WINNERS OF

THE KAVLI PRIZE℠

THE KAVLI PRIZE IN ASTROPHYSICS

RONALD W. P. DREVER
California Institute of Technology,
USA

KIP S. THORNE
California Institute of Technology,
USA

RAINER WEISS
Massachusetts Institute of Technology,
USA

"for the direct detection of gravitational waves"

THE KAVLI PRIZE IN NANOSCIENCE

GERD BINNIG
Former Member of IBM Zurich
Research Laboratory, Switzerland

CHRISTOPH GERBER
University of Basel,
Switzerland

CALVIN QUATE
Stanford University,
USA

"for the invention and realization of atomic force microscopy, a breakthrough in measurement technology and nanosculpting that continues to have a transformative impact on nanoscience and technology"

THE KAVLI PRIZE IN NEUROSCIENCE

EVE MARDER
Brandeis University,
USA

MICHAEL MERZENICH
University of California San Francisco,
USA

CARLA SHATZ
Stanford University,
USA

"for the discovery of mechanisms that allow experience and neural activity to remodel brain function"

The Kavli Prize is a partnership between The Norwegian Academy of Science and Letters, The Kavli Foundation (USA) and The Norwegian Ministry of Education and Research. HRH Crown Prince Haakon presents the Kavli Prize to the 2016 Laureates on September 6, 2016 at a ceremony in Oslo, Norway.

www.kavliprize.org

Sequel System

The new Sequel System is based on Pacific Biosciences' proven single molecule, real-time (SMRT) technology and contains 1 million zero-mode waveguides per SMRT Cell. The Sequel System is ideal for projects such as rapid and cost-effective generation of high-quality, whole-genome de novo assemblies. It can provide characterization of a wide variety of genomic variation types, including those in complex regions not accessible with short-read or synthetic long-range sequencing technologies, while simultaneously revealing epigenetic information.

Pacific Biosciences
For info: 650-521-8000
www.pacb.com

Ion Chromatography System

The Dionex Integrion High-Pressure Ion Chromatography (HPIC) system is intuitive, easy to use, and capable of addressing challenging laboratory workflows. The Dionex Integrion HPIC system delivers features previously available only on Thermo Scientific high-end systems, including high-pressure capability and optional electrochemical detection. With a simple, logical, flow-based plumbing layout and integrated performance features, including whole-system smart monitoring, the Dionex offers fast run times in a robust and reliable system. Additional features may include easy-to-install ion chromatography polyetheretherketone viper fittings, as well as a detachable tablet, a consumables device monitor, a thermally regulated detector compartment, and the Thermo Scientific Dionex Chromeleon Chromatography Data System.

Thermo Fisher Scientific
For info: 800-556-2323
www.thermoscientific.com

Automated Colony Counter

The new aCOLyte 3 HD is a next-generation, automated colony counter for microbiologists who demand a sensitive, affordable system to quickly and accurately count colonies of all sizes and colors. The aCOLyte 3 HD features a high-resolution megapixel charge-coupled device (CCD) camera for accurate detection of different colored microbial colonies as small as 0.1 mm in diameter. The system's powerful software can analyze pour, spread, and spiral plates of up to 90-mm diameter, generating stunning full-color plate images and precise counts in seconds. The results can be directly transferred to Excel and other software packages to avoid keying and scanning errors, guaranteeing accurate GLP-compliant reporting and full data traceability every time. The aCOLyte 3 HD is ideal because it can be easily connected via USB port to a microbiologist's own tablet, laptop, desktop PC, or a computer purchased with the system.

Synbiosis
For info: +44-(0)-1223-727125
www.synbiosis.com

Multimode Reader

The Spark 20M multimode microplate reader offers tailor-made solutions to suit virtually any drug discovery or advanced life science research application. This freely configurable system gives researchers access to new techniques and features intended to enhance and streamline biochemical and cell-based workflows. At the heart of the instrument are Spark's unique Fusion Optics and a powerful, high-frequency xenon flash lamp, which can be combined with any choice of high-performance detection modules to ensure a perfect workflow match. Options include an enhanced fluorescence module designed to improve sensitivity and increase the speed of high-throughput screening, and the newly developed Te-Cool cooling module that uniquely allows the measurement chamber temperature to be set below the ambient room temperature for more accurate and reliable results. The Spark 20M's cell-handling capabilities have also been extended, with a new automated cell-imaging and confluence measurement feature.

Tecan
For info: +41-(0)-44-922-81-11
www.tecan.com/spark20m

Ultrasound Research System

The RK-50 is a stand-alone, versatile, preclinical system that enables scientists to take advantage of the many powerful applications of focused ultrasound (FUS). Through the use of standard stereotaxic targeting methods facilitated by image-guided treatment-planning software, the RK-50 can deliver precise doses of FUS through an intact skull to small structures in the rodent brain. The RK-50 is particularly well suited for blood-brain barrier disruption. This technology represents a noninvasive alternative to stereotaxic injections that has been used to deliver a variety of agents to the brain, including chemotherapeutics, small interfering RNA amyloid antibodies, genes, contrast agents, nanoparticles, and stem cells.

FUS Instruments
For info: 647-238-7146
www.fusinstruments.com

Waveform Generator

A new ultra-high frequency arbitrary waveform generator (UHF-AWG) enables fast and intuitive waveform programming with sequence branching for quantum computing, nuclear magnetic resonance spectroscopy, and mixed-signal device testing customers. The UHF-AWG is a dual-channel, 600-MHz AWG with 128-megasample waveform memory per channel and 1.8-gigasample-per-second temporal and 14-bit vertical resolution. Integrated detection options include a pulse counter, multiple demodulators, an oscilloscope, and a boxcar averager. Signal generation and detection merged into a single instrument minimizes feedback times and experimental setup. The AWG is fully integrated into the LabOne instrument control software that provides high-level AWG commands. Pulse sequences and waveforms can be easily defined and adjusted. The UHF-AWG features standard waveform playback and amplitude modulation. In amplitude modulation mode, each AWG channel shapes one of up to eight internally generated sine wave signals and does not require uploading the entire waveform. The UHF-AWG has easy upgrade paths.

Zurich Instruments
For info: +41-(0)-44-515-0410
www.zhinst.com

Electronically submit your new product description or product literature information! Go to www.sciencemag.org/about/new-products-section for more information.

Newly offered instrumentation, apparatus, and laboratory materials of interest to researchers in all disciplines in academic, industrial, and governmental organizations are featured in this space. Emphasis is given to purpose, chief characteristics, and availability of products and materials. Endorsement by *Science* or AAAS of any products or materials mentioned is not implied. Additional information may be obtained from the manufacturer or supplier.

ZHEJIANG UNIVERSITY CALLS FOR GLOBAL TALENTS

Brief Introduction of Zhejiang University

Located in the historical and picturesque city of Hangzhou, Zhejiang University is a prestigious institution of higher education with a long history. After a hundred years of construction and development, Zhejiang University has become a comprehensive research university with distinctive features and relatively great impact at home and abroad. Research at Zhejiang University spans 12 academic disciplines, covering philosophy, economics, law, education, literature, history, art, science, engineering, agriculture, medicine, management and etc. In all 22 disciplines of ESI, there are 18 disciplines leading to top 1% in the world. Zhejiang University has always been committed to cultivating talent with excellence, advancing science and technology development, serving for social well-being, and promoting advanced culture with the spirit best manifested by the university motto "Seeking the Truth and Pioneering New Trails".

Zhejiang University has long been holding the educational philosophy of putting people foremost, cultivating students in an all-round way, seeking the truth and pioneering new trails in search of excellence, and is committed to cultivating future leaders with an international perspective.

Brief Introduction of Hundred Talents Program

Zhejiang University (ZJU) is seeking faculty candidates for highly competitive, well funded, and newly launched Hundred Talents Program. This program covers all colleges and departments at ZJU. Successful candidates are expected to establish internationally competitive and independent research program in cutting-edge areas of relevant field. According to their qualification, candidates should have demonstrated commitment to excellence in teaching and research, which is comparable to the academic achievements of assistant professor or associate professor in world-renowned universities.

Know More of Our Talent Programs

Except for the Hundred Talents Program, there are a number of talent recruitment programs and open job opportunities for high-end talents worldwide, as for details please visit http://talent.zju.edu.cn/redir.php?catalog_id=20038&object_id=40799, or scan the QR code of recruitment programs of ZJU below.

Zhejiang University sincerely invites excellent talents to join us and together to create a glorious future for Zhejiang University and its people.

Contact: Talent Office, ZJU
Tel: +86-571-88981345 ,
+86-571-88981390
Fax: +86-571-88981976
E-mail: tr@zju.edu.cn

• What We Offer

Successful candidate will be employed as ZJU100 Professor who is qualified to supervise doctoral student. ZJU will offer a decent compensation with the opportunity to purchase one of the apartments reserved for high-end talents, a good facilitate of office and laboratory space as well as internationally competitive startup packages will be provided.

• How to Apply

Qualified applicants are strongly encouraged to submit your application electronically to tr@zju.edu.cn with the following materials in PDF format: a comprehensive CV, a statement of research and teaching plan, certificates of academic degrees, 3 samples of major publications and a list of 3 to 5 references with detailed contact information.

• Qualifications and Requirements

Candidates are expected to be about 35 years old. Successful applicants should hold a doctoral degree of world-renowned university and postdoctoral experiences are preferred. Successful applicants are supposed to work full-time and deliver excellent research and teaching at ZJU. The spirits of "Seeking the Truth and Pioneering New Trails" are expected.

invitrogen

One conductor, a symphony of enzymes

Finally, a complete, one-buffer system–for beautifully simple cloning

Introducing the Invitrogen™ Anza™ Restriction Enzyme Cloning System:

- One buffer for all restriction enzymes
- One digestion protocol for all DNA types
- Complete digestion in 15 minutes
- Overnight digestion without star activity

Choose simplicity at **thermofisher.com/Anza**

ThermoFisher SCIENTIFIC

Science Careers Advertising

For full advertising details, go to ScienceCareers.org and click For Employers, or call one of our representatives.

Tracy Holmes
Worldwide Associate Director
Science Careers
Phone: +44 (0) 1223 326525

THE AMERICAS

E-mail: advertise@sciencecareers.org
Fax: +1 (202) 289 6742

Tina Burks
Phone: +1 (202) 326 6577

Nancy Toema
Phone: +1 (202) 326 6578

Online Job Posting Questions
Phone: +1 (202) 312 6375

EUROPE / INDIA / AUSTRALIA / NEW ZEALAND / REST OF WORLD

E-mail: ads@science-int.co.uk
Fax: +44 (0) 1223 326532

Sarah Lelarge
Phone: +44 (0) 1223 326527

Kelly Grace
Phone: +44 (0) 1223 326528

Online Job Posting Questions
Phone: +44 (0) 1223 326528

JAPAN

Katsuyoshi Fukamizu (Tokyo)
E-mail: kfukamizu@aaas.org
Phone: +81 3 3219 5777

Hiroyuki Mashiki (Kyoto)
E-mail: hmashiki@aaas.org
Phone: +81 75 823 1109

CHINA / KOREA / SINGAPORE / TAIWAN / THAILAND

Ruolei Wu
E-mail: rwu@aaas.org
Phone: +86 186 0082 9345

Danny Zhao
E-mail: dzhao@aaas.org
Phone: +86 131 4114 0012

All ads submitted for publication must comply with applicable U.S. and non-U.S. laws. *Science* reserves the right to refuse any advertisement at its sole discretion for any reason, including without limitation for offensive language or inappropriate content, and all advertising is subject to publisher approval. *Science* encourages our readers to alert us to any ads that they feel may be discriminatory or offensive.

ScienceCareers
FROM THE JOURNAL SCIENCE AAAS

ScienceCareers.org

POSITIONS OPEN

MORRIS COLLEGE

Morris College, a private four year Liberal Arts College in Sumter, South Carolina, is seeking to fill the following position(s):

COMPUTER SCIENTIST: To teach introductory Computer Science courses and introductory Cybersecurity courses and to develop courses for a concentration in Cybersecurity in an NNSA grant supported position. M.S. or Ph.D. in Computer Science with a background in Cybersecurity. Must be available August 2016

Submit a letter of application, personal resume, three letters of recommendation and official academic transcripts to: **Director of Personnel, Morris College, 100 W. College St., Sumter, SC 29150-3599.** *Morris College is an Equal Opportunity/Affirmative Action Employer.*

FOOD AND DRUG ADMINISTRATION CENTER FOR BIOLOGICS EVALUATION & RESEARCH

Director, Office of Cellular, Tissue, and Gene Therapies

The FDA's Center for Biologics Evaluation and Research (CBER), is searching for an Office Director for the Office of Cellular, Tissue, and Gene Therapies (OCTGT). The Director of OCTGT directs a staff of medical officers, interdisciplinary scientists, and health science administrators responsible for research and review related to the development, manufacturing, testing, and use of cellular, tissue and gene therapies, including tumor vaccines, as well as other products. The Office Director also serves as CBER's regulatory and medical expert on gene therapies, human cells and tissues and other products regulated by the Office.

Qualifications: Candidates must be U.S. citizens. Candidates with an M.D. with relevant training and extensive experience are highly desired. All candidates must possess specialized knowledge and experience in the development and regulation of medical products, including the evaluation of safety, effectiveness, and product quality; strong leadership and significant executive management experience; excellent interpersonal skills to deal effectively with multi-disciplinary teams and diverse stakeholders; and outstanding oral and written communication skills. Knowledge of the FDA's regulatory and review process is preferred.

Medical Officer candidates for Civil Service or U.S. Commissioned Corps must possess a valid license to practice medicine in any state in the United States. Board certification or eligibility in Internal Medicine, Hematology, or Medical Oncology is highly desirable.

Education completed in foreign colleges or universities may be used to meet qualification requirements if you can show that the foreign education is comparable to that received in an accredited educational institution in the United States. Applicants should provide such evidence when applying.

This position may also be filled by appointment in the U.S. Public Health Service, Commissioned Corps.

Salary: Salary is commensurate with education and experience, and Medical Officers are eligible for physician market pay (Title 38). An excellent benefits package is also available.

Location: The position is located on the FDA Campus in Silver Spring, Maryland. Relocation expenses will be paid.

Who may apply: All qualified U.S. Citizens.

How to apply: Submit resume or curriculum vitae with cover letter by **July 31, 2016** to website: **CBER.Employment@fda.hhs.gov**. Please reference Job Code: OCTGTOD-16-001-AAAS

The Department of Health and Human Service is an Equal Opportunity Employer with a smoke free environment.

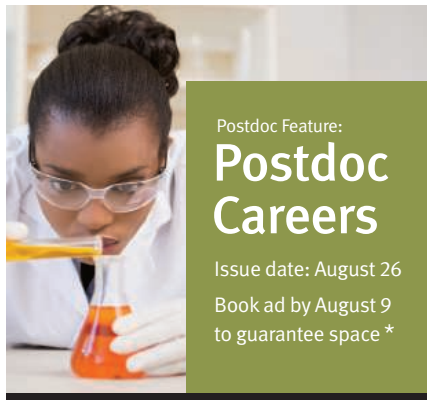

Postdoc Feature:
Postdoc Careers
Issue date: August 26
Book ad by August 9 to guarantee space *

There's only one *Science*.

Why choose this Postdoc Feature your advertisement?

- Relevant ads lead off the career section with a special "Postdoc" banner.

Expand your exposure by posting your print ad online:

- Link on the job board homepage directly to postdoc positions
- Dedicated landing page for postdoc positions.

*Ads accepted until August 19 if space allows.
Produced by the *Science*/AAAS Custom Publishing Office.

SCIENCECAREERS.ORG

ScienceCareers
FROM THE JOURNAL SCIENCE AAAS

To book your ad:
advertise@sciencecareers.org

The Americas
202 326 6582

Europe/RoW
+44 (0) 1223 326500

China/Korea/Singapore/Taiwan
+86 186 0082 9345

Japan
+81 3 3219 5777

暨南大學 JINAN UNIVERSITY

Institute of Nanophotonics, Jinan University Invites Hight-Level Overseas Talents and Outstanding Young Talents

Institute of Nanophotonics, Jinan University is a newly established institution directly affiliated to the university and located in the new campus of Jinan University in Panyu District, Guangzhou, China.

The institute is directed by Professor Baojun Li, the Distinguished Professor of Changjiang Scholars and the winner of National Science Fund for Distinguished Young Scholars. The aim of the institute is to become a world-class research institute with high international reputation in the discipline of optics and photonics.

Institute of Nanophotonics focuses on the following four cutting-edge, fundamental and innovative research directions: (1) Nanophotonic materials and devices, (2) Optical trapping and manipulation, (3) Bionanophotonics, (4) Nanophotonics for energy. To adapt to the new national strategy and the new development of the university, the Institute of Nanophotonics cordially invites high-level overseas talents and outstanding young talents.

Requirements

1) Have obtained Ph.D from world famous universities or research institutions, and under 40 years old (45 for those who are extraordinarily excellent).

2) Have reached the world first-class research level in his or her field and have published excellent academic papers of significant impact in peer-reviewed journals either as the first author or the corresponding author.

3) Be hard-working, highly ethical and self-motivated, and good at team-working.

4) Priority will be given to the candidates who are (i) Distinguished Young Scholars in Thousand Talents Program, (ii) the holder of Outstanding Youth Fund in NNSF, (iii) Young Scholar in Changjiang Scholars, or (iv) Outstanding Young Talent.

Salary and Benefits

1) For successful candidates, Jinan University will offer internationally competitive salary, housing allowance, scientific research funding, etc.

2) For fresh graduates and postdoctoral fellows, the salary, subsidy and allowance will be following the related policy of Jinan University.

Contact information

Contact: Professor Baojun Li

E-mail: stslbj@outlook.com or wu2002li@163.com

Address: South Campus of Jinan University, Xingye Avenue East 855, Panyu Distinct, Guangzhou 511443, China

西南交通大學 Southwest Jiaotong University

Southwest Jiaotong University, Chengdu, China Invites Applications for the Academic Positions

Southwest Jiaotong University (SWJTU), founded in 1896 and located in Chengdu, the capital of Sichuan province--China's dynamically growing West. SWJTU is an elite university with national key multidisciplinary "211" and "985 Feature" projects directly managed by the Ministry of Education.SWJTU is currently on the strategic "Developing and Strengthening the University by Introducing and Cultivating talents" campaign. Thus, you are cordially invited to apply for the following academic positions. More information is available at *http://www.swjtu.edu.cn/*

Positions and Requirements

A. High-level Talented Leaders: Candidates should be qualified to be listed in national top talents programs such as Program of Global Experts, Top Talents of National Special Support Program, "Chang Jiang Scholars", China National Funds for Distinguished Young Scientists and National Award for Distinguished Teacher.

B. Young Leading Scholars: Candidates are preferable to be listed or qualified for the following programs: National Thousand Young Talents Program,The Top Young Talents of National Special Support Program (Program for Supporting Top Young Talents), Science Foundation for the Excellent Youth Scholars.

C. Excellent Young Academic Backbones

D. Excellent Doctors and Post Doctoral Fellows

Please contact Mr. Yu Wang, Ms. Ye Zeng,Ms.Qing Ya Wang

Telephone number: +86-28-66367238/ 66366202

Email: talent@swjtu.edu.cn

Address: Human Resources Department, SWJTU, Western Park of High-Tech Zone, Chengdu, Sichuan, China, 611756

第三軍醫大學

Recruiting High-level Medical Talents in the Third Military Medical University, Chongqing, China

The Third Military Medical University (TMMU), with a history of over 70 years, is located in the mountain city of Chongqing, one of the four municipalities directly under the jurisdiction of the Central Government of China. This university is a national key university, one of the military "2110 Project" key universities , and one of the first universities allowed to grant doctor's degree and to offer eight-year medical education program in China. Now, the TMMU is seeking high-level medical talents from home and abroad.

1. Positions and Remuneration Packages

1)Members of the national "One Thousand Talents Long–term Program": A settling-down allowance of 3 million yuan and 8-million-yuan research fund with an annual salary of 1 million yuan.

2)Members of the national "One Thousand Yong Talents Program": A settling-down allowance of 1 million and 500 thousand yuan and 5-million-yuan research fund with an annual salary of 400 thousand yuan.

2. Qualifications for the Position

1)Having the nationality of the People's Republic of China;

2)Be patriotic and willing to be devoted to national defense and health;

3)Having a strong academic and research ability, and be capable of undertaking major scientific research programs and engaging in original academic researches.

3.Salary and Benefits and Further More Information please check this link www.edu.cn/tmmu

Contact Person: Ms. Fan

Tel: +86-23-68752105 13883596876

Email: sydrcb@sina.com

Address: Cadre Office of Politics Department, Third Military Medical University, Gaotanyan No.30 Center Street, Shapingba District, Chongqing 400038, P.R.China.

ASSISTANT PROFESSOR

The University of Texas at Austin invites applications for a tenure-track faculty position at the Assistant Professor level in the Department of Integrative Biology. We seek a scientist whose work integrates perspectives from disparate fields of biology and spans levels of biological organization to ask big questions about the diversity and dynamics of life on Earth. The candidate's research should complement the department's existing strengths in evolution, ecology, behavior, genomics, and computational biology. We are also interested in candidates whose research program would benefit from the department's core resources in collections and field stations.

Candidates must have a strong research record, including influential publications and ability to obtain extramural research funding. Demonstrated excellence in teaching is also important, particularly the use of innovative teaching strategies. In addition, we seek candidates who contribute to diversity and equal opportunity within higher education, through their teaching, research, and service. The appointment will be made at the Assistant Professor level. A PhD or equivalent is required at the time of appointment, and postdoctoral research experience is expected.

Applicants should submit the following items, via Interfolio at **apply.interfolio.com/35641** with a cover letter, CV, research statement, teaching statement, and up to five reprints/preprints. Applicants should also arrange, through Interfolio, for three confidential letters of recommendation to be submitted. Applications received prior to **August 31, 2016** will be given full consideration. For additional information about the department, please go to https://integrativebio.utexas.edu/.

The University of Texas at Austin, as an Equal Opportunity/Affirmative Action Employer, complies with all applicable federal and state laws regarding nondiscrimination and affirmative action. The University is committed to a policy of equal opportunity for all persons and does not discriminate on the basis of race, color, national origin, age, marital status, sex, sexual orientation, gender identity, gender expression, disability, religion, or veteran status in employment, educational programs and activities, and admissions.

University of Zurich[UZH]

Faculty of Science

The Faculty of Science at the University of Zurich invites applications for a

Professor of Synthetic Biology (assistant tenure-track, associate or full)

in order to join the Department of Molecular Life Sciences.

Since Synthetic Biology is a new research area at the University of Zurich, we seek applicants who are internationally leading and are well established in the field. They must be able to attract and inspire new researchers in this field to contribute to and lead the growth of Synthetic Biology research in the Zurich area. The position is explicitly open-rank, encouraging applications at both the assistant professor (tenure-track), associate professor and full professor level. The successful candidate has an established high-profile track record and a proven ability to publish high-impact scientific work and attract 3rd party money.

Ideally, the candidate's research has sufficient affinity with ongoing research activities at the University in the areas of network biology, quantitative cell biology, single-cell biology and biological noise and physics of soft/biological/active matter, but excellence in research will be the primary criterion for selection. Contributing to the existing undergraduate and graduate teaching efforts (in English or German) in biology will also constitute an integral part of the position.

The University of Zurich provides generous research support, including dedicated funds for personnel and running expenses, and highly competitive start-up packages. Zurich's scientific environment includes a rich spectrum of research activities in computational science, engineering, chemistry, physics and biology and provides extensive opportunities for collaborations with research groups at the Faculty of Science of the University of Zurich and at the Eidgenössische Technische Hochschule Zürich (ETHZ). Also, it offers membership to various international graduate schools jointly run by the university and the ETHZ to recruit the best PhD students. The University of Zurich and the city of Zurich also offer a stimulating cultural environment and are family-friendly.

Application packages should include a motivation letter, a full curriculum vitae, a vision statement of research and teaching interests outlining major unsolved problems and how they could be tackled and the names and addresses of three potential referees. Documents should be addressed to Prof. Dr. Bernhard Schmid, Dean of the Faculty of Science, University of Zurich, and uploaded as **a single PDF file** to http://www.mnf.uzh.ch/SB by 3. August 2016. A brief questionnaire will have to be filled out at the beginning of the upload process. For further information, please contact Prof. Dr. Lucas Pelkmans at lucas.pelkmans@imls.uzh.ch.

The University of Zurich is an equal opportunities employer.

10 ways that *Science* Careers can help advance your career

1. Register for a free online account on **ScienceCareers.org**.
2. Search thousands of job postings and find your perfect job.
3. Sign up to receive e-mail alerts about job postings that match your criteria.
4. Upload your resume into our database and connect with employers.
5. Watch one of our many webinars on different career topics such as job searching, networking, and more.
6. Download our career booklets, including Career Basics, Careers Beyond the Bench, and Developing Your Skills.
7. Complete an interactive, personalized career plan at "my IDP."
8. Visit our Career Forum and get advice from career experts and your peers.
9. Research graduate program information and find a program right for you.
10. Read relevant career advice articles from our library of thousands.

Visit **ScienceCareers.org** today — all resources are free

ScienceCareers
FROM THE JOURNAL SCIENCE AAAS

By **Melanie L. Blanchette**

The measure of success

When I was a Ph.D. student, a respected professor at our school had a heart attack in his office and died. As he was whisked away to the ambulance, I numbly watched familiar faces in the department succumb to shock. I didn't know it at the time, but this deeply troubling experience would shape my thinking about how to craft my academic career after I faced my own life-changing illness. While I was a postdoc, a sudden neurological disorder left me unable to walk, took my vision, and held me in the grip of vertigo and crushing migraines. With the help of a small army of health professionals, I began to improve. My brain started compensating for the lost neurons, and my muscles learned to fire again, but I don't know whether I will ever recover completely. This harsh reality check has made me think seriously about why academia promotes unhealthy work habits and how I can pursue the research I love while also taking care of myself.

Prior to my illness, I worked extremely long hours, sometimes even sleeping in my office if I faced a deadline. I hoped that my hard-won achievements would eventually be judged worthy of tenure. When I returned to work after my illness—despite its severity, I took just 2 months off because of dwindling sick leave, increasing medical bills, and no certainty of ongoing employment—I fell back into the academic achievement trap. I spent all my time working and worrying, and my health began to decline again.

But fear of a relapse made me question my actions and, ultimately, the trajectory of my career. I thought about the professor who died. I thought about a friend who left academia because the pace and environment had negative mental and physical effects. I realized that my years in academia had eroded my mental health. I didn't want to hurt myself permanently by pursuing career advancement at all costs, but I didn't want to leave either. So I decided to accept my physical limitations and—an even more difficult task—shed my prejudices about what a successful career looks like.

Now, with the support of academic and industry mentors, I am building a nontraditional academic path. I am still a university research fellow, but my research into how mining companies can decrease their environmental impact is funded by industry. For these funders, what matters more than my publication record or the "prestige" of my institution is my creativity, integrity, and ability to produce rigorous science that solves real-world problems. I feel like a pressure valve has been released in my life, easing the worries and long hours and allowing me to better manage my illness. And I find applied research immensely satisfying. Watching nutrient-rich water rejuvenate an acidic mine pit lake, I have seen that my work has value beyond contributing to my h-index. Perhaps most importantly, I was well enough to be there to witness it.

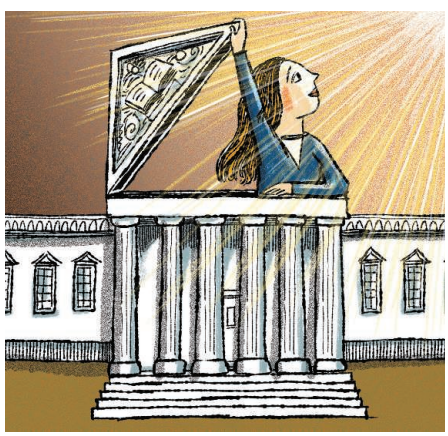

"I ... shed my prejudices about what a successful career looks like."

My illness made me think about my behavior and health in a way that I hadn't earlier in my career. Now, when I'm tired, I rest—even if I'm in the field. My actions and the direction of my career have surprised some of my colleagues, who sometimes make off-the-cuff comments about my "laziness." These hurt, but I know that I'm doing the right thing for myself. I hope that others will also prioritize their personal well-being, even if it means letting go of deeply held beliefs about what we are "supposed" to do for our careers.

According to the numbers, my chances for long-term success in academia don't look great. Women and people with disabilities are underrepresented, and belonging to both groups puts me in a particularly difficult position. But rather than focusing on what members of underrepresented groups need to do to "adapt" to academic culture, we should be interrogating the system itself, which expects all of us to work excessively at the expense of our physical and mental health. Maybe we need new measures of success. ■

Melanie L. Blanchette is a research fellow at Edith Cowan University in Perth, Australia. Send your story to SciCareerEditor@aaas.org.